Test Particle Studies of Acceleration and Transport in Solar and Tokamak Plasmas

Robert McKay

A Thesis presented for the degree of
Doctor of Philosophy

Astronomy and Astrophysics Group
Department of Physics and Astronomy
University of Glasgow
Glasgow, G12 8QQ

October 2008

Test Particle Studies of Acceleration and Transport in Solar and Tokamak Plasmas

Robert McKay

Submitted for the degree of Doctor of Philosophy
October 2008

Abstract

A test particle approach is used to study two distinct plasma physics situations. In the first case, the collisionless response of protons to cold plasma fast Alfvén waves propagating in a non-uniform magnetic field configuration (specifically, a two-dimensional X-point field) is studied. The field perturbations associated with the waves, which are assumed to be azimuthally-symmetric and invariant in the direction orthogonal to the X-point plane, are exact solutions of the linearized ideal magneto-hydrodynamic (MHD) equations. The protons are initially Maxwellian, at temperatures that are consistent with the cold plasma approximation. Two kinds of wave solution are invoked: global perturbations, with inward- and outward-propagating components; and purely inward-propagating waves, localised in distance from the X-point null, the wave electric field $\mathbf{E}$ having a preferred direction. In both cases the protons are effectively heated in the direction parallel to the magnetic field, although the parallel velocity distribution is generally non-Maxwellian and some protons are accelerated to highly supra-thermal energies. This heating and acceleration can be attributed to the fact that protons undergoing $\mathbf{E} \times \mathbf{B}$ drifts due to the presence of the wave are subject to an effective force in the direction parallel to $\mathbf{B}$. The localised wave solution produces more effective proton heating than the global solution, and successive wave pulses have a synergistic effect. This process, which could play a role in both solar coronal heating and late-phase heating in solar flares, is effective for all ion species, but has a negligible direct effect on electrons. However, both electrons and heavy ions would be expected to acquire a temperature comparable

to that of the protons on collisional timescales.

In the second case the same approach is used to study the collisional transport of impurity ions (carbon, mainly, although tungsten ions are also simulated) in spherical tokamak (ST) plasmas with transonic and subsonic toroidal flows. The efficacy of this approach is demonstrated by reproducing the results of classical transport theory in the large aspect ratio limit. The equilibrium parameters used in the ST modelling are similar to those of plasmas in the MAST experiment. The effects on impurity ion confinement of both counter-current and co-current rotation are determined. Various majority ion density and temperature profiles, approximating measured profiles in rotating and non-rotating MAST plasmas, are used in the modelling. It is shown that transonic rotation (both counter-current and co-current) has the effect of reducing substantially the confinement time of the impurity ions. This effect arises primarily because the impurity ions, displaced by the centrifugal force to the low field region of the tokamak, are subject to a collisional diffusivity that is greater than the flux surface-averaged value of this quantity. For a given set of plasma profiles, the carbon ions are found to be significantly less well-confined in co-rotating plasmas than in counter-rotating plasmas, although the difference in confinement time between co- and counter-rotation lessens as the mass of the impurity increases. In the case of carbon ions the poloidal distribution of losses exhibits a pronounced up/down asymmetry that is consistent with the direction of the net vertical drift of the impurity ions. Increasing the mass of the impurity ion is also found to significantly decrease the confinement time in the rotating cases, though the confinement time for the case of a stationary plasma is increased. Such studies of impurity transport within tokamaks are important because it is desirable to expel impurity ions from the plasma to avoid both dilution of the fuel ions and unacceptable radiation losses from the plasma.

Declaration

The work in this thesis is based on research carried out at the Astronomy & Astrophysics Group in the Department of Physics and Astronomy, University of Glasgow, Scotland. No part of this thesis has been submitted elsewhere for any other degree or qualification and is all my own work unless referenced to the contrary in the text.

Acknowledgements

The irony of this thesis is that, having written it, I now feel vaguely like I'm ready, that I now know enough - more or less - to actually do a half-decent job of my PhD. Which is slightly annoying. I guess that means that the training process wasn't completely wasted on me, but it would have been nice to have been equipped with some of the myriad information I've accumulated three years ago. Anyway, to the acknowledgements - apologies if this rambles on for a length of time that puts even tearful Hollywood Oscar-winning speeches to shame, but I'm making damn sure to milk this and mentioning everyone that I want to mention. If I forgot a name, my sincerest apologies - it's not personal.

Firstly, thanks to my two supervisors, Dr. Lyndsay Fletcher and Dr. Ken McClements. Lyndsay's passion and enthusiasm for the Sun and all things solar is amazing...Ken's knowledge of plasma physics is extremely thorough, and his efforts to impart it to me will not be forgotten. I hope both of them did not get thoroughly sick of me asking daft questions, months after I really ought to have asked them! Appreciation also to Chippy Thyagaraja for his thoughts and input. I should also mention PPARC/STFC for giving me money, and a very big thanks to UKAEA Culham for going above and beyond the call of duty financially not just once, but twice - much appreciated.

Secondly, thanks to my family - my mum, dad and brother - for raising me right and giving me the best opportunities possible, and putting up with the endless moaning and stress about exams and studying and research. They deserve a medal for that alone, god knows. Thanks to Sandra, for feeding me on Tuesdays! And thanks to the dog, the happy bundle of fur we knew as Sheba, now sorely missed. The spirit was willing, right to the end, but the flesh was weak. We all miss you

very much. (Update - new dog labradoodle Dusty has just as much, if not more, "get-up-and-go"!)

Thirdly, thanks to the "Bob Harvey Collective" (don't ask), the gang who made my years at uni all the worthwhile. In no particular order they are: Craig Stark (World Plasma Champion and Bob Harvey founder), Jen Toher (who also appreciates the genius of the chip wrap), Iain Martin (the archetypal scientist and another Geometry Wars convert), Mairi McCallum (scarily good Wii Sports boxer), Andy Gilston (the Road Trip-Master General), Gordon Hill (techie geek and all round Mac boy), Jenn Scott (who hates James Allen even more than I do), Jennifer Pollock (a.k.a. Battle Jen), Laura Reid (who could stress for Scotland!), Helen Scott (the celebrity coastguard) and Alan Cumming (car enthusiast extraordinaire).

Thanks to the Astro group here at Glasgow, for being cool and helpful and for buying biscuits (nearly) every day. Special mentions to my office mates Eamonn Scullion (1st year) and Procheta Mallik (2nd/3rd year) for being funny, bonkers (in the case of Eamonn) and allowing me near-complete impunity over the temperature control of the office, allowing me to have the room at a constant oh-my-god-how-hot-is-it-in-here Centigrade. A big shout to the "Solar Self-Help" group, of which Hazel (the most enthusiastic solar physicist PhD.-type I know) and I are founder members - it's good to have a place where we can move from the darkness of ignorance to the light of understanding, or something. More special mentions to: Craig M, for many games of badminton amongst other things; Fiona S, who was always happy to discuss internet-streamed snooker championships; Russell and Colin, who get the 80's video games/afternoon biscuit thing, respectively, as much as I do; Ed B, for having a very similar sense of humour; Hugh P and Ross for, between them, knowing at least something about virtually everything; and cheers to Luis for that innate ability to walk into the office, take one look at what I'm doing and instantly know thirty-seven times as much about it as I do, but always offer that information straight up. Finally in this category, thanks to Iain Sim for his tireless work in propping up the Astro Difference Engine and continually fixing the F95 compiler, and thanks to Daphne Davidson, (now former) Group Secretary, for all the help with bureaucracy, claim forms, and random stationery. The group will struggle to

function without her.

I am indebted to my high school physics teacher, Mrs. Donohoe - if she hadn't taken over from the lame duck teacher our class had prior, and taught us the subject in an enthusiastic and comprehensive yet easily digestible way, I seriously doubt I would even have managed a Credit level pass at Standard Grade, let alone the Higher/CSYS.

And finally, before we get this thing off and running, thanks to Iain Broudie and his Lightning Seeds for the perfect, shimmering, shiny pop that was and still is my soundtrack (we're still waiting for the new album, but the wait is almost over, ten long years since the last one), and, most importantly of all, thanks to Formula 1 for being my passion, my drive and my *raison d'être*. God knows I couldn't have done it without them.

Right, let's do this!

Summary

The work of this thesis has been quite diverse, taking in as it has a mixture of both solar physics and tokamak plasma physics. The underlying connection between the two projects has been in the approach taken, by calculating the orbits of test particles within the relevant electric and magnetic fields.

Chapter 1 consists of a qualitative overview of the structure of the Sun, magnetic reconnection and solar flares. Chapter 2 is an overview of fusion plasma physics: issues concerning tokamak plasma equilibrium, classical transport and impurities are discussed. The nature of these topics means that a more mathematical description than Chapter 1 is included. Chapter 3 is devoted to the test particle approach, explaining the algorithm employed to model them in our codes throughout the course of the thesis. Chapter 4 is a discussion of some published work on fast Alfvén wave heating and acceleration of ions in a non-uniform magnetoplasma, and Chapters 5 and 6 consist of (also published) work on the collisional transport of impurity ions in a rotating spherical tokamak plasma: both Chapters 4 and 6 include detailed reviews of recent literature. Chapter 7 is a discussion of potential future work that could be attempted, and expands upon exactly how some of it could be achieved.

Contents

List of Figures

List of Tables

"Feel like a sundial in the shade
Where flowers fade"

The Lightning Seeds
"Where Flowers Fade"

Chapter 1

Solar Astrophysics

1.1 The Sun: An Introduction

Eight light-minutes away from us lies an extraordinarily complex astrophysical body. Bound by its own self-gravity yet held up due to the pressure of the incessant nuclear reaction occurring within, the burning ball of gas we know as the Sun, the closest star to Earth, dominates our planetary system. Approximately 98% of the mass of the Solar System is attributable to the Sun, with its radius of $R_\odot = 6.96 \times 10^8$m and mass of $M_\odot = 1.989 \times 10^{30}$kg [1] dwarfing even the gas giants of Jupiter and Saturn. For 4.5 billion years this body has provided energy, in the form of radiated heat and light, in quantities so large as to render them virtually meaningless to humans: the energy output of the Sun *per second*, approximately 3.86×10^{26}J, is around 6 orders of magnitude higher than the approximate 5×10^{20}J of energy the human race used in the entire *year* of 2004. And yet, for all the superlatives and astronomically large numbers we can assign to the Sun, it remains a relatively young, relatively small, relatively *ordinary* star. However, the next nearest star, Proxima Centauri, is so far away that the light that we observe from it was radiated over 4 years prior to our detection, and so our ordinary Sun receives our extraordinary attention as the most practical example of stellar physics we can comfortably study. This is not to ignore the important fact that the small distance, in cosmological terms, between

us and the Sun means that we are constantly affected by its continually-varying activity, in the form of geomagnetic storms, aurorae, and climactic variability. Thus observing and studying the Sun has motivations of both practical and theoretical interest. Additionally, the Sun's relative banality means that we can be comfortable that that which we are studying and learning is extrapolatable and applicable across stellar physics in general, and that we are not studying some isolated, extreme case.

The earliest observations of the Sun were naturally crude, with observations being made either with the naked eye or during rare solar eclipses. The invention of the telescope in the 17th century provided the first tool remotely capable of resolving any fine detail on the solar disc, with the discovery of sunspots (dark patches on the solar disk), usually attributed to Galileo Galilei, the first major observational breakthrough. By continually recording the number of observed sunspots over many decades and even centuries, it has been determined that the Sun has experienced periodic levels of activity on both short and longer periods: around every 11 years or so the number of sunspots, an indirect measure of the activity of the Sun, peaks and falls - this is known as the *sunspot cycle*. On longer timescales, sunspot number has been seen to vary irregularly and unpredictably - for example, sunspot activity almost entirely disappeared for a period of around 70 years during the 17th century, a time known as the *Maunder Minimum*. Hale's discovery that sunspots were magnetic [2], with each spot having a partner with opposite magnetic polarity, was a key one. A sunspot is darker than the surrounding photosphere because the magnetic field inhibits heat transport via convection and cross-field conduction there, and so the sunspot plasma is cooler than the surrounding plasma. The understanding that magnetic fields played an important role in the Sun was the primer for most of the research that has come since.

Observational techniques today are considerably more advanced than the primitive methods used to make the initial observations of the Sun. The arrival of the computer and space ages, with complex satellites using multiple detectors and systems, has given us the ability to put mini-observatories above our atmosphere. This is especially important if we want to observe in windows of the electromagnetic spectrum that the atmosphere of the Earth is particularly good at blocking out,

such as X-rays, gamma rays, and ultraviolet (UV) light. Studies of the Sun at these wavelengths have become the norm, given the extreme energetic violence of many solar processes such as flares, though multi-wavelength and multi-instrument studies are important in providing an overall picture of the Sun's structure and processes: this is illustrated in Figures 1.1 and 1.2. Note that the images in Figure 1.2 are not all taken at the same time.

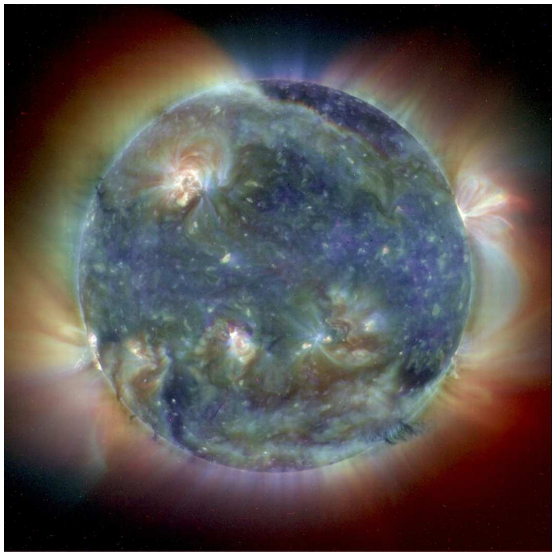

Figure 1.1: A composite image taken by SoHO (Solar and Heliospheric Observatory), which combines data taken by the EIT (Extreme ultraviolet Imagining Telescope) instrument from three wavelengths, namely, 171, 195 and 284 Å (denoted by red, yellow and blue respectively). Image from *http://sohowww.nascom.nasa.gov/gallery/images/trico1.html*.

Over the last two decades several important observing space missions, such as Yohkoh, TRACE, SoHO, RHESSI *et al.* have recorded a wealth of data from the Sun. Much work has been carried out in attempting to reconstruct the all-important magnetic fields by combining these observations with theory and simulation (see Figure 1.3). Observations of the magnetic field come from magnetograms, which make use of the quantum-mechanical Zeeman splitting effect of spectral lines. The degeneracy of an electronic configuration will be broken by the presence of a magnetic field, which causes a spectral line to split into multiple components. The splitting in wavelength is proportional to the field, and so this can be used to determine the line of sight magnetic field strength of the solar surface, where the fields of sunspots break through - estimates suggest the field strength of sunspots is approximately

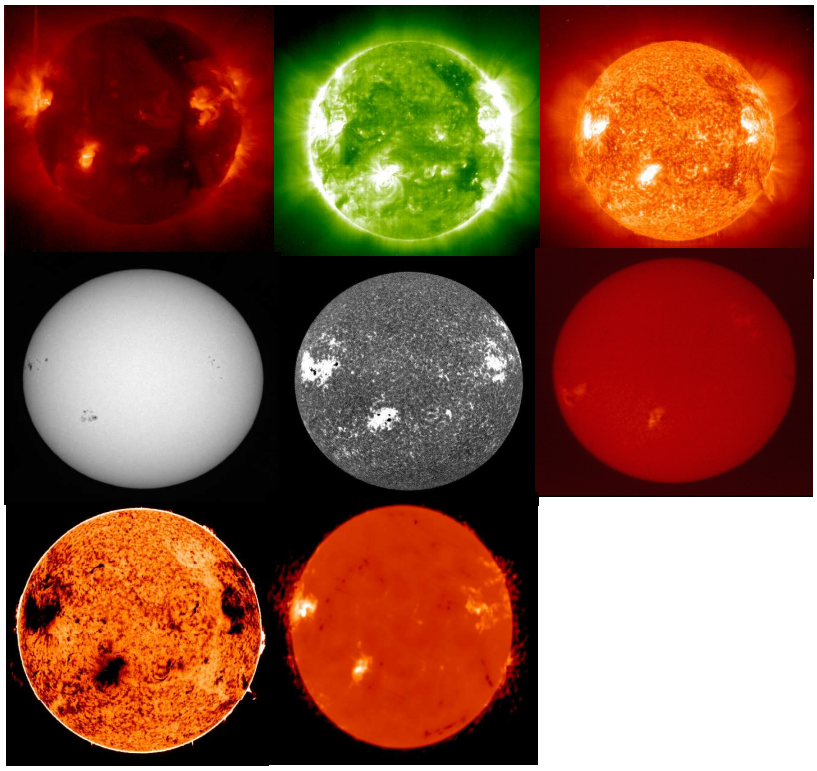

Figure 1.2: Multiwavelength images of the Sun in (from top left to right): X-ray (Yohkoh), UV (SoHO), EUV (SoHO), visible white light (BBSO), calcium-K (BBSO), H_α (Learmonth), Infra-red (NSO) and radio (Nobeyama). Images from *http://coolcosmos.ipac.caltech.edu/*.

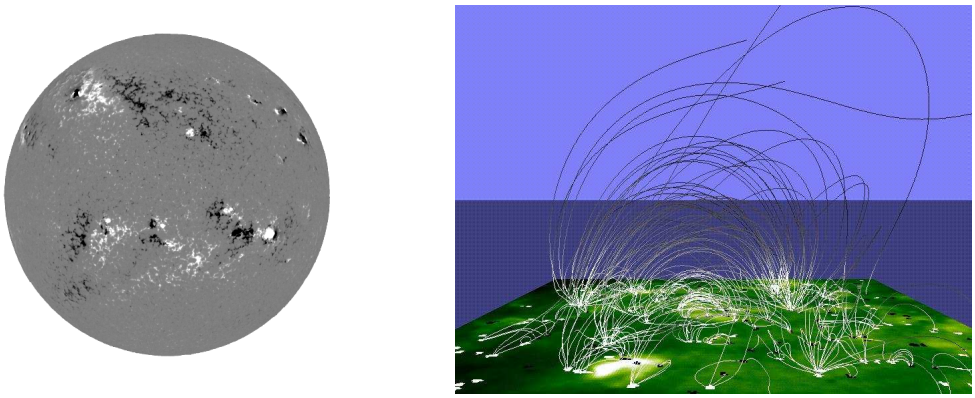

Figure 1.3: Left - Magnetogram of the Sun, taken by MDI (Michelson-Doppler Imager, onboard SoHO). The darker areas are regions of "south" (inward-directed) magnetic polarity and the whiter areas are "north" (outward-directed) magnetic polarity. Image from *http://solar-center.stanford.edu/images/890407.gif*. Right - a reconstruction of the "magnetic carpet" of the Sun. Image from *http://umbra.nascom.nasa.gov/ssu/view1.jpg*.

0.01-0.1T. Reconstructing the field lines themselves is difficult, involving the use of magnetic fields calculated by assuming them to be either potential ($\nabla \times \mathbf{B} = 0$) or force-free ($\mathbf{j} \times \mathbf{B} = 0$), under reasonable boundary conditions which we do not go into in detail here.

1.2 Structure of the Sun

Having hundreds of gigabytes of data from the observing missions mentioned in the previous section has allowed us to improve upon our knowledge of the outer layers of the Sun's atmosphere, which are transparent to electromagnetic radiation. The same is not true of the solar interior, but helioseismology, coupled with complex computer models of stellar structure, has helped crystallise our understanding of the various "layers" that make up the Sun's overall composition, as illustrated by Figure 1.4. In this section we briefly examine each layer in turn, starting from the centre of the Sun and working outwards.

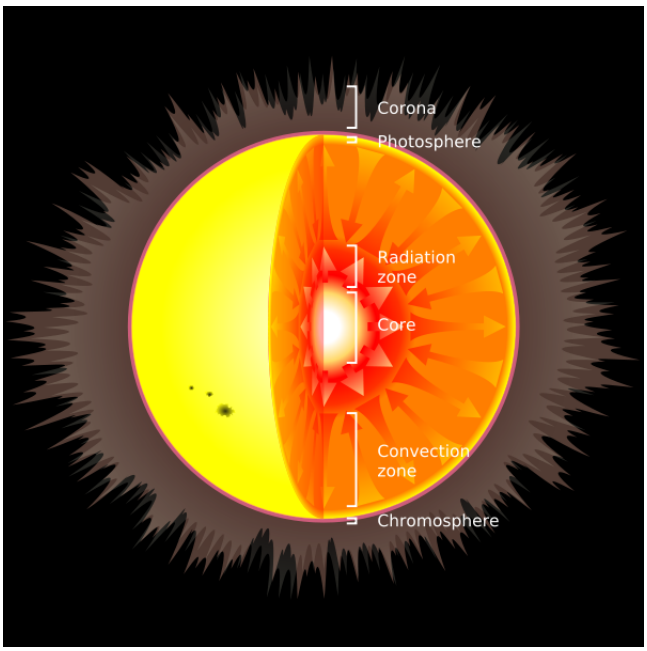

Figure 1.4: Artist's impression of the structure of the Sun. Image from *http://en.wikipedia.org/wiki/Image:Solar_internal_structure.svg*.

1.2.1 Core

Extending to a radius of approximately $0.2R_{\odot}$, the *core* has the highest temperatures and densities of the whole Sun: the temperature is estimated to be around 15 million K, and the density approximately 1.5×10^5 kg m^{-3} [3]. The core is where the thermonuclear fusion reactions occur that provide the Sun with energy by creation of heavier elements such as helium (He) from lighter ones such as hydrogen (H) by the process of *fusion*, as evidenced by the observation of neutrinos (byproducts of these fusion reactions - Chapter 2 contains more detail on this) at Earth originating from the Sun. At the start of the Sun's life, the mass fraction of hydrogen at the core was approximately 0.71, and that of helium was around 0.27 (the remainder was trace amounts of heavier elements such as carbon (C), nitrogen (N) and oxygen (O)), but as the Sun has aged those values have changed to $\simeq 0.34$ and 0.64 respectively as fusion depletes the hydrogen fuel source.

1.2.2 Radiative and convective zones

The energy produced in the core is transported outwards by two different methods. The *radiative zone*, extending from around $0.2R_{\odot}$ to $0.7R_{\odot}$, transfers the energy produced in the core by various contributions to the opacity of the solar atmosphere through processes such as bound-bound, free-free or bound-free absorption [4]. In *bound-bound* absorption, a bound electron orbiting an atomic nucleus absorbs the energy of a photon, causing it to make a transition to a higher bound state. If the energy of the incident photon is greater than the ionisation potential, the electron can escape the atom and become free - this process is known as *bound-free* absorption. Bound-bound transitions produce the emission and absorption lines in the solar spectrum, whereas bound-free transition produce continua such as the Balmer and Lyman series. In *free-free* absorption a free electron can either gain or lose energy as it moves in the Coulomb field of an atom or ion, resulting in either the emission or absorption of a photon. This process is responsible for, amongst others, the coronal X-ray continuum emission. There are also additional contributions from Thomson scattering of photons by free electrons, which is a continuum scattering process with

no wavelength dependence, and the continuum of heavier elements. In the *convective zone*, which takes over from $0.7R_\odot$ for the remainder of the solar radius, the energy transfer mechanism is thermal convection: large flows of plasma carry hot material to the surface, and as it cools near the top, falls back down to the bottom of the plasma column and receives more heat, starting the process again. This process can be observed as "granulation" on the surface of the Sun.

Radiative transfer does not occur in the convective zone (the plasma is not dense or hot enough) and convective transfer does not occur in the radiative zone - a transition layer known as the *tachocline* separates the two sharply-differing zones. The density of the radiative zone (and to a lesser extent the convective zone) is such that the photons only travel a very brief distance between interactions, and it takes many orders of magnitude more time for the photons to reach the surface of the Sun from the core than to reach the Earth from the Sun's edge (estimates put the photon travel time within the Sun to be between 10^4 and 2×10^5 years [3], compared to the 8 light minutes travel time to Earth) despite the fact the net distance (i.e. not the actual distance of the random walk of the photon) travelled to the photosphere is much less.

1.2.3 Photosphere

The *photosphere* is the visible surface of the Sun. Below this layer the Sun is opaque to visible light. The photosphere is the "sharp edge" of the Sun because the optical depth τ changes dramatically with height over a very short distance: in the isothermal plane-parallel approximation

$$\tau = \sigma n(0) h e^{-z/h} \tag{1.1}$$

where σ is the scattering cross-section, $n(0)$ is the number density of particles at the surface of the Sun, and h the isothermal "scale height" of the atmosphere

$$h = \frac{2k_B T}{m_p g} \tag{1.2}$$

where k_B is Boltzmann's constant, T the temperature of the photosphere (around

6000K), m_p the proton mass and g the local gravity ($g = GM_\odot/R_\odot^2$). Equation 1.1 arises from hydrostatic equilibrium in a plane-parallel atmosphere, combined with the definition of optical depth in terms of opacity. The opacity in the photosphere is due to a combination of (wavelength-dependent) effects, such as H^- ion bound-free and free-free transitions, as well as Thomson scattering and other contributions. As such normally a mean opacity, known as the *Rosseland mean opacity* (κ), is defined. With these assumptions, τ falls by a factor e in exactly 1 scale height (360 km) - and since

$$\frac{h}{R_\odot} \simeq 5 \times 10^{-4}, \tag{1.3}$$

we see a sharp edge to the photosphere: τ goes from being much greater than 1 to much less than 1 in around a thousandth of a solar radius.

1.2.4 Atmosphere

In the same way that Earth's atmosphere can be divided into layers such as the mesosphere, troposphere, stratosphere etc., the same can be done for the Sun's atmosphere (all the layers above the photosphere). The *chromosphere* is a very thin layer, around 2000 km thick, which is seen in H_α as a pink emission rim during eclipses (or through H_α filters). Around 500 km above the photosphere the temperature of the chromosphere drops to a minimum of about 4300K [4] but above this level the temperature climbs steadily, reaching a peak of roughly 10^4K, before jumping by a factor of approximately 10 in just a few hundred kilometres in a region known as the *transition region* (see Figure 1.5), which joins the chromosphere with the *corona*. The corona is a very hot (1-2 million K), irregular zone extending out to several solar radii. The corona is seen in the X-ray continuum, in UV emission lines, and in white light, for example with a coronagraph or during an eclipse (Figure 1.6).

Many years spent observing the solar atmosphere has revealed the presence of various large-scale structures in the corona, chromosphere and photosphere (Section 1.5.1 discusses coronal structures). A combination of fluid mechanics and electromagnetism known as *magnetohydrodynamics* (MHD) is capable of providing a good

description of such large scale disturbances. In the next section we shall discuss MHD in more detail.

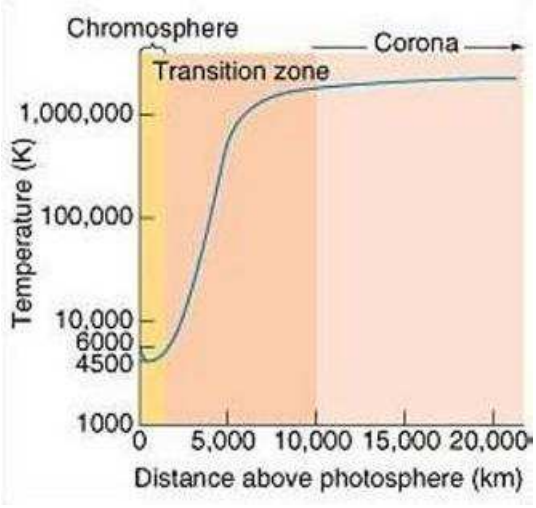

Figure 1.5: Variation of temperature across the chromosphere, transition region and corona. Image from *http://cseligman.com/text/sun/sunlayer2.jpg*.

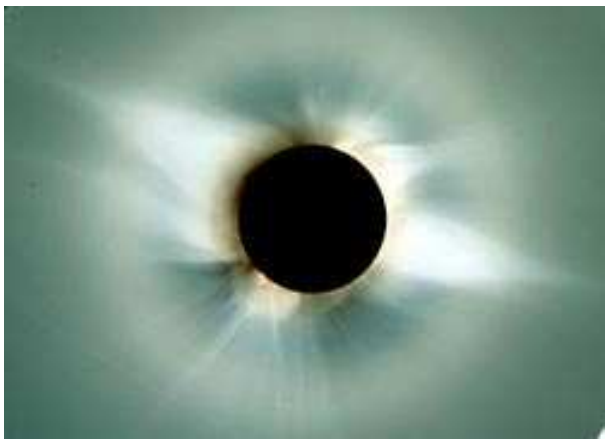

Figure 1.6: Photograph of the corona in white light made with a coronagraph. Image from *http://sunearthday.nasa.gov/2007/multimedia/gal_019.php*.

1.3 MHD and Alfvén Waves

1.3.1 Magnetohydrodynamics

Throughout this thesis, and indeed throughout the fields of solar astrophysics and tokamak plasma physics in general, the physics of MHD is utilised. Thus a short

section recapping the simplifications and equations of MHD, and from them the derivation of the propagating wave modes that an MHD plasma can support, is in order. The model equations are simply stated [5] - firstly, the standard hydromagnetic equations for a single fluid plasma, namely:

$$\frac{\partial \rho}{\partial t} + \nabla \cdot (\rho \mathbf{v}) = 0 \tag{1.4}$$

$$\rho \left(\frac{\partial}{\partial t} + \mathbf{v} \cdot \nabla \right) \mathbf{v} = -\nabla p + \mathbf{j} \times \mathbf{B} \tag{1.5}$$

$$\left(\frac{\partial}{\partial t} + \mathbf{v} \cdot \nabla \right) \left(p \rho^{-5/3} \right) = \frac{2}{3} \rho^{-5/3} \eta J^2 \tag{1.6}$$

$$\mathbf{E} + \mathbf{v} \times \mathbf{B} = \eta \mathbf{j}, \tag{1.7}$$

assuming both scalar pressure and resistivity, where

$$n_{tot} = n_i + n_e \tag{1.8}$$

$$\rho = \rho_i + \rho_e = n_i m_i + n_e m_e \tag{1.9}$$

$$\mathbf{v} = (\rho_i \mathbf{v}_i + \rho_e \mathbf{v}_e)/\rho \tag{1.10}$$

$$q = q_i n_i - e n_e \tag{1.11}$$

$$\mathbf{j} = n_i q_i \mathbf{v}_i - n_e e \mathbf{v}_e \tag{1.12}$$

$$p = p_i + p_e \tag{1.13}$$

are the equations for number density n, mass density ρ, bulk velocity $\mathbf{v}$, charge density q, total current $\mathbf{j}$ and total pressure p respectively, and subscripts i and e denote ions and electrons. Equations 1.4-1.7 are the continuity, momentum and energy equations, and Ohm's Law, respectively.

These equations are combined with the reduced electromagnetic equations

$$\nabla \times \mathbf{B} = \mu_0 \mathbf{j} \tag{1.14}$$

$$\nabla \times \mathbf{E} = -\frac{\partial \mathbf{B}}{\partial t} \tag{1.15}$$

$$\nabla \cdot \mathbf{B} = 0 \tag{1.16}$$

$$\nabla \cdot \mathbf{E} = 0, \tag{1.17}$$

where $\mathbf{E}$ and $\mathbf{B}$ are the electric and magnetic fields respectively and μ_0 is the vacuum permeability. The motivation behind this model lies in characterising slow timescale/long wavelength behaviour, hence the removal of the displacement current term $\mu_0 \epsilon_0 \frac{\partial \mathbf{E}}{\partial t}$ from Ampère's Law (Eq. 1.14), due to its association with high-frequency effects. This results in a relatively simple system, but with the penalty that electromagnetic waves cannot be described in this model. Additionally other simplifications are made, such as ignoring the $\frac{1}{nq}\mathbf{j} \times \mathbf{B}$ Hall current term of Ohm's law, Eq. 1.7 (which arises from the nature of current flow in a conductor). In the special case where $\eta = 0$, i.e. the plasma is perfectly-conducting, this model is known as "ideal MHD". From these equations, the general dispersion relation for waves in a uniform ideal MHD plasma can be derived.

1.3.2 Ideal MHD wave modes

To look for small departures or perturbations from an ideal MHD stationary equilibrium with uniform pressure and density, equations 1.4-1.7 can be linearised to give:

$$\frac{\partial \rho_1}{\partial t} + \rho_0 \nabla \cdot \mathbf{v}_1 = 0 \tag{1.18}$$

$$\rho_0 \frac{\partial \mathbf{v}_1}{\partial t} = -\nabla p_1 + \mathbf{j}_1 \times \mathbf{B}_0 \tag{1.19}$$

$$\frac{\partial p_1}{\partial t} = \frac{\gamma p_0}{\rho_0} \frac{\partial \rho_1}{\partial t} \tag{1.20}$$

$$\mathbf{E}_1 + \mathbf{v}_1 \times \mathbf{B}_0 = 0 \tag{1.21}$$

where subscripts 0 denote the equilibrium quantity and 1 the perturbation to the equilibrium. The assumption of uniform equilibrium pressure means that we are

assuming that the equilibrium is force-free, and $\mathbf{j}_0 = 0$. It is worth pointing out that one *could* still have an equilibrium current in this case - it is possible to have a force-free equilibrium with $\mathbf{j}_0$ finite - but it would have to be orthogonal to the equilibrium field. Assuming that all the perturbations behave as $\exp[i(\mathbf{k}\cdot\mathbf{r} - \omega t)]$, then the equations 1.18-1.20 and 1.15, 1.16 give

$$-i\omega\rho_1 + \rho_0 i\mathbf{k}\cdot\mathbf{v}_1 = 0 \tag{1.22}$$

$$\omega\mathbf{v}_1\rho_0 = \mathbf{k}p_1 + \left(\frac{\mathbf{B}_0\cdot\mathbf{B}_1}{\mu_0}\right)\mathbf{k} - \left(\frac{\mathbf{k}\cdot\mathbf{B}_0}{\mu_0}\right)\mathbf{B}_1 \tag{1.23}$$

$$p_1 = c_s^2\rho_1 \tag{1.24}$$

$$\omega\mathbf{B}_1 = (\mathbf{k}\cdot\mathbf{v}_1)\mathbf{B}_0 - (\mathbf{k}\cdot\mathbf{B}_0)\mathbf{v}_1 \tag{1.25}$$

$$\mathbf{k}\cdot\mathbf{B}_1 = 0 \tag{1.26}$$

respectively, where the sound speed c_s is defined as

$$c_s = \sqrt{\frac{\gamma p_0}{\rho_0}} \tag{1.27}$$

where $\gamma = 5/3$ is the ratio of specific heats. Choosing $\mathbf{B}$ to be along the z-axis and the angle between $\mathbf{k}$ and $\mathbf{B}$ to be θ, and defining the unit vectors $\hat{\mathbf{b}}$ and $\hat{\mathbf{z}}$ by the expressions $\mathbf{B_0} = B_0\hat{\mathbf{b}}$ and $\mathbf{k} = k\hat{\mathbf{z}}$ respectively, the above equations can be combined to give

$$[\omega^2 - k^2c_A^2(\hat{\mathbf{z}}\cdot\hat{\mathbf{b}})]\mathbf{v}_1 = [k^2(c_s^2+c_A^2)\hat{\mathbf{z}} - k^2c_A^2(\hat{\mathbf{z}}\cdot\hat{\mathbf{b}})\hat{\mathbf{b}}]\times(\hat{\mathbf{z}}\cdot\mathbf{v}_1) - k^2c_A^2(\hat{\mathbf{z}}\cdot\hat{\mathbf{b}})(\hat{\mathbf{b}}\cdot\mathbf{v}_1)\hat{\mathbf{z}} \tag{1.28}$$

where the *Alfvén velocity* c_A is defined as

$$c_A = \sqrt{\frac{B^2}{\mu_0\rho}}. \tag{1.29}$$

Considering the component of $\mathbf{v}$ perpendicular to $\hat{\mathbf{z}}$ shows that there is a mode with

$$\omega^2 = c_A^2k^2\cos^2\theta = c_A^2k_z^2 \tag{1.30}$$

- this is known as the *Alfvén mode* or the *shear wave*, and has a wave vector moving in the z-direction (parallel to the magnetic field) at the Alfvén speed, as plasma is displaced perpendicular to both the wave vector and the magnetic field.

Considering the velocity components of Eq. 1.28 in the $\hat{\mathbf{z}}$ and $\hat{\mathbf{b}}$ direction gives the equations

$$[\omega^2 - k^2(c_s^2 + c_A^2)](\hat{\mathbf{z}} \cdot \mathbf{v}_1) = -k^2 c_A^2 \cos\theta(\hat{\mathbf{b}} \cdot \mathbf{v}_1) \tag{1.31}$$

$$\omega^2(\hat{\mathbf{b}} \cdot \mathbf{v}_1) = k^2 c_s^2 \cos\theta(\hat{\mathbf{z}} \cdot \mathbf{v}_1) \tag{1.32}$$

respectively, which can be simplified to give the dispersion relation

$$\frac{\omega^2}{k^2} = \frac{1}{2}\left(c_s^2 + c_A^2\right) \pm \frac{1}{2}\sqrt{\left[(c_s^2 + c_a^2)\right]^2 - 4c_s^2 c_A^2 \cos^2\theta}. \tag{1.33}$$

This describes the *magnetosonic* modes, where the + solution corresponds to the fast wave and the − solution the slow wave. These modes involve compression of plasma along the magnetic field. In the fast magnetosonic wave magnetic pressure fluctuations are in phase with thermal pressure fluctuations and reinforce each other. The opposite is true in the slow magnetosonic mode: the magnetic and thermal pressures are out of phase and thus oppose each other. In Chapter 4 we shall return to ideal MHD waves in plasmas in the context of coronal heating.

1.4 Magnetic Reconnection

The Sun is incredibly active, dynamic, and energetic, and the key to this is the action of the complex magnetic field structures interspersed throughout the underlying structure of the Sun. Even when the Sun is in a quiet phase, microflares and nanoflares continually occur, particles are accelerated, plasma is heated, energy is released: the term "quiet" can only be considered relative in this case. One of the big challenges in solar physics is understanding exactly how this activity is powered, and how charged particles can be accelerated to moderately relativistic and ultra relativistic energies in solar flares. It is postulated that the energy required comes from the release of stored magnetic energy in a nonideal process known as magnetic reconnection [6]. Reconnection is the mechanism whereby energy-loaded magnetic fields reconfigure to a lower energy state, thus liberating free energy, in some process where oppositely directed components of the magnetic field approach each other,

break, and rejoin in a new configuration. In this section a brief overview of some of the basic physics behind reconnection is discussed, along with a short description of two well-known reconnection models.

1.4.1 Magnetic induction and frozen-in fields

An important concept of reconnection is that of the motion of the magnetic field lines in the plasma. In order to establish what the lines do, we consider a nonideal plasma (i.e. resistivity $\eta \neq 0$) - then Ohm's Law is

$$\mathbf{E} + \mathbf{v} \times \mathbf{B} = \eta \mathbf{j}. \tag{1.34}$$

Thus, from Eq. 1.15

$$\frac{\partial \mathbf{B}}{\partial t} = -\left(\nabla \times \mathbf{E}\right) = -\left(\nabla \times \eta \mathbf{j}\right) + \nabla \times \left(\mathbf{v} \times \mathbf{B}\right). \tag{1.35}$$

Ampére's Law (Eq. 1.14) means that

$$\frac{\partial \mathbf{B}}{\partial \mathbf{t}} = -\frac{\eta}{\mu_0}\left[\nabla \times \left(\nabla \times \mathbf{B}\right)\right] + \nabla \times \left(\mathbf{v} \times \mathbf{B}\right), \tag{1.36}$$

assuming uniform η, and using the vector identity

$$\nabla \times \left(\nabla \times \mathbf{B}\right) = \nabla\left(\nabla \cdot \mathbf{B}\right) - \nabla^2 \mathbf{B} \tag{1.37}$$

and Eq. 1.16 we can see that

$$\frac{\partial \mathbf{B}}{\partial t} = \nabla \times \left(\mathbf{v} \times \mathbf{B}\right) + \frac{\eta}{\mu_0}\nabla^2 \mathbf{B}. \tag{1.38}$$

This is known as the *induction* equation - the first term on the right hand side represents the advection of field by the flow, and the second term represents the dissipation of the field due to resistivity. Normally in the solar atmosphere resistivity is very low (and, approximately, ideal MHD applies), so the equation simplifies to

$$\frac{\partial \mathbf{B}}{\partial t} = \nabla \times \left(\mathbf{v} \times \mathbf{B}\right). \tag{1.39}$$

If we now consider the magnetic flux through a surface $\mathcal{S}$, moving with the stream velocity $\mathbf{v}$, the flux Φ is given by

$$\Phi = \iint_{\mathcal{S}} \mathbf{B} \cdot d\mathbf{S} \tag{1.40}$$

and so it can be seen that the convective derivative of Φ is then

$$\frac{D\Phi}{Dt} = \iint_{\mathcal{S}} \frac{\partial \mathbf{B}}{\partial t} \cdot d\mathbf{S} + \oint_{L} \mathbf{B} \cdot (\mathbf{v} \times d\mathbf{l}) \tag{1.41}$$

where L is the boundary of the surface. Since

$$\oint_{L} \mathbf{B} \cdot (\mathbf{v} \times d\mathbf{l}) = -\oint_{L} (\mathbf{v} \times \mathbf{B}) \cdot d\mathbf{l} = -\iint_{\mathcal{S}} \nabla \times (\mathbf{v} \times \mathbf{B})\, d\mathbf{S} \tag{1.42}$$

by Stoke's theorem, then

$$\frac{D\Phi}{Dt} = \iint_{\mathcal{S}} \left[\frac{\partial \mathbf{B}}{\partial t} - \nabla \times (\mathbf{v} \times \mathbf{B}) \right] \cdot d\mathbf{S}. \tag{1.43}$$

In ideal MHD the right hand side of Eq. 1.43 is zero - this is the "frozen-in flux" condition. As long as this is valid then the magnetic field lines are "stuck" to the fluid and will move with the plasma as it moves. This allows magnetic field to arrange into reconnection-suitable configurations featuring oppositely-directed but closely-approaching field lines, such as a magnetic X-point (also known as a magnetic null). Reconnection can occur close to these null points.

1.4.2 The magnetic X-point

Priest and Forbes [6] provide a mathematical description of the null point by expanding the two-dimensional field near the neutral point in a Taylor series, in terms of a magnetic flux function A (the z-component of the magnetic vector potential) which gives

$$A = \frac{B_0}{2r_0}(y^2 - \bar{\alpha}^2 x^2). \tag{1.44}$$

Here r_0 is the length-scale over which the field varies. The corresponding field components are given by

$$B_x = B_0 \frac{y}{r_0} \tag{1.45}$$

and

$$B_y = B_0 \bar{\alpha}^2 \frac{x}{r_0} \tag{1.46}$$

so that B_x and B_y are zero on the x- and y-axes respectively. There are two distinct cases, depending on whether the constant $\bar{\alpha}$ is greater than or less than zero: $\bar{\alpha} > 0$ produces hyperbolic field lines ($\bar{\alpha} < 0$ gives elliptical field lines, resulting in an O-type neutral point), which are plotted in Figure 1.7 for $\bar{\alpha}$ =1. We can see that the neutral point gains its name from the limiting field lines with equation $y = \pm\bar{\alpha}x$ that pass through the origin - the *separatrices* - which form an "X" shape. Many authors have used X-points, which occur naturally when there are two or more sources of magnetic field, as a paradigm to study magnetic reconnection for both solar flare and coronal heating models because of their (relative) analytical simplicity. Often the model is extended, with an "X-line" structure being used, that is, a 2D X-point structure with a finite magnetic field component B_z in the third dimension, which is parallel to the reconnection electric field. This allows a particle to gyrate around this parallel field and stay in the X-point region (and hence the acceleration zone)

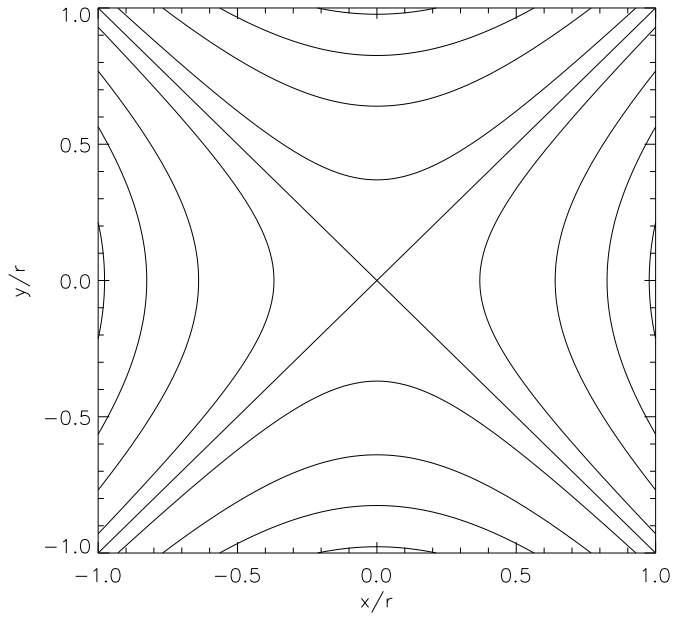

Figure 1.7: Two-dimensional magnetic X-point with $\bar{\alpha} = 1$.

for a longer period of time: for example Hamilton and co-workers [7] studied proton acceleration at an X-line, self-consistently generating a parallel E-field from the flux function corresponding to a reconnecting eigenmode of the X-point.

In 2D a magnetic X-point tends to be locally unstable, and so may collapse (Figure 1.8) to form a current sheet (a thin current-carrying layer across which the magnetic field changes in magnitude or direction or both).

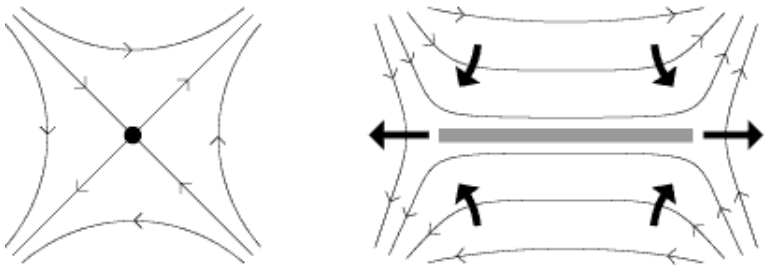

Figure 1.8: The collapse of a magnetic X-point into a current sheet. Image from *www-solar.mcs.st-andrews.ac.uk*.

Dissipation allows the field lines to break and reconnect: this liberates the stored magnetic energy which can then heat a plasma and accelerate particles to high energies: theoretical details on more precise descriptions of reconnection were given by the Sweet-Parker and Petschek models. The work in this thesis is more concerned with the X-point configuration than the actual process of reconnection, but a brief discussion and comparison of the two is included below for context. Observationally, Figure 1.9 illustrates an example of plasma within what is thought to be a coronal X-point structure (as observed by TRACE) where the field lines of two sunspots of the same polarity meet and are deflected sideways, forming an X-point structure (the left section is clearly visible, but the right section may be at a different temperature and thus is not so clearly visible) so there is good evidence that X-point structures occur in the solar corona and thus studies involving them are of interest.

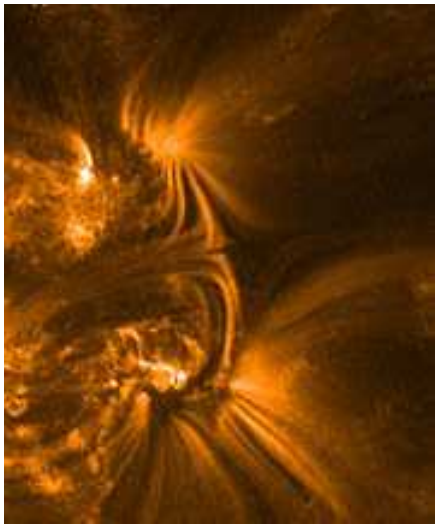

Figure 1.9: A snapshot, taken on 4th September 2000, of two active regions observed with TRACE in the 171Å passband. Image from *http://soi.stanford.edu/results/ SolPhys200/Schrijver/TRACEpodarchive4.html*.

1.4.3 Sweet-Parker and Petschek reconnection

The two most well-known reconnection models are those of Sweet-Parker (Parker's quantitative model was inspired by Sweet's qualitative description) and Petschek. The Sweet-Parker model suggested that, between the opposing magnetic fields about to undergo reconnection, a region of magnetic diffusion (much longer than it is wide) lies along the boundary, as shown in Figure 1.10 (top). Outside of the diffusion region, the plasma β (the ratio of the thermal pressure to the magnetic pressure) is considerably below unity (magnetic pressure dominates) and the field lines are frozen-in to the plasma, as described in Section 1.4.1., and cannot penetrate one another and mix. Inside the diffusion region, however, β is considerably higher than unity (thermal pressure dominates) because the magnetic field tends to zero at the boundary between the oppositely-directed field lines. The curvature of the magnetic field lines means that the curl of the field in the diffusion region is nonzero and thus from Eq. 1.14 a current $\mathbf{j}$ exists in the diffusion region, and hence a component of the Lorentz force $\mathbf{j} \times \mathbf{B}$ also exists along the current sheet. The resistivity of this current layer allows magnetic flux from either side to diffuse into and through the current layer. The $\mathbf{j} \times \mathbf{B}$ force accelerates this plasma to a velocity equivalent to the

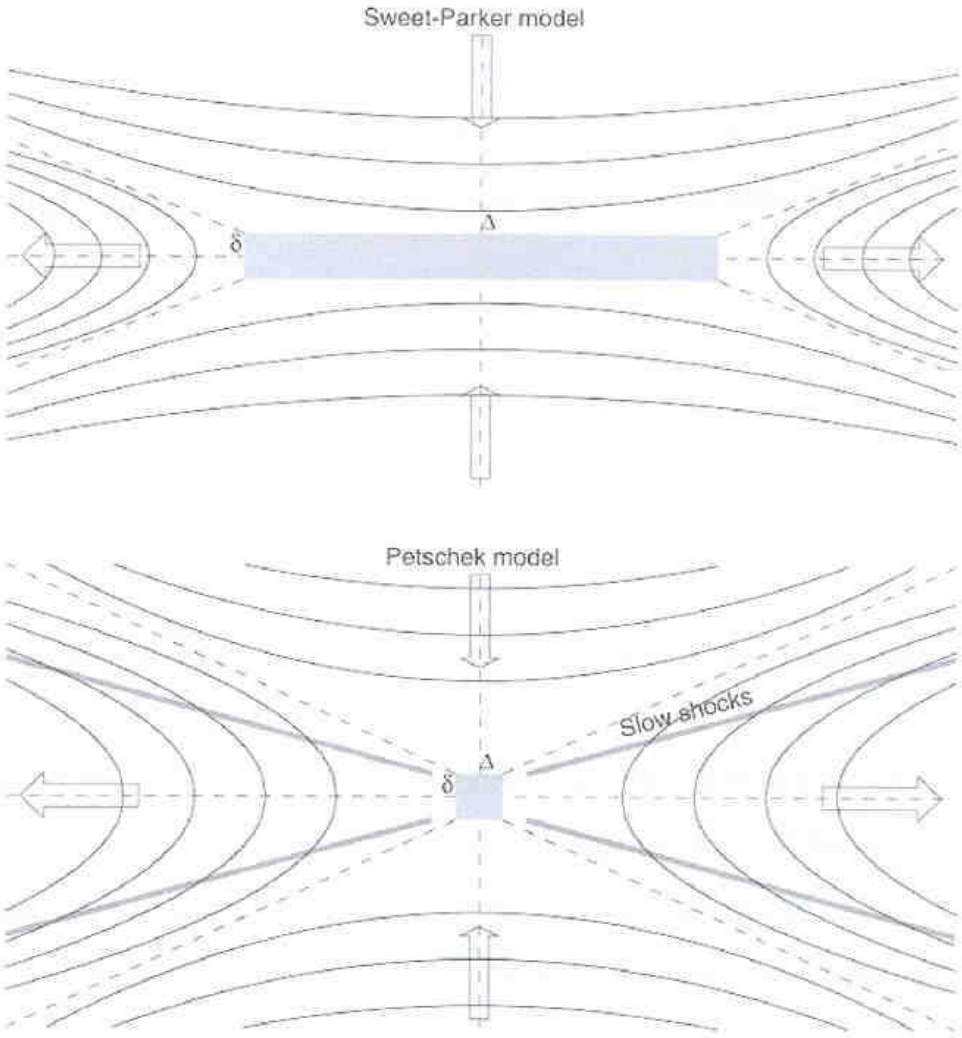

Figure 1.10: Simple diagram of the Sweet-Parker reconnection model (top) and the Petschek model (bottom) - the grey lines indicate the slow-mode shocks. Image from Aschwanden [8].

inflow Alfvén speed - this is how reconnection converts magnetic energy to kinetic energy. The plasma is channeled into the outflow region as shown in Figure 1.10(a).

A key parameter of the Sweet-Parker model is the Lundquist number, S, given by

$$S = \frac{v_A L}{\eta}, \tag{1.47}$$

where v_A is the Alfvén speed, L is the length of the reconnecting layer and η is the resistivity. This parameter is of the order 10^8-10^{12} in the corona [8] and thus gives

a very thin reconnection layer. This leads to a reconnection rate M_0, defined to be the Mach number ratio of the external inflow speed v_0 to the Alfvèn outflow speed v_A, of

$$M_0 = \frac{1}{\sqrt{S}}, \tag{1.48}$$

that is too slow for, for example, a solar flare. Larger magnetic gradients and currents are required to speed up the process. The Petschek model attempts to address this problem by reducing the size of the diffusion area (see Figure 1.10 (bottom)), as well as considering slow magnetoacoustic shocks in the outflow region, where the plasma flow speed changes abruptly. The slow shock fronts are efficient at converting magnetic energy to kinetic energy. Analysis of the Petschek model can be shown to give a reconnection rate that is dependent on the logarithm of the resistivity,

$$M_0 \simeq \frac{\pi}{8 \ln S}, \tag{1.49}$$

which is approximately three orders of magnitude faster than Sweet-Parker reconnection [8], though remains a controversial model.

These two models are among the simplest cases examinable. Numerical simulations and observations only increase our belief that in reality the problem is more complex. Sweet-Parker and Petschek are examples of *steady* reconnection, but in practice the *bursty* nature of solar flares suggests the process is anything but steady. Besides, the complexity of reconnection is only magnified when the third dimension is taken into account, as the number of possible reconnection topologies increases dramatically.

1.5 Coronal Heating

How the corona is heated has been a long-standing problem in solar physics: as we saw, the corona is significantly hotter than the photosphere, which is puzzling as the second law of thermodynamics dictates that heat flows from a hotter to a colder body. Thus the corona cannot be heated by the photosphere - at least, not by thermal conduction. So how *is* the corona heated? A definitive model proves

elusive, though many mechanisms have been suggested: see e.g. Browning [9] for a review. The corona continually loses heat by radiation and by conduction down to the atmospheric layers below, as well as driving the solar wind which convects heat away from the Sun. Estimates suggest the total amount of power lost from the corona is of the order of 10^{21}J s^{-1} [4]. Thus to maintain the corona at its current temperature any heating mechanism must balance these losses. The inhomogeneity of the corona means that these losses vary in different regions.

Current thinking tends to suggest heating comes from one of two different general mechanisms: either magnetic reconnection, or magnetic waves. In reality both are likely to be important. Coronal heating by magnetic waves shall be discussed within the context of the work on fast wave heating and acceleration of ions contained in Chapter 4.

1.5.1 Structure in the corona

The corona is a very tenuous layer of the solar atmosphere, around 8 orders of magnitude less dense than the photosphere. Observed in X-rays, several different coronal structures can be seen all over the Sun. Dark regions (see left image of Figure 1.11) are known as *coronal holes*, which are structures that have their magnetic fields open at the solar surface and extend some large distance into interplanetary space.

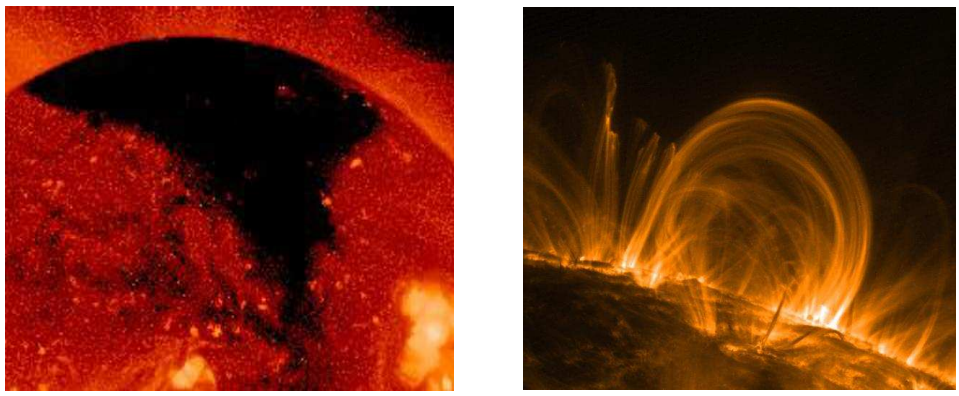

Figure 1.11: Left - image of a coronal hole, taken by Yohkoh. Image from *www.moonraker.com.au/techni/solar.htm.* Right - image of a coronal loop, taken by TRACE. Image from *http://www.cosmiclight.com/imagegalleries/sun.htm.*

It is expected that they eventually return to the surface of the Sun, for consistency with Maxwell's equations, though it is not known exactly how this happens. *Coronal loops* are magnetically closed structures, both their footpoints being anchored somewhere in the surface of the Sun (see right image of Figure 1.11). They generally have a semi-toroidal structure, and often have a helical structure due to stressed, twisted, nonpotential magnetic field topologies. Additionally a third type of coronal structure, the *X-ray bright point* (XBP), exists: these are compact, small, bi-polar regions of transient brightening that showed up as a point in early X-ray cameras, hence their name. XBP's can appear in great numbers and have a lifespan typically of a few hours, and a density a few times greater than that of the typical corona.

These three features all have different heating requirements due to their different loss rates (estimated by Withbroe & Noyes [11] - see Table 1.1), and so may all be heated by different mechanisms. For now, at least in terms of XBP's, it is believed that magnetic reconnection is the heating source. One possible model to understand this is called the *Converging Flux Model* [6], which explains how an XBP can form as two regions of opposing magnetic polarity approach each other. Once the poles are close enough an X-point forms on the surface, which then rises as the magnetic fragments continue to approach, and the energy released and plasma channeled through the X-point structure forms the XBP. As the fragments continue to move towards each other, eventually the X-point reverses direction, moving back towards the photosphere. Finally the magnetic fragments meet in the photosphere and collide, annihilating each other in a process known as *cancellation*, resulting in the disappearance of the X-point and the magnetic fragments. In most cases this process is played out by a bipolar pair of magnetic fragments emerging in a supergranule cell, and moving towards the cell boundary. Upon reaching the boundary the fragments can then merge and cancel with one of the opposite-polarity regions of magnetic flux that accumulate around the edges of supergranular cells all over the surface of the Sun.

On larger scales than XBP's, it is thought that *nanoflares* are an important feature. Nanoflares consist of numerous tiny transient EUV brightenings which release approximately 9 orders of magnitude less energy than the largest flares (and

Table 1.1: Estimated loss rates of coronal features

Feature	Loss rate (Wm^{-2})
Quiet region	300
Coronal hole	800
Active region	(0.5-1)$\times 10^4$

hence the name). They are thought to have similar properties to large flares, but they differ in that they do not need such large magnetic fields and thus can occur everywhere in the quiet Sun, and not just in active regions. Although they release much less energy than large flares, their considerable number (of the order of 10^5 events over the whole Sun at any one time [13]) makes them a likely candidate to explain the large-scale heating of the corona.

1.6 Flare Physics

A solar flare is a sudden and dramatic eruption of radiated energy (up to 10^{25-26} J) and accelerated particles. First observed in 1859 by Carrington and Hodgson as a localised brightening of a sunspot group (see Figure 1.12), flares have been studied intensely ever since. As mentioned previously, it is thought that the energy that powers a flare comes from the reconnection and re-organisation of stressed magnetic fields to a lower energy state. Generally a flare can be divided into three distinct

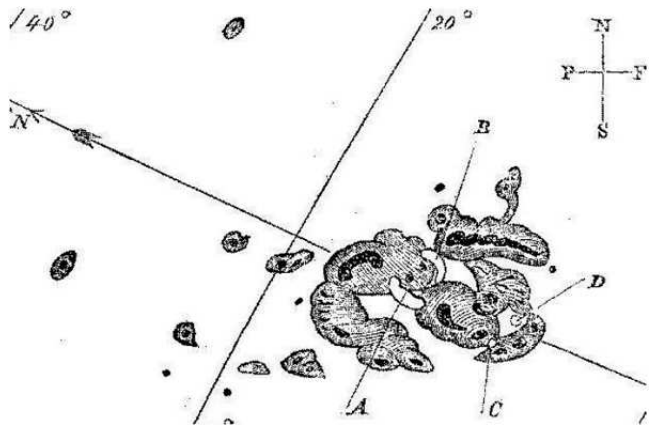

Figure 1.12: Carrington's [10] diagram of the first observed solar flare, seen as a brief brightening of the two patches at A and B, either side of the group of sunspots.

phases (see Figure 1.13). First there is an initial *preflare* phase where stored energy builds up over a period of several minutes to a few hours, which may be seen as an enhancement in X-ray radiation - an indication of small-scale or low-level energy release, as opposed to one of energy storage itself, and is not necessarily located at the site of the flare itself. The most dramatic phase is the middle *impulsive* one, where the peak levels of emission are observed - most evident in hard X-rays, but the optical, UV and EUV bands see intense emission too. The impulsive phase is very short, lasting perhaps just a few minutes, and the observed levels of emitted radiation will then tail off slowly over a longer period of several hours in what is referred to as the *gradual* phase.

Figure 1.13 gives a schematic overview of flare emission at different wavelengths, but what is actually occurring within the Sun to produce these observations? Many general paradigms have been developed to try to explain the trends of flares: a widely accepted model is one proposed by Carmichael, Sturrock, Hirayama, Kopp and Pneuman, and further developed by, among others, Tsuneta [14]. A version

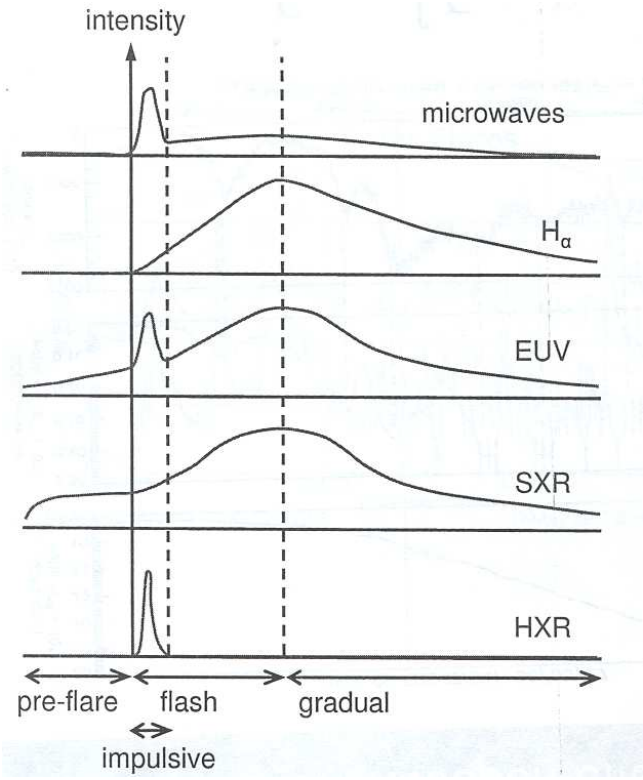

Figure 1.13: Timeline of emission of typical flare in 6 energy bands. Image from Priest [12].

of this 2D description (modified from [14], as a result of Yohkoh observations of an erupting structure beginning before the start of a flare that occurred on the solar limb on December 2nd 1991, as well as data obtained from numerical MHD simulations) is shown in Figure 1.14. In this model a loop structure starts to rise and elongate, stretching the overlying magnetic field, and thus forming a current sheet. As the loop continues to rise an X-point structure is formed underneath it, and magnetic reconnection occurs. Plasma is drawn into the diffusion region from the sides around the X-point, and accelerated by slow shock ridges. The energy released in the reconnection process accelerates particles downwards in beams, where some collide with cooler, denser material lower down at the top of the coronal loop (and thus forming a hard X-ray looptop) and some are channeled down to the chromosphere, where they heat and evaporate plasma, which fills the loop (and forming a bright soft X-ray loop). The footpoints of this loop are observed as two H_α "ribbons". As the X-point continues to rise and reconnect these ribbons are seen to move apart as the separation distance between the footpoints increases. Above the reconnection

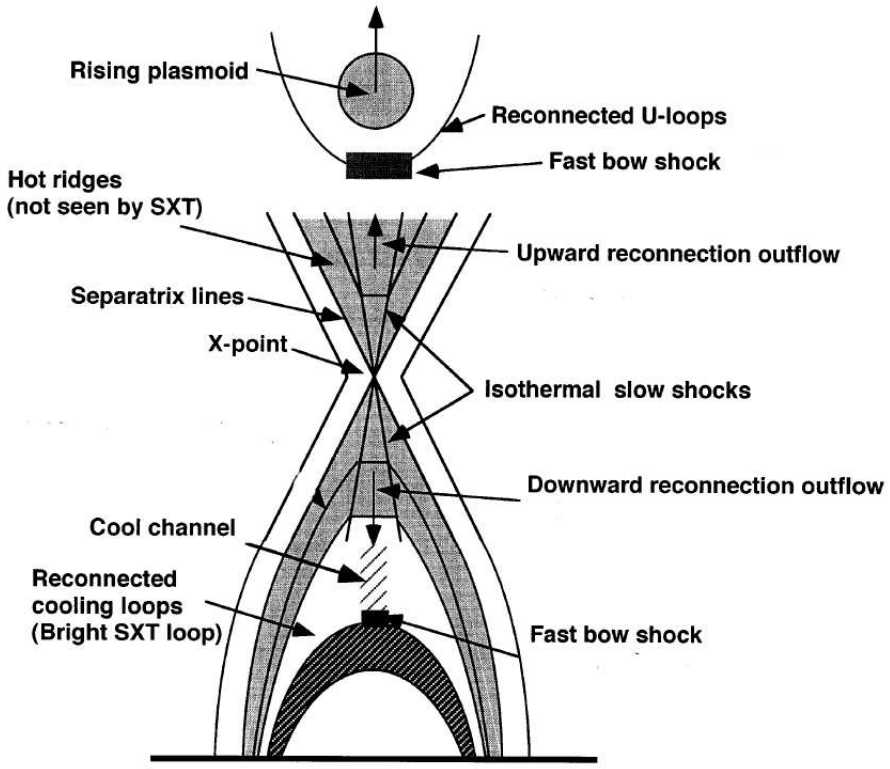

Figure 1.14: A modified version of the CSHKP standard model for a solar flare. Image from Tsuneta [14].

area there is also outflow of material, which forms a shock front as it comes into contact with a rising loop structure: a remnant of the reconnection process, which may evolve into a plasmoid structure.

Undoubtedly this model explains many of the observed signatures of flares, though some of the exact details of the process are still not very well understood. From the point of view of this thesis, this is largely unimportant: in the context of the work carried out in solar astrophysics, we will content ourselves with trying to understand possible acceleration mechanisms of particles within the X-point structure.

"Man defines the coordinates...but the result comes from God"

Prof. Merkulov

Chapter 2

Fusion Plasma Physics

2.1 Conditions for Fusion

The aim of achieving commercially-useful nuclear fusion has long been one of the "holy grail" concepts, not just of physics, but of scientific research in general. The promise of near-limitless yet relatively clean energy is a powerful motivator in a world debating the impacts of climate change and finite fossil fuel dependence. Nuclear power, in both conventional, successful fission and attempted fusion works on the principle of exploiting the binding energy of the atomic nucleus. Binding energy per nucleon increases with baryon number until iron is reached, the iron nucleus having the greatest binding energy per nucleon of any species. A steady decrease of binding energy per nucleon past the iron nucleus is seen. Fission relies on heavy reactant nuclei being split and forming lighter, more tightly-bound product nuclei, plus energy. Fusion takes the opposite approach in the fusing together of two light nuclei reactants, such as hydrogen or helium (or anything lighter than iron), producing a product that is lighter than the sum of the initial reactants, releasing energy as a result. The process is made difficult by the electrostatic repulsion of the two positively-charged reactant nuclei - to successfully fuse the reactants, the Coulomb barrier between the two must be overcome, which requires, amongst other things, high temperatures of the reactants. Fortunately the energy required to do this is

reduced by the process of quantum mechanical tunneling, meaning that it is not necessary for the fuel ions to have kinetic energies equal to or greater than the potential barrier. From an astrophysical point of view, nuclear fusion is the power source behind a star, such as our Sun. However, the demands of star and laboratory differ somewhat. The Sun's primary fusion reactions are proton-proton based, turning six protons into a ^{4}He nucleus via reactions such as:

$$p + p \longrightarrow {}^2\mathrm{D} + e^+ + \nu$$

$${}^2\mathrm{D} + p \longrightarrow {}^3\mathrm{He} + \gamma$$

This set of reactions is only a small part of the overall picture (in total 3 proton-proton chains exist, along with the CNO cycle, and helium, carbon, oxygen and silicon burning, which we do not go into here). However the cross-sections for these reactions are too small to produce a significant fusion yield in the laboratory and thus reactions involving more reactive isotopes of hydrogen, deuterium and tritium, are utilised instead:

$${}^2\mathrm{D} + {}^2\mathrm{D} \longrightarrow {}^3\mathrm{T} + p$$

$${}^2\mathrm{D} + {}^2\mathrm{D} \longrightarrow {}^3\mathrm{He} + n$$

$${}^2\mathrm{D} + {}^3\mathrm{T} \longrightarrow {}^4\mathrm{He} + n$$

The third reaction releases an energy of 17.6 MeV (compared to the 0.26 MeV produced in the deuterium-producing reaction in the stellar p-p chain), and is favoured because of the relatively low temperatures required to achieve a useful reaction cross-section: a D-T reactor would be able to operate at around 10 keV. However, tritium does not occur naturally (although it can be "bred" by bombarding lithium with neutrons) and so a D-D reactor has the advantage of using reactant fuel that is much more plentiful, with the disadvantage that the reactor would have to operate at a much higher temperature of around 25 keV.

As mentioned previously, in order to facilitate any nuclear fusion reaction, the Coulomb barrier repulsive electrostatic potential between the two nuclei must be overcome. To do this, the particles must be heated sufficiently to provide them

with high thermal velocities, and confined to a certain region for a sufficiently long period to provide the opportunity of collision. At the high temperatures required for fusion (for example, 10 keV corresponds approximately to 10^8 K), the reactant nuclei are fully ionised, meaning that the fuel is a plasma. The critical issue is to engineer a plasma that produces sufficient heating from the fusion reaction products to maintain the temperature of the plasma against the inevitable unavoidable energy losses (e.g. bremsstrahlung radiation or heat conduction to the device walls) without resorting to external power input. The break-even point when the power from fusion reaction equals these losses is known as "ignition". The minimum conditions required for ignition can be represented in terms of the plasma electron density n_e and the energy confinement time τ_e in the well-known Lawson criterion [15]

$$n_e\tau_e \geq 1.5 \times 10^{20}\mathrm{sm}^{-3}, \tag{2.1}$$

where

$$\tau_e = \frac{W}{P_{loss}}, \tag{2.2}$$

W being the energy content of the system and P_{loss} being the rate of energy loss of the system. Arguably a more useful quantity, however, is that of the "triple product" of density, temperature and confinement time

$$n_eT\tau_e \geq 10^{21}\ \mathrm{keV\ sm}^{-3}. \tag{2.3}$$

The values quoted here are for the D-T reaction. The exact figures are dependent on a number of subtle factors, such as the exact fusion reaction under consideration, impurity content of the plasma, assumed plasma profiles etc. (for example, for parabolic density and temperature profiles the right hand side of Eq. 2.3 should be multiplied by 5). The challenge to physicists is to build a device capable of meeting the Lawson criterion. Confinement by material walls alone is impractical, given the large temperatures involved, and so magnetic confinement has been turned to in an attempt to solve the problem. Many different magnetic confinement devices have been devised and operated with varying degrees of success, such as the Z-pinch, the

reversed-field pinch and the stellarator, but the tokamak has largely become the standard device in the international fusion research program.

2.2 Tokamaks

The tokamak (derived from the Russian phrase **to**roidal'naya **ka**mera ee **ma**gnitnaya **k**atushka, meaning toroidal chamber with magnetic coils) is a plasma confinement device that employs both toroidal and poloidal magnetic fields. Figure 2.1 shows a schematic view of a tokamak, and Figure 2.2 shows the geometry and magnetic field configuration.

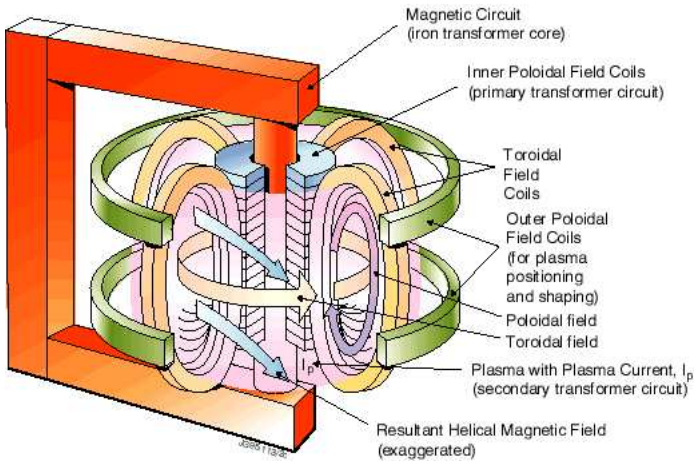

Figure 2.1: A schematic view of a tokamak device. Image from *www.splung.com/content/sid/5/page/fusion.*

The toroidal field B_φ is generated by currents passing through external coils. Plasma current flowing in the toroidal direction generates a poloidal magnetic field B_θ, which is typically much smaller than the toroidal field. The combination of B_φ and B_θ results in field lines that have a helical trajectory around the torus. The use of toroidal configuration means that it is convenient to use cylindrical coordinates (R, φ, Z) where R is distance from the torus symmetry axis, φ is azimuthal (toroidal) angle and Z is vertical distance. These coordinates are defined by

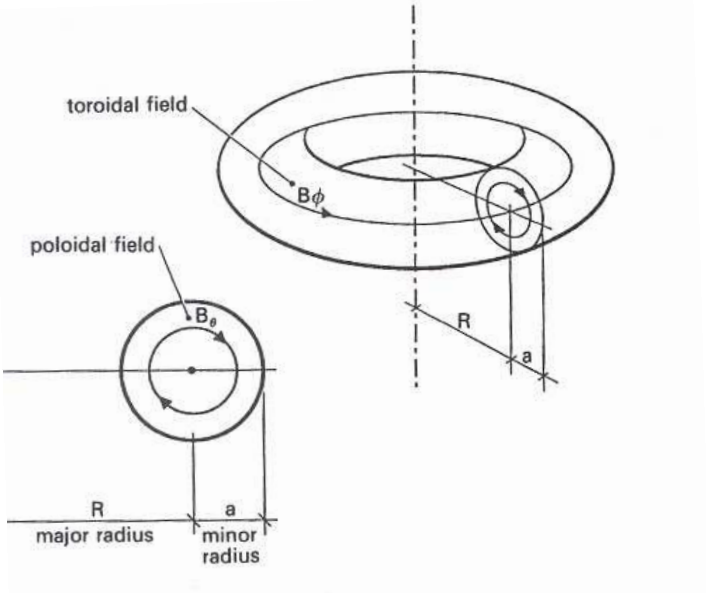

Figure 2.2: Magnetic field geometry of a tokamak. Image from Dendy [16].

$$R = \sqrt{x^2 + y^2}$$

$$\varphi = \tan^{-1}(y/x)$$

$$Z = z.$$

In the case of tokamaks with circular poloidal cross-section, it is also useful to define the minor radial coordinate of the tokamak, r, and the poloidal angle θ,

$$r = \sqrt{(R - R_0)^2 + Z^2}$$

$$\theta = \tan^{-1}\left(\frac{Z}{R - R_0}\right)$$

respectively. At the edge of the plasma $r = a$, the minor radius.

Two general classes of tokamak exist. "Spherical tokamaks" (ST) have much smaller aspect ratios (the ratio of the major radius to the minor radius, $A = R_0/a$) than conventional tokamaks - Figure 2.3 compares the shape of a conventional tokamak to a spherical one. Typically, ST's have an aspect ratio of less than 1.5, compared to, for example JET's aspect ratio of $A = 3.1$, giving them a much tighter toroidal shape. This tighter shape is regarded as having certain advantages over the conventional large designs. Scaling laws mean that tighter aspect ratios give

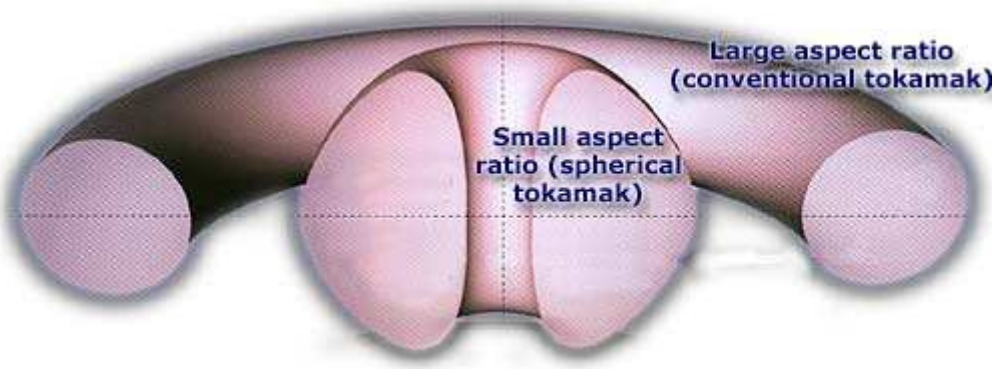

Figure 2.3: Comparison of aspect ratios of conventional and spherical tokamaks. Image from *http://www.fusion.org.uk/st/advantages.html*.

a higher value for the plasma β (the ratio of the plasma pressure to the magnetic pressure), meaning that the plasma is more efficiently confined and the densities and temperatures required for ignition are made easier to achieve. The predecessor to MAST, START (Small Tight Aspect Ratio Tokamak), achieved the world record for attained volume-averaged plasma β at approximately 40% [17], more than trebling the previous world record held by DIII-D, a conventional large aspect-ratio device. Additionally tight aspect ratio tokamaks have the advantage of being much cheaper to build, as the machine is much smaller, and the power output of electricity per tonne of nuclear island structure is much lower. However certain physics and engineering issues remain to be solved with the spherical tokamak but the initial promise shown by START has led to many other ST's being commissioned.

MAST (Mega Ampère Spherical Tokamak), also situated at Culham in Abingdon, achieved first plasma in 1998, and the physics programme began in earnest in December 1999. MAST's main aims are to address key physics issues for ITER, complementing and extending data from conventional tokamaks, as well as exploring the potential of the spherical tokamak as the basis for a fusion power plant and/or components test facility. Some of the important design parameters of MAST are listed in Table 2.1 [18], along with the actual values achieved so far, from the Annual Report of the EURATOM/UKAEA Fusion Programme (2006/07) [19].

Table 2.1: MAST operating parameters

	Design	Achieved
Minor radius a (m)	0.65	0.65
Major radius R_0 (m)	0.85	0.85
Aspect ratio	≥ 1.4	1.3
Toroidal field (tesla)	0.52	0.52
Max. plasma current (MA)	2	1.35
Electron cyclotron heating power (MW)	1.5	0.9
Neutral-beam injection power (MW)	5	3.5
Plasma volume (m^3)	10	10

2.3 Plasma Equilibrium

2.3.1 Flux functions

Plasma confinement is achieved by the combination of toroidal and poloidal magnetic field. The addition of the poloidal field is required to create an equilibrium in which the plasma pressure forces are balanced by the magnetic forces. Consider the MHD momentum equation

$$\rho \frac{D\mathbf{u}}{Dt} = -\nabla P + \mathbf{j} \times \mathbf{B} + \rho \mathbf{g} \tag{2.4}$$

where $\mathbf{u}$ is the fluid velocity of an element of plasma, P its pressure, ρ is its density, $\mathbf{j}$ the current and $\mathbf{B}$ is the magnetic field (and D/Dt is the convective derivative). If equilibrium conditions are assumed and flows are neglected then D/Dt is zero, and if gravity is also neglected then Eq. 2.4 reduces to

$$\mathbf{j} \times \mathbf{B} = \nabla P, \tag{2.5}$$

which, when combined with Ampère's Law (Eq. 1.14) describes the pressure, field and current distribution of a static MHD equilibrium, where $\mathbf{B}$, $\mathbf{j}$ and ∇P are mutually perpendicular. In a tokamak plasma, this means that magnetic field lines and lines of current lie wrapped around nested surfaces of constant pressure, called

flux surfaces. This is described by the poloidal magnetic flux function ψ, which is constant on a given surface, and thus satisfies

$$\mathbf{B} \cdot \nabla\psi = 0. \tag{2.6}$$

In the case of tokamaks the equilibrium configuration is toroidally-symmetric and so ψ depends only on R and Z. Hence Eq. 2.6 reduces to

$$B_R \frac{\partial\psi}{\partial R} + B_Z \frac{\partial\psi}{\partial Z} = 0. \tag{2.7}$$

Combining this equation with $\nabla \cdot \mathbf{B} = 0$ (which becomes

$$\frac{1}{R}\frac{\partial}{\partial R}(RB_R) + \frac{\partial B_Z}{\partial Z} = 0$$

because the divergence of a vector $\mathbf{V}$ in cylindrical polar coordinates is

$$\nabla \cdot \mathbf{V} = \frac{1}{h_1 h_2 h_3}\left[\frac{\partial}{\partial x_1}(h_2 h_3 V_1) + \frac{\partial}{\partial x_2}(h_1 h_3 V_2) + \frac{\partial}{\partial x_3}(h_1 h_2 V_3)\right]$$

where V_1, V_2 and V_3 are the components of $\mathbf{V}$, and $h_1 = 1$, $h_2 = R$ and $h_3 = 1$ in cylindrical coordinates) gives

$$B_R = -\frac{1}{R}\frac{\partial\psi}{\partial Z} \tag{2.8}$$

$$B_Z = \frac{1}{R}\frac{\partial\psi}{\partial R}. \tag{2.9}$$

Under steady state conditions, and generally in MHD because of the exclusion of short timescales, $\nabla \cdot \mathbf{j} = 0$. The current density $\mathbf{j}$ also satisfies an equation analogous to Eq. 2.7. Hence in the same way, a flux function for the current, f, can also be derived, because of the symmetry of $\mathbf{j}$ and $\mathbf{B}$, and is related to the poloidal current density by the equations

$$j_R = -\frac{1}{R}\frac{\partial f}{\partial Z} \tag{2.10}$$

$$j_Z = \frac{1}{R}\frac{\partial f}{\partial R}. \tag{2.11}$$

From Ampère's law,

$$j_R = \frac{1}{\mu_0}\left[\frac{1}{R}\frac{\partial B_Z}{\partial \varphi} - \frac{\partial B_\varphi}{\partial Z}\right] \tag{2.12}$$

$$j_Z = \frac{1}{\mu_0}\left[\frac{1}{R}\frac{\partial}{\partial R}(RB_\varphi) - \frac{1}{R}\frac{\partial B_R}{\partial \varphi}\right] \tag{2.13}$$

and the $\partial/\partial\varphi$ terms drop out due to the axisymmetry of the system, leaving

$$j_R = -\frac{1}{\mu_0}\frac{\partial B_\varphi}{\partial B_Z} \tag{2.14}$$

$$j_Z = \frac{1}{\mu_0}\frac{1}{R}\frac{\partial}{\partial R}(RB_\varphi) \tag{2.15}$$

Comparing Eqs. 2.10 and 2.11 with 2.14 and 2.15 gives

$$f = \frac{RB_\varphi}{\mu_0}, \tag{2.16}$$

relating the current flux function to the toroidal magnetic field. By taking the scalar product of Eq. 2.5 with $\mathbf{j}$,

$$\mathbf{j}\cdot(\mathbf{j}\times\mathbf{B}) = \mathbf{j}\cdot\nabla\mathbf{P} \tag{2.17}$$

i.e.

$$\mathbf{j}\cdot\nabla P = 0 \tag{2.18}$$

and hence

$$\frac{\partial f}{\partial R}\frac{\partial P}{\partial Z} - \frac{\partial f}{\partial Z}\frac{\partial P}{\partial R} = 0. \tag{2.19}$$

It follows from Eq. 2.19 that f can be expressed as a function of P, which is itself a function of ψ and thus $f = f(\psi)$.

2.3.2 The Grad-Shafranov equation

The equilibrium equation $\mathbf{j}\times\mathbf{B} = \nabla P$ can be written instead as

$$\mathbf{j}_p \times \mathbf{i}_\varphi B_\varphi + j_\varphi \mathbf{i}_\varphi \times \mathbf{B}_p = \nabla P, \tag{2.20}$$

where $\mathbf{B}_p$ is the poloidal magnetic field, $\mathbf{j}_p$ is the poloidal current density and $\mathbf{i}_\varphi$ is the unit vector in the φ direction. The equations 2.8, 2.9 and 2.14, 2.15 can be contracted to

$$\mathbf{B}_p = \frac{1}{R}(\nabla\psi \times \mathbf{i}_\varphi) \tag{2.21}$$

$$\mathbf{j}_p = \frac{1}{R}(\nabla f \times \mathbf{i}_\varphi). \tag{2.22}$$

Substituting these two equations into Eq. 2.20 gives

$$-\frac{B_\varphi}{R}\nabla f + \frac{j_\varphi}{R}\nabla\psi = \nabla P \tag{2.23}$$

(remembering, from vector calculus, that

$$\mathbf{a} \times (\mathbf{b} \times \mathbf{c}) = \mathbf{b}(\mathbf{a} \cdot \mathbf{c}) - \mathbf{c}(\mathbf{a} \cdot \mathbf{b})$$

$$(\mathbf{a} \times \mathbf{b}) \times \mathbf{c} = -\mathbf{c} \times (\mathbf{a} \times \mathbf{b})$$

and hence

$$(\nabla f \times \mathbf{i}_\varphi) \times B_\varphi = -\left[\nabla f(\mathbf{i}_\varphi B_\varphi \cdot \mathbf{i}_\varphi) - \mathbf{i}_\varphi(\mathbf{i}_\varphi B_\varphi \cdot \nabla f)\right]$$

$$j_\varphi \mathbf{i}_\varphi \times (\nabla\psi \times \mathbf{i}_\varphi) = \nabla\psi(j_\varphi \mathbf{i}_\varphi \cdot \mathbf{i}_\varphi) - \mathbf{i}_\varphi(j_\varphi \mathbf{i}_\varphi \cdot \nabla\psi)$$

and that $\mathbf{i}_\varphi \cdot \nabla f = \mathbf{i}_\varphi \cdot \nabla\psi = 0$ also). Now

$$\nabla f(\psi) = \frac{df}{d\psi}\nabla\psi \tag{2.24}$$

$$\nabla P(\psi) = \frac{dP}{d\psi}\nabla\psi, \tag{2.25}$$

and substituting these into Eq. 2.23 results in

$$j_\varphi = R\frac{dP}{d\psi} + B_\varphi\frac{df}{d\psi}. \tag{2.26}$$

Also, substituting Eq. 2.16 in gives

$$j_\varphi = RP' + \frac{\mu_0}{R}ff'. \tag{2.27}$$

The toroidal component from Ampère's law gives

$$j_\varphi = \frac{1}{\mu_0}\left[\frac{\partial B_R}{\partial Z} - \frac{1}{R}\frac{\partial}{\partial R}(RB_Z)\right] \tag{2.28}$$

and substituting in B_R and B_φ from Eqs. 2.8 and 2.9 produces

$$\mu_0 j_\varphi = -\frac{1}{R}\frac{\partial^2\psi}{\partial Z^2} - \frac{1}{R}\left[R\frac{\partial}{\partial R}\left(\frac{1}{R}\frac{\partial\psi}{\partial R}\right)\right]. \tag{2.29}$$

Finally, substituting for j_φ from Eq. 2.27 gives

$$R\frac{\partial}{\partial R}\frac{1}{R}\frac{\partial\psi}{\partial R} + \frac{\partial^2\psi}{\partial Z^2} = -\mu_0 R^2 P'(\psi) - \mu_0^2 f(\psi)f'(\psi), \tag{2.30}$$

which is known as the Grad-Shafranov equation, and is the equilibrium equation for an axisymmetric system such as a tokamak.

2.3.3 Solov'ev solutions

A solution to the Grad-Shafranov equation for a spherical tokamak was first investigated by Solov'ev [21] and later examined by Freidberg [22]. To make progress, special models that invoke simple choices for the free functions P(ψ) and f(ψ) (whilst still retaining the important physics) are made. The special model invoked here is

$$\mu_0 P' = -C \tag{2.31}$$

$$ff' = A \tag{2.32}$$

where A and C are constants. The result is not derived here, simply stated:

$$\psi = -\frac{A}{2}Z^2 + \frac{C}{8}R^4 + c_1 + c_2R^2 + c_3\left(R^4 - 4R^2Z^2\right). \tag{2.33}$$

It is straightforward to verify that Eq. 2.33 is a solution of the Grad-Shafranov equation, with the c_1, c_2 and c_3 terms being solutions of the homogeneous (vacuum) equation and the A and C terms representing a particular integral. This equation can be rewritten as

$$\psi = \frac{C\gamma}{8}\left[(R^2 - R_a^2)^2 - R_b^4)\right] + \frac{C}{2}\left[(1-\gamma)R^2 - \frac{A}{C}\right]Z^2 \tag{2.34}$$

where the constants γ, R_a and R_b replace c_1, c_2 and c_3, and the flux function has been normalised so that $\psi(R, Z) = 0$ on the plasma surface. The magnetic axis thus corresponds to the point $R = R_a$, $Z = 0$, and the outer midplane edge of the plasma is located at the point $R = (R_a^2 + R_b^2)^{1/2}$, $Z = 0$. If the constant C is denoted instead by ψ_0 (if the plasma current is taken to be in the negative φ direction then ψ_0 is positive and $\psi \leq 0$ throughout the plasma), R_a is instead denoted by R_0, and A is set equal to zero (which means that RB_φ is assumed to be constant; this is the vacuum solution for B_φ and is an acceptable approximation for our purposes), then

$$\psi(R, Z) = \psi_0 \left\{ \frac{\gamma}{8} \left[(R^2 - R_0^2)^2 - R_b^4 \right] + \frac{1 - \gamma}{2} R^2 Z^2 \right\} \tag{2.35}$$

which we shall return to in Chapter 6. The contours of constant ψ of the particular analytical solution with parameters $\gamma = 0.8$, $R_0 = 0.964$m, and $R_b = 0.93$m is plotted in Figure 2.4.

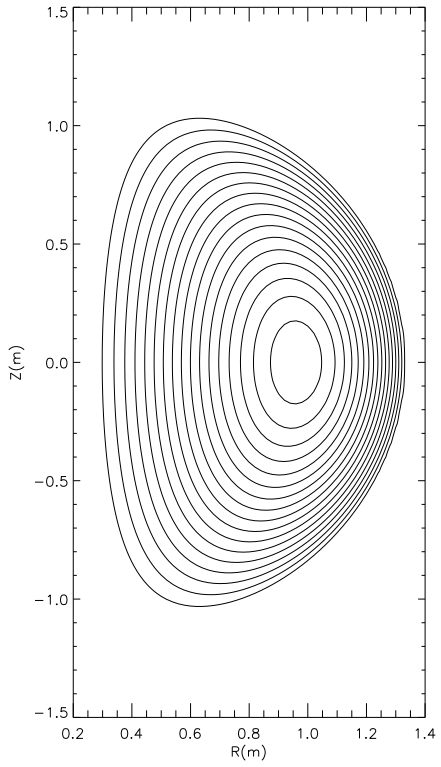

Figure 2.4: Equilibrium flux surfaces for a MAST-like plasma corresponding to an analytic solution of the Grad-Shafranov equation with parameters as given in the text.

2.3.4 Plasma safety factor

A key measure of a tokamak is the plasma safety factor, q_s. The magnetic field lines wind helically around the magnetic surfaces upon which they are located (see Figure 2.5). The safety factor measures the pitch of the field lines as they follow these helical paths around the tokamak: a field line will perform q_s circuits of the symmetry axis over the course of a single circuit in the poloidal direction. The q_s-value of a tokamak plasma is an important factor in defining its stability. Kadomtsev [23] derives an expression for this safety factor: considering the length of an arc in the toroidal direction gives the distance $Rd\varphi$, and defining the distance covered in the poloidal direction whilst moving through toroidal angle $d\varphi$ to be ds, then the ratio of these quantities is equivalent to the ratio of the corresponding field components, i.e.

$$\frac{B_\varphi}{B_\theta} = \frac{Rd\varphi}{ds}, \tag{2.36}$$

and therefore

$$d\varphi = \frac{B_\varphi}{RB_\theta} ds. \tag{2.37}$$

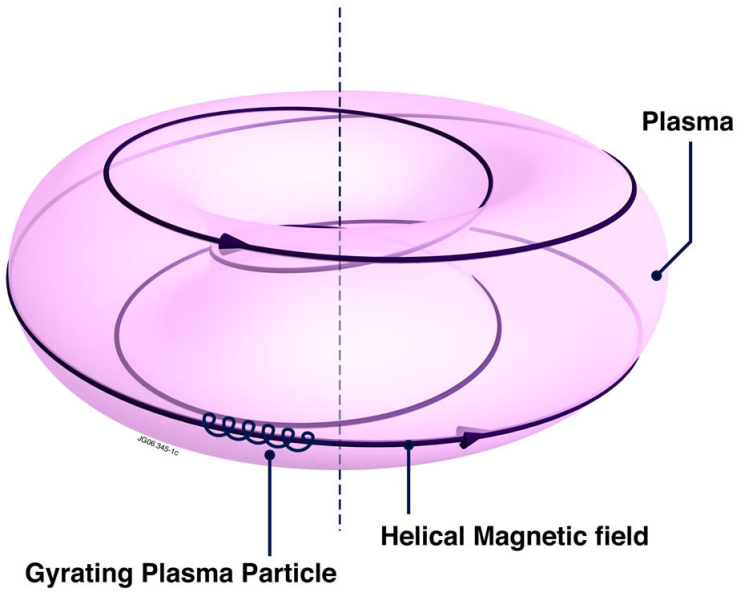

Figure 2.5: Illustration of the helical structure of the magnetic field in a tokamak. Image from *http://www.jet.efda.org/pages/focus/plasma-edge/images/fig03.jpg*.

Defining the safety factor q_s as

$$q_s = \frac{\Delta\varphi}{2\pi}, \tag{2.38}$$

where $\Delta\varphi$ is the change in toroidal angle on a field line as it traces out one poloidal circuit, we find that

$$q_s = \frac{1}{2\pi} \oint \frac{B_\varphi}{RB_\theta} ds \tag{2.39}$$

and taking the large aspect-ratio approximation, we obtain

$$q_s = \frac{rB_\varphi}{RB_\theta}, \tag{2.40}$$

where r is the minor radius of the flux surface and R is the major radius, and B_φ and B_θ are the toroidal and poloidal magnetic fields. Remembering our assumption that RB_φ is constant, and thus f is constant (from Eq. 2.16) and $A = 0$ (from Eq. 2.32), then from Ampère's law it then follows that the toroidal field is given by

$$B_\varphi = \frac{B_0 R_0}{R} \tag{2.41}$$

where B_0 is the value of B at $R = R_0$.

In reality the safety factor has a radial profile across the magnetic axis, determined by the density profile of the toroidal current, $j(r)$. Considering Ampère's law

$$\oint_C \mathbf{B} \cdot d\mathbf{l} = \mu_0 \int\int_S \mathbf{J} \cdot d\mathbf{S} = \mu_0 I_{enclosed} \tag{2.42}$$

or equivalently

$$2\pi r B_\theta = \mu_0 I(r) \tag{2.43}$$

where the current inside r is given by

$$I(r) = 2\pi \int_0^r j(r') r' dr' \tag{2.44}$$

and inserting Eq. 2.40 for q_s gives

$$q_s(r) = \frac{2\pi r^2 B_\varphi}{\mu_0 I(r) R_0} \tag{2.45}$$

or, at the edge of the plasma $r = a$,

$$q_s(a) = \frac{2\pi a^2 B_\varphi}{\mu_0 I R_0} \tag{2.46}$$

where I is the total current. The safety factor is important in determining the stability of a tokamak plasma - as a rule of thumb the higher the value of q_s, the greater the stability of the plasma.

2.4 Individual Particle Dynamics

Before plunging into the complex theory of particle dynamics in a device such as a tokamak (and a solar magnetic field), it is useful to start from a basic viewpoint of charged particle dynamics and consider briefly some of the drifts an ion may experience in increasingly-complicated magnetic and electric field geometries.

2.4.1 Particle motion in uniform fields

The motion of a single particle of charge q, mass m in magnetic and electric fields $\mathbf{B}$ and $\mathbf{E}$ is determined by the Lorentz force equation

$$m\frac{d\mathbf{v}}{dt} = q\left(\mathbf{E} + \mathbf{v} \times \mathbf{B}\right). \tag{2.47}$$

In the absence of electric fields, and assuming uniform magnetic field, the trajectories of ions and electrons exhibit simple harmonic oscillation at the *gyrofrequency* $\omega_c = qB/m$ by following circular orbits with radius

$$r_L = \frac{mv_\perp}{qB}, \tag{2.48}$$

r_L being known as the Larmor radius, and $v_\perp$ the component of velocity perpendicular to the magnetic field. If there is a component of velocity parallel to the magnetic field, this results in a helical drift. By taking the scalar product of Eq. 2.47 with velocity, i.e.

$$m\mathbf{v} \cdot \frac{d\mathbf{v}}{dt} = q\mathbf{v} \cdot (\mathbf{v} \times \mathbf{B}) \tag{2.49}$$

it follows that

$$m\mathbf{v} \cdot \frac{d\mathbf{v}}{dt} = \frac{d}{dt}\left(\frac{1}{2}m\mathbf{v}^2\right) = 0. \tag{2.50}$$

Thus the kinetic energy of the particle remains constant - the magnetic field does no work on the particle. This is something to bear in mind when simulating test particles, which we will return to later.

2.4.2 $\mathbf{E} \times \mathbf{B}$ drift

If there is a uniform, constant magnetic field and a non-zero electric field then work can be done on the particle. A component of $\mathbf{E}$ *parallel* to $\mathbf{B}$ results in acceleration in the direction of $\mathbf{B}$ whereas a component of $\mathbf{E}$ *perpendicular* to $\mathbf{B}$ results in the drift of a particle across magnetic field lines. Qualitatively it occurs because when the particle moves in the direction of the electric field it is accelerated, which increases the velocity and hence the size of the Larmor radius. As the particles returns against the electric field, $v_\perp$ decreases and thus the radius of the orbit decreases as well. The net result of this is shown in Figure 2.6.

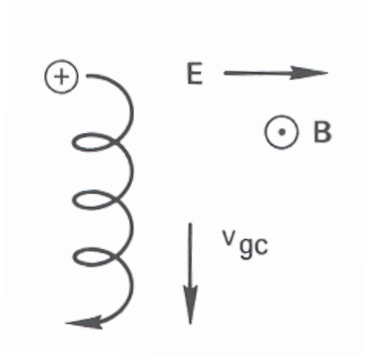

Figure 2.6: Illustration of an ion experiencing the $\mathbf{E} \times \mathbf{B}$ drift. Image from Chen [24].

It can be shown that the velocity of the drift of the particle's guiding centre is given by

$$\mathbf{v}_{gc} = \frac{\mathbf{E} \times \mathbf{B}}{B^2} \tag{2.51}$$

- note this drift is independent of the mass, charge and energy of the particle.

2.4.3 Curvature drift

If the magnetic field is not uniform, but is instead curved, then a charged particle moving along its trajectory will experience a centripetal force

$$\mathbf{F}_{cen} = \frac{mv_{\parallel}^2}{R_c}\hat{\mathbf{r}} \tag{2.52}$$

where R_c is the radius of curvature of the field line, as shown in Figure 2.7. The drift velocity corresponding to this force is

$$\mathbf{v}_{cur} = \frac{mv_{\parallel}^2}{qR_c^2}\frac{\mathbf{R}_c \times \hat{\mathbf{B}}}{B^2}. \tag{2.53}$$

Thus the particle will drift either into or out of the plane in which the curvature lies, depending on the charge state of the particle. In practice curvature drifts are generally accompanied by grad-B drifts, which we will now discuss.

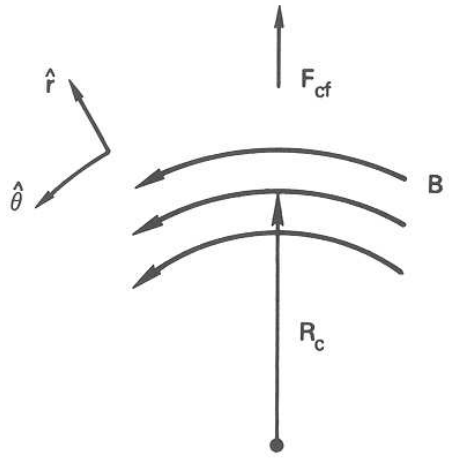

Figure 2.7: Illustration of forces on a particle in a curved magnetic field. Image from Chen [24].

2.4.4 Grad-B drift

Uniform magnetic fields make particle orbits much simpler to calculate, but in reality fields are not as simple as that. If the magnetic field has a transverse gradient then ions and electrons drift perpendicular to both the magnetic field and the direction of the gradient (see Figure 2.8) at the velocity

$$\mathbf{v}_{\nabla B} = \pm\frac{1}{2}v_{\perp}r_L\frac{\mathbf{B}\times\nabla B}{B^2}, \tag{2.54}$$

This is qualitatively similar to the $\mathbf{E}\times\mathbf{B}$ drift: as the particle moves from a region of low to high field strength, the Larmor radius decreases, and the converse is obviously true. Ions and electrons drift in different directions determined by their charge: the plus sign in Eq. 2.54 applies for the case of ions and the minus sign applies for electrons.

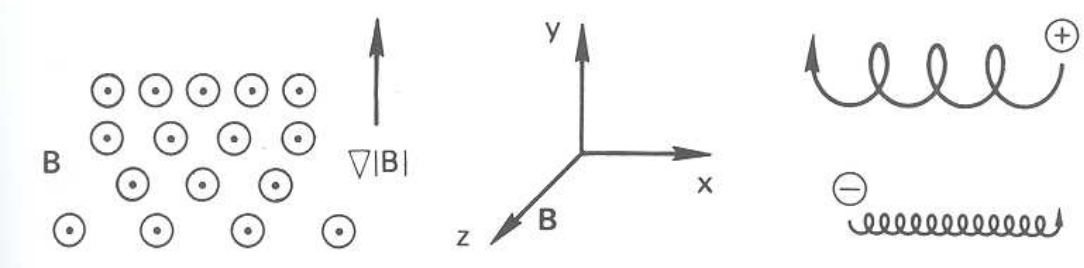

Figure 2.8: Illustration of the grad-B drift for positively and negatively charged ions. Image from Chen [24].

2.4.5 Polarisation drift

The polarisation drift comes about as a result of having a *time-dependent* electric field perpendicular to the magnetic field. An ion, initially at rest, will move in the direction of this electric field when it is applied. When the ion has a velocity then it undergoes the normal $q\mathbf{v}\times\mathbf{B}$ gyration. If the electric field were constant, then there would be no further v_p drift, only the usual $\mathbf{E}\times\mathbf{B}$ drift. However, with the electric field varying, when it changes direction there is a momentary drift in the opposite direction, as shown in Figure 2.9. The polarisation drift is a result of the finite time needed to affect the inertia of the particle. The drift velocity corresponding to this force can be shown to be [24]

$$v_p = \pm\frac{1}{\omega_c B}\frac{d\mathbf{E}}{dt} \tag{2.55}$$

- ions and electrons drift in opposite directions (where again the plus sign applies for ions and the minus sign for electrons), thereby producing a net polarisation current proportional to the rate of change of the electric field.

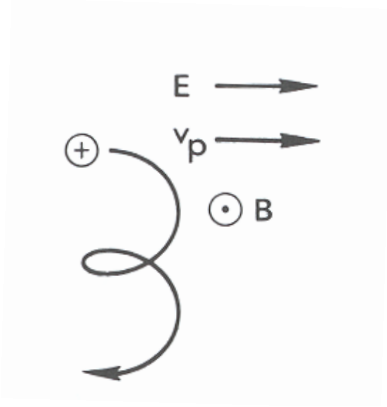

Figure 2.9: Illustration of ion undergoing the polarisation drift.

2.5 Classical Transport

Particles gyrating around a magnetic line of force can be diffused across the field lines by collisions with other particles by means of a random walk. If an ion collides with another charged particle the direction of travel of the ion is changed and the particle gyrates around a different field line. Thus the guiding centre of the particle drifts - generally in the direction opposite to the gradient of the number density of the particles. We can derive an expression to determine the relative step-size of the random walk of the guiding centre by considering resistive diffusion in a cylinder, which is governed by Ohm's Law and the equation of pressure balance. Crossing the former with $\mathbf{B}$ and substituting the latter gives

$$\mathbf{E} \times \mathbf{B} + (\mathbf{v} \times \mathbf{B}) \times \mathbf{B} = \eta_{\perp} \nabla p \tag{2.56}$$

From geometry

$$(\mathbf{v} \times \mathbf{B}) \times \mathbf{B} = -\mathbf{v}_{\perp} B^2 \tag{2.57}$$

and thus

$$\mathbf{v}_{\perp} = \frac{\mathbf{E} \times \mathbf{B}}{B^2} - \frac{\eta_{\perp} \nabla p}{B^2}. \tag{2.58}$$

where $\eta_{\perp}$ is the resistivity perpendicular to the field. Considering this in cylindrical coordinates then gives

$$v_r = \frac{E_{\theta} B_z - E_z B_{\theta}}{B^2} - \eta_{\perp} \frac{1}{B^2} \frac{dp}{dr}. \tag{2.59}$$

The first term on the right hand side of this equation is the $\mathbf{E} \times \mathbf{B}$ drift velocity required to maintain the condition that the particle motions are such that the magnetic flux through any element of fluid in a plasma with zero resistivity remains constant. The second term is the contribution from resistive effects to this velocity. From this diffusive flux term a diffusion coefficient can be derived: multiplying Eq. 2.59 by the particle density n, taking the electric field $\mathbf{E} = 0$ (the first term on the right hand side disappearing as a consequence), and assuming a constant temperature T, then $dp/dr = k_B T dn/dr$ (where k_B is Boltzmann's constant) and thus

$$nv_r = n\eta_\perp \frac{k_B T}{B^2} \frac{dn}{dr} \tag{2.60}$$

- a particle flux which can be equated to a diffusion coefficient, D, driven by a density gradient. To determine D, we can write the plasma-β as $\beta = nk_B T/(B^2/2\mu_0)$, and hence

$$D = \frac{\eta_\perp \beta}{2\mu_0}. \tag{2.61}$$

Defining the thermal speed v_T by $v_T = \sqrt{(2k_B T/m)}$, then it follows that $\beta = nmv_T^2/(B^2/\mu_0)$. Using the well-known relation between diffusivity and collision time τ for the perpendicular resistivity $\eta_\perp = m/nq^2\tau$ (where q is the particle charge), combined with the expression for the Larmor radius of a thermal particle $r_L \simeq mv_T/qB$, then we get

$$D = \frac{m}{nq^2\tau} \frac{1}{2\mu_0} \frac{nmv_T^2}{B^2/\mu_0} \simeq \frac{r_L^2}{2\tau} \sim \frac{r_L^2}{\tau}, \tag{2.62}$$

which is the classical diffusion coefficient - that is, classically, a particle undergoes a random-walk across the field lines where the step length is of the order of a Larmor orbit width r_L, rather than the collisional mean free path λ_m, as illustrated in Figure 2.10. By decreasing r_L, i.e. by increasing B, we can slow down the perpendicular diffusion of charged particles.

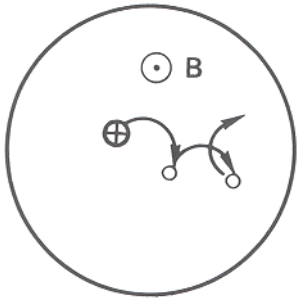

Figure 2.10: Illustration of the diffusion of a charged particle across magnetic field lines via collisions. Image from Chen [24].

2.6 Neoclassical Theory

Having taken the time to introduce the various drifts above, as well as the collisional transport theory for a uniform, cylindrical plasma, we can begin to put these together and extend to the case of a non-uniform field such as that in a torus. Deforming a cylinder into an axisymmetric torus destroys poloidal symmetry because the toroidal field on the inside of the plasma is stronger than that of the outside (since B_φ is proportional to 1/R), which has important effects on transport. Collisional transport in a torus is known as *neoclassical theory* - classical transport is insufficient to describe the collisions: theoretically predicted collisional transport rates exceed classical transport by an order of magnitude, or more. In this section we examine why this is the case.

2.6.1 Trapped particles and banana orbits

We saw in Section 2.4.1 that particles will gyrate around uniform magnetic field lines, and that their total kinetic energy $\mathcal{E} = mv_\parallel^2/2 + mv_\perp^2/2$ is conserved in the absence of electric fields. Extending the theory to a non-uniform field such as those found in the tokamak results in additional drift effects occurring, such as the previously-introduced curvature drift. Particles on the outer side of the torus, where the magnetic field is weaker, can be *trapped* in poloidal and toroidal angle: as the orbit moves towards a region of stronger magnetic field, the transverse kinetic energy increases

and the parallel energy decreases. If the particle does not have a sufficiently large component of velocity parallel to the magnetic field then it cannot penetrate into the stronger magnetic field region and hence are "bounced" by the magnetic mirrors (because of the conservation of magnetic moment μ). The poloidal projection of an orbit of this type traces out a "banana"-type shape, and hence these orbits are known as *banana orbits*, as illustrated in Figures 2.11 and 2.12. This is because the particle drift velocity, v_d, is a combination of two drifts, namely, the curvature drift (Eq. 2.53) and the ∇B (Eq. 2.54) drift. The important drift in a torus comes about as a result of the variation in toroidal magnetic field strength. Consider an ion in a plasma where the toroidal magnetic field is in the -φ direction. In this case the ∇B drift is vertically downwards. Thus if the particle is in the top half of the torus the particle drifts inside the magnetic surface towards the plasma centre, and the opposite is true in the lower half of the torus - the particle drifts outside of the magnetic surface, away from the plasma centre. This gives a finite width to a trapped particle orbit. If the particle has sufficient $v_{\|}$ the particle continues to circulate around the torus, and the particle is known as a *passing* or *transit* particle. Both passing and trapped particles lie on toroidally symmetric drift surfaces. Particles are displaced across flux surfaces, which we can show by temporarily assuming the absence of collisions (this will be discussed further below), and considering the conservation of *toroidal canonical momentum* [20].

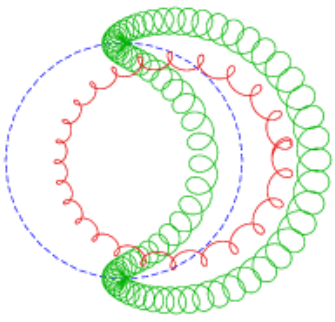

Figure 2.11: A banana orbit (green) and a passing particle orbit (red) relative to a magnetic flux surface (blue). Image from *http://www.rijnh.nl/research/fusion_physics/computational_plasma_physics/images/banana.gif*.

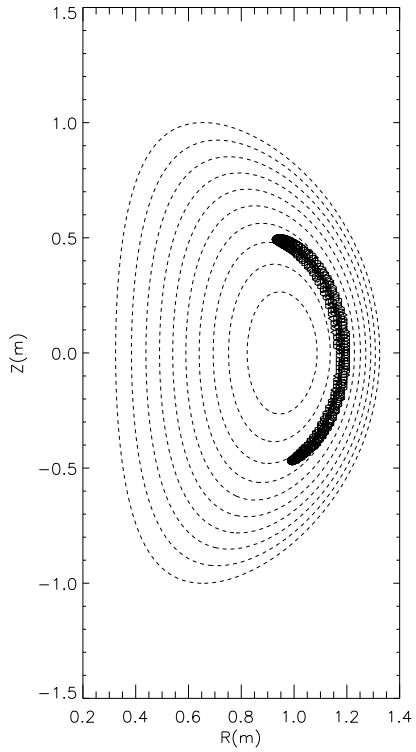

Figure 2.12: `CUEBIT` calculation of a 2.5keV proton banana orbit within a MAST-like equilibrium.

Starting from the toroidal component of the equation of motion in the absence of electric fields $m\dot{\mathbf{v}} = q(\mathbf{v} \times \mathbf{B})$, i.e.

$$m\frac{d}{dt}\left(Rv_\varphi\right) = qR\left(-v_R B_z + v_z B_R\right) \tag{2.63}$$

and using the fact that $B_R = -1/R(\partial\psi/\partial Z)$, $B_Z = 1/R(\partial\psi/\partial R)$, means that

$$m\frac{d}{dt}\left(Rv_\varphi\right) = -qR\left(\frac{v_R}{R}\frac{\partial\psi}{\partial R} + \frac{v_z}{R}\frac{\partial\psi}{\partial Z}\right) = -q\left(\mathbf{v}\cdot\nabla\right)\psi. \tag{2.64}$$

Since $\partial\psi/\partial t = 0$,

$$\frac{d\psi}{dt} = \mathbf{v}\cdot\nabla\psi \tag{2.65}$$

then

$$m\frac{d}{dt}(Rv_\varphi) + q\frac{d\psi}{dt} = 0 \tag{2.66}$$

or, in other words

$$\frac{dp_\varphi}{dt} = 0 \tag{2.67}$$

where

$$p_\varphi = mRv_\varphi + q\psi \tag{2.68}$$

is the toroidal canonical momentum, a conserved quantity in the absence of collisions. The fact that p_φ is a constant means that orbits involve changes in ψ, i.e. are displaced across flux surfaces. We will return to p_φ invariance in Chapter 5 in the context of our numerical algorithm, but for the moment continue to consider the implications of this. The condition for collisions to prevent trapping can be obtained by considering the mirror force $F = -\mu dB/ds$ (where s is the distance along a field line) and the invariant magnetic moment of a particle, $\mu = mv_\perp^2/2B$. Writing the major radial coordinate as $R = R_0 + r\cos\theta$ and the inverse aspect ratio $\epsilon = r/R_0$, the variation in toroidal magnetic field strength can be written as

$$B_\varphi = \frac{B_0 R_0}{R} = \frac{B_0 R_0}{R_0 + r\cos\theta} = \frac{B_0 R_0}{R_0(1+\epsilon\cos\theta)} \simeq B_0(1-\epsilon\cos\theta) \tag{2.69}$$

if ϵ is assumed to be small. Since kinetic energy is conserved, i.e. $\mathcal{E} = m(v_\parallel^2 + v_\perp^2)/2$ ($v_\parallel$ and $v_\perp$ being instantaneous values of those variables on the orbit of the particle), then

$$v_\parallel^2 = \frac{2\mathcal{E}}{m} - v_\perp^2 \tag{2.70}$$

where, since kinetic energy is conserved in the absence of collisions and electric fields, ϵ is a constant. Invariance of μ means that

$$\frac{mv_{\perp 0}^2}{2B_0} = \frac{mv_\perp^2}{2B}, \tag{2.71}$$

where the subscript 0 denotes the value of a variable at $\theta = 90°$, and thus

$$v_\perp^2 = (1-\epsilon\cos\theta)v_{\perp 0}^2 \tag{2.72}$$

resulting in

$$v_{\parallel}^2 = \frac{2\mathcal{E}}{m} - (1 - \epsilon\cos\theta)v_{\perp 0}^2 \tag{2.73}$$

Reflection occurs when the parallel velocity of the particle reaches zero and reverses sign, which can occur if $2\mathcal{E}/m - v_{\perp 0}^2 < \epsilon v_{\perp 0}^2$. In other words reflection occurs for those particles which have $v_{\parallel 0}^2 < \epsilon v_{\perp 0}^2$, leading to the general condition

$$v_{\parallel} \lesssim \epsilon^{1/2} v_{\perp} \tag{2.74}$$

- which is an approximate upper limit on the parallel component of velocity a particle with arbitrary θ must have to be trapped. Further analysis shows that the equation of motion of a bounce particle is given approximately by [20]

$$\frac{d^2 s}{dt^2} = -\omega_b^2 s \tag{2.75}$$

where s is the distance along a field line, and the bounce frequency ω_b is

$$\omega_b = \frac{v_{\perp}}{q_s R_0}\left(\frac{r}{2R_0}\right)^{1/2}. \tag{2.76}$$

The average time taken for a particle to be scattered by collisions out of the trapped region of velocity space is determined by the square of the pitch angle cosine at the trapped-passing boundary, i.e.

$$\tau_{detrap} \sim \tau_{coll}\left(\frac{v_{\parallel}}{v}\right)^2 \simeq \frac{2r}{R_0}\tau_{coll}. \tag{2.77}$$

For particles to be no longer trapped the detrapping time must be smaller than the bounce time $\tau_b = 1/\omega_b$. Combining the above gives then the following condition for detrapping

$$\tau_{coll} \lesssim \left(\frac{R_0}{r}\right)^{3/2} \frac{q_s R_0}{\sqrt{2}v_{\perp}}, \tag{2.78}$$

i.e. for particles satisfying this inequality the banana width has no meaning, since the particles are scattered collisionally through large angles before undergoing a single bounce orbit. Those particles which do *not* satisfy the inequality in Eq. 2.78 are displaced across the flux surface by a distance of the order of the width of the

banana orbit of the particle. A thermal trapped particle with longitudinal velocity $v_\parallel \sim \epsilon^{1/2} v_\perp$ has a banana width given by [25]

$$\Delta = \frac{m v_\parallel}{q B_\theta} \tag{2.79}$$

which can be written as

$$\Delta = \frac{m v_\perp}{q B_0} \frac{v_\parallel}{v_\perp} \frac{B_0}{B_\theta}. \tag{2.80}$$

Since $v_\parallel / v_\perp \simeq \epsilon^{1/2}$ and $m v_\perp / q B_0 = r_L$

then

$$\Delta \simeq \frac{B_0}{B_\theta} \left(\frac{r}{R_0} \right)^{1/2} r_L \tag{2.81}$$

i.e.

$$\Delta \simeq q_s \epsilon^{-1/2} r_L, \tag{2.82}$$

that is, a factor of $q_s / \epsilon^{1/2}$ bigger than the step length associated with classical diffusion, the Larmor radius r_L. This is coupled with the fact that the *effective* collision frequency is *also* enhanced, due to weaker collisions being required to shift a particle from one banana orbit to another (as the region of phase space in which particles are trapped is very narrow) compared to the classical case. The effective collision frequency is given by $\nu \simeq \nu_{coll} / \epsilon$, as we saw from the equation for the detrapping time τ_{detrap} (Eq. 2.77). For the small collisionality of the banana regime, the trapped particles dominated the transport. The fraction of particles which are trapped is of the order $\sim \epsilon^{1/2}$, thus resulting in a banana regime diffusion coefficient D_b of [20]

$$D_b \sim D_c q_s^2 \epsilon^{-3/2} \tag{2.83}$$

where $D_c \simeq r_L^2 / \tau$, i.e. there is an enhancement factor of $q_s^2 / \epsilon^{3/2}$.

2.6.2 The Pfirsch-Schlüter effect

The trapped particle effect described in the previous section is one of two major neoclassical effects, and as we saw is only present when the collision frequency is less than the bounce frequency of the trapped particles. The other important ramification, due to the toroidal geometry, is *always* present, and is known as the *Pfirsch-Schlüter effect*, which is an extension of the resistive diffusion in a plasma, as discussed in Section 2.5, to the toroidal regime. Toroidal geometry complicates the situation because, even though the plasma pressure on a given flux surface is constant, at larger major radii the geometry of the torus means that the flux surface area is larger - thus a pressure imbalance exists, leading to a net force outwards along the major radius. This is balanced by an internal magnetic force, produced by an additional longitudinal current specific to the torus: this is known as the Pfirsch-Schlüter current. The formal mathematical derivation of the value of this current in a plasma with circular cross-section is complex - the result is simply stated here [20]:

$$j_{\parallel} = -\frac{2r}{RB_{\theta}}\frac{dp}{dr}\cos\theta \tag{2.84}$$

The pressure gradient term on the right hand-side of Eq. 2.59 is modified by the effect of this current such that

$$v_r = \frac{E_{\theta}B_z - E_z B_{\theta}}{B^2} - \eta_{\perp}\frac{\nabla_{\perp}p}{B^2}\left(1 + \frac{2\eta_{\parallel}}{\eta_{\perp}}q_s^2\right) \tag{2.85}$$

- the Pfirsch-Schlüter diffusion is enhanced by a factor of $2q_s^2\eta_{\parallel}/\eta_{\perp}$ over the classical cylindrical diffusion coefficient D_c by this additional current, i.e.

$$D_{PS} = D_c\left(1 + 2\frac{\eta_{\parallel}}{\eta_{\perp}}q_s^2\right). \tag{2.86}$$

In the classical case as given by Spitzer's theory, $\eta_{\parallel}/\eta_{\perp} \simeq 1/2$. So if $q_s > 1$, as is normally the case in a tokamak, then we see a smaller enhancement than that of the banana regime, by a factor of $1/\epsilon^{3/2}$.

2.6.3 Collisionality regimes

Coulomb collisions determine the minimal level of transport in a tokamak plasma. Neoclassical transport describes the enhancement to collisional transport in toroidal gemoetry: the exact enhancement is determined by the collision frequency of the plasma. If a trapped particle completes at least one full bounce orbit before being detrapped by collisions the particle is said to be in the *banana regime*. This regime applies at high temperatures where the collision frequency is low. At low temperatures the collision frequency is high and the particles are said to be in the *Pfirsch-Schlüter regime*. We saw in the previous two sections the relationship between the classical and Pfirsch-Schlüter/banana regime diffusion coefficients. Figure 2.13 displays the dependence of the diffusion coefficient for the differing values of collisional frequency.

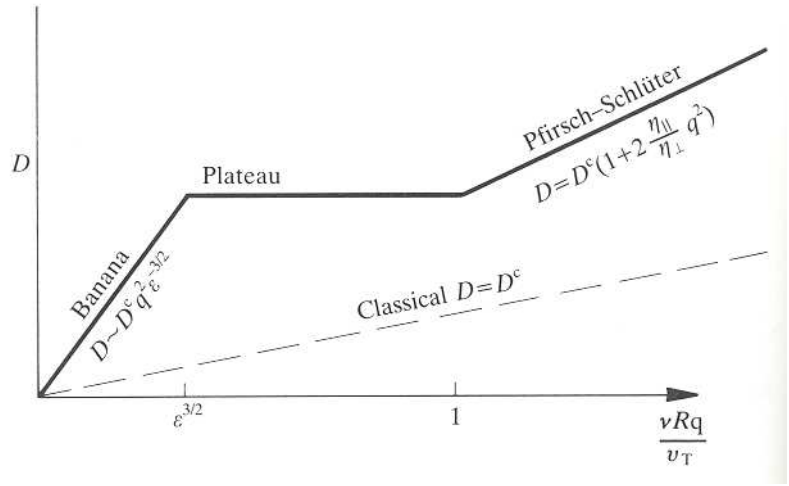

Figure 2.13: Collisional regimes and the variation of the diffusion coefficient D with collision frequency ν. Image from Wesson [20].

The banana regime applies when the following condition is satisfied:

$$\nu < \frac{\epsilon^{3/2} v_T}{R q_s}, \tag{2.87}$$

where v_T is the thermal speed of the particles, and the Pfirsch-Schlüter regime takes over at

$$\nu > \frac{v_T}{Rq_s}. \tag{2.88}$$

The collision frequency range $\epsilon^{3/2} v_T / Rq_s < \nu < v_T / Rq_s$ that separates these two extremes is known as the *plateau* regime, a region where untrapped, slowly-transiting particles contribute to the transport. In this intermediate regime the step-length is proportional to the square root of the collision time τ, and hence $D = \delta^2/\tau$ (where δ is the radial step size in one collision time) is independent of τ, i.e. the plateau regime diffusion coefficient D_P is independent of collision frequency, to a first approximation. In reality the three regimes are more complex than the approximate regimes depicted in Figure 2.13. Comparing the rates of diffusion it can be seen that the neoclassical enhancement over the classical level of diffusion is considerably higher for the banana regime than the other 2 regimes, due to the much larger characteristic step-length of the particle orbit after a Coulomb collision. This shall be discussed in the context of our work in Chapter 6.

2.6.4 The Ware pinch effect

The Ware pinch [26] is an effect felt by trapped particles, resulting from the action upon them of the toroidal electric field, which has a particular direction around the torus. As the trapped particle orbits in its banana shape around a given flux surface, the force from the electric field results in a drift velocity, which can be seen from the equation of motion, displacing the orbit slightly.

$$m\dot{v}_\varphi = q\left[E_\varphi + (\mathbf{v} \times \mathbf{B})_\varphi\right] \tag{2.89}$$

Over a full bounce period the integral of the term on the left-hand side of Eq. 2.89 is zero and so the steady state time average is also equal to zero and thus

$$\left\langle (\mathbf{v} \times \mathbf{B})_\varphi \right\rangle = -E_\varphi \tag{2.90}$$

and since

$$(\mathbf{v} \times \mathbf{B})_\varphi = v_Z B_R - v_R B_Z = -\frac{1}{R}\left[\mathbf{v} \cdot \nabla\psi\right] = v_\perp B_\theta, \tag{2.91}$$

where $v_\perp$ is the velocity perpendicular to the flux surface, then the pinch velocity, averaged over time, is

$$\langle v_\perp \rangle = -\frac{E_\varphi}{B_\theta}. \tag{2.92}$$

Since $v_\perp$ is equivalent to a radial velocity, the net result of this effect (shown in Figure 2.14) is a radially-inward motion meaning that trapped particles can accumulate towards the centre of a tokamak plasma.

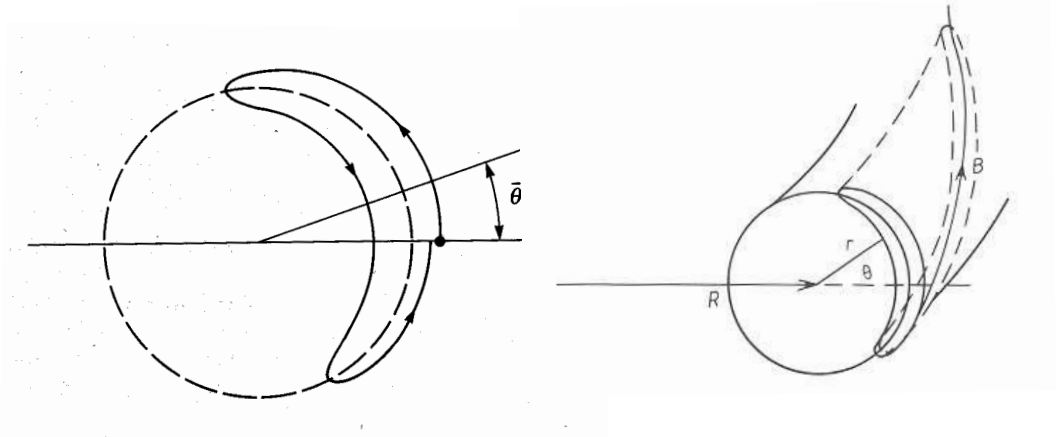

Figure 2.14: Left: Illustration of the Ware Pinch effect. Image from Wesson [20]. Right: Poloidal projection of a banana orbit in a tokamak with a toroidal magnetic field. Image from Kadomtsev [23].

2.7 Impurities in Tokamaks

The presence of impurities in a tokamak plasma has important consequences for both the safety and the operational performance of any thermonuclear fusion device [27]. Impurities dilute the concentration of the plasma fuel ions and cause the radiation losses by bremsstrahlung to be enhanced, and thus understanding their transport within a tokamak is important. The surfaces exposed to hot plasma in many fusion tokamaks are covered in carbon, either in the form of graphite or carbon-fibre composites, because of the excellent thermal properties of the element. However, the erosion rate of carbon at high temperatures is large, although processes to dope the carbon, such as boronization or siliconization, may improve the erosion properties (though in the process the thermal characteristics may be degraded). The

evaporation and sublimation of wall material which has been thermally overloaded (perhaps due to plasma disruptions) can result in carbon atoms entering the plasma [28], being ionised, subjected to radial cross-field transport processes and potentially penetrating the plasma core.

Impurities can be restricted from entering the plasma by keeping the particles away from the vacuum vessel as much as possible by using material limiters and magnetic divertors. Also, heavier metals such as tungsten (W) are now being considered for main chamber plasma facing components [29], in particular the divertor, because of the lower erosion rates associated with these materials (though high-Z impurities bring different problems with them, such as higher radiation losses). In addition, the helium "ash" produced naturally by the successful fusion reactions in the core of the burning plasma may also cause problems. This ash must be transported out of the core sufficiently rapidly so as to not accumulate to a level that dilutes the main fuel ions - each heavy ion provides Z electrons and thus at any given electron density, assuming quasineutrality, each heavy ion replaces Z hydrogen ions. The theory of neoclassical impurity transport is well-developed, and we will return to this in Chapter 6.

"All exact science is dominated by the idea of approximation"

Bertrand Russell

Chapter 3

The Test Particle Approach

3.1 Why Use Test Particles?

Modelling the evolution of a plasma is a very complex problem. In order to make progress in areas of astrophysics and fusion physics, sometimes analytically tractable mathematics is not sufficiently well-developed to be of use. Computer simulations can be used, not as a replacement to traditional theory and experiment, but as a useful "third way" designed to complement both of the former: experiments and devices can be expensive and difficult to build, maintain and operate, data difficult to obtain, interpret and compare with theory. Computer simulations can help bridge the gap by providing a perfectly controlled, easily repeatable environment, coupled with the obvious ability to perform rapidly millions of repetitive calculations that a human would take months to do. Importantly, computer simulations allow the examination of non-linear behaviour in plasmas, which is difficult to do analytically. Of course computer simulations have down-sides and disadvantages too, and this must be kept in mind when using them, but for the most part they have become a hugely important aid in furthering plasma physics research.

Having established the need for simulations, the next problem is to establish the best method of modelling a plasma computationally. A plasma involves the complicated interaction of many individual particles - electrons and ions (and, in

partially-ionised plasmas, neutral atoms) - and, conceptually at least, the simplest approach is to integrate numerically the equations of motion of the particles, together with Maxwell's equations. However the huge number of particles involved in any laboratory or astrophysical plasma (as an example, 1 cubic metre of a tokamak plasma contains typically around 10^{20} ions [16]) renders this approach untenable under current (and even foreseeable) computer processing powers. Simulation of plasma physics by computers is then likely to follow one of the hierarchical methods of analytical plasma modelling, depending on the time and length scales the investigation demands, such as kinetic theory, two-fluid theory, or MHD. There are various different ways to model these computationally. Kinetic codes provide the most accurate, fundamental description of the physics (in terms of describing the velocity distribution function of the plasma), while fluid codes describe plasmas in terms of macroscopic quantities, which makes things simpler but risks not correctly modelling some of the underlying physics. Hybrid codes use some combination of the two, treating some components of the system as a fluid and other components kinetically (for an example of a description of a hybrid code, see e.g. Swift [31]). Each approach has its own advantages and disadvantages. An alternative method is the test particle approach that we concentrate on with our own full-orbit particle algorithm. In a full-orbit simulation, the Lorentz force equation is solved to obtain the complete orbit of a particle. Some test particle approaches treat the charged particle motion as a superposition of a relatively fast circular motion around a point called the *guiding centre* and the slow drift of this point: the full-orbit approach has the advantage over this guiding centre approximation in that it is more accurate and is essential when the Larmor radius is a significant fraction of the magnetic field scale length. Moreover when collisions are included, cross-field collisional scattering occurs automatically if the full orbit is calculated. The nature of the algorithm used in our code is such that particle energy is conserved to machine accuracy in the absence of non-magnetic forces for arbitrary values of the time-step. The main disadvantage of our test particle simulations is their failure to consider the back reaction of the particles to the fields imposed upon it. Charged particles travelling through electric and magnetic fields generate their own, additional, self-fields, which

should then be taken into account for a proper self-consistent description. However, we proceed by assuming that these particles do not significantly affect the overall field: this is known as the *test particle assumption*. This assumption is valid provided that the number of test particles is small compared to the number of bulk plasma ions and electrons, so that the particles make an insignificant contribution to the plasma current and charge density. It is trivially true in the sense that the number of particles simulated is negligible compared to the number of particles in the real plasma. The actual test is whether the currents and charges of the test particle species are still negligible when the number of computational particles is scaled up to a realistic number.

The test particle approach is certainly satisfactory in our impurity transport calculations (see Chapters 5 & 6) because we model a trace species in the plasma. The criterion in this case is that product of charge Ze and number density n of the impurities is small compared to that of the bulk ions - if the flows are comparable this ensures that the impurities do not contribute significantly to either the current or the charge density. In the case of the solar physics magnetic X-point calculations (see Chapter 4) the situation is different because we model bulk ions. The main justification for the test particle approach in this case is that the equivalent beta of the simulated ion distribution is small, so that the cold plasma ideal MHD model (i.e. ideal MHD in the limit in which the plasma pressure is small compared to the magnetic pressure) used to calculate the fields remains valid.

3.2 A Test Particle Algorithm

As noted in Chapter 2, magnetic fields alone do no work on charged particles, so in order to simulate orbits accurately, it is necessary to ensure that the total energy of any particle (that is, the kinetic energy plus the potential energy) in static magnetic fields is conserved to an acceptable level by the numerical scheme used.

The test particle code employed throughout the work contained in this thesis is based on the `CUEBIT` (**CU**lham **E**nergy-conserving Or**BIT**) code developed by K.G. McClements and A. Thyagaraja at UKAEA Culham Division, and applied by

Hamilton and co-workers [7,32,33]. In its simplest form it is designed to solve the Lorentz force equations for a test particle (of mass m, and charge Ze) in a magnetic field $\mathbf{B}$, namely:

$$m\frac{d\mathbf{v}}{dt} = Ze\mathbf{v} \times \mathbf{B}(\mathbf{x}) \tag{3.1}$$

$$\frac{d\mathbf{x}}{dt} = \mathbf{v} \tag{3.2}$$

Here $\mathbf{B(x)}$ is the magnetic field at position vector $\mathbf{x}$, $\mathbf{v}$ is the velocity of the particle, and there is no electric field $\mathbf{E}$ present. The `CUEBIT` code approximates these equations via the finite difference system

$$m\frac{\mathbf{v}^{i+1} - \mathbf{v}^{i}}{\Delta t} = Ze\left(\frac{\mathbf{v}^{i+1} + \mathbf{v}^{i}}{2}\right) \times \mathbf{B}\left(\frac{\mathbf{x}^{i+1} + \mathbf{x}^{i}}{2}\right) \tag{3.3}$$

$$\frac{\mathbf{x}^{i+1} - \mathbf{x}^{i}}{\Delta t} = \frac{\mathbf{v}^{i+1} + \mathbf{v}^{i}}{2} \tag{3.4}$$

where superscripts i and $i+1$ denote the values of x and v at successive time steps.

We can evaluate the order of accuracy of the algorithm by considering, for simplicity, the one-dimensional equation

$$\frac{dx}{dt} = v(t). \tag{3.5}$$

By Taylor expanding $x(t)$ about its value midway between the old timestep (i) and the new timestep (i+1) we get

$$x^{i+1} = x^{i+1/2} + \frac{\Delta t}{2}\frac{dx}{dt}|_{i+1/2} + \frac{\Delta t^2}{8}\frac{d^2x}{dt^2}|_{i+1/2} + \mathcal{O}(\Delta t^3) \tag{3.6}$$

$$x^{i} = x^{i+1/2} - \frac{\Delta t}{2}\frac{dx}{dt}|_{i+1/2} + \frac{\Delta t^2}{8}\frac{d^2x}{dt^2}|_{i+1/2} + \mathcal{O}(\Delta t^3) \tag{3.7}$$

where $\mathcal{O}(\Delta t^3)$ represents terms in third order and above in Δt. Subtracting Eq. 3.7 from 3.6 and dividing by Δt we obtain

$$\frac{dx}{dt}|_{i+1/2} = \frac{x^{i+1} - x^{i}}{\Delta t} + \mathcal{O}(\Delta t^2). \tag{3.8}$$

Hence, if we evaluate v in Eq. 3.5 midway in time between the old and new timesteps, the scheme is second order accurate. The same argument applies to all 6 components of the Lorentz force equation and hence the algorithm employed by `CUEBIT` is second order accurate. A Runge-Kutta approach would give a higher order of accuracy than this relatively simple scheme, but the Runge-Kutta approach works most effectively when the fields are smooth, which may not necessarily be the case in idealised plasma physics models like MHD (e.g. current layers, shocks). The algorithm allows the reproduction of essential features of charged particle orbits without having to assume values of the timestep Δt that are very small compared to the Larmor period $2\pi m/ZeB$.

The scheme conserves energy exactly by approximating the velocity on the right hand side of Eq. 3.3 by its average value at the time steps i and $i+1$: this can be seen by taking the scalar product of this equation with $\mathbf{v}^{i+1} + \mathbf{v}^i$, which gives

$$m\frac{\left(\mathbf{v}^{i+1}\right)^2 - \left(\mathbf{v}^i\right)^2}{\Delta t} = 0 \tag{3.9}$$

and hence

$$(v^{i+1})^2 = (v^i)^2. \tag{3.10}$$

This makes it possible to obtain accurate results with relatively long time steps. If $\mathbf{v}^i = (v_x^i, v_y^i, v_z^i)$, and $\mathbf{v}^{i+1} = (v_x^{i+1}, v_y^{i+1}, v_z^{i+1})$, then Eq. 3.3 can be written explicitly in the form

$$\mathbf{A} \cdot \mathbf{v}^{i+1} = \mathbf{B} \cdot \mathbf{v}^i \tag{3.11}$$

where the matrices $\mathbf{A}$ and $\mathbf{B}$ are given by

$$\mathbf{A} = \begin{pmatrix} 1 & -\alpha_z & \alpha_y \\ \alpha_z & 1 & -\alpha_x \\ -\alpha_y & \alpha_x & 1 \end{pmatrix}, \tag{3.12}$$

$$\mathbf{B} = \begin{pmatrix} 1 & \alpha_z & -\alpha_y \\ -\alpha_z & 1 & \alpha_x \\ \alpha_y & -\alpha_x & 1 \end{pmatrix}, \tag{3.13}$$

where $\alpha_x = (ZeB_x/2m)\Delta t, \alpha_x = (ZeB_y/2m)\Delta t$, and $\alpha_z = (ZeB_z/2m)\Delta t$. The solution of Eq. 3.11 for v^{i+1} in terms of v^i is

$$\mathbf{v}^{i+1} = \mathbf{A}^{-1} \cdot \mathbf{B} \cdot \mathbf{v}^i. \tag{3.14}$$

To find the inverse of $\mathbf{A}$, $\mathbf{A}^{-1}$, we use the formula for the inverse of a general matrix $\mathbf{G}$

$$\mathbf{G} = \begin{pmatrix} a & b & c \\ d & e & f \\ g & h & i \end{pmatrix},$$

which is

$$\mathbf{G}^{-1} = \frac{1}{a(ei-fh) - b(di-fg) + c(dh-eg)} \begin{pmatrix} (ei-fh) & (ch-bi) & (bf-ce) \\ (fg-di) & (ai-cg) & (cd-af) \\ (dh-eg) & (bg-ah) & (ae-bd) \end{pmatrix}.$$

Applying this formula to $\mathbf{A}$ results in

$$\mathbf{A}^{-1} = \frac{1}{1+\alpha_x^2+\alpha_y^2+\alpha_z^2} \begin{pmatrix} 1+\alpha_x^2 & \alpha_z+\alpha_x\alpha_y & \alpha_x\alpha_z-\alpha_y \\ \alpha_x\alpha_y-\alpha_z & 1+\alpha_y^2 & \alpha_y\alpha_z+\alpha_x \\ \alpha_x\alpha_z+\alpha_y & \alpha_y\alpha_z-\alpha_x & 1+\alpha_z^2 \end{pmatrix}, \tag{3.15}$$

and hence

$$\mathbf{A}^{-1}\cdot\mathbf{B} = \frac{1}{1+\alpha_x^2+\alpha_y^2+\alpha_z^2} \begin{pmatrix} 1+\alpha_x^2-\alpha_y^2-\alpha_z^2 & 2(\alpha_x\alpha_y+\alpha_z) & 2(\alpha_z\alpha_x-\alpha_y) \\ 2(\alpha_x\alpha_y-\alpha_z) & 1-\alpha_x^2+\alpha_y^2-\alpha_z^2 & 2(\alpha_y\alpha_z+\alpha_x) \\ 2(\alpha_z\alpha_x+\alpha_y) & 2(\alpha_z\alpha_y-\alpha_x) & 1-\alpha_x^2-\alpha_y^2+\alpha_z^2 \end{pmatrix}, \tag{3.16}$$

using the standard rules for matrix multiplication.

The code makes a first approximation to the value of $\mathbf{v}^{i+1}$ by replacing $(\mathbf{x}^{i+1} + \mathbf{x}^{\mathbf{i}})/2$ with $\mathbf{x}^i$ on the right hand side of Eq. 3.3. Having obtained this value, we can enter it into Eq. 3.4, solve for a first estimate of $\mathbf{x}^{i+1}$, which is in turn substituted

back into 3.3 for a more accurate estimation of $\mathbf{v}^{i+1}$ and so on - the estimates converge with successive iterations, though in practice we find that 3 iterations are sufficient to give an accurate solution.

3.3 Generating Maxwellian Test Particle Distributions

In gases and plasmas, the temperature is defined by the distribution of velocities of the individual particles that make up the bulk material. The Maxwellian distribution is the velocity distribution function of a system in thermal equilibrium. The distribution of speeds can be written as:

$$f(v) = 4\pi \left(\frac{m}{2\pi k_B T}\right)^{3/2} v^2 \exp\left[-\frac{mv^2}{2k_B T}\right] \tag{3.17}$$

where T is temperature of the Maxwellian, k_B is Boltzmann's constant and m the mass of the particle. As such, when studying test particles in a plasma in thermal equilibrium, it is appropriate at $t = 0$ to assign them at random a velocity taken from a Maxwellian distribution. This can be done in FORTRAN by using the NAG (Numerical Algorithms Group) routine **G05DDF**, which returns a pseudo-random real number taken from a Gaussian distribution [34] (other methods exist). This function has two parameters: the mean of the distribution from which the random number is selected, and the standard deviation, which is the square root of the variance. By multiplying a random number from this distribution (with mean equal to zero and variance $\sigma = 1$) with the root mean square velocity

$$\left\langle v^2 \right\rangle^{1/2} = \sqrt{\frac{k_b T}{m}} \tag{3.18}$$

the three velocity components of the particle can be generated. Producing sufficient particle velocities this way can then be shown to form a Maxwellian distribution by binning them in a histogram, as shown in Figures 3.1 and 3.2, where the component of velocity in the x-direction is plotted for 10^4 and 10^5 particles respectively for a distribution at a temperature of T=1MK. The size of the bins for both histograms

is equivalent to 2000 ms^{-1}. Obviously the more particles we have the less noisy the distribution will be, although of course simulations with more particles take longer to run.

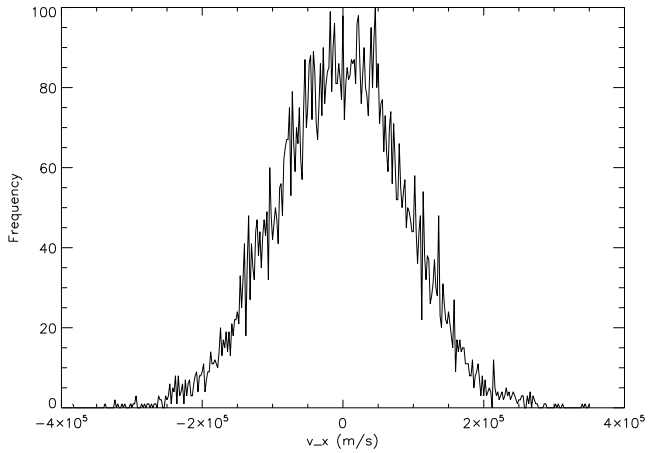

Figure 3.1: Test particle v_x velocity component generated by `CUEBIT` for 10^4 protons, at a distribution temperature of T=1MK.

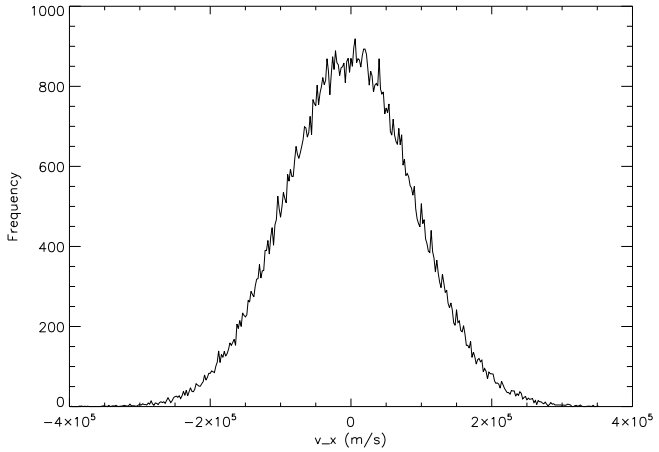

Figure 3.2: Test particle v_x velocity component generated by `CUEBIT` for 10^5 protons, at a distribution temperature of T=1MK.

3.4 Addition of Non-Magnetic Forces

The `CUEBIT` algorithm can be extended to include the effect of collisions by modifying Eq. 3.1 as follows:

$$m\frac{d\mathbf{v}}{dt} = Ze(\mathbf{v}\times\mathbf{B}) - \frac{m\mathbf{v}}{\tau} + m\mathbf{r}(t). \tag{3.19}$$

Here τ is the collision time, which for simplicity is assumed to be independent of velocity - this being appropriate when computing the trajectories of test ions whose speeds are less than the bulk ion thermal speed, which is the case for massive impurity ions with temperature comparable to that of the bulk ions (see Chapters 5 and 6). The function $\mathbf{r}(t)$ is a random force that represents the stochastic nature of Coulomb collisions, in much the same way that Ermak and Buckholz [35] simulate Brownian motion with a random force as included in the ordinary Langevin equation of motion. The individual components of $\mathbf{r}(t)$, the numbers r_x, r_y and r_z, are random numbers that are chosen independently for each particle at each timestep, with zero mean and variance

$$\sigma^2 = \frac{v_i^2}{\tau\Delta t} \tag{3.20}$$

where $v_i = (2T/m)^{1/2}$ is the thermal speed of the ions corresponding to a specified temperature T, in energy units, and Δt is the time step used in the code [35]: choosing this value of the variance ensures that the test particles evolve from an arbitrary initial state to a Maxwellian distribution at temperature T. This can be shown by neglecting the Lorentz force term in Eq. 3.19 and considering just the x-component, i.e.

$$\frac{dv_x}{dt} = -\frac{v_x}{\tau} + r_x, \tag{3.21}$$

which can be approximated by the finite difference equation

$$\frac{v_x^{n+1} - v_x^n}{\Delta t} = -\frac{v_x^{n+1} + v_x^n}{2\tau} + r_x \tag{3.22}$$

where n labels a particular timestep. Solving Eq. 3.18 for v_x^{n+1} we obtain

$$v_x^{n+1} = \left(\frac{1-\Delta t/2\tau}{1+\Delta t/2\tau}\right) v_x^n + \left(\frac{\Delta t}{1+\Delta t/2\tau}\right) r_x. \tag{3.23}$$

Taking the average of 3.23 over the test particle distribution

$$\left\langle v_x^{n+1} \right\rangle = \left(\frac{1 - \Delta t/2\tau}{1 + \Delta t/2\tau} \right) \langle v_x^n \rangle + \left(\frac{\Delta t}{1 + \Delta t/2\tau} \right) \langle r_x \rangle \tag{3.24}$$

and bearing in mind that $\langle r_x \rangle = 0$, then

$$\left\langle v_x^{n+1} \right\rangle = \left(\frac{1 - \Delta t/2\tau}{1 + \Delta t/2\tau} \right) \langle v_x^n \rangle . \tag{3.25}$$

As $\left(\frac{1-\Delta t/2\tau}{1+\Delta t/2\tau}\right)$ is less than 1, then any initial directed velocity will decay to zero on timescales long compared to τ. Squaring both sides of Eq. 3.23 gives

$$\left(v_x^{n+1}\right)^2 = \left(\frac{1 - \Delta t/2\tau}{1 + \Delta t/2\tau} \right)^2 (v_x^n)^2 + \left(\frac{1 - \Delta t/2\tau}{1 + \Delta t/2\tau} \right) \left(\frac{\Delta t}{1 + \Delta t/2\tau} \right) v_x^n r_x + \left(\frac{\Delta t}{1 + \Delta t/2\tau} \right)^2 r_x^2. \tag{3.26}$$

Averaging over the distribution, and making use of the fact that $\langle v_x^n r_x \rangle = 0$, then this becomes

$$\left\langle \left(v_x^{n+1}\right)^2 \right\rangle = \left(\frac{1 - \Delta t/2\tau}{1 + \Delta t/2\tau} \right)^2 \langle (v_x^n)^2 \rangle + \left(\frac{\Delta t}{1 + \Delta t/2\tau} \right)^2 \langle r_x^2 \rangle . \tag{3.27}$$

For times much longer than τ, it is expected that $\langle v_x^2 \rangle$ will relax to a constant value given by

$$\left\langle v_x^2 \right\rangle = \frac{1}{\sqrt{\pi} v_i} \int_{-\infty}^{\infty} v_x^2 e^{-v_x^2/v_i^2} dv_x = \frac{v_i^2}{2} = \frac{T}{m}. \tag{3.28}$$

Setting both $\left\langle \left(v_x^2\right)^2 \right\rangle$ and $\left\langle \left(v_x^{n+1}\right)^2 \right\rangle$ equal to this value in Eq. 3.27 we obtain

$$\left\langle r_x^2 \right\rangle = \frac{v_i^2}{\tau \Delta t}. \tag{3.29}$$

$\langle r_x^2 \rangle$ can be identified as the variance of the distribution from which r_x is selected, and thus this result matches the result stated in Eq. 3.20.

Equation 3.19 can be approximated by the finite difference equation

$$\mathbf{A} \cdot \mathbf{v}^{i+1} = \mathbf{B} \cdot \mathbf{v}^i + \mathbf{c} \tag{3.30}$$

where $\mathbf{c}$ is a vector representing the collisional forces and $\mathbf{A}, \mathbf{B}$ are the same as previously. When the non-magnetic force is of the form given by the second and third terms on the right-hand side of Eq. 3.19, then we can write

$$\mathbf{c} = -\frac{\Delta t}{\tau}\bar{\mathbf{v}} + \Delta t\mathbf{r}(t) \tag{3.31}$$

where $\bar{\mathbf{v}} = (\mathbf{v}^{i+1} + \mathbf{v}^{i})/2$.

Treating $\mathbf{c}$ explicitly, Eq. 3.30 has formal solution

$$\mathbf{v}^{i+1} = \mathbf{A}^{-1} \cdot \mathbf{B} \cdot \mathbf{v}^{i} + \mathbf{A}^{-1} \cdot \mathbf{c} \tag{3.32}$$

with $\mathbf{A}^{-1}$ as given before. Using this scheme we can incorporate collisions into our simulations without too much difficulty, as we will see in Chapters 5 and 6.

"The way to do fieldwork is never to come up for air until it is all over"

Margaret Mead

Chapter 4

Fast Alfvén Wave Heating and Acceleration of Ions in a Non-Uniform Magnetoplasma

Note: The material in this chapter has been published in the Astrophysical Journal. The reference is:
McKay R J, McClements K G, and Fletcher L: "Fast Alfvén Wave Heating and Acceleration of Ions in a Nonuniform Magnetoplasma" *ApJ.* **658**, 631 (2007)

4.1 Introduction: Our Work in Context

As we saw in Chapter 1, the origin of thermal plasma temperatures of the order of 10^6K in the solar corona has been a major issue in solar physics for several decades. Although the majority of spectral line diagnostics only provide information on electron temperatures, Lyman α line width measurements indicate that coronal protons have a similar temperature to the electrons (see e.g. the review by Noci [36]). Even higher coronal electron temperatures, up to around 4×10^7K, are associated with the gradual phase of solar flares [37]. Theoretical models of coronal heating, involving either waves generated by bulk flows in the photosphere or *in situ* magnetic

reconnection, have generally been based purely on MHD or two-fluid theory (e.g. Stasiewicz [38]), although very recently particle-in-cell methods have also been used (Tsiklauri *et al.* [39]). MHD waves have been widely considered as a possible mechanism for coronal heating because of the large energy flux they can carry into the corona from lower in the solar atmosphere, although there is disagreement on exactly which MHD mode may be the most likely candidate. For example, Browning [9] suggests that the slow magnetoacoustic wave does *not* actually contain sufficient energy flux, and that as the fast mode is likely to be totally internally reflected in the chromosphere (and hence evanescent there) the Alfvén wave is the most likely candidate. However Porter and co-workers [40], whilst favouring the fast wave (possibly generated during reconnection events in the corona), also suggest that the energy flux from the slow mode in previous analyses of observational data may have been underestimated by a factor of as much as 100. Regardless of which mode is responsible, in all cases an important question concerns the mechanism upon which the energy within the MHD mode is converted into kinetic energy in the plasma. Porter discounted the Alfvén mode on the basis of the difficulty of dissipating it due to its incompressibility, but it is largely the case that any MHD mode in a plasma with coronal properties suffers from the same disinclination to dissipate (due to the extremely low viscosity and resistivity) - and thus any wave heating mechanism for the corona must include an effective damping mechanism. Several different models have been proposed, such as *phase mixing* and *resonant absorption*, and the role of MHD turbulence is also expected to be important in generating wave cascades to increasingly small scales and speeding up damping. Additionally, damping mechanisms generated for one wave mode may still be accessible by other propagating modes via the process of mode conversion, discussed further below.

Observationally, the past decade has been extremely fruitful in terms of the detection of coronal MHD waves, as both satellite and ground-based technology has improved in its ability to resolve the spatial and temporal fluctuations that have been observed for a significantly longer period of time. An example of which are *quasi-periodic pulsations* (QPP's), which have been observed over a wide frequency band - from radio waves to hard X-rays - and generally have periods from a few tenths of

a second to several minutes. QPP's with periods greater than a few seconds are of interest because they are associated with MHD oscillations of coronal loops - see, for example, Nakariakov and Verwichte [41] for a recent review. Foullon and co-workers [42] studied two sequences of QPP in the X-ray band for solar flare pulsations observed on February 5 and 6, 2003, using data from the RHESSI satellite. The modulation of this flaring emission causes periodic energisation of electrons in the flaring loop, and was interpreted to be due to MHD oscillations with the phase speed suggesting that fast magnetoacoustic kink modes were the most likely candidate for this modulation. Nakariakov *et al.* proposed that fast magnetoacoustic waves in a non-flaring loop could interact with a nearby flaring active region [43], to propose an explanation to observations of the coupling of oscillations in nearby loops with QPP of flaring energy release. These papers only added to the growing body of evidence for the presence of propagating fast waves in the solar corona, after Verwichte and co-workers observed propagating transverse waves in an open magnetic structure using TRACE [44]. The supra-arcade (which resembles a fan of bright, hot rays) above the post-flare loop arcade associated with a flare event on the 21st April 2002 was analysed. Between the rays, dark sunward-moving structures or trails can be seen, which are known as "tadpoles". The tadpole-ray boundaries are seen to oscillate transversely, and these oscillations were interpreted as being fast magnetoacoustic kink wave trains guided by the vertical ray-tadpole structure.

We address the problem of coronal plasma heating using the alternative approach of computing the orbits of test particles in the field of an ideal MHD wave propagating in a non-uniform equilibrium magnetic field. Studying the plasma at the test particle level is useful in helping to understand how the plasma is energised by the wave. Specifically, we consider a fast Alfvén wave in a two-dimensional X-point configuration (a fast Alfvén wave being a fast magnetoacoustic wave in the limit where the plasma pressure becomes negligible [45]). Magnetic X-points have a long-established role in theories of both solar flares and coronal heating because, as discussed in Chapter 1, they represent a paradigm for studying magnetic reconnection and particle acceleration in a relatively simple analytical framework. For example, Craig and McClymont [46] showed that the magnetic relaxation of a perturbed X-

point dissipated energy on timescales that may account for thermal energy release during the gradual phase of a solar flare, whilst Hassam and Lambert [47] illustrated the role of X-points in the formation of current sheets, and pointed out the implications for solar coronal heating models. Additionally, the fact that the magnetic field strength tends to zero at the null means that close to the null the Lorentz force is very weak and thus particles in this region are effectively unmagnetised and can be accelerated to high velocities if an electric field is present - for examples of studies of particle acceleration in X-point configurations see Hamilton and co-workers [7,32]. Magnetic X-points are also of great interest to the laboratory plasma physics community, since they occur frequently in magnetic confinement experiments (e.g. Myra *et al.* [48]). Moreover, the properties of MHD modes in X-point equilibrium fields have been studied by many authors, beginning with Bulanov & Syrovatskii [49] who considered the case of wave propagation in a two-dimensional configuration with zero equilibrium current and zero plasma pressure. In this scenario the shear and fast Alfvén waves are decoupled, as in the case of a uniform equilibrium plasma, provided that there are no variations in the longitudinal direction (normal to the X-point plane). The modes become coupled [50], leading to the possibility of shear waves being converted to fast waves, if the magnetic field has a longitudinal component: this mode conversion process has recently been studied in detail [51]. It has been proposed that fast waves could also be generated from shear waves as a result of refraction in coronal holes [52], and it has also been suggested recently that the coronal heating requirements could be provided by fast waves resulting from the propagation of shear waves in a plasma with a transverse density gradient [53]. The possible role of the fast mode in coronal heating has been investigated in detail from a purely fluid perspective [40].

At first sight it is not obvious that ideal MHD waves such as the fast mode should play any significant role in particle acceleration, since the ideal form of Ohm's law introduced in Chapter 1

$$\mathbf{E} + \mathbf{v} \times \mathbf{B} = 0, \tag{4.1}$$

$\mathbf{E}$ and $\mathbf{B}$ being the electric and magnetic fields and $\mathbf{v}$ the plasma flow, precludes

the possibility of a parallel electric field $E_\parallel \equiv \mathbf{E} \cdot \mathbf{B}/B$, and perpendicular electric fields generally produce only a cross-field drift in the particle motion. One could invoke the presence of resistive and electron inertial terms in the generalized Ohm's law to argue that the $\mathbf{E}$ field associated with a fast wave can in general have a parallel component, but the impact of this $E_\parallel$ on particle acceleration is limited by the fact that both the resistive length scale and the collisionless skin depth in the solar corona are extremely small compared to observed macroscopic scale lengths [54]. However, Miller *et al.* [55] proposed that a spectrum of fast waves could nevertheless account for the production of energetic electrons in flares: in this model acceleration occurs because electrons with finite magnetic moment μ are subject to a force $-\mu\nabla_\parallel B$ arising from the non-uniform magnetic field associated with the waves. This phenomenon, referred to as transit-time damping or transit-time magnetic pumping [56], has also been invoked to account for the acceleration of energetic particles in the interplanetary medium [57] and has been observed directly in tokamak experiments (e.g. Start *et al.* [58]). For the case of fast waves in a low β plasma, transit-time damping is normally considered to be relevant only for electrons, since ions cannot satisfy the condition for the transit time of a particle in a single wavelength to equal the wave period:

$$\omega \simeq k c_A = k_\parallel v_\parallel, \tag{4.2}$$

where ω is the wave frequency, k is the wavenumber, c_A is the Alfvén speed, and $k_\parallel$, $v_\parallel$ are the components of the wave vector and particle velocity parallel to $\mathbf{B}$. However, a change in $v_\parallel$ can result from any spatial or temporal variation in the direction of the magnetic field. Spatial variations could of course be present in the equilibrium field as well as the wave field. We aim to quantify this process for the case of ions (in particular protons) in an X-point magnetic equilibrium perturbed by a fast wave.

4.2 Model

The equilibrium field in our model $\mathbf{B}_E$ has a two-dimensional X-point structure of the form given by Eqs. 1.45 and 1.46 with $\bar{\alpha} = 1$, i.e.

$$\mathbf{B}_E = \frac{B_0}{r_0} \left(y\hat{\mathbf{x}} + x\hat{\mathbf{y}} \right), \tag{4.3}$$

where $\hat{\mathbf{x}}$ and $\hat{\mathbf{y}}$ denote unit vectors in the x and y directions, and B_0 is the field magnitude at $r = (x^2+y^2)^{1/2} = r_0$. The equilibrium current and the equilibrium flow are both taken to be zero. Following authors such as Bulanov & Syrovatskii [49], McClements and co-workers [54], Craig & Watson [59], and McLaughlin & Hood [60], we seek fast wave solutions of the linearised, cold plasma ideal MHD equations for this equilibrium. The waves, like the equilibrium, are assumed to be invariant in the z-direction, and can be represented in terms of perturbations to a magnetic flux function $\psi(x, y)$ such that $\mathbf{B} = \nabla \times (\psi\hat{\mathbf{z}})$ where $\hat{\mathbf{z}}$ is the unit vector in the z direction, so that the field perturbation is confined to the (x, y) plane, and hence ψ is equal to A given by Eq. 1.44 with $\bar{\alpha} = 1$. From Ampère's law the perturbed current $\mathbf{j}$ then lies in the $\hat{\mathbf{z}}$ direction, and the Lorentz force $\mathbf{j} \times \mathbf{B}_E$ is in the (x, y) plane, orthogonal to the equilibrium field.

4.2.1 Generalised fast wave solution

Following McClements *et al.* [61] we consider compressible perturbations of a two-dimensional current-free magnetic X-point in the limit of low plasma β, in the ideal MHD limit. Our starting point is the ideal Ohm's Law (Eq. 4.1), along with the momentum and induction equations. The momentum equation can be written as

$$\frac{\partial \mathbf{v}}{\partial t} + (\mathbf{v} \cdot \nabla)\, \mathbf{v} = \frac{1}{\rho}\mathbf{j} \times \mathbf{B}. \tag{4.4}$$

If $\mathbf{B} = \nabla \times \mathbf{A}$ where

$$\mathbf{A} = \psi\hat{\mathbf{z}} \tag{4.5}$$

then the induction equation becomes

$$\frac{\partial \mathbf{A}}{\partial t} = \mathbf{v} \times (\nabla \times \mathbf{A}). \tag{4.6}$$

From vector calculus

$$\mathbf{v} \times (\nabla \times \mathbf{A}) = \nabla(\mathbf{v} \cdot \mathbf{A}) - (\mathbf{v} \cdot \nabla)\mathbf{A} - \mathbf{A} \times (\nabla \times \mathbf{v}) - (\mathbf{A} \cdot \nabla)\,\mathbf{v} \tag{4.7}$$

which simplifies to

$$\mathbf{v} \times (\nabla \times \mathbf{A}) = -\,(\mathbf{v} \cdot \nabla)\,\mathbf{A} \tag{4.8}$$

if there are no variations in the z-direction and flows are in the (x, y) plane only. Thus, from equations 4.5 and 4.8, we have

$$\frac{\partial \psi}{\partial t} + (\mathbf{v} \cdot \nabla)\,\psi = 0. \tag{4.9}$$

Combining Ampère's law $\nabla \times \mathbf{B} = \mu_0 \mathbf{j}$ with Eq. 4.5 gives

$$\mathbf{j} = \frac{1}{\mu_0}\left[\nabla \times (\nabla \times \psi \hat{\mathbf{z}})\right] \tag{4.10}$$

which, assuming ψ is invariant in the z-direction, reduces to

$$\mathbf{j} = -\frac{\hat{\mathbf{z}}}{\mu_0}\nabla^2 \psi \tag{4.11}$$

and inserting into the momentum equation gives

$$\frac{\partial \mathbf{v}}{\partial t} + (\mathbf{v} \cdot \nabla)\,\mathbf{v} = -\frac{1}{\mu_0 \rho}\nabla^2 \psi\,(\nabla \psi) \tag{4.12}$$

We linearise equations 4.9 and 4.12 by neglecting terms of second order in $\mathbf{v}$ and setting $\psi = \psi_E + \tilde{\psi}$, where

$$\psi_E = \frac{B_0}{2r_0}\left(y^2 - x^2\right). \tag{4.13}$$

In polar coordinates $x = r\cos\varphi$, $y = r\sin\varphi$, where φ denotes azimuthal angle, and the trigonometric relation $\sin^2\varphi - \cos^2\varphi = -\cos 2\varphi$ means that Eq. 4.13 simplifies to

$$\psi_E = -\frac{B_0 r^2}{2r_0}\cos 2\varphi. \tag{4.14}$$

In this equation B_0 is the unperturbed magnetic field in the (x, y) plane at radius $r = r_0$. If we assume that the perturbation $\tilde{\psi}$ is azimuthally symmetric and that $\left|\nabla\tilde{\psi}\right|$ is much smaller than $|\nabla\psi_E|$, i.e. the magnetic field perturbation is small compared to the local equilibrium field (an assumption we shall return to in Section 4.3.5), then Eqs. 4.9 and 4.12 become, respectively

$$\frac{\partial\tilde{\psi}}{\partial t} + (\mathbf{v}\cdot\nabla)\,\psi_E = 0 \tag{4.15}$$

and

$$\frac{\partial\mathbf{v}}{\partial t} = -\frac{1}{\mu_0\rho_0}\left(\nabla^2\tilde{\psi}\right)(\nabla\psi_E) \tag{4.16}$$

where ρ_0 is the unperturbed, equilibrium density, which is assumed to be uniform. These equations can be combined into a single equation for $\tilde{\psi}$: integrating 4.16 with respect to time, i.e.

$$\mathbf{v} = -\frac{1}{\mu_0\rho_0}\nabla\psi_E\int\nabla^2\tilde{\psi}dt = \frac{B_0 r}{\mu_0\rho_0 r_0}(\cos 2\varphi, -\sin 2\varphi, 0)\int\nabla^2\tilde{\psi}dt. \tag{4.17}$$

Defining a function $v(r, t)$ by writing

$$v = \frac{B_0 r}{\mu_0\rho_0 r_0}\int\nabla^2\tilde{\psi}dt \tag{4.18}$$

we obtain the scalar momentum equation

$$\frac{\partial v}{\partial t} = \frac{B_0 r}{\mu_0\rho_0 r_0}\nabla^2\tilde{\psi}. \tag{4.19}$$

In the cold plasma limit that we are assuming here, the MHD continuity and energy equations are not required. The continuity equation is purely passive in the sense that its solutions do not affect the variables that we are interested in, i.e. the flow velocity and the perturbation to the magnetic field. The linearised induction and momentum equations form a closed set of equations, in which the density appears

only as an unperturbed quantity, and thus to close the system we require only the linearised ideal MHD induction equation, which, from Eq. 4.15, becomes

$$\frac{\partial\tilde{\psi}}{\partial t} = \frac{vB_0 r}{r_0} \tag{4.20}$$

since

$$(\mathbf{v}\cdot\nabla)\,\psi_E = -\left[v(\cos 2\varphi, -\sin 2\varphi, 0)\cdot\left(\frac{\partial}{\partial r}, \frac{1}{r}\frac{\partial}{\partial\varphi}, \frac{\partial}{\partial Z}\right)\right]\frac{B_0 r^2}{2r_0}\cos 2\varphi = -\frac{vrB_0}{r_0}. \tag{4.21}$$

Normalizing r to r_0, t to the Alfvén time $\tau_A \equiv r_0(\mu_0\rho_0)^{1/2}/B_0$ and $\tilde{\psi}$ to $B_0 r_0$ (henceforth we omit the tilde from this quantity), we can obtain, from equations 4.19 and 4.20 respectively,

$$\frac{\partial\psi}{\partial t} = vr \tag{4.22}$$

$$\frac{\partial v}{\partial t} = \frac{\partial}{\partial r}\left(r\frac{\partial\psi}{\partial r}\right) \tag{4.23}$$

and combining these two equations gives the second-order equation

$$\frac{\partial^2\psi}{\partial t^2} = r\frac{\partial}{\partial r}\left(r\frac{\partial\psi}{\partial r}\right). \tag{4.24}$$

It is straightforward to verify that Eq. 4.24 has general solution

$$\psi = f(\ln r + t) + g(\ln r - t). \tag{4.25}$$

Here the (arbitrary) functions f and g represent, respectively, inward- and outward-propagating waves. In the next subsection we discuss particular choices of f and g such that $\partial\psi/\partial r = 0$ at $r = 0$: this boundary condition must be imposed to ensure that the solutions are both mathematically regular and consistent with the linear approximation [54,61].

We invoke two distinct types of fast wave perturbation to the MHD equations: a global perturbation, with inward- and outward-propagating components and an oscillatory longitudinal electric field; and a purely inward-propagating wave, initially

localised at the system boundary, the electric field having a preferred sign in the longitudinal direction.

4.2.2 Fast wave solutions: global perturbation

We consider first the case of a global perturbation, with ψ and v initially given by

$$\frac{\partial \psi}{\partial r} = \xi \sin(\pi r), \qquad v = 0, \tag{4.26}$$

where ξ is a constant. The boundary conditions are the same as those used by McClements and co-workers [61]. Setting $\partial\psi/\partial r = 0$ for all time at $r = 0$ ensures consistency with the linear approximation since the equilibrium field has a null at the X-point, whilst the same requirement at $r = 1$ thereby ensures that there is zero Poynting flux through this surface (note that Poynting flux is defined only for electromagnetic waves, and therefore is not strictly defined in the context of MHD plasmas, but is commonly used within MHD to represent the advection of magnetic energy perturbations). Since we do not require that $v = 0$ at $r = 1$, through the boundary there is a local mass flow. However the radial component of the velocity vector has a $\cos 2\theta$ dependence and thus the integrated mass flux through the boundary is zero - after $t = 0$ there is no net flux of energy in or out of the system. With these boundary conditions, the complete solution for ψ is [61]

$$\psi = -\frac{\xi}{2\pi}\left[\cos(\pi r e^{t}) + \cos(\pi r e^{-t})\right], \qquad t < -\ln r \tag{4.27}$$

$$\psi = -\frac{\xi}{2\pi}\left[\cos\left(\frac{\pi e^{-t}}{r}\right) + \cos(\pi r e^{-t})\right], \quad t > -\ln r. \tag{4.28}$$

To derive this, we integrate Eq. 4.26 with respect to r to give

$$\psi(r, t = 0) = -\frac{\xi}{\pi}\cos \pi r = -\frac{\xi}{2\pi}(\cos \pi r + \cos \pi r) \tag{4.29}$$

noting that the two terms in the brackets can be identified with snapshots at $t = 0$ of inward- and outward-propagating waves, and, rewriting Eq. 4.25 as

$$\psi = f\left(re^{t}\right) + g\left(re^{-t}\right) \tag{4.30}$$

we immediately see that Eq. 4.27 is a solution. However it is not the complete solution, because we must satisfy the zero Poynting flux boundary condition $\partial\psi/\partial r = 0$ ar $r = 1$ - differentiating Eq. 4.27 with respect to r, and inserting $r = 1$, gives

$$\frac{\partial\psi}{\partial r} = \frac{\xi}{2}\left[e^{t}\sin\left(\pi e^{t}\right) + e^{-t}\sin\left(\pi e^{-t}\right)\right], \tag{4.31}$$

which does not satisfy the required condition for $t \neq 0$. However the solution 4.28 *does* satisfy this condition. It is of the form given by Eq. 4.30, and if we insert $t = -\ln r$ into both solutions we see that they both reduce to $-\xi/2\pi\left[\cos(\pi) + \cos(\pi r^2)\right]$, i.e. they match for $r = e^{-t}$, so taking into account these points we can be confident that equations 4.27 and 4.28 are the complete solution.

In general, in full electromagnetism the electric field is given by

$$\mathbf{E} = -\nabla\Phi - \frac{\partial\mathbf{A}}{\partial t} \tag{4.32}$$

where Φ is the electrostatic potential, if there is one. In our model, the electric field must be consistent with that given by the ideal Ohm's law. Since, in the fluid solution, both $\mathbf{v}$ and $\mathbf{B}$ lie in the (x, y) plane, it follows from Ohm's law that $\mathbf{E}$ lies in the z-direction. Moreover, as invariance in the z-direction is assumed, $\partial\Phi/\partial z = 0$, the electric field cannot have an electrostatic component and so Eq. 4.32 reduces to

$$\mathbf{E} = -\frac{\partial\mathbf{A}}{\partial t} = -\frac{\partial\psi}{\partial t}\hat{\mathbf{z}} \tag{4.33}$$

Evaluating E_z for the flux perturbation given by equations 4.27 and 4.28 we obtain

$$E_z = \frac{r\xi}{2}\left[e^{-t}\sin(\pi r e^{-t}) - e^{t}\sin(\pi r e^{t})\right], \qquad t < -\ln r \tag{4.34}$$

$$E_z = \frac{r\xi e^{-t}}{2}\left[\frac{1}{r^2}\sin\left(\frac{\pi e^{-t}}{r}\right) + \sin(\pi r e^{-t})\right], \quad t > -\ln r \tag{4.35}$$

It is worth pointing out that the same result can be derived from considering Eq. 4.1 after linearisation, i.e. $\mathbf{E} = -\mathbf{v}\times\mathbf{B}_E$, and using $\mathbf{B}_E$ and $\mathbf{v}$ from equations 4.3 and 4.22 respectively. We can plot the field profiles of the perturbations $\partial\psi/\partial r$ and $-\partial\psi/\partial t$ for typical solar flare parameters of density and magnetic field, which we take to be $n = 10^{16}$ m^{-3} and $B = 0.03$T, in order to display how the magnetic and

electric field perturbations evolve in time across the radial extent of the X-point configuration. This is shown in Figures 4.1 and 4.2 respectively. Since both ψ and $\partial\psi/\partial r$ are continuous functions of r (in particular there is no discontinuity in either ψ or $\partial\psi)/\partial r$ at $t = -\ln r$) thus there are no sharp changes in the solution shape. Additionally, the solutions for v and $\partial v/\partial r$ are also continuous. Since the induction and momentum equations are first order, continuity of $\partial\psi/\partial r$ and $\partial v/\partial r$ ensures validity of the linearisation process.

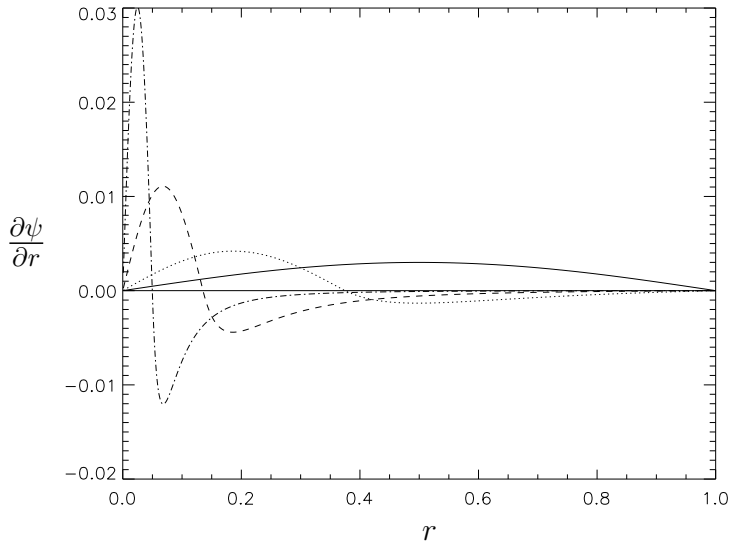

Figure 4.1: Time evolution of $\partial\psi/\partial r$ for a perturbation of the form given by Eqs. 4.27 and 4.28 with solar flare-like parameters: the curves correspond to $t = 0$ (solid line), $t = 1$ (dotted line), $t = 2$ (dashed line) and $t = 3$ (dashed-dotted line), where t is normalised to the Alfvén time τ_A. The r scale is normalised to the radial size of the system r_0. The quantity $\partial\psi/\partial r$ is plotted in dimensionless units.

The electric field is initially zero throughout the domain and, at any given r, oscillates between positive and negative values. Due to the presence of e^t in Eq. 4.31 the azimuthal magnetic field perturbation $B_\varphi \equiv -\partial\psi/\partial r$ is unbounded. Thus, for any specified initial perturbation amplitude, the linear approximation must eventually break down in some region of the domain. Both figures show how the field energy becomes increasingly concentrated at the null, highlighting the well-known ability of this configuration to focus and accrete electromagnetic energy at the X-point: the exact rate and level of build-up depends on the specific values of density, magnetic field strength, and perturbation amplitude that are chosen.

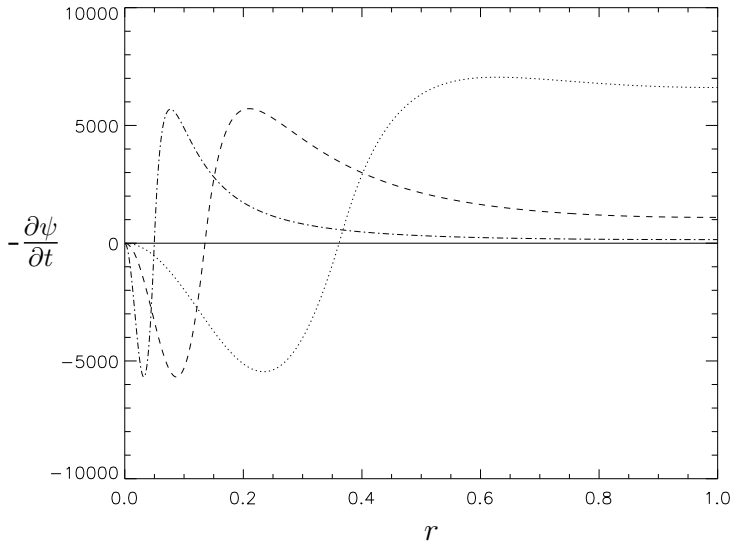

Figure 4.2: Time evolution of $E_z = -\partial\psi/\partial t$ for a perturbation of the form given by Eqs. 4.27 and 4.28 with solar flare-like parameters: the curves correspond to $t = 0$ (solid line), $t = 1$ (dotted line), $t = 2$ (dashed line) and $t = 3$ (dashed-dotted line), where t is normalised to the Alfvén time τ_A. The r scale is normalised to the radial size of the system r_0. The quantity $-\partial\psi/\partial t$ is plotted in dimensionless units.

4.2.3 Fast wave solutions: localised perturbation

It is also of interest to consider a wave pulse that is localised at any instant to a specific part of the domain and propagates in one radial direction only. Specifically, we set $g = 0$ and consider a solution for the electric field of the form

$$\frac{\partial\psi}{\partial t} = \xi \exp\left[-\frac{(\ln r + t)^2}{\delta u_1^2}\right], \quad t < -\ln r \tag{4.36}$$

$$\frac{\partial\psi}{\partial t} = \xi \exp\left[-\frac{(\ln r + t)^2}{\delta u_2^2}\right], \quad t > -\ln r \tag{4.37}$$

where δu_1 and δu_2 are constants. It is apparent that this represents an inward-propagating wave pulse, initially localised close to $r = 1$: if $\delta u_1 \neq \delta u_2$ the pulse is asymmetric. The gradient of the leading edge of the pulse is determined by δu_1, while that of the trailing edge is determined by δu_2. For an inward-propagating wave, $\partial\psi/\partial(\ln r)$ is equal to $\partial\psi/\partial t$, in which case the azimuthal magnetic field perturbation is given by

$$B_\varphi = -\frac{\partial\psi}{\partial r} = -\frac{\xi}{r}\exp\left[-\frac{(\ln r + t)^2}{\delta u_1^2}\right], \quad t < -\ln r \tag{4.38}$$

$$B_\varphi = -\frac{\partial\psi}{\partial r} = -\frac{\xi}{r}\exp\left[-\frac{(\ln r + t)^2}{\delta u_2^2}\right], \quad t > -\ln r \tag{4.39}$$

We can see that $B_\varphi \to 0$ as $r \to 0$, as required by the fact that there is a null at the X-point. At $r = 0$ we have $\ln r \to -\infty$, hence $(\ln r)^2$ tending to $+\infty$, and thus the exponential factor $\exp[-(\ln r)^2]$ tends to zero, which happens faster than the $1/r$ term tends to infinity. The boundary between the two forms of the solution propagates inwards as they are matched at earlier values of r as t increases. This is consistent with the inward-propagating nature of the wave.

The flux function itself is given (modulo an arbitrary constant) by the expressions

$$\psi = \frac{\sqrt{\pi}\delta u_1 \xi}{2}\left[1 - \mathrm{erf}\left(-\frac{\ln r + t}{\delta u_1}\right)\right], \quad t < -\ln r \tag{4.40}$$

$$\psi = \frac{\sqrt{\pi}\xi}{2}\left[\delta u_1 + \delta u_2 \mathrm{erf}\left(\frac{\ln r + t}{\delta u_2}\right)\right], \quad t > -\ln r \tag{4.41}$$

where erf is the error function

$$\mathrm{erf}(z) = \frac{2}{\sqrt{\pi}}\int_0^z e^{-t^2} dt \tag{4.42}$$

- this can be seen by differentiating Eqs. 4.40 and 4.41 and making use of the fact that

$$\frac{d}{dx}\left[\mathrm{erf(x)}\right] = \frac{2}{\sqrt{\pi}}\left(e^{-x^2}\right).$$

At any given instant ψ is a monotonic increasing function of r; the magnetic flux perturbation thus has a shock-like radial profile, although it is not a true shock solution since it was obtained from the linearised MHD equations. We can plot the quantities $\partial\psi/\partial r$ and $-\partial\psi/\partial t$, as we did in Section 4.2.2, to see how the magnetic and electric field perturbations vary with time across the radius of the system. Figures 4.3 and 4.4 show $\partial\psi/\partial r$ and $-\partial\psi/\partial t$ for an asymmetric wave pulse $\delta u_2 > \delta u_1$ with solar flare-like parameters of density and magnetic field as given previously. Figure 4.5 shows $\partial\psi/\partial r$ for a symmetric wave pulse $\delta u_1 = \delta u_2$. We see that, as

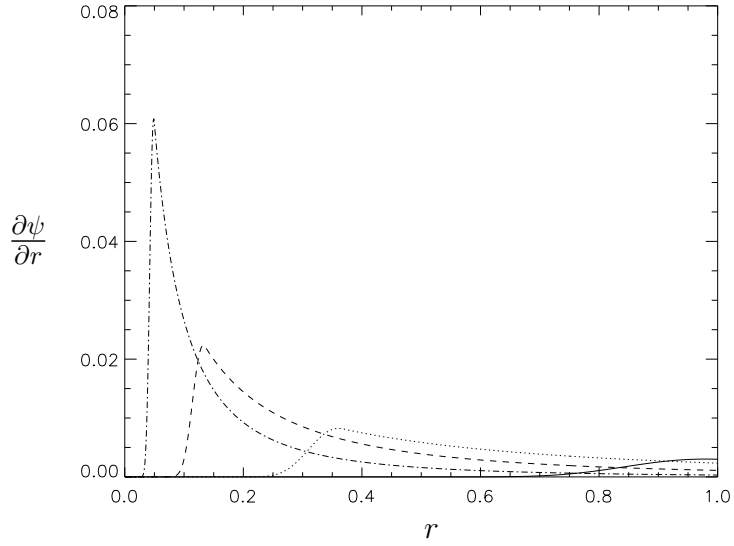

Figure 4.3: Time evolution of $\partial\psi/\partial r$ for a perturbation of the form given by Eqs. 4.38 and 4.39: the curves correspond to $t = 0$ (solid line), $t = 1$ (dotted line), $t = 2$ (dashed line) and $t = 3$ (dashed-dotted line), where t is normalised to the Alfvén time τ_A. The r scale is normalised to the radial size of the system r_0. The quantity $\partial\psi/\partial r$ is plotted in dimensionless units. In this pulse $\delta u_2 > \delta u_1$.

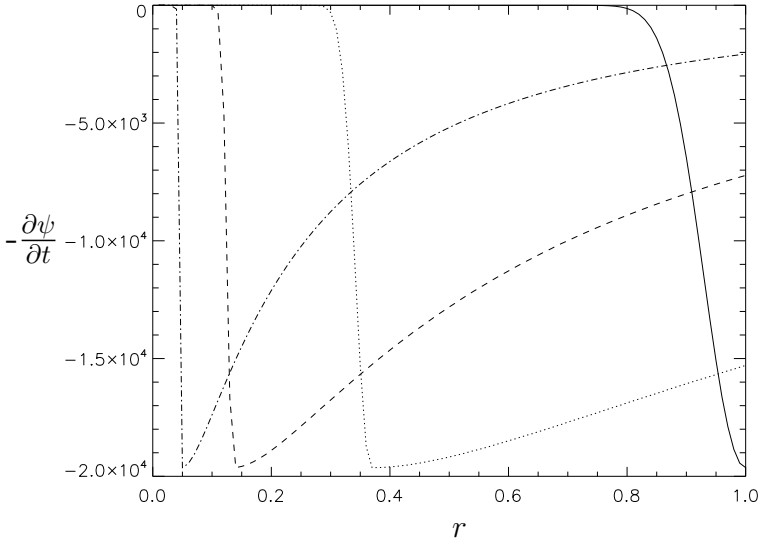

Figure 4.4: Time evolution of $E_z = -\partial\psi/\partial t$ for a perturbation of the form given by Eqs. 4.36 and 4.37, multiplied by -1: the curves correspond to $t = 0$ (solid line), $t = 1$ (dotted line), $t = 2$ (dashed line) and $t = 3$ (dashed-dotted line), where t is normalised to the Alfvén time τ_A. The r scale is normalised to the radial size of the system r_0. The quantity $-\partial\psi/\partial t$ is plotted in dimensionless units. In this pulse $\delta u_2 > \delta u_1$.

before, the wave profiles become increasingly concentrated as they approach the null. We can also see the effect of decreasing δu_2, in Figure 4.5, which decreases the time taken for the fields of the trailing edge of the pulse to fall to zero. Again, the exact values of the parameters chosen determine exactly how the perturbations evolve, but in all cases the general trends are similar.

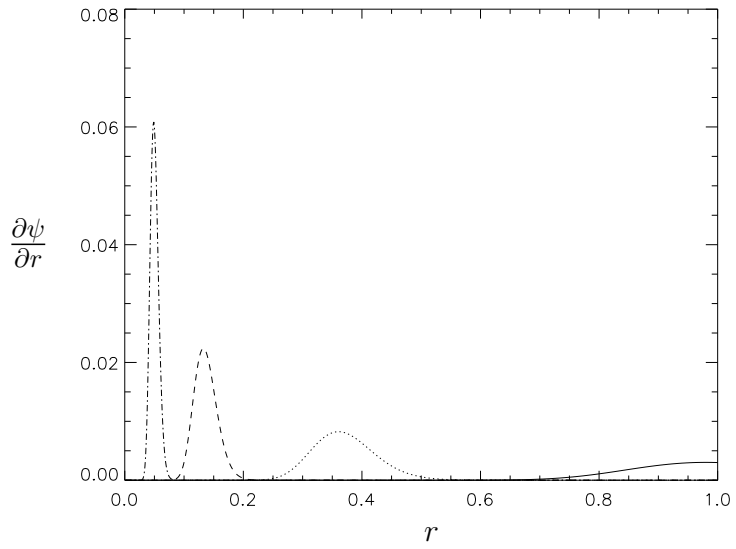

Figure 4.5: Time evolution of $\partial\psi/\partial r$ for a perturbation of the form given by Eqs. 4.40 and 4.41: the curves correspond to $t = 0$ (solid line), $t = 1$ (dotted line), $t = 2$ (dashed line) and $t = 3$ (dashed-dotted line), where t is normalised to the Alfvén time τ_A. The r scale is normalised to the radial size of the system r_0. The quantity $\partial\psi/\partial r$ is plotted in dimensionless units. In this pulse $\delta u_2 = \delta u_1$.

4.3 Test particle Simulations

4.3.1 Use of fast wave solution in CUEBIT

We use `CUEBIT` to study the acceleration of particles by the fast Alfvén wave pulses introduced above. Since field and fluid variations in the z-direction are neglected, the canonical momentum

$$p_z \equiv m_p v_z + e\psi, \tag{4.43}$$

where m_p and e are particle mass and charge, is an exact invariant of the Lorentz force equation, even in the presence of wave perturbations that violate particle energy conservation. To see this, consider the fast wave perturbation described previously: the z-component of the Lorentz force equation becomes

$$m\frac{dv_z}{dt} = -q\frac{\partial\psi}{\partial t} - qv_x\frac{\partial\psi}{\partial x} - qv_y\frac{\partial\psi}{\partial y} \tag{4.44}$$

where q is particle charge. We can rewrite Eq. 4.44 in the form

$$m\frac{dv_z}{dt} = -q\left\{\frac{\partial\psi}{\partial t} + \frac{dx}{dt}\frac{\partial\psi}{\partial x} + \frac{dy}{dt}\frac{\partial\psi}{\partial y}\right\}. \tag{4.45}$$

Now the rate of change of ψ along the trajectory of the particle is

$$\frac{d\psi}{dt} = \frac{\partial\psi}{\partial t} + (\mathbf{v}\cdot\nabla)\psi = \frac{\partial\psi}{\partial t} + \frac{dx}{dt}\frac{\partial\psi}{\partial x} + \frac{dy}{dt}\frac{\partial\psi}{\partial y} \tag{4.46}$$

hence Eq. 4.45 reduces to

$$\frac{d}{dt}\left(mv_z + q\psi\right) = 0 \tag{4.47}$$

and we deduce that $p_z = mv_z + q\psi$ is a constant of the motion, as stated previously.

We can use this fact as a numerical check: whereas `CUEBIT` is designed to ensure that kinetic energy is always conserved to machine accuracy in the absence of electric fields, canonical momentum conservation is not explicitly part of the algorithm, and thus plays an important role in benchmarking the code. We shall see that p_z is only well-conserved in the code if the time step Δt is sufficiently short. This is a key constraint on the numerical parameters used in our simulations.

4.3.2 Conditions for validity of fast wave solution

We have used ideal MHD to obtain the analytical fast wave solution, which means that we are neglecting the displacement current in Ampère's law. This is acceptable, since the solution varies on the Alfvén timescale, and we are adopting parameters such that the Alfvén speed is much smaller than the speed of light. We also require that the single fluid momentum equation and Ohm's law can be written in the form

$$\rho\frac{\partial \mathbf{v}}{\partial t} = \mathbf{j}\times\mathbf{B}, \tag{4.48}$$

$$\mathbf{E} + \mathbf{v}\times\mathbf{B} = 0. \tag{4.49}$$

Now, to justify the neglect of collisions in CUEBIT we should neglect collisions (and dissipation generally) in the fluid model as well. The dissipationless momentum equations for the ion and electron fluids can be written as

$$m_e n_e\left(\frac{\partial \mathbf{v}_e}{\partial t} + (\mathbf{v}_e\cdot\nabla)\,\mathbf{v}_e\right) = -\nabla p_e - n_e e(\mathbf{E}+\mathbf{v}_e\times\mathbf{B}), \tag{4.50}$$

$$m_i n_i\left(\frac{\partial \mathbf{v}_i}{\partial t} + (\mathbf{v}_i\cdot\nabla)\,\mathbf{v}_i\right) = -\nabla p_i + n_i e(\mathbf{E}+\mathbf{v}_i\times\mathbf{B}), \tag{4.51}$$

where subscripts e and i refer respectively to electrons and ions, and we have assumed that the ions are singly charged. We can set $n_e = n_i \equiv n$ provided that the wavelength of the perturbation we are dealing with is large compared to the Debye length. This condition is trivially satisfied: the initial wavelength is the system size ($\sim 10^6$m) whereas $\lambda_D \sim 10^{-3}$m in the solar corona. Since our fluid model is strictly linear, and we have no equilibrium flows, we can also drop the advective derivatives in the momentum equations, which thus reduce to

$$m_e n\frac{\partial \mathbf{v}_e}{\partial t} = -\nabla p_e - ne(\mathbf{E}+\mathbf{v}_e\times\mathbf{B}), \tag{4.52}$$

$$m_i n\frac{\partial \mathbf{v}_i}{\partial t} = -\nabla p_i + ne(\mathbf{E}+\mathbf{v}_i\times\mathbf{B}). \tag{4.53}$$

With the single fluid density $\rho = (m_i+m_e)n$ and velocity $\mathbf{v} = (m_i\mathbf{v}_i + m_e\mathbf{v}_e)/(m_i+m_e)$, then adding Eqs. 4.52 and 4.53, using $\mathbf{j} = ne(\mathbf{v}_i - \mathbf{v}_e)$ and $p = p_i + p_e$, we obtain

$$\rho\frac{\partial \mathbf{v}}{\partial t} = \mathbf{j}\times\mathbf{B} - \nabla p. \tag{4.54}$$

Using Ampère's law $\nabla\times\mathbf{B} = \mu_0\mathbf{j}$ and the vector identity

$$(\nabla\times\mathbf{B})\times\mathbf{B} = -\frac{1}{2}\nabla\mathbf{B^2} + (\mathbf{B}\cdot\nabla)\,\mathbf{B}, \tag{4.55}$$

we can re-write Eq. 4.54 in the form

$$\rho\frac{\partial \mathbf{v}}{\partial t} = -\nabla\left(\frac{B^2}{2\mu_0} + p\right) + \frac{1}{\mu_0}(\mathbf{B}\cdot\nabla)\,\mathbf{B}. \tag{4.56}$$

With the momentum equation written in this form, it is clear that we may neglect the pressure gradient term if the plasma beta $\beta = 2\mu_0 p/B^2 \ll 1$. This assumption generally holds in the solar corona, except close to the null of a two-dimensional magnetic X-point (or a 2.5D X-line with zero guide field). We thus recover the momentum equation used in the fast wave solution.

We still have to consider Ohm's law. The generalised form can be written as

$$\mathbf{E} + \mathbf{v} \times \mathbf{B} = \eta \mathbf{j} + \frac{m_e}{ne^2}\frac{\partial \mathbf{j}}{\partial t} + \frac{1}{ne}\left(\mathbf{j} \times \mathbf{B} - \nabla p_e\right). \tag{4.57}$$

We can neglect the resistivity term, since this arises from dissipation, and we can also neglect the electron inertia term ($\propto \partial\mathbf{j}/\partial t$) provided that the typical length scale is large compared to the electron skin depth, c/ω_{pe} (where ω_{pe} is the electron plasma frequency), and so Ohm's law reduces to

$$\mathbf{E} + \mathbf{v} \times \mathbf{B} = \frac{1}{ne}\left(\mathbf{j} \times \mathbf{B} - \nabla p_e\right). \tag{4.58}$$

The ∇p_e term in this equation can be omitted for the same reason as the ∇p term in the single fluid momentum equation. We are thus left with an Ohm's law which differs from the ideal MHD form only through the presence of the Hall term, $\mathbf{j}\times\mathbf{B}/ne$. Since $\mathbf{j} = ne(\mathbf{v}_i - \mathbf{v}_e)$, the Hall term can be neglected if

$$\frac{|\mathbf{v}_i - \mathbf{v}_e|}{\mathbf{v}} \ll 1. \tag{4.59}$$

In the fast wave solution both $\mathbf{v}$ and $\mathbf{j}$ are perturbations, so the perturbation amplitude is irrelevant as far as Eq. 4.59 is concerned. From the linearised single fluid momentum equation (Eq. 4.19),

$$\frac{\partial v}{\partial t} = \frac{B_0 r}{\mu_0 \rho_0 r_0}\nabla^2 \tilde{\psi} \tag{4.60}$$

and $j = -(1/\mu_0)\nabla^2\tilde{\psi}$ we have

$$\left|\frac{\partial \mathbf{v}}{\partial t}\right| = \frac{jB_0 r}{\rho_0 r_0}. \tag{4.61}$$

Since $\mathbf{v}$ is changing on a timescale of order $\tau_A = r_0/c_{A0} = r_0(\mu_0 m_i n)^{1/2}/B_0$, it follows from Eq. 4.61 that

$$\frac{|\mathbf{v}_i - \mathbf{v}_e|}{|\mathbf{v}|} \sim \frac{j/ne}{jr\mu_0^{1/2}/\rho_0^{1/2}} = \frac{(m_i n)^{1/2}}{ner\mu_0^{1/2}} = \frac{(m_i n c^2 \epsilon_0)^{1/2}}{ner} \tag{4.62}$$

since $c^2 = 1/\epsilon_0\mu_0$, and thus

$$\frac{|\mathbf{v}_i - \mathbf{v}_e|}{|\mathbf{v}|} \sim \frac{c}{r\omega_{pi}} \tag{4.63}$$

where $\omega_{pi} = (ne^2/m_i\epsilon_0)^{1/2}$ is the ion plasma frequency. The length scale c/ω_{pi} is referred to as the ion skin depth. Equations 4.59 and 4.63 indicate that the Hall term should be taken into account, i.e. ideal MHD ceases to be strictly valid, inside a circle of radius $r = c/\omega_{pi}$. We shall return to this in the next section in the context of the parameters used in our simulations, but it is sufficient to say at the moment that the use of ideal MHD is valid except in a region very close to the null, where the neglect of plasma pressure also ceases to be valid.

4.3.3 Treatment of collisions

As discussed in Chapter 3, collisions can be readily included in `CUEBIT`, but are neglected in this instance on the basis that our test particles interact with the fast Alfvén wave pulses for a time that is less than one collision time (see below). Specifically, a sufficient condition for the collisionless assumption to be valid is that the particle collision time is longer than the time taken for a fast Alfvén pulse to propagate across the system, since the particle can only undergo acceleration in the presence of the wave. To quantify this, we note that the collision time for protons with a Maxwellian distribution at temperature T is [45]

$$\tau_i = \frac{3^{1/2} 6\pi\epsilon_0^2 (k_B T)^{3/2} m_p^{1/2}}{ne^4 \ln\Lambda}, \tag{4.64}$$

where ϵ_0 is the permittivity of free space, k_B is Boltzmann's constant, m_p and e are now specifically the proton mass and charge, n is the proton number density and $\ln\Lambda$ is the Coulomb logarithm, given by [62]

$$\ln\Lambda = 23 - \ln\left[\frac{ZZ'(\mu+\mu')}{\mu T_{i'} + \mu' T_i}\left(\frac{n_i Z^2}{T_i} + \frac{n_{i'} Z'^2}{T_{i'}}\right)^{1/2}\right]$$

for ion-ion collisions, where n_i represents number density, T_i represents ion temperature in eV, masses are given in units of the proton mass $\mu = m_i/m_p$, Z is the ion charge state and field particle species are delineated by a prime. The fast Alfvén wave transit time is of the order of τ_A: requiring this to be shorter than τ_i leads to the condition

$$k_B T_i > \left[\frac{r_0 \mu_0^{1/2} e^4 \ln\Lambda}{3^{1/2} 6\pi\epsilon_0^2 B_0}\right]^{2/3} n. \tag{4.65}$$

In this chapter we examine the acceleration of test particle protons in two particular solar scenarios of interest, namely those of quiet coronal heating and late-phase flare heating. Typical parameter values for the quiet corona are $n = 10^{14}\mathrm{m}^{-3}$, $T = 10^6\mathrm{K} \equiv 1\mathrm{MK}$ and $B = 0.001\mathrm{T}$, while (as mentioned previously) typical late-phase flare values are $n = 10^{16}\mathrm{m}^{-3}$, $T = 10\mathrm{MK}$ and $B = 0.03\mathrm{T}$. A typical length scale for a coronal magnetic structure is $10^7\mathrm{m}$, but for the majority of our simulations we set $r_0 = 10^6\mathrm{m}$. A smaller system size means that we are not required to simulate our particles for such a long period of time (and we shall show that our results are essentially independent of the system size in any case). With these values, and taking $m_i = m_p$, the proton mass, we find that $c/\omega_{pi} \sim 2 \times 10^{-5} r_0$ for the quiet corona case and $c/\omega_{pi} \sim 2 \times 10^{-6} r_0$ for the flare case. Thus, we reiterate our conclusion that the use of ideal MHD is valid except in a region very close to the null.

In the simulations the protons initially have Maxwellian distributions with temperatures that are less than the observed values, namely $10^5\mathrm{K}$ for the quiet corona and $10^6\mathrm{K}$ for the flaring scenario, in order to determine the extent to which the observed conditions can be realized in the model. To evaluate the right hand side of Eq. 4.65 we identify B with B_0 and use values of the Coulomb logarithm that are appropriate for ion-ion collisions (for the quiet coronal heating case $\log\Lambda \simeq 17.6$ and for the late-phase flare heating case $\log\Lambda \simeq 18.8$), we find that, in both cases, our artificially low initial temperatures lie close to the values given by the right hand side of Eq. 4.65. In the quiet corona case, the value of the left hand side is 8.6 eV, compared to the right hand side, 18.4 eV, and in the flare heating case, the left-hand side $k_B T_i = 86.3$ eV compared to the right-hand side value of 199.3 eV. Although the left hand side terms are slightly lower than the right hand side terms, they are

of the same order, and so the regimes are only marginally collisional - thus is it legitimate to simplify the problem by neglecting collisions. Additionally, we will show that the fast Alfvén wave pulses invariably cause the effective proton temperature to rise, so that the protons become more collisionless as each simulation progresses.

4.3.4 Testing the code

Before we start simulating protons moving in the perturbed magnetic X-point it is important to check that the code is performing as we expect and require it to - that is, that the quantities p_z and (in the absence of the perturbation) energy are conserved to high accuracy. We check this first for a proton travelling in an unperturbed X-point field - the result of which is shown in Figure 4.6.

The proton is launched from coordinates $x/r_0 = 0.5, y/r_0 = 0$ with an energy of 0.86 keV. The magnetic field at the boundary $B_0 = 0.03$T and the scale size of the system $r_0 = 10^6$m. The particle is tracked for 10^7 timesteps where each timestep is one-tenth of a Larmor period at the system boundary: this equates to approximately 2.2 seconds in real time. We see that both p_z and E are conserved to high numerical accuracy, of order of approximately 1 part in 10^{12}, over a significant number of time steps of the code, which means that we can be confident that the code itself is numerically robust. When a fast wave perturbation is applied to the equilibrium field, there is a finite, non-potential electric field and so the total particle energy is no longer conserved. However, p_z is still well conserved in the presence of a perturbation, as we shall see in Section 4.4.

4.3.5 Simulation details

For each simulation the code was used to compute the trajectories and energies of 10,000 protons with initial positions in the (x, y) plane chosen randomly from a uniform spatial distribution. Only the trajectories of particles initially lying in an annulus $0.2 \leq r/r_0 \leq 0.8$ were computed: the region $r/r_0 < 0.2$ was excluded in order to minimize the likelihood of particles encountering wave fields that violated the linear approximation used in the fluid model; the region $r/r_0 > 0.8$ was excluded

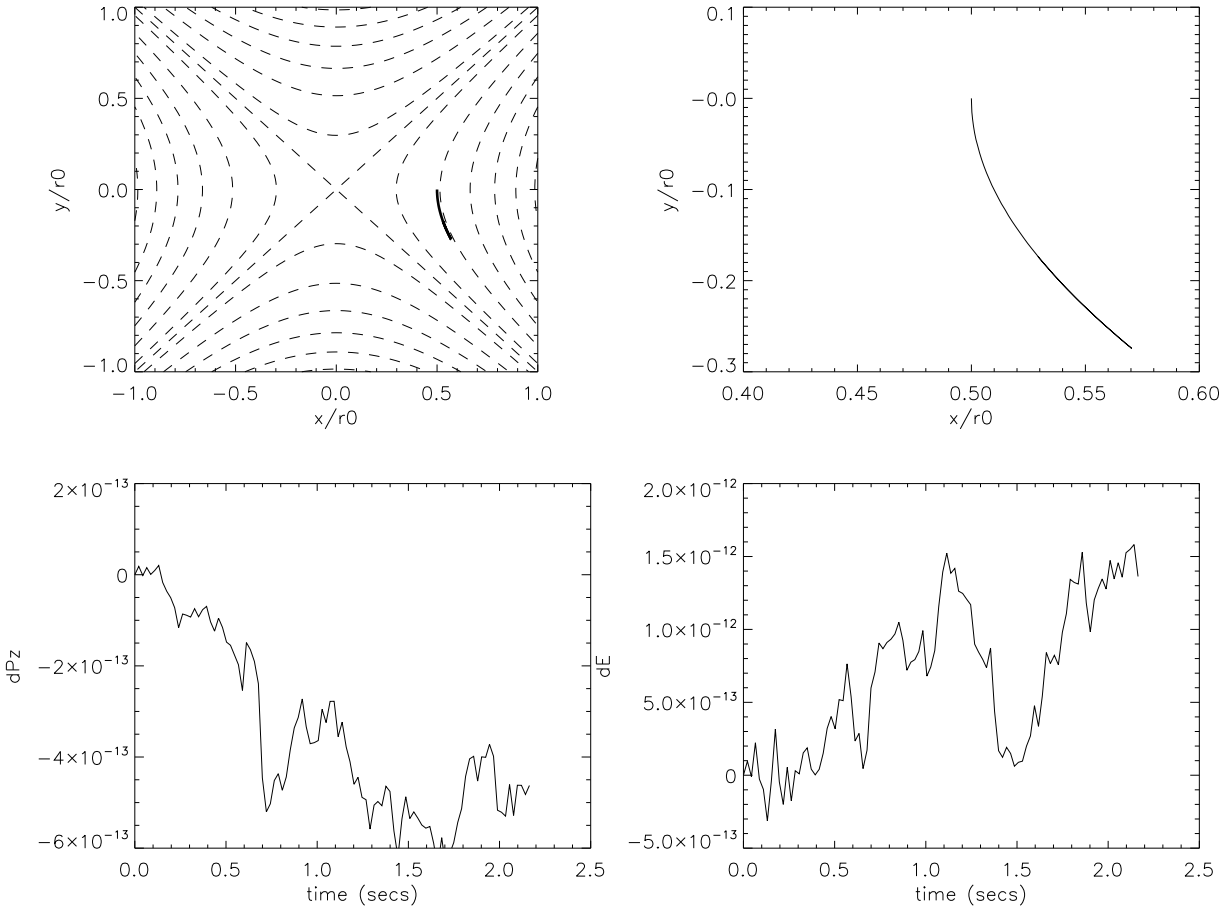

Figure 4.6: Tracking the orbit of a proton in an unperturbed magnetic X-point with parameters as described in the text: the top left plot is of the particle's overall position in the X-point with the magnetic field lines overlayed in dashed lines, the top right plot is a zoomed-in view of the orbit, the bottom left plot is the fractional deviation in canonical momentum p_z and the bottom right plot shows the fractional deviation in energy E for the duration of the simulation.

to ensure, in the case of the localised fast wave solution, that the particles initially lay in a region undisturbed by the wave. As indicated previously, the initial proton velocity distributions were Maxwellian, with zero net drift. This is consistent with the two wave solutions discussed in the previous subsection, insofar as both are characterized by the initial condition $v = 0$ in the domain in which the particles are initialized. The duration of each simulation was determined by the time required for the wave electric field to fall to a negligible value at the positions of the particles simulated. In all the simulations, the orbit computation was stopped for a given

particle if it crossed the surface $r = r_0$; such particles were included in the final energy distribution. If the linearisation condition was violated (i.e. if the wave magnetic field ceased to be small compared to the equilibrium field at the position of the particle: an expression for this will be derived in the next subsection), or if p_z ceased to be conserved to one part in 100, the particle orbit calculation was immediately stopped and the particle was not included in the final distribution.

4.3.6 The linear approximation

The condition for neglecting nonlinear terms in the MHD equations for a finite amplitude fast wave perturbation of a two-dimensional X-point equilibrium can be derived as follows: the magnetic field can be written as $\mathbf{B} = \nabla\psi \times \hat{\mathbf{z}}$, where ψ is a flux function and $\hat{\mathbf{z}}$ is the unit vector in the z-direction, as discussed in Section 4.2. As we are considering only variations in the (x,y) plane, then $\nabla\psi$ is orthogonal to $\hat{\mathbf{z}}$ and thus

$$B = |\nabla\psi| = |\nabla\psi_E + \nabla\tilde{\psi}| \tag{4.66}$$

and therefore

$$B^2 = (\nabla\psi_E)^2 + 2\nabla\psi_E \cdot \nabla\tilde{\psi} + (\nabla\tilde{\psi})^2. \tag{4.67}$$

We can ignore the $(\nabla\tilde{\psi})^2$ term as being negligible, since it is 2nd order in the perturbation amplitude. The condition for the linear approximation to be valid thus becomes

$$\frac{|2\nabla\psi_E \cdot \nabla\tilde{\psi}|}{(\nabla\psi_E)^2} \ll 1 \tag{4.68}$$

Remembering that

$$\psi_E = -\frac{B_0 r^2}{2r_0}\cos 2\varphi$$

from Eq. 4.14 previously, then

$$\nabla\psi_E = \frac{B_0 r}{r_0}(-\cos 2\varphi, \sin 2\varphi, 0)$$

and

$$(\nabla\psi_E)^2 = \frac{B_0^2 r^2}{r_0^2}.$$

Since $\tilde{\psi}$ depends only on r and t it follows that $\nabla\tilde{\psi} = (\partial\tilde{\psi}/\partial r)\hat{\mathbf{r}}$, and thus Eq. 4.68 reduces to

$$\frac{2r_0}{B_0 r}\cos 2\varphi\frac{\partial\tilde{\psi}}{\partial r} \ll 1 \tag{4.69}$$

so, provided that this inequality is true, the wave magnetic field is smaller than the equilibrium field and the linearisation carried out in Section 4.2.1 can be justified.

4.4 Results: Global Perturbation

4.4.1 Individual particle orbits

With n, T, B_0 and r_0 specified previously for the two scenarios of interest, the only remaining parameter left to be determined for the global perturbation case is the initial perturbation amplitude, ξ. We set $\xi = 0.1$, so that the peak initial magnetic field perturbation is 10% of the equilibrium magnetic field at $r = r_0$ (although it could reasonably be argued that a perturbation any bigger than this would no longer be truly linear). To demonstrate how the protons respond to the fast wave perturbation, we plot the trajectory of a single specific particle, launched from the same coordinates $x/r_0 = 0.5, y/r_0 = 0$, for the quiet corona scenario (whose parameters are outlined previously). Additionally we plot the time evolution of the electric field E_z and fractional deviation of p_z from its initial value, shown in Figure 4.7, and the time evolution of the total energy of the particle, in Figure 4.8.

It is worth first pointing out that this particle meets all the criteria for inclusion in our final results - the critical condition of Eq. 4.69 is met, and p_z is still conserved to good approximation in the presence of a perturbation (although it is not as well-conserved as in the unperturbed case). The apparent anti-correlation between E_z and p_z is of no physical significance - it is purely numerical, since it was shown that p_z is conserved by the equations (see Eq. 4.47), and in any case the fractional deviation

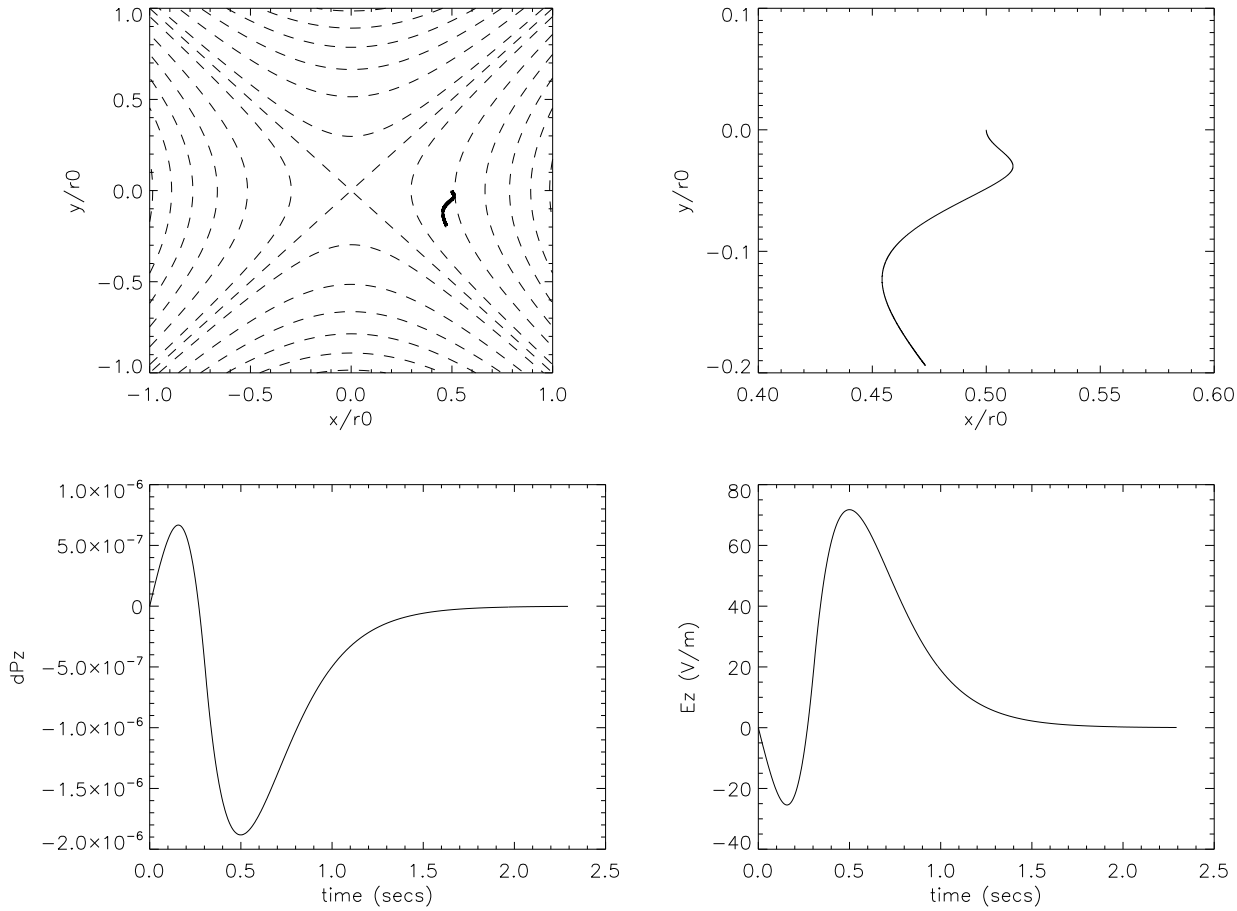

Figure 4.7: A proton in a magnetic X-point for the global perturbation case, using the quiet corona parameters: the top left plot is of the particle's overall position in the X-point, the top right plot is a zoomed-in view of the orbit, and the bottom left and right plots show the fractional deviation in canonical momentum p_z and the value of the electric field E_z for the duration of the simulation.

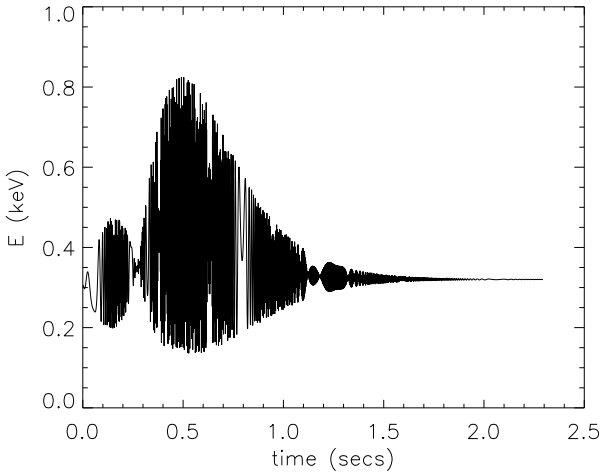

Figure 4.8: Time evolution of the energy of the particle whose trajectory is plotted in Figure 4.7.

of p_z from its initial value is very small. Examining the plot of energy, we see that, although the particle gains large amounts of energy as the wave perturbation passes through the X-point, most of that energy is lost in the second half-wave cycle. However, the particle still ends the simulation with more energy than it started with: to be precise, the passage of the wave increases the energy of the particle by 4.5%. Some particles gain *and* keep large amounts of energy - Figure 4.9 displays the important quantities for one such particle, which ends the simulation with an increase in E of a factor of more than 200 - but we will see in Sections 4.4.2 and 4.5.2 that typically very few particles are accelerated by such significant amounts. Most protons gain relatively small amounts of energy, and some lose energy.

4.4.2 Distribution of particles

Considering now a distribution of 10^4 particles in our simulations, Figure 4.10 shows the proton energy distributions for both the quiet corona (left hand plot) and flaring corona (right hand plot) scenarios outlined above, and Figure 4.11 shows the corresponding distributions of proton energy increments ΔE. In units of τ_A the total simulation times are comparable: in both cases the electric field encountered by the particles had decayed sufficiently by the end of the simulation that the energy distribution had essentially relaxed to a steady state. The appearance of high energy tails in these plots indicates that the final energy distributions are not strictly Maxwellian (indeed, the final velocity distributions in the simulations are generally anisotropic: we will discuss this point in Sect. 4.8). However, computing an equivalent temperature $T_f \equiv 2\mathcal{E}/(3k_B)$, where $\mathcal{E}$ is the mean energy of the particles at the end of the simulation, we obtain $T_f = 0.151$MK for the quiet corona case and $T_f = 1.550$MK for the flaring case, i.e. in both cases the effective temperature has increased by about 50%. Repeating the simulations for two different sets of 10^4 particles for both cases yields final temperatures of $T_f = 0.149, 0.154$MK for the quiet corona scenario and $T_f = 1.534, 1.568$MK for the flaring case, giving standard deviations of 1.36% and 0.90% respectively. Thus these figures are broadly consistent with the predicted noise level expected in a simulation with 10^4 particles (less the number removed due to breaking the linearisation condition or conservation of momentum, which is of

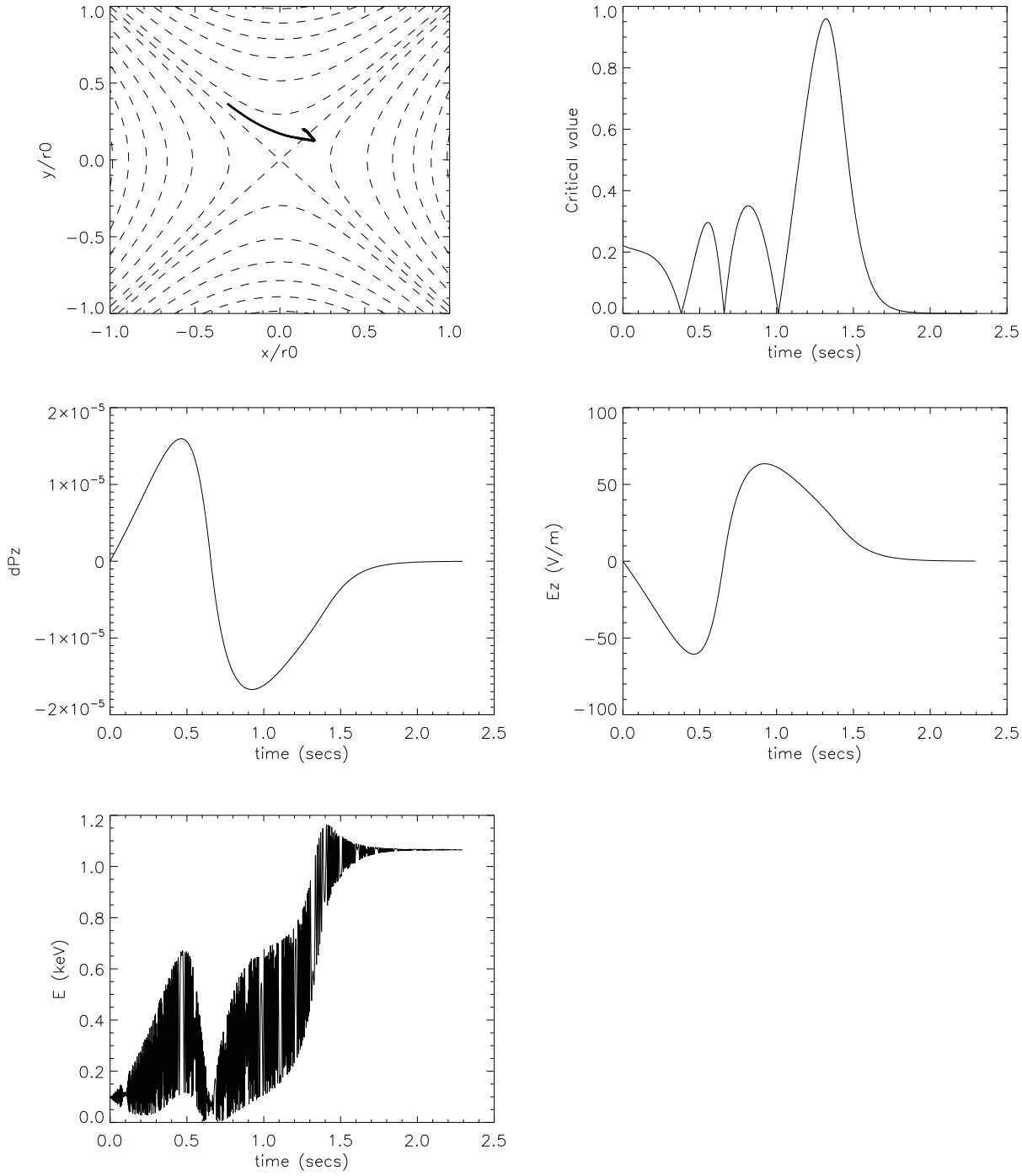

Figure 4.9: A less "typical" proton for the global wave perturbation, quiet corona parameter case, launched from $x = 0.13r_0, y = 0.2r_0$: the top left plot displays the trajectory of the particle, the top right figure shows evolution of the critical value (the quantity on the left hand side of Eq. 4.69), the middle left and right plots show the fractional change in p_z and E_z respectively, and the bottom left plot illustrates the variation in energy with time.

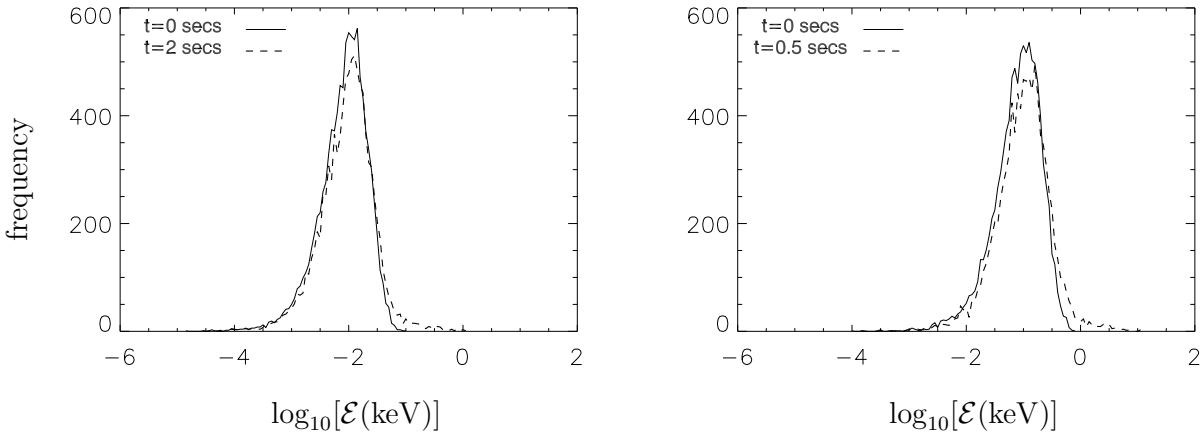

Figure 4.10: Initial (solid curves) and final (dashed curves) proton energy distributions for the case of a global field perturbation: the left hand plot corresponds to the quiet corona scenario, with $T = 0.1$MK and total simulation time $t = 2$s ($\simeq 4.4\tau_A$); the right hand plot corresponds to the flaring scenario with $T = 1$MK and $t = 0.5$s ($\simeq 3.3\tau_A$). In both cases $\xi = 0.1$.

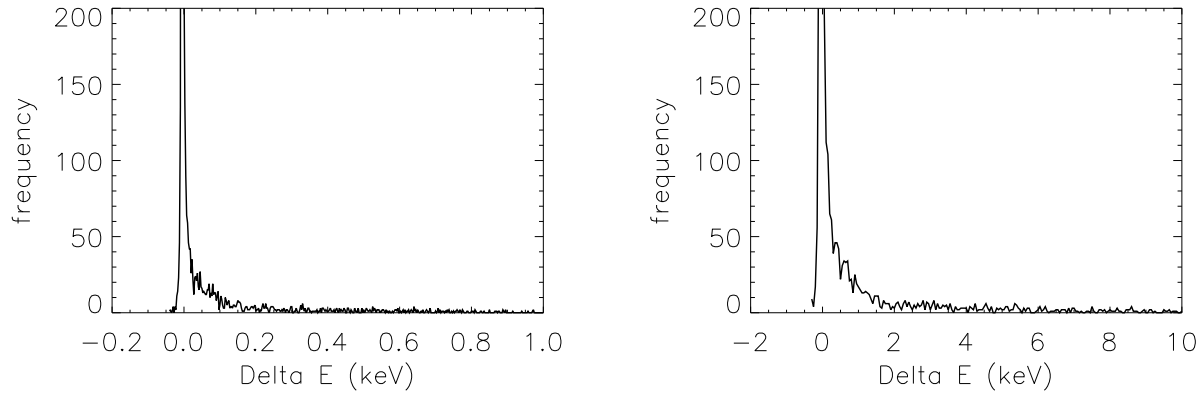

Figure 4.11: Distribution of changes in proton energy ΔE at $t = 2$s for the quiet corona simulation (left) and $t = 0.5$s for the late-phase flare simulation (right).

the order of 400-500 particles in these simulations).

4.5 Results: Localised Perturbation

4.5.1 Individual Particle Orbits

For the localised perturbation we must specify the parameters δu_1 and δu_2, which determine the gradients of the leading and trailing edges of the pulse respectively,

in addition to the perturbation amplitude ξ. We consider two different cases, one in which δu_1, δu_2=0.2 and one where δu_1=0.2, δu_2=2; in both cases we again set ξ=0.1. Figure 4.12 shows the orbit of a particle for the former case, using the late-phase flare scenario parameters of density and magnetic field and launched from coordinates $x = -0.25r_0, y = 0.42r_0$, and Figure 4.13 shows the energy of this particle. This perturbation passes through the system very quickly, and thus the period of time when the particle is highly energised and moving rapidly is relatively short, so the particle travels a much shorter distance within the X-point in comparison with the global perturbation case. Figure 4.14 compares the wave propagation time for the two different cases of δu_2 as seen by this proton - increasing this value decreases the gradient of the trailing edge of the pulse and it thus takes longer to propagate through the system. Again, this proton exhibits very similar characteristics to the protons in the previous section, in that it only gains a relatively small amount of energy (about 11.2% in this particular case) though as we will see in the next section, the localised perturbation is more efficient at accelerating particles.

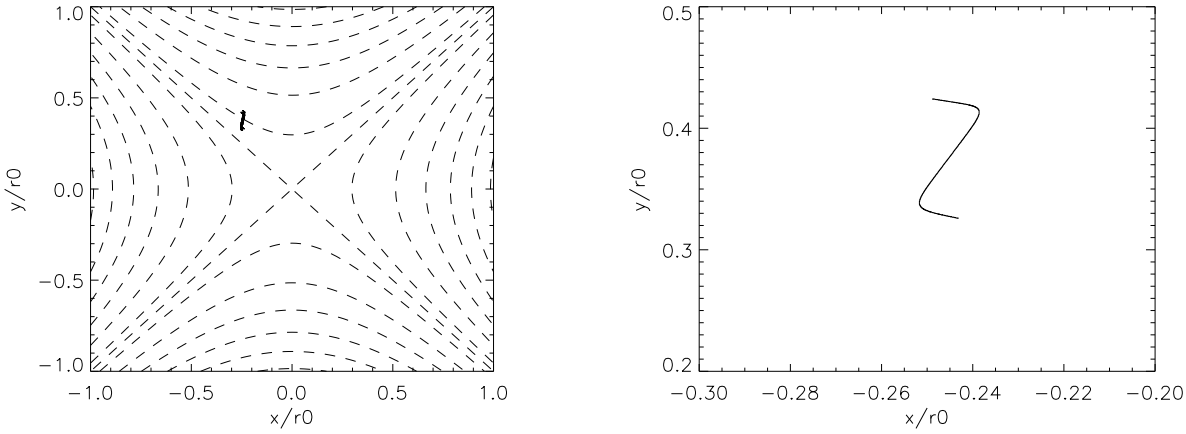

Figure 4.12: Trajectory of a proton in a magnetic X-point for the localised perturbation case, using the late-phase flare parameters with δu_2=0.2 and launched from $x = -0.25r_0, y = 0.42r_0$.

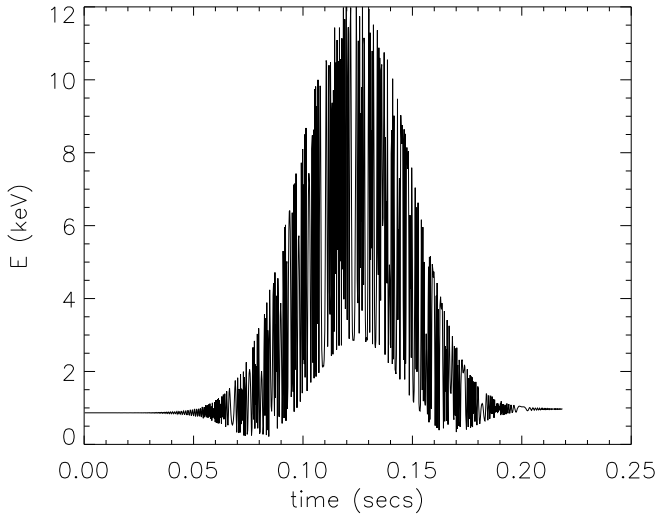

Figure 4.13: The energy variation for the proton whose orbit is displayed in Fig. 4.12.

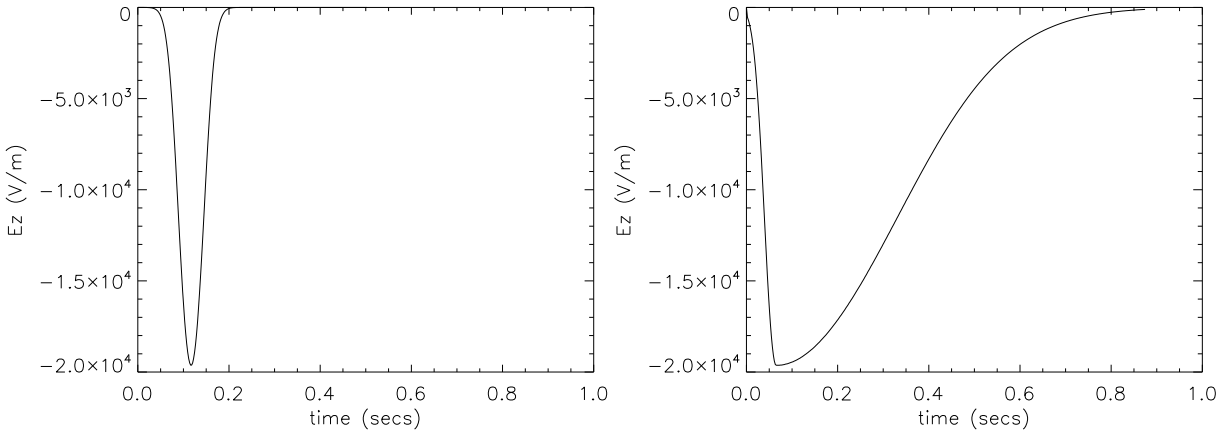

Figure 4.14: Comparison of electric field variation with time for the proton in Figure 4.12 for the two cases δu_2=0.2 (*left*) and δu_2=2 (*right*). The value of δu_1 is 0.2 for both cases.

4.5.2 Particle Distributions

Again we consider the resultant energy distribution of 10^4 protons: examining the quiet corona scenario first the results for the two cases of $\delta u_2 = 0.2, 2$ are shown in Figure 4.15. Computing an equivalent final proton temperature on the same basis as before, we obtain 0.2MK for the left-hand plot and 2.5MK for the right-hand plot. Thus, in both cases the local perturbation has a greater heating effect than the global perturbation, dramatically so when the pulse is asymmetric, with an extended trailing edge. However, it is evident that the final distributions are

again nonthermal, with a high energy tail extending up to several keV in the case of the asymmetric pulse. It is also instructive to compute the distributions of $v_{\|}$ and velocity component perpendicular to the local magnetic field $v_{\perp}$ for the particles at the beginning and end of the simulation; these are plotted in Figs. 4.16-4.19. The significance of these results will be discussed in Section 4.8, but for the moment we note that the $v_{\|}$ distributions are broadened to a significantly greater extent than the $v_{\perp}$ distributions.

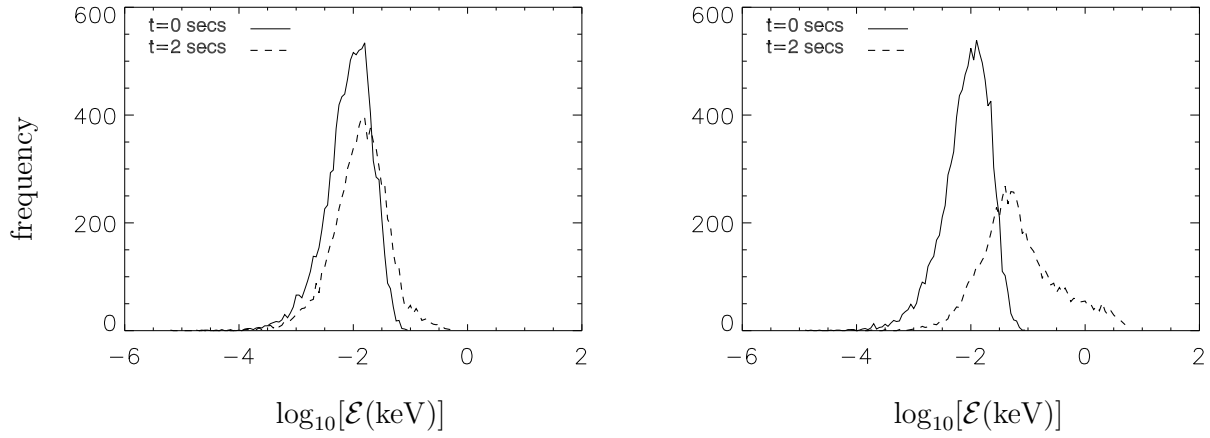

Figure 4.15: Initial (solid curves) and final (dashed curves) proton energy distributions for the case of a localised field perturbation with initial amplitude $\xi = 0.1$: the parameters are those of the quiet corona scenario. The total simulation time is equal to 4.4 Alfvén times. The left-hand plot corresponds to $\delta u_1 = 0.2$, $\delta u_2 = 0.2$; the right-hand plot corresponds to $\delta u_1 = 0.2$, $\delta u_2 = 2$.

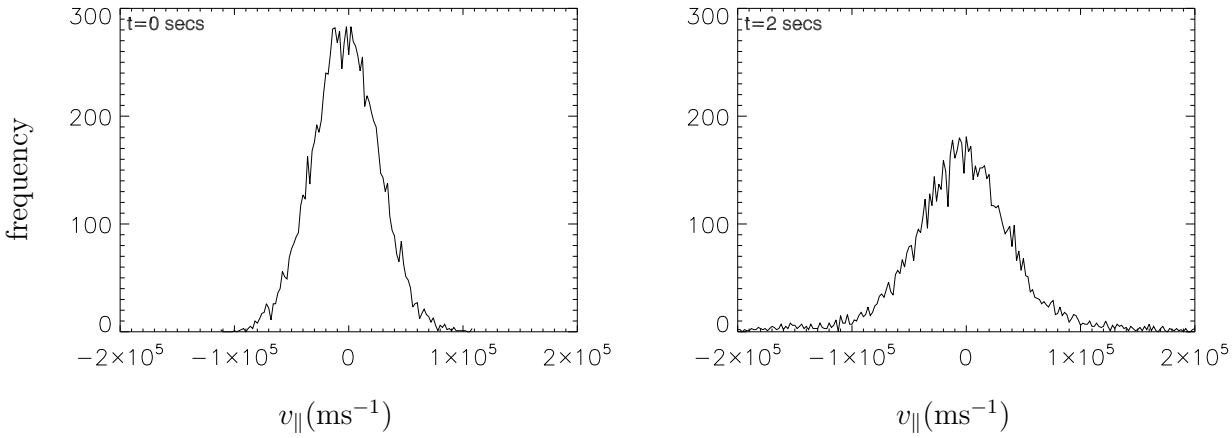

Figure 4.16: Parallel proton velocity distributions at $t = 0$ (left) and $t = 2$s (right) corresponding to the energy distributions shown in the left-hand plot of Fig. 4.15.

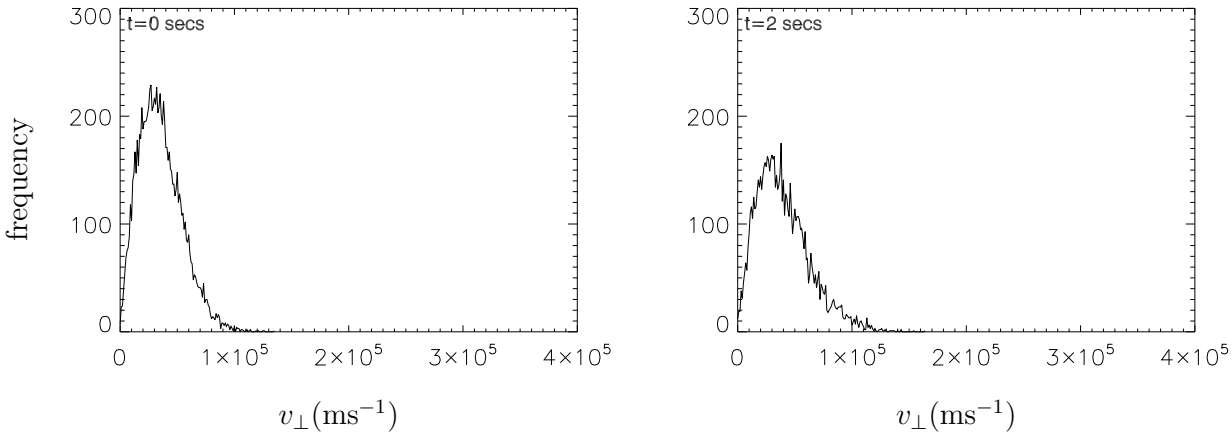

Figure 4.17: Perpendicular proton velocity distributions at $t = 0$ (left) and $t = 2$s (right) corresponding to the energy distributions shown in the left-hand plot of Fig. 4.15.

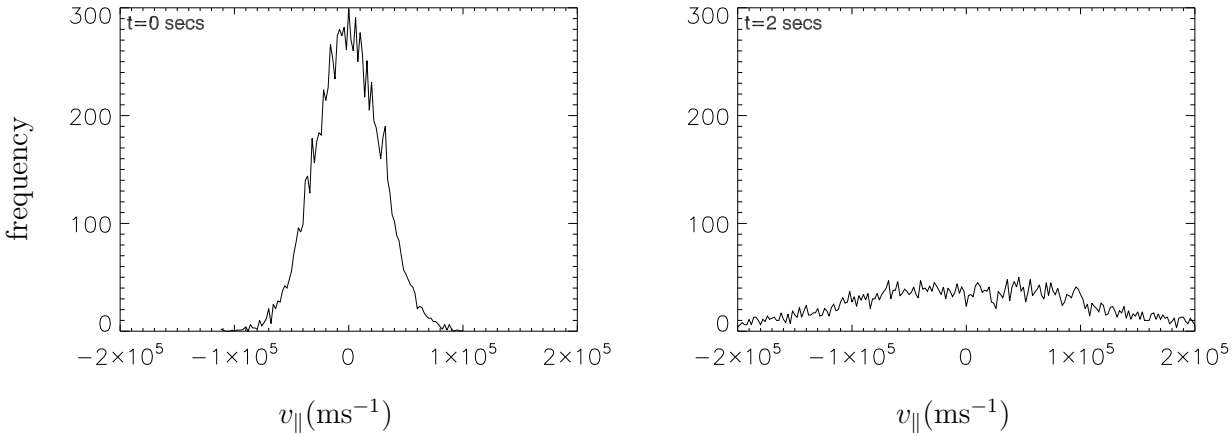

Figure 4.18: Parallel proton velocity distributions at $t = 0$ (left) and $t = 2$s (right) corresponding to the energy distributions shown in the right-hand plot of Fig. 4.15.

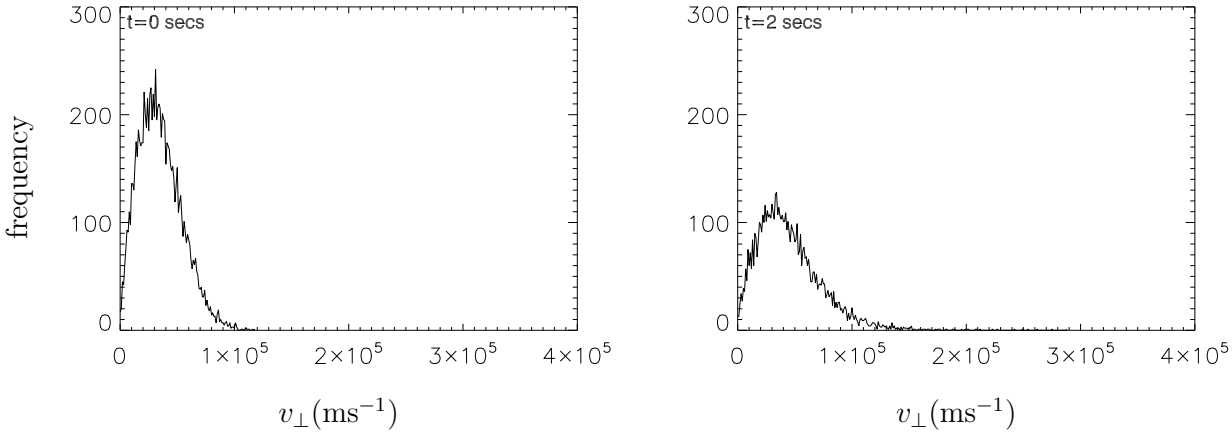

Figure 4.19: Perpendicular proton velocity distributions at $t = 0$ (left) and $t = 2$s (right) corresponding to the energy distributions shown in the right-hand plot of Fig. 4.15.

Figure 4.20 illustrates the proton energy distributions for the flare scenario, again for the two cases of $\delta u_2 = 0.2$ (*left*) and 2 (*right*), and Figure 4.21 shows the corresponding distributions of proton energy increments ΔE (for reference, in the $\delta u_2 = 0.2$ simulation no particles went out of bounds, 1730 broke the linearisation condition and 4 broke the momentum conservation condition while in the $\delta u_2 = 2$ simulation 732 particles went out of bounds, 2922 broke the linearisation condition and 2 broke the momentum conservation condition). Interpreting the av-

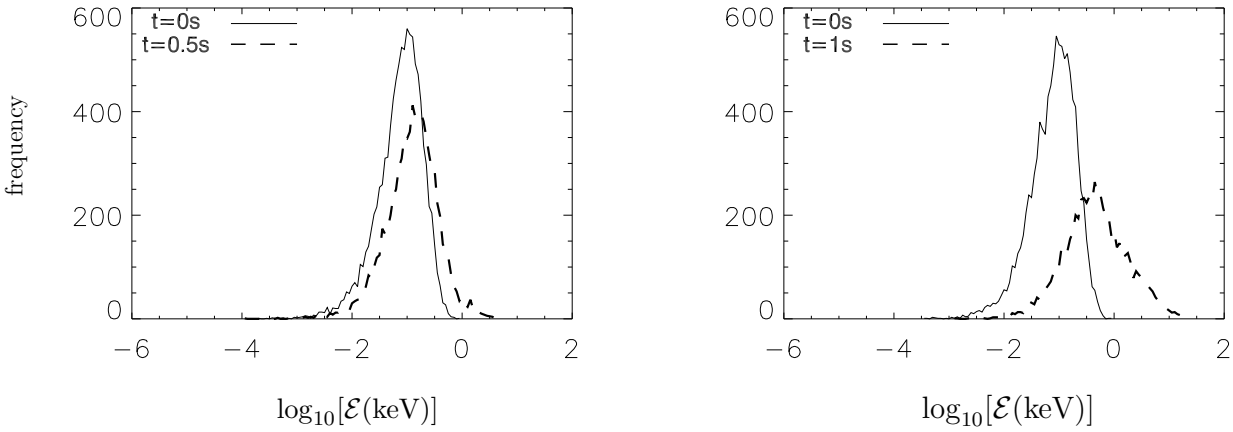

Figure 4.20: Initial (solid curves) and final (dashed curves) proton energy distributions for the case of a localised field perturbation with initial amplitude ξ =0.1: the parameters are those of the late-phase flare scenario. The left panel corresponds to δu_1=0.2, δu_2=0.2, and has a total simulation time equal to 3.3 τ_A. The right panel corresponds to δu_1=0.2, δu_2=2, and has a total simulation time equal to 6.6 τ_A.

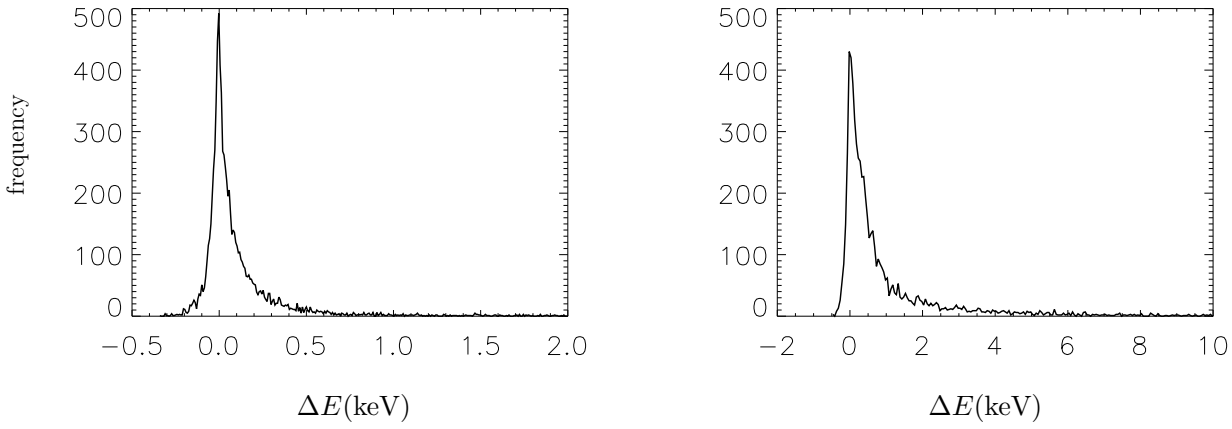

Figure 4.21: Distribution of changes in proton energy ΔE at t=0.5s (left) and t=1s (right) for the late-phase flare simulations.

erage energy of each distribution $\mathcal{E}$ in the same way as before, we infer equivalent temperatures of 1.95MK for the left-hand plot and 9.42MK for the right-hand plot. Thus, in both the flare and quiet corona scenarios the final effective temperature rises rapidly with δu_2, increasing by factors of about 2 for $\delta u_2 = 0.2$ and between approximately 10-20 for $\delta u_2 = 2$. The plots of ΔE indicate that most of the protons are accelerated (or decelerated in some cases) by relatively small amounts, up to about 0.5keV and 3 keV for the two flare cases, although a few particles are invariably accelerated to highly supra-thermal energies. This last point can be illustrated by the following: for a Maxwellian distribution at 9.42MK, approximately 0.002% of the particles would have energies greater than 10keV. However, we find that there are 69 such particles out of a total of 10000 in this particular simulation, i.e. approximately 0.69%. For a Maxwellian distribution at 9.42 MK, the probability of seeing particles with energies greater than 20keV is so small as to be virtually negligible, so the fact that approximately 0.05% of the particles have energies in this range, although a small number, is still significant. The total number of particles used in the simulation is sufficiently large that the excess number of particles in the tail (compared to that expected on the basis of a Maxwellian distribution) is statistically significant, and so the high energy tail in the left hand frame of Fig. 4.21 appears to be real.

Figures 4.22-4.25 show the parallel and perpendicular velocity distributions of all the protons within the simulation boundaries before and after the simulation for the 2 cases respectively (for the case with δu_2 =2, the distributions are plotted at $t = 0.5$ seconds: technically the simulation is not complete but the velocity distributions do not change dramatically over the remaining period of time, $\simeq$ 0.3s, for which the wave electric field is not negligible). Figure 4.26 displays the final parallel and perpendicular velocity distributions for particles lying within a particular range of values of r and φ. Comparing Figs. 4.24 and 4.26, we note that the $v_{\|}$ distribution is somewhat narrower at a given spatial location than it is for the entire domain: we will return to this result in the next section.

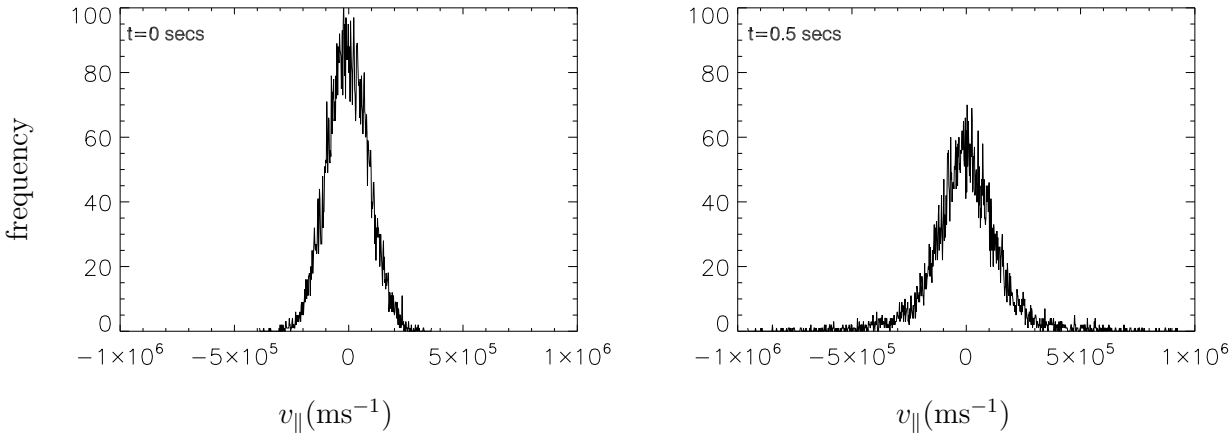

Figure 4.22: Parallel proton velocity distributions at $t = 0$ (left-hand panel) and $t = 0.5$s (right-hand panel) corresponding to the energy distributions shown in the left hand panel of Fig. 4.20.

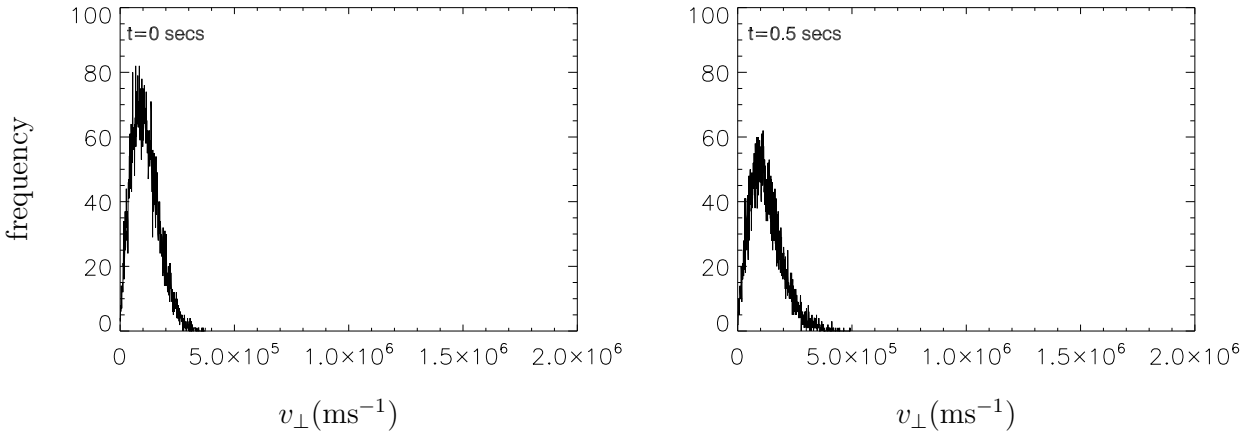

Figure 4.23: Perpendicular proton velocity distributions at $t = 0$ (left) and $t = 0.5$s (right) corresponding to the energy distributions shown in the left panel of Fig. 4.20.

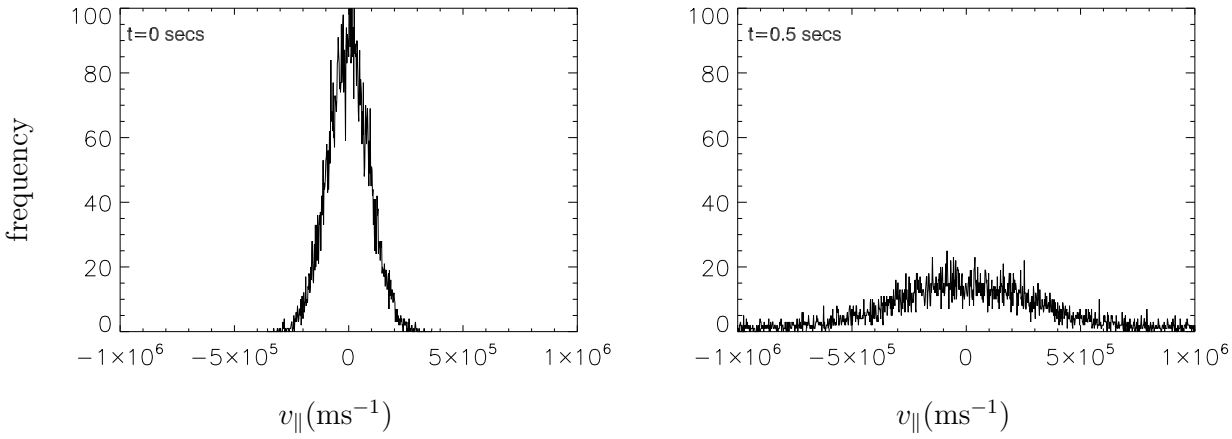

Figure 4.24: Parallel proton velocity distributions at $t = 0$ (left) and $t = 0.5$s (right) corresponding to the energy distributions shown in the right-hand panel of Fig. 4.20.

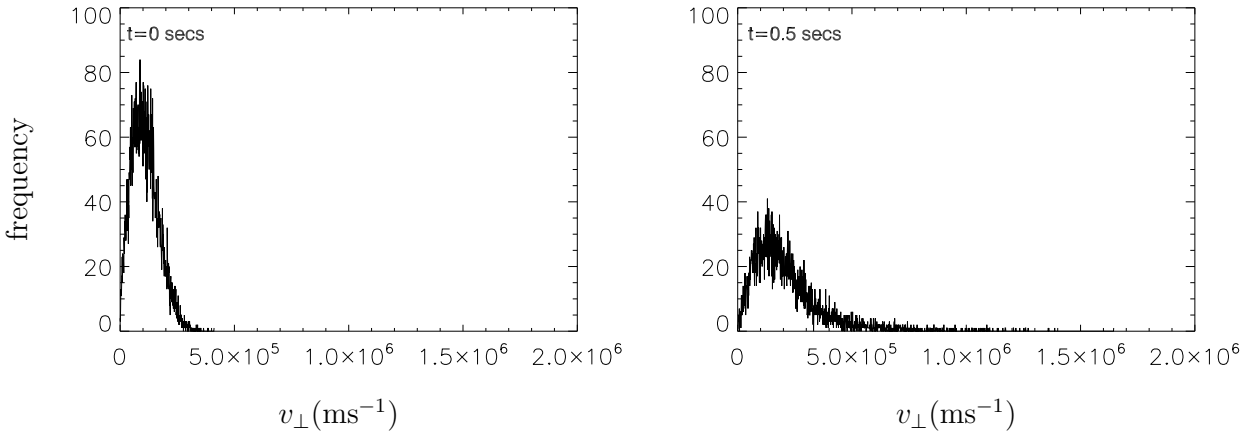

Figure 4.25: Perpendicular proton velocity distributions at $t = 0$ (left) and $t = 0.5$s (right) corresponding to the energy distributions shown in the right-hand panel of Fig. 4.20.

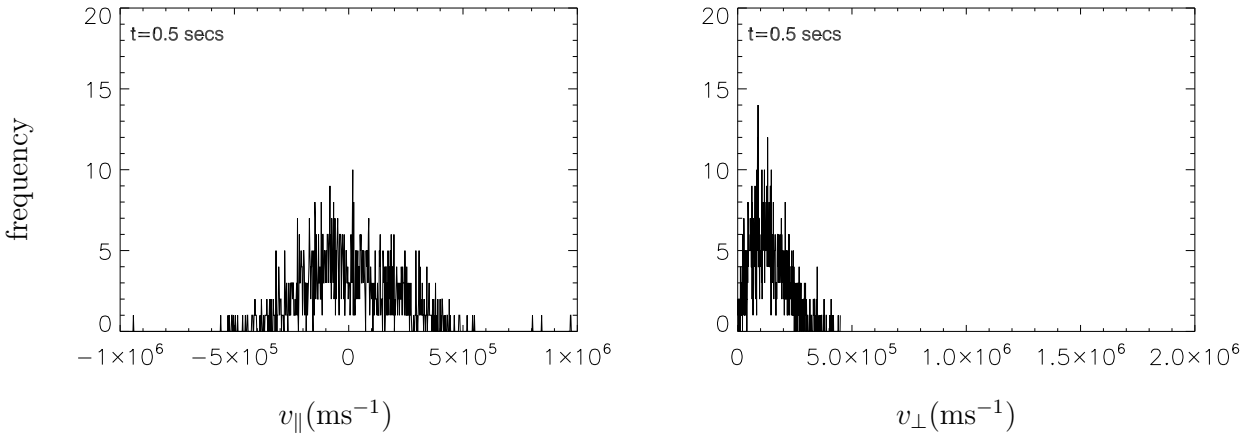

Figure 4.26: Parallel (left) and perpendicular (right) velocity distributions of protons, at t=0.5s, lying in the region defined by $0.8 \leq r/r_0 \leq 1$, $0 \leq \varphi \leq \pi$ for the flare simulation with $\delta u_1 = 0.2$, $\delta u_2 = 2$.

We have also found that the results are similar, though not identical, if the particles are started from rest rather than a finite temperature, as illustrated in Figure 4.27: the final effective temperature of the proton distribution launched from rest is 8.78MK, compared to the 9.42MK of the distribution launched with a temperature of 1MK.

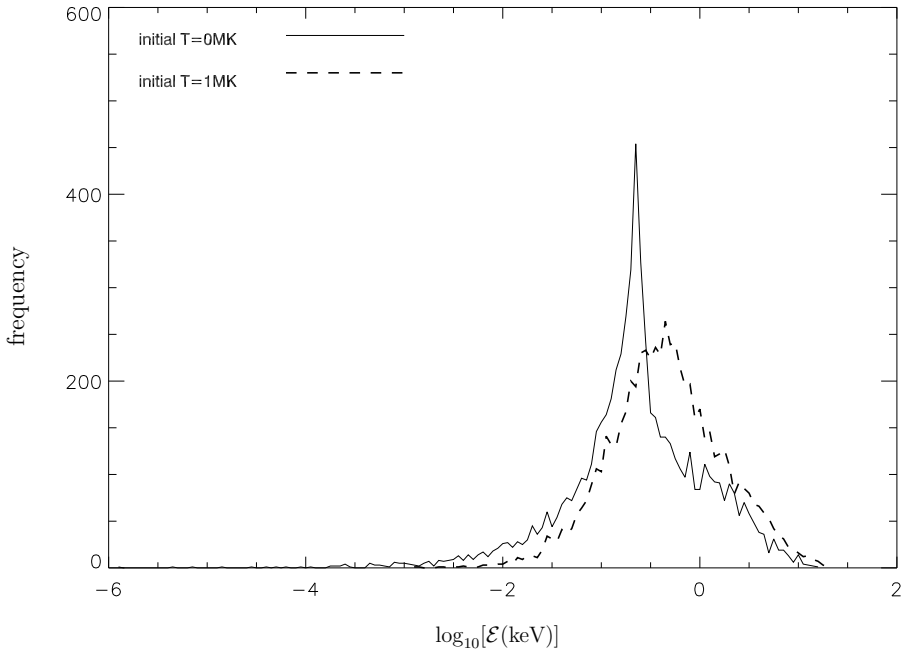

Figure 4.27: Final distributions of proton energy $\mathcal{E}$ at t = 1s for the late-phase flare simulation with δu_2=2, starting the protons from rest (solid) and with T=1MK (dashed).

In summary, comparing the responses of the proton population to the various wave perturbations discussed above, we see that the localised perturbation with $\delta u_1 = \delta u_2 = 0.2$ produces an effective temperature increase which is about twice that resulting from a global perturbation with the same initial amplitude, while the localised perturbation with $\delta u_1 = 0.2$, $\delta u_2 = 2$ causes the effective temperature to increase by about a factor of 10-20. We will discuss the heating and acceleration mechanism, and the reasons for its sensitivity to the wave parameters, in Section 4.8.

4.6 Results: Two Wave Pulses

It is also instructive to investigate the response of the test particles to two successive localised wave pulses. Specifically we consider two identical localised pulses with initial amplitude $\xi = 0.06$, profile parameters $\delta u_1 = 0.2$, $\delta u_2 = 2$, and peaks separated in time by 1 s. As in previous sections we consider an individual particle first, in this case launched from coordinates $x = 0.4r_0, y = 0.2r_0$: Figure 4.28 shows the usual important quantities for this proton over the duration of the simulation, namely the

trajectory within the X-point (plus a zoomed-in orbit plot), the fractional variation in the canonical momentum p_z, and the energy E in keV.

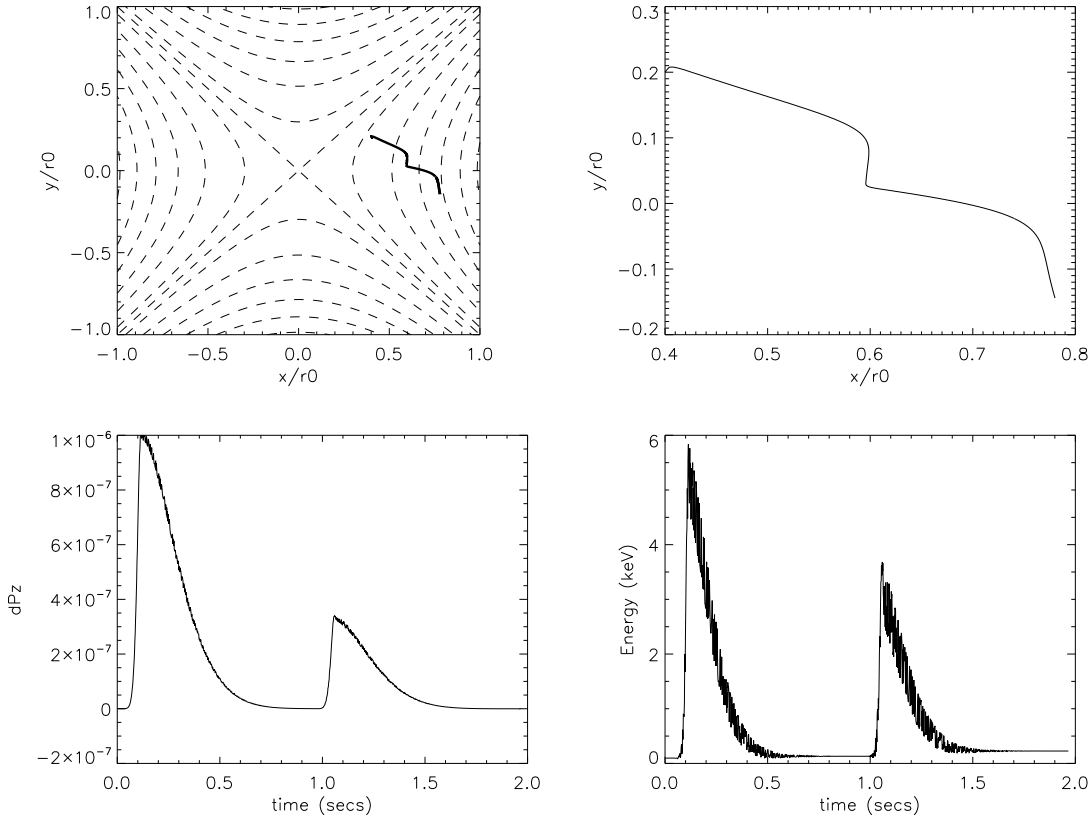

Figure 4.28: Simulation of proton launched from coordinates $x = 0.4r_0$, $y = 0.2r_0$ within X-point configuration in which two localised wave pulses are launched, with initial perturbation amplitude $\xi = 0.06$, δu_1=0.2, δu_2=2 and the initial temperature is $T = 1$MK, $n = 10^{16}\mathrm{m}^{-3}$ and $B_0 = 0.03$T. From top left to bottom right the figures are the trajectory of the proton within the X-point, a zoomed-in display of this trajectory, the variation in fractional deviation of canonical momentum p_z with time and the variation of total particle energy with time.

Figure 4.29 also illustrates the change in energy ΔE by showing the energy at 4 equally-spaced times throughout the simulation as each wave pulse propagates through the X-point (this shows the long-term trend more clearly than plotting the energy at every timestep), as well as illustrating the electric field E_z the particle is subjected to. The resulting energy distributions of the 10^4 protons are then plotted in Fig. 4.30. Using the average energies of these distributions to compute effective temperatures as before, we find that after the first wave pulse the effective

temperature is $T = 3$MK and after the second pulse $T = 8.7$MK. The average gain in energy ΔE of the protons due to their interaction with the first wave pulse is 0.4keV; the corresponding figure for the second pulse is 0.58keV.

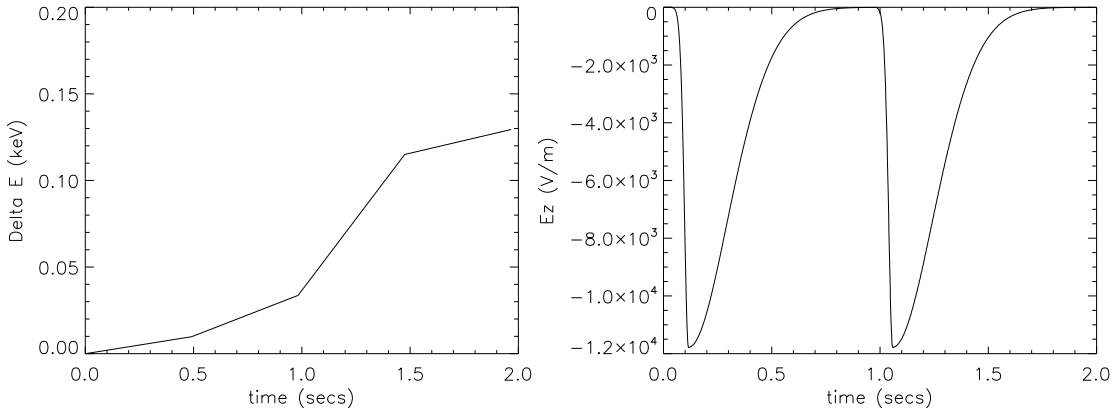

Figure 4.29: The change in energy ΔE with time, evaluated at four equally-spaced intervals in time during the proton simulation in Figure 4.28, and the variation in electric field E_z as seen by that particle.

We conclude that wave pulses of this type heat the protons to an even greater effective temperature when the protons have already been energized by a previous pulse; the pulses thus have a synergistic effect on the proton population. We can see this in the change in energy of the single particle plotted previously: the first wave pulse increases the particle's energy by approximately 0.03 keV, whereas the second increases the energy by about 0.13 keV. These values are considerably less than those quoted above as the "average" gain in energy of a proton. We saw previously in the plots of ΔE in Sections 4.5.2 and 4.6.2 that most particles *overall* gained only a relatively small amount of energy from the passing of the wave pulse. This was particularly true in the case of the global perturbation, where many particles gained significant amounts of energy *during* the peak of the wave pulse, though most of this energy was lost in the second-half of the wave cycle as E_z reversed in direction, and only a relatively small number of protons that did not either break the linearisation condition, exited the boundary of the system, or violated the requirement of p_z conservation, actually ended the simulation with a significant increase in energy. Here, however, Figure 4.30 clearly shows a shift of the entire distribution, so, in this

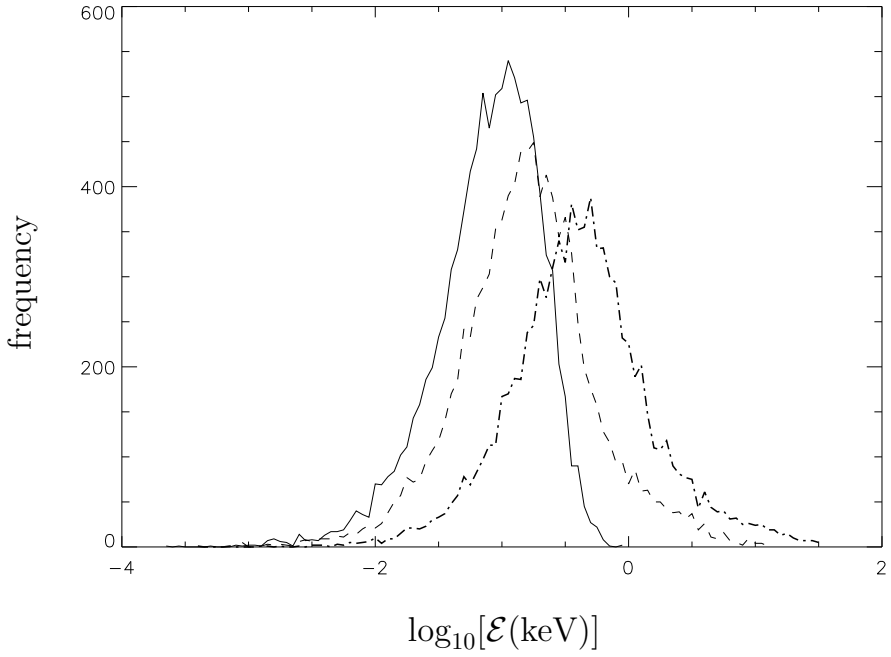

Figure 4.30: Proton energy distributions at $t = 0$ (solid curve), $t \simeq 3.3\tau_A$ (dashed curve) and $t \simeq 6.6\tau_A$ (dashed-dotted curve), following the passage of two successive localised fast wave pulses with initial perturbation amplitude $\xi = 0.06$, δu_1=0.2, δu_2=2. The initial temperature is $T = 1$MK, the plasma density is $n = 10^{16}\mathrm{m}^{-3}$ and the magnetic field at the system boundary is $B_0 = 0.03$T.

case, we are *not* dealing with a situation in which a small number of superthermal particles out in the tail are skewing the results - instead the bulk of the protons are being accelerated by significant amounts, particularly by the second wave pulse.

4.7 Interpretation

To understand the results presented above one must examine the behaviour of individual particles in the assumed wave fields. We consider first of all the response of a proton in a uniform, time-independent magnetic field $\mathbf{B} = B\hat{\mathbf{z}}$ to a uniform electric field $\mathbf{E} = E(t)\hat{\mathbf{x}}$ that rises ($t < 0$) and then decays ($t > 0$) exponentially: this is a simplified representation of the fields encountered by a test particle in the case of the asymmetric localised wave pulse.

Taking initially the case of a purely decaying electric field, the x and y components of the Lorentz force equation become

$$\dot{v}_x = \Omega \left(v_y + v_E e^{-\gamma t} \right) \tag{4.70}$$

$$\dot{v}_y = -\Omega v_x \tag{4.71}$$

where $v_E = E/B$ is the $\mathbf{E} \times \mathbf{B}$ drift speed at $t = 0$, $\Omega = qB/m$ is the cyclotron velocity and γ is a constant that determines the rate of decay of the electric field. Differentiating Eq. 4.71 with respect to time and eliminating $\dot{v}_x$ using Eq. 4.70, we obtain

$$\ddot{v}_y + \Omega^2 v_y = -\Omega^2 v_E e^{-\gamma t}, \tag{4.72}$$

which is the equation of a simple harmonic oscillator with an exponentially-decaying drive. This equation can be solved exactly for arbitrary initial conditions by using the standard technique of finding a particular integral and adding it to the complementary function. The complete solution is

$$v_y = \alpha \cos \Omega t + \beta \sin \Omega t - \frac{\Omega^2 v_E e^{-\gamma t}}{\gamma^2 + \Omega^2} \tag{4.73}$$

where α and β are constants, determined by the initial conditions. With $v_x = -\dot{v}_y/\Omega$ from Eq. 4.71, we then have

$$v_x = \alpha \sin \Omega t - \beta \cos \Omega t - \frac{\Omega \gamma v_E e^{-\gamma t}}{\gamma^2 + \Omega^2}. \tag{4.74}$$

Imposing the initial conditions $v_x = v_y = 0$ at $t = 0$ gives

$$\alpha = \frac{\Omega^2 v_E}{\gamma^2 + \Omega^2} = v_E \tag{4.75}$$

$$\beta = -\frac{\gamma \Omega v_E}{\gamma^2 + \Omega^2} = -\frac{\gamma v_E}{\Omega} \tag{4.76}$$

if $\gamma^2 \ll \Omega^2$. We can now crudely approximate the electric fields given by Eqs. 4.40 and 4.41 by an exponential rise ($t < 0$) followed by an exponential decay ($t > 0$),

with different time constants $1/\gamma_1$ and $1/\gamma_2$ respectively. We do this by putting $\gamma = -\gamma_1$ in Eqs. 4.73 and 4.74, and requiring that $v_x, v_y \to 0$ as $t \to -\infty$, which gives $\alpha = \beta = 0$ and hence the solution for $t < 0$ as

$$v_x = \frac{\gamma_1 \Omega v_E e^{\gamma_1 t}}{\gamma_1^2 + \Omega^2} \tag{4.77}$$

$$v_y = -\frac{\Omega^2 v_E e^{\gamma_1 t}}{\gamma_1^2 + \Omega^2}. \tag{4.78}$$

The particle energy increases monotonically in this phase, irrespective of the values of γ_1 and Ω. Evaluating v_x and v_y for $t = 0$ from Eqs. 4.77 and 4.78 results in $v_x = \gamma_1 \Omega v_E/(\gamma_1^2 + \Omega^2)$ and $v_y = -\Omega^2 v_E/(\gamma_1^2 + \Omega^2)$, and using these expressions to define new initial conditions by inserting them into 4.73 and 4.74, we get

$$\alpha = \Omega^2 v_E \left(\frac{1}{\gamma_2^2 + \Omega^2} - \frac{1}{\gamma_1^2 + \Omega^2} \right), \tag{4.79}$$

$$\beta = -\Omega v_E \left(\frac{\gamma_1}{\gamma_1^2 + \Omega^2} + \frac{\gamma_2}{\gamma_2^2 + \Omega^2} \right). \tag{4.80}$$

for $t \geq 0$. Thus, in general there is a Larmor gyration in the particle motion at $t > 0$. However, if both γ_1^2 and γ_2^2 are much smaller than Ω^2, as in the case of MHD waves of the type invoked in our test particle simulations, we find that

$$\alpha \simeq \frac{\gamma_1^2 - \gamma_2^2}{\Omega^2} v_E, \tag{4.81}$$

$$\beta \simeq -\frac{\gamma_1 + \gamma_2}{\Omega} v_E. \tag{4.82}$$

We thus have $|\alpha| \ll v_E$, $|\beta| \ll v_E$, indicating that the amplitude of the Larmor gyration is small compared to the peak $\mathbf{E} \times \mathbf{B}$ drift. Since the electric field decays monotonically to zero, the net energy gained by the particle is very small.

We now consider in more detail the behaviour of a single proton in the actual $\mathbf{E}$ and $\mathbf{B}$ fields used in the simulations. We have used `CUEBIT` to compute the orbit of an initially stationary proton accelerated by a localised field perturbation with $\xi = 0.1$, $\delta u_1 = 0.2$ and $\delta u_2 = 2$. The equilibrium plasma parameters were taken to be $B_0 = 0.01\mathrm{T}$, $r_0 = 10^7\mathrm{m}$, $n = 10^{14}\mathrm{m}^{-3}$. The temporal evolution of the particle

energy is shown in Figure 4.31 and its trajectory is plotted in Figure 4.32: it can be seen that the wave pulse causes the particle to acquire a net energy, of about 64keV, which is comparable in magnitude to the peak energy (about 125keV).

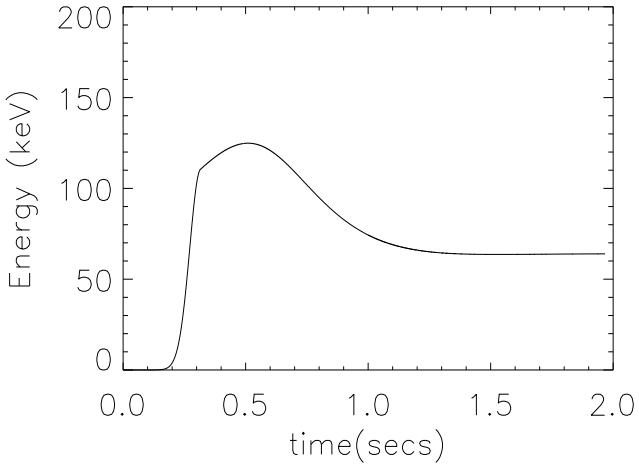

Figure 4.31: Energy versus time of a proton initially at rest at $r = 5 \times 10^6$m, $\varphi = 40°$. The perturbation is of the form given by Eqs. 4.40 and 4.41, with $\delta u_1 = 0.2$, $\delta u_2 = 2$. The perturbation amplitude at $t = 0$ is 0.1. The equilibrium field parameters are $B_0 = 0.01$T, $r_0 = 10^7$m, $n = 10^{14}\text{m}^{-3}$.

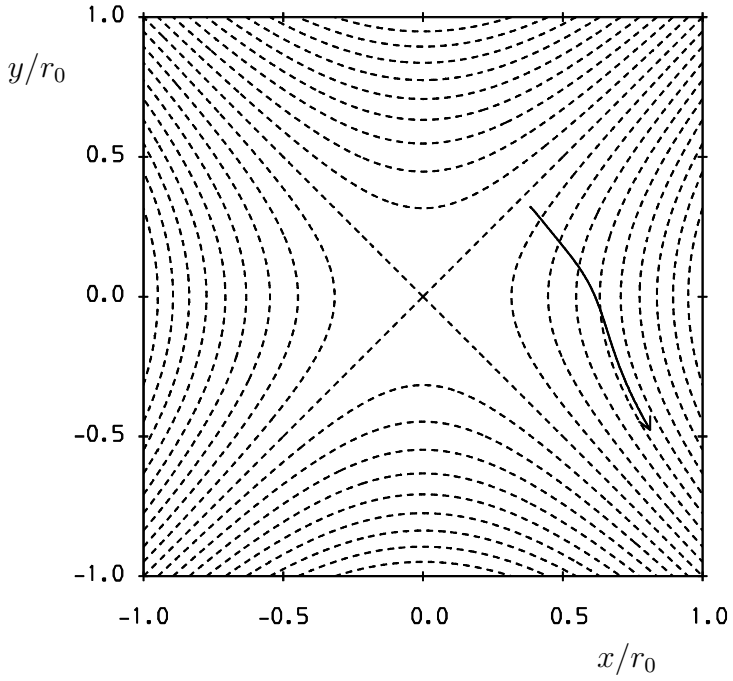

Figure 4.32: The solid curve shows the trajectory in the (x, y) plane of the particle whose energy evolution is shown in Fig. 4.31; the particle is initially near the separatrix and moves in the direction indicated by the arrow.

Other single-particle runs of `CUEBIT` show that the net energy gain increases roughly as δu_2^2 : Fig. 4.33 shows the average net increase in energy of a simulated population of 500 protons against increasing δu_2^2. The above calculation cannot account for this large energy increment: the rise and decay times of the electric field corresponding to the assumed values of δu_1 and δu_2 are such that the net energy gain implied by Eqs. 4.73 and 4.74 is negligibly small compared to that observed in the simulations.

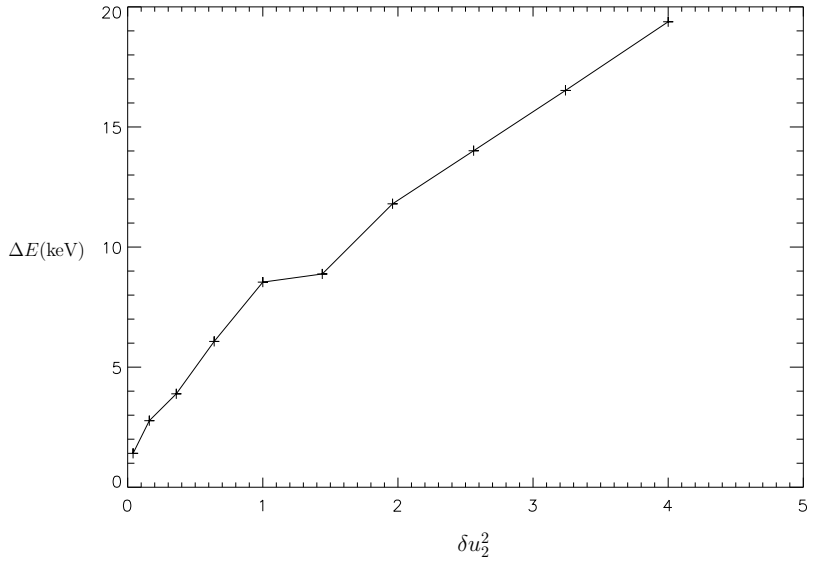

Figure 4.33: The average net gain in energy ΔE of 500 protons for the case of a localised perturbation where δu_1=0.2, for various values of δu_2. The system size is $r_0 = 10^7$m, the value of the magnetic field at the system boundary $B_0 = 0.01$T, the plasma density $n = 10^{14}\mathrm{m}^{-3}$, and the size of the perturbation $\xi = 0.1$. The total simulation time is 2 seconds.

We have examined the temporal behavior of $v_\parallel$ and $v_\perp$ for the initially-stationary proton whose energy and trajectory are plotted in Figures 4.31 and 4.32. After a period in which the dominant motion is an $\mathbf{E} \times \mathbf{B}$ drift, $v_\perp$ becomes very small as the electric field decays to zero, whereas $|v_\parallel|$ rises to a finite, slowly-varying value, so that asymptotically we have $|v_\parallel| \simeq v$. This can be understood as follows. Since $v_\parallel = \mathbf{v} \cdot \mathbf{B}/B$ we deduce that

$$\dot{v}_\parallel = \frac{1}{B}\dot{\mathbf{v}} \cdot \mathbf{B} + \mathbf{v} \cdot \frac{d}{dt}\left(\frac{\mathbf{B}}{B}\right), \tag{4.83}$$

where $m_p\dot{\mathbf{v}} = e(\mathbf{E} + \mathbf{v} \times \mathbf{B})$. The first term on the right hand side of Eq. 4.83 vanishes since $\mathbf{B} \cdot (\mathbf{v} \times \mathbf{B}) \equiv 0$ and, in our particular problem, $\mathbf{E}$ is orthogonal to $\mathbf{B}$.

Since d/dt is the time derivative in a frame moving with the particle, the equation reduces to

$$\dot{v}_{\parallel} = \mathbf{v} \cdot \left[\frac{\partial \mathbf{b}}{\partial t} + (\mathbf{v} \cdot \nabla)\, \mathbf{b} \right], \tag{4.84}$$

where $\mathbf{b} = \mathbf{B}/B$ is the unit vector in the direction of $\mathbf{B}$. The proton is thus subject to inertial forces in the parallel direction due to temporal and spatial variations in $\mathbf{b}$. Examination of individual particle orbits computed using `CUEBIT` shows that the Larmor gyration component of $v_{\perp}$ is generally small compared to the $\mathbf{E} \times \mathbf{B}$ drift speed $v_E \simeq E_z/B_E$, as one might expect from the calculation for uniform fields presented above. Before the particle has acquired a finite $v_{\parallel}$, the velocity on the right hand side of Eq. 4.84 is thus essentially equal to v_E. Both of the terms on the right-hand side can produce a change in $v_{\parallel}$: the time-evolving part of $\mathbf{b}$ associated with the wave is in general not parallel to $\mathbf{b}$, and the fact that the field changes direction in the frame of a particle moving across it ensures that the $(\mathbf{v} \cdot \nabla)\mathbf{b}$ term is also finite even when $\mathbf{v}$ is orthogonal to $\mathbf{b}$. The acceleration is limited by the fact that the $\mathbf{E} \times \mathbf{B}$ drift speed falls to zero, on a timescale determined by the value of δu_2 in the case of the localised perturbation. If δu_2 is increased, the particle has more time to be accelerated parallel to the field, and so the asymptotic particle energy is also increased.

It should be noted that the cold plasma fluid model used in the simulations incorporates the $\mathbf{E} \times \mathbf{B}$ drift but does not allow the possibility of finite plasma pressure. The distributions that we observe in the simulations cannot in fact be characterized by a scalar pressure since they are highly anisotropic. This is entirely consistent with the cold plasma fluid model provided that the components of the pressure tensor remain small compared to the magnetic pressure throughout the domain that is being simulated: this condition is invariably satisfied.

The interpretation proposed above leads to a number of easily-testable predictions regarding the scaling of asymptotic particle energy with various parameters. The maximum value of $v_{\perp}$ is approximately equal to $v_E = E_z/B_E \simeq \xi r_0/\tau_A = \xi c_A$, and the magnitudes of both $\partial \mathbf{b}/\partial t$ and $(\mathbf{v} \cdot \nabla)\mathbf{b}$ are of the order of ξ/τ_A. Since the right hand side of Eq. 4.84 has a large value for about an Alfvén time, we deduce

that the change in $v_\parallel$ is approximately

$$\delta v_\parallel = \xi^2 c_A. \tag{4.85}$$

It should be noted that $\delta v_\parallel$ is independent of particle mass and charge, and therefore the result is equally applicable to electrons and ions. However, since the electron thermal speed is typically comparable to c_A in the solar corona and $\delta v_\parallel \ll c_A$, we would expect the direct effect of a single wave pulse on the electron population to be negligible, and indeed running `CUEBIT` for electrons rather than protons we find that this is the case. The predicted $\delta v_\parallel$ is also independent of the system size, r_0. This is again borne out by numerical results obtained for a given initial value of r/r_0 and a range of values of r_0, although the system size becomes significant when r_0 is so small that large numbers of particles escape before the electric field has fallen to zero. Physically, the insensitivity of $\delta v_\parallel$ to r_0 is due to the fact that although the parallel acceleration time is proportional to τ_A and hence r_0, the strength of the force causing the acceleration is inversely proportional to the magnetic field scale length, which in this particular geometry is also of the order of r_0. The two effects cancel out, and the net change in $v_\parallel$ is therefore independent of the system size.

For a particle starting from rest the asymptotic energy is given by

$$\mathcal{E} \sim \frac{1}{2} m_p \xi^4 c_A^2. \tag{4.86}$$

Single particle runs confirm the scaling with parameters in Eq. 4.86 (see Figure 4.34) although the absolute value of the particle energy can be considerably less than or greater than that given by the equation. In the case of pulse-like localised perturbations, the time in which a particle is accelerated parallel to $\mathbf{B}$ can be shorter or longer than τ_A, depending on the value chosen for δu_2. In the case of the global perturbation, the final energy appears to be limited by the fact that E_z can change sign, thereby reducing the average $v_\perp$ of a proton during the period in which it is interacting with the wave. For a particle starting from rest at a given position, the change in energy is of course unique. However, particles starting from a range of initial positions can pass through a given region of space at a given time with a range of values of $v_\parallel$, i.e. it is possible for the wave pulse to produce a velocity distribution

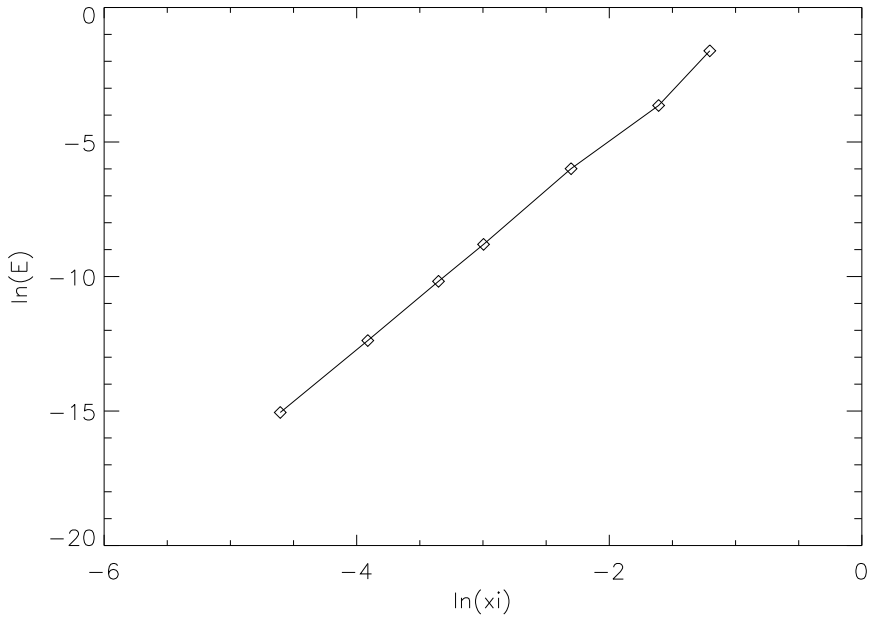

Figure 4.34: The asymptotic energy versus perturbation amplitude ξ (both in logarithms) of a single proton launched from rest from coordinates $x = 0.38r_0$, $y = -0.14r_0$ in an X-point equilibrium disturbed by the global wave perturbation, using the quiet corona simulation parameters. The gradient of the line is approximately 3.9, leading to the conclusion that asymptotic energy approximately scales with ξ^4.

of finite width, even if all the particles start from rest. The $v_\perp$ distributions generally have a narrow width, determined by the specified initial ion temperature, whereas the $v_\parallel$ distributions are much broader, with a characteristic temperature of the order of the energy given by Eq. 4.86. For the entire system the $v_\perp$ distribution is still narrow, whereas the $v_\parallel$ distribution is even broader than that found in a specified region (cf. Figs. 4.24 and 4.26). If $\mathcal{E}$ given by Eq. 4.86 is interpreted as a typical thermal energy, the corresponding thermal plasma energy density is of the order of ξ^2 times the wave energy density, and the final plasma beta $\beta \sim 2\mu_0 n\mathcal{E}/B^2 = 2\mathcal{E}/m_p c_A^2$ is of the order of ξ^4. Since ξ must be less than unity for the fluid solution to be valid, it follows that the condition for the cold plasma approximation to remain valid throughout a simulation is automatically satisfied. Conversely, according to this interpretation, the perturbation amplitude that would be required to produce a plasma with a given beta is $\xi \sim \beta^{1/4}$. However, it should be noted that β is not an input parameter of the model, and therefore the predicted heating efficiency

is independent of this parameter. The model requires that β be negligibly small throughout each simulation, otherwise the cold plasma fast Alfvén wave solution would be inapplicable. The plasma beta is generally assumed to be low in the solar corona: typically accepted values of this parameter lie in the range $0.01 \rightarrow 0.1$ [63,64]. In flares the plasma pressure is considerably greater than it is in the quiet corona, but since the magnetic field in flaring regions is also believed to be relatively high, the plasma beta is still likely to be less than unity [65].

4.8 Discussion and Conclusions

We have used a test particle full orbit code to investigate the collisionless response of protons to cold plasma fast Alfvén waves propagating in a two-dimensional magnetic X-point configuration, exploiting the fact that exact solutions of the linearised MHD equations exist for this particular geometry. Two specific types of fast wave solution have been invoked: a global perturbation, with inward- and outward-propagating components; and a purely inward-propagating, pulse-like wave, initially localised at a specified distance from the X-point null, the wave electric field having a preferred sign in the longitudinal direction orthogonal to the plane of the magnetic field $\mathbf{B}$. We have shown that in both cases the protons are effectively heated in the direction parallel to $\mathbf{B}$, although heating is more effective in the case of the pulse-like wave, particularly when the pulse is asymmetric, and some protons are accelerated to parallel velocities well in excess of the effective thermal speed. Acceleration can occur along the magnetic field despite the absence of a parallel component in the wave electric field $\mathbf{E}$ because the protons acquire a large $\mathbf{E} \times \mathbf{B}$ drift speed, and are subject to an effective force in the direction parallel to $\mathbf{B}$ due to the combined effect of a time-varying magnetic field associated with the wave and the spatial variation of the equilibrium field. This process is somewhat similar to the transit-time damping proposed by Miller and co-workers [55] as a mechanism for the acceleration of electrons in flares, but differs in that the perpendicular particle motion is primarily due to the $\mathbf{E} \times \mathbf{B}$ drift rather than Larmor gyration and the magnetic field gradient arises primarily from the equilibrium field rather than the wave field.

Wave pulses have been shown to have a cumulative, synergistic effect on the effective parallel proton temperature, indicating that high effective temperatures could result from a succession of relatively low amplitude wave pulses. Since the parallel acceleration is independent of particle mass and charge, particles of all species acquire the same increment in $v_{\|}$: the change in energy associated with this parallel motion is consequently proportional to mass, and therefore the mechanism is even more effective for heavy ions than it is for protons, but it has a negligible direct effect on electrons. It is interesting to note in this context that *in situ* measurements of heavy ions in the solar wind, carried out using the Ulysses spacecraft, have indeed revealed a linear scaling of kinetic temperature with ion mass [66]. On the other hand, one would expect both electrons and heavy ions to relax to a temperature comparable to that of the protons in the more collisional environment of the low corona.

The ξ^4 scaling in Eq. 4.86 indicates that rather large perturbation amplitudes would be required in order for a single wave pulse to have a significant effect. Observations of nonthermal line broadening suggest that the fluid velocity associated with wave perturbations in the inner corona is no more than about 30 kms^{-1} [9]; assuming $c_A \sim 2000$ kms^{-1} (an appropriate figure for the quiet corona), this implies $\xi < 0.015$. Under normal circumstances direct observational information on MHD wave amplitudes in the solar corona is only available in the case of waves with periods of the order of several minutes, much longer than those of the waves in our simulations [67]. However, oscillations with periods of a few seconds were detected during the total eclipse of August 11 1999 [68]. Analysis of this eclipse data by Cooper and co-workers [69] suggests that the waves were fast Alfvénic in character with amplitudes of around 5%, comparable to the 6% initial amplitude assumed in our two-pulse simulation. We have shown that successive wave pulses can have a cumulative, synergistic effect on the proton population. Significant heating could thus result from a train of relatively low amplitude pulses. Moreover, as we saw earlier, the amplitude of a fast Alfvén wave pulse tends to increase as it approaches a magnetic null, due to the steepening effect of the variation in c_A (also compare with Figures 1 and 2 in McClements *et al.* [54]). Our results indicate that the degree of

effective heating is fairly sensitive to the pulse profile. There are few (if any) observational constraints on fast Alfvén wave pulse profiles in the solar corona. However, all of the profiles we have invoked represent exact, physically-realizable solutions of the cold plasma ideal MHD equations, which have a qualitatively-similar effect on the proton population.

It is important to note that the essential elements of the proposed heating mechanism, namely transient changes in the perpendicular velocity of ions and the presence of a parallel force on those ions, are generic to all magnetoplasma configurations with a perpendicular variation in field line direction that are perturbed by MHD waves. The mechanism is thus not restricted to the case of a two-dimensional magnetic null. Indeed, the interpretation presented indicates that the mechanism is ineffective close to the null, since the local Alfvén speed vanishes at that point (cf. Eq. 4.86). It is, however, convenient to use a two-dimensional X-point equilibrium since such a configuration has the essential property of having magnetic field lines that change direction in the frame of a particle moving across them while being sufficiently simple that exact analytical solutions of the linearised cold plasma MHD equations can be found. Porter and co-workers [40] noted that the source of MHD waves in the corona could lie either in the photosphere or the corona itself. In the particular context of X-point geometry, one may conjecture that inward-propagating waves could have originated from mode conversion of shear Alfvén waves driven by photospheric convection, while outward-propagating waves could have been generated as a result of non-steady magnetic reconnection in the vicinity of the null. However, the propagation direction of the wave is essentially irrelevant in the model as far as heating and particle acceleration are concerned: the process we have identified is thus generic to both of the broad categories of coronal heating scenario that have been discussed in the literature (namely, dissipation of remotely-generated waves and local reconnection). The model is also applicable to late-phase heating in flares, although in this case it is more probable that the fast wave in question would have originated from local reconnection.

"With half the race gone, there is still half the race left to go"

Murray Walker

Chapter 5

Test Particle Simulations of Collisional Impurity Transport in a Large Aspect Ratio Tokamak Plasma

Note: Material in this (and the following) chapter has been published in the journal Plasma Physics & Controlled Fusion. The reference is:
McKay R J, McClements K G, Thyagaraja A, and Fletcher L: "Test-particle Simulations of Collisional Impurity Transport in Rotating Spherical Tokamak Plasmas" *Plasma Phys. Control. Fusion* **50**, 065017 (2008)

5.1 Introduction

In our fast wave proton simulations it was not neccessary to include the effects of collisions, as discussed previously. However, our next aim is to model collisional transport of impurity ions in a tokamak, and for this we need to introduce collisional effects to the `CUEBIT` code, as discussed in Chapter 3. In this chapter we discuss this and spend some time ensuring that the code functions as it is supposed to, and we

make sure the code reproduces the effects of standard Coulomb collisions by benchmarking it against an analytically-derived transport equation. In Chapter 6 radial profiles of the bulk plasma density n and temperature T, upon which the collision time τ depends, will be specified, but for now, for the purposes of benchmarking the code, a single value for τ will be stipulated.

5.2 Conservation of p_φ in Collisionless Orbits

In Chapter 2 we showed that the quantity $p_\varphi = mRv_\varphi + Ze\psi$ is conserved in an axisymmetric field in the absence of collisions - see Eq. 2.68. Additionally, in Chapter 4 we discussed the conservation of longitudinal canonical momentum p_z in a perturbed two-dimensional X-point configuration, and how we tested `CUEBIT` to ensure this was replicated in the test particle simulations. Similarly we can test `CUEBIT`'s conservation of p_φ, in an axisymmetric field and in the absence of collisions: like p_z in the perturbed X-point configuration, this quantity is not quite so well-conserved as energy is in `CUEBIT`, but, provided the timestep is sufficiently short, we expect it to be conserved to an acceptable level of accuracy.

We check that `CUEBIT` is performing as we require it to by applying it to collisionless test particles in the specific, simple case of a non-rotating, large aspect ratio tokamak with circular flux surfaces. We must specify the major and minor radii, R_0 and a, as well as the toroidal field at the magnetic axis $R = R_0$. We also need to choose a function for the poloidal flux - for this purpose we use the following expression:

$$\psi = \psi_0 \left[(R - R_0)^2 + Z^2 \right], \tag{5.1}$$

where the plasma boundary lies at $r = [(R - R_0)^2 + Z^2]^{1/2} = a$. To determine an appropriate value for ψ_0 we need to consider the plasma safety factor, q_s, as introduced in Chapter 2. We simulate a fully-ionised carbon ion ($Z = 6$, $A = 12$, where Z and A are the atomic number and mass number respectively) in a JET-like plasma with $R_0 = 3$m, $a = 1$m, $B_0 = 3$T (where B_0 is the toroidal magnetic field at $R = R_0$), and $q_s = B_0/2\psi_0 = 3$. The carbon ion is launched at major radius $R =$

3.5m in the midplane ($Z = 0$), with velocity components $v_R = v_\varphi = 2\times10^6 \mathrm{ms}^{-1}$ (the launch point and velocity components are chosen entirely arbitrarily). The particle is simulated for 3×10^4 timesteps, where each timestep is taken to be one-tenth of the Larmor period of the particle at the magnetic axis (this corresponds to a physical time of approximately 0.13 milliseconds). Figure 5.1 shows the orbit projected onto a poloidal cross-section of the plasma. Figures 5.2 and 5.3 plot the variation in fractional deviation of energy, $\Delta E/E$, and toroidal canonical momentum, $\Delta p_\varphi/p_\varphi$ with time.

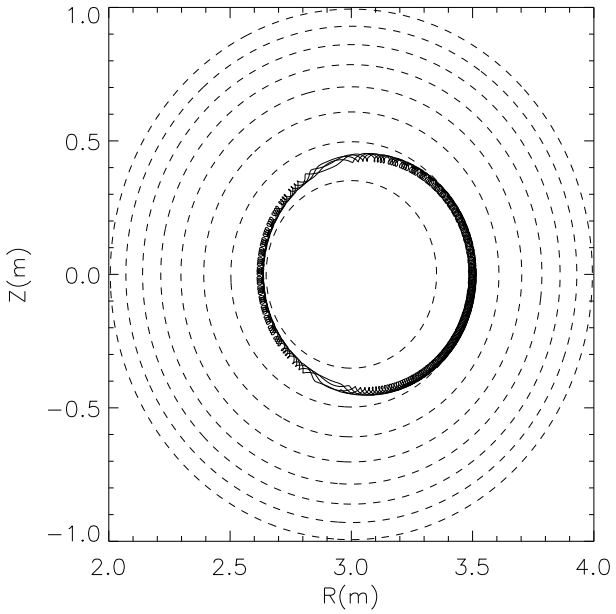

Figure 5.1: Orbit of C^{6+} impurity in plasma with JET-like parameters, launched from $R = 3.5$m, $Z = 0$ with $v_R = v_\varphi = 2 \times 10^6 \mathrm{ms}^{-1}$, $v_Z = 0$ and simulated for 30000 timesteps where each timestep is one-tenth of a Larmor period.

We see that, as we saw in the previous Chapter, the energy is effectively conserved to a very high level, with variations only of order of 1 part in 10^{14}. We also see that the canonical momentum is conserved, less well than the energy (about 8 or 9 orders of magnitude less) but still to a sufficient degree. This is as a result of this conservation not being physically intrinsic in the code - the important point to note is that p_φ is an exact invariant of the Lorentz force equation, but is not an exact invariant of the finite difference approximation to the Lorentz force equation that we are using. The p_φ component varies on two timescales, one very short (due to the very short timescales associated with the Larmor orbits) and one longer (due

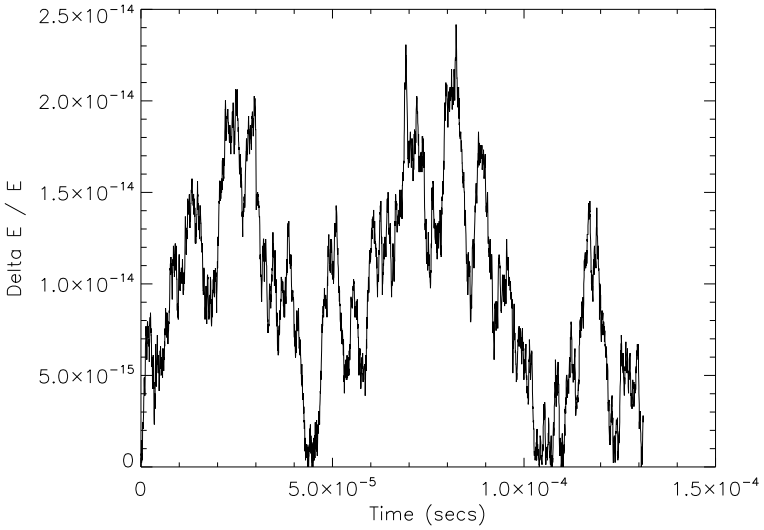

Figure 5.2: Variation of fractional deviation in energy for the C^{6+} ion shown in Figure 5.1.

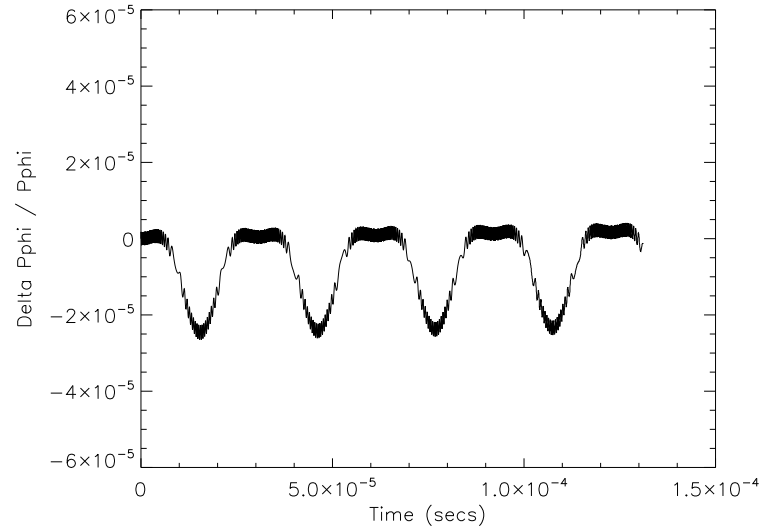

Figure 5.3: Fractional variation in toroidal canonical momentum p_φ for the C^{6+} ion whose orbit is shown in Figure 5.1.

to the periodic nature of the particle moving from the stronger field inner region to the weaker field outer region of the tokamak).

It is of interest to investigate how varying the size of the timestep Δt affects conservation of p_φ: Figures 5.4 and 5.5 show the result of increasing the timestep to half a Larmor period and 1 Larmor period respectively (this has no effect on energy conservation). In the latter figure we see that p_φ variance is beginning to reach significant levels - which increase over time - and thus the output of the code may

become increasingly unphysical. So although it may be tempting to increase the timestep to simulate longer timescales (or alternatively simulate the same timescale with fewer timesteps and decrease the computational resources needed), there is a trade-off in the accuracy of the results obtained, which must always be borne in mind. For this reason our simulations generally use a timestep Δt of one-tenth of a Larmor period.

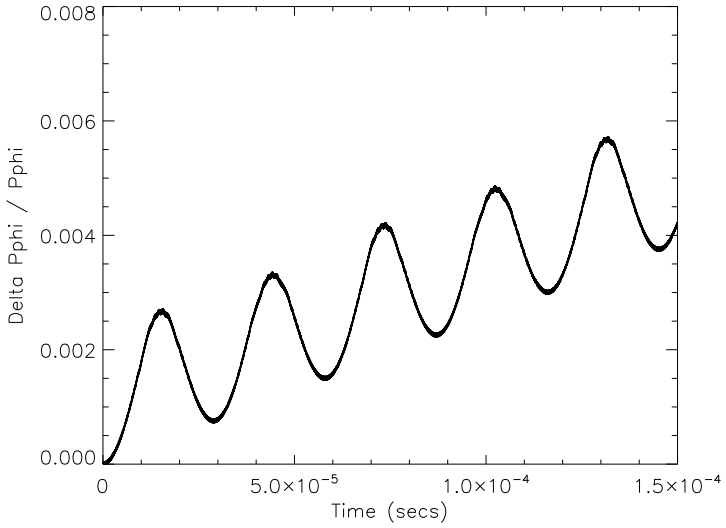

Figure 5.4: Fractional variation in toroidal canonical momentum p_φ for the C^{6+} ion shown in Figure 5.1, simulated with a timestep Δt equal to half a Larmor period.

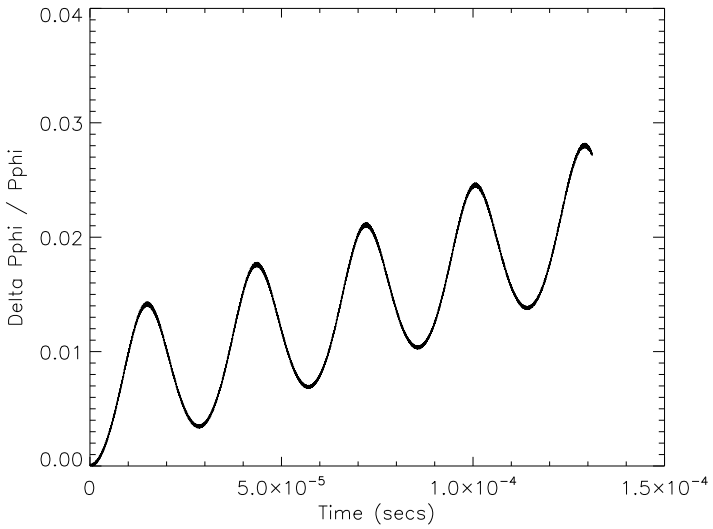

Figure 5.5: Fractional variation in toroidal canonical momentum p_φ for the C^{6+} ion shown in Figure 5.1 simulated with a timestep Δt equal to one Larmor period.

5.3 Testing Thermalisation in Collisional Code

Before investigating the collisional transport of impurity ions in a rotating spherical tokamak, we test the collisional version of `CUEBIT` by applying it to test particles in the same plasma equilibrium as before, assuming a constant specified collision time and $\mathbf{E} = \mathbf{0}$, and comparing the output to a particular analytic solution of the transport problem. For this purpose we use the expression for poloidal flux introduced in the previous section, with

$$\psi_0 = \frac{\mu_0 R_0 I_p}{4\pi a^2} \tag{5.2}$$

where μ_0 is the permeability of free space and I_p is the plasma current. We again take $RB_\varphi \equiv R_0 B_0$ to be a constant.

A test was performed using the same JET-like parameters as previously, with a plasma current $I_p = 3$MA (giving a slightly lower value for the plasma safety factor, $q_s = 1.67$). An artificially low value was adopted for the collision time in order to minimise the impact of modifications to purely classical transport arising from drift orbit effects: τ was set equal to 10^{-6}s . This is still much longer than the particle cyclotron period ($\sim$ 40ns). A total of 10^4 fully ionised carbon ions (C^{6+}) were launched from the magnetic axis at $t = 0$ with a Maxwellian velocity distribution at $T = 100$ eV. The temperature specified in the variance of the noise terms (given by Eq. 3.16) was 1 keV. The bulk ions were assumed to have zero net toroidal rotation, i.e. v_φ equal to zero. The mean velocity components and temperatures of the C^{6+} distribution were computed after the simulation completed 50 collision times - the results of this are shown in Table 5.1.

The mean velocity components are of the order of 1% of the thermal velocity, and the fractional deviations of the temperature from the expected value are also around 1% or less: this seems to be consistent with Poisson statistics for 10^4 particles ($\sqrt{N}/N$=0.01), and so the first and second moments of the simulated distribution appear to be consistent with relaxation to the expected Maxwellian - thus we conclude that our treatment of collisions produces thermalisation of test particles to the expected distribution. We can check further that this is the case by computing

Table 5.1: Flows and temperatures computed from first and second moments of C^{6+} velocity distribution after 50 collision times in JET-like plasma

Quantity	Value	Units
$< v_x >$	575	ms^{-1}
$< v_y >$	787	ms^{-1}
$< v_z >$	-158	ms^{-1}
T_x	0.992	keV
T_y	1.002	keV
T_z	1.004	keV

the skewness and kurtosis statistics. If these are small compared to unity then the distributions are close to being truly Maxwellian. We use the following expressions for sample skewness g_1 and kurtosis g_2, respectively

$$g_1 = \frac{\frac{1}{N}\sum_{i=1}^{N}(v_i - \bar{v})^3}{\left[\frac{1}{N}\sum_{i=1}^{N}(v_i - \bar{v})^2\right]^{3/2}} \tag{5.3}$$

$$g_2 = \frac{\frac{1}{N}\sum_{i=1}^{N}(v_i - \bar{v})^4}{\left[\frac{1}{N}\sum_{i=1}^{N}(v_i - \bar{v})^2\right]^{2}} - 3, \tag{5.4}$$

where v_i denotes a velocity component of the i^{th} particle in the simulation and $\bar{v}$ denotes the mean value of that velocity component, and display the results in Table 5.2.

Table 5.2: Skewness and kurtosis statistics of C^{6+} velocity distribution

	v_x	v_y	v_z
skewness	-4.9×10^{-2}	9.6×10^{-3}	2.2×10^{-3}
kurtosis	-5.3×10^{-2}	2.0×10^{-2}	6.9×10^{-2}

The fact that these values are much less than unity reinforces our confidence that the collisional scheme we employ produces the desired results, at least as far as the thermalisation of the impurity ions is concerned. We still need to benchmark our scheme against the analytic solution of the transport equation, which will be derived in Section 5.5.

5.4 Particle Orbits in Presence of Collisions

To illustrate the effect of collisions on the impurity ions in the tokamak, we plot the orbit of one of the particles simulated in the previous section, but for a longer time (about 10^7 timesteps, which corresponds to approximately 40 milliseconds) in order to show the ion migrating across the magnetic flux surfaces. Figures 5.6, 5.7 and 5.8 show the resulting trajectories when the collision time τ is set equal to 10^{-7}, 10^{-6} and 10^{-5} seconds respectively. The bulk ion temperature is 1 keV as before. In each case the initial velocity of the carbon impurity ion is the same: $v_R = 2.9 \times 10^4$ ms^{-1}, $v_\varphi = 0$, $v_Z = -1.5 \times 10^5$ ms^{-1}. We see that the particle undergoes a random walk in coordinate space, but the aggregate radial excursion from the initial position, r, clearly diminishes as the collision time is increased, as seen in Figure 5.9, and as expected from the classical diffusivity $D_\perp \propto \tau^{-1}$ as discussed in Section 2.5.

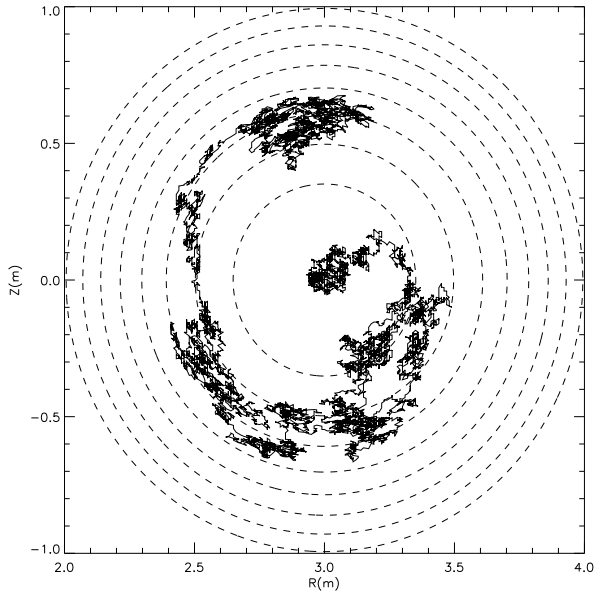

Figure 5.6: Orbit of C^{6+} impurity ion in plasma with JET-like parameters, launched from the magnetic axis $R = R_0$, $Z = 0$ with an initial velocity as given in the text and simulated for approximately 40 ms. The collision time τ is set equal to 10^{-7} seconds.

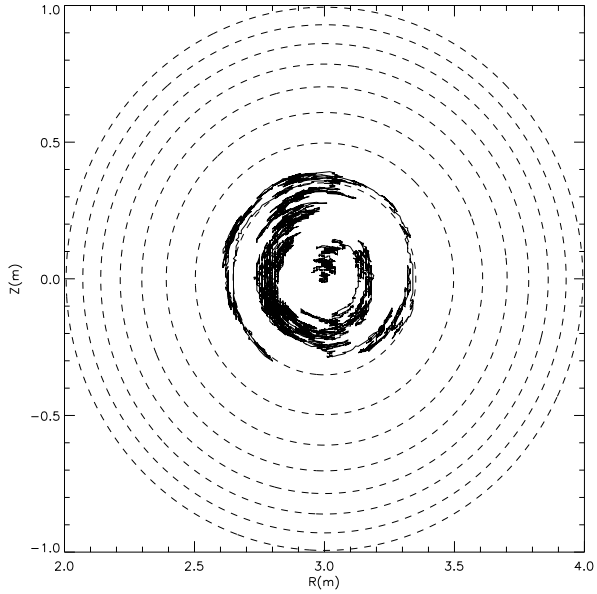

Figure 5.7: Orbit of C^{6+} impurity in plasma with JET-like parameters, launched from the magnetic axis $R = R_0$, $Z = 0$ with an initial velocity as given in the text and simulated for approximately 40 ms. The collision timescale τ is set equal to 10^{-6} seconds.

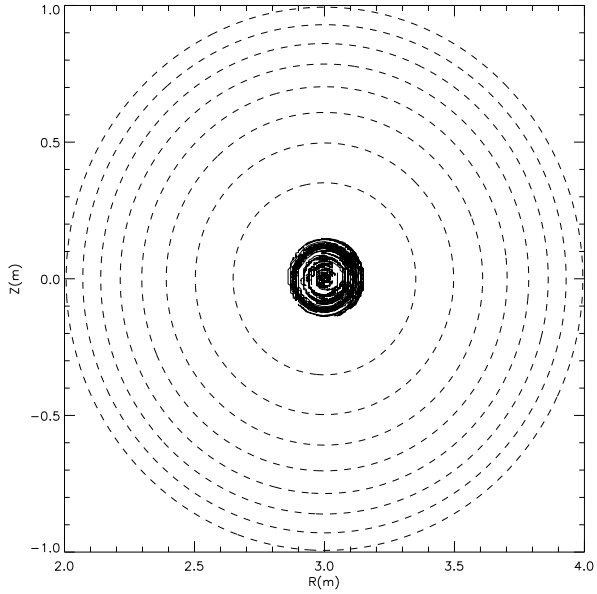

Figure 5.8: Orbit of C^{6+} impurity in plasma with JET-like parameters, launched from the magnetic axis $R = R_0$, $Z = 0$ with an initial velocity as given in the text and simulated for approximately 40 ms. The collision timescale τ is set equal to 10^{-5} seconds.

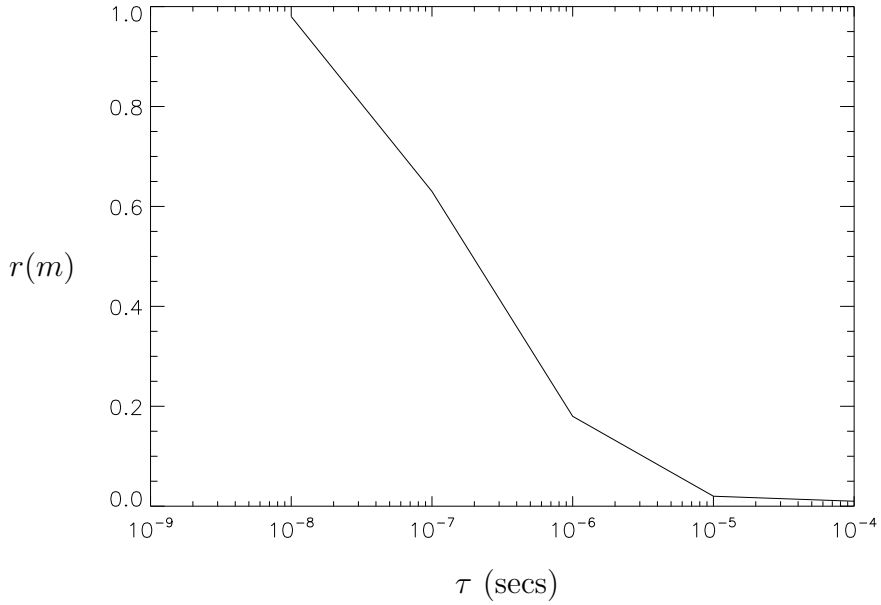

Figure 5.9: Aggregate radial excursion r from the magnetic axis of a C^{6+} impurity ion versus collision time τ. The initial velocity of the particle is given in the text and the simulation time is approximately 40 ms.

We can understand the migration of the particle by comparing the collision time to that of the time taken to perform a passing orbit. For strongly-passing particles, the frequency of poloidal rotation is given by (see Wesson [20]) $\omega_p = (B_\theta/B)v_\parallel/r$ and the time taken to complete a poloidal orbit of the tokamak in the absence of collisions is of the order of $\tau_p = 2\pi/\omega_p$. By calculating the value of τ_p for the particle whose trajectory is plotted in Figure 5.8 and comparing it to the actual (prescribed) collision time for that particle (10^{-5} seconds), as we see in Figure 5.10, then it is clear that, although for large periods of the time the particle collides on a timescale shorter than the passing orbit timescale, there are some periods when the converse is true. During these intervals the ion remains close to a given flux surface. The important thing to note is that whilst this is happening, the particle is not colliding with the bulk ions and thus not migrating across the flux surfaces. If the collision time τ is decreased to $\tau = 10^{-6}$s, the periods where the ion is travelling on a trapped orbit are much shorter and much less frequent and thus the radial migration of the particle is greatly accelerated (resulting in the type of trajectory seen in Figure 5.7). Decreasing τ still further results in the particle not being in the regime $\tau_p < \tau$ at all, instead simply colliding continuously in the random walk we see in Figure 5.6.

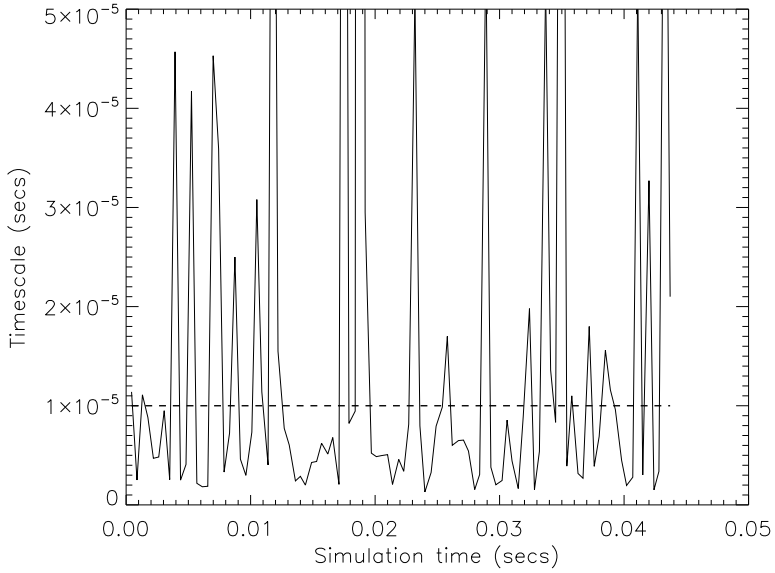

Figure 5.10: Comparison of the passing orbit timescale τ_p (solid line) against the prescribed collision time $\tau = 10^{-5}$s (dashed line) for the C^{6+} impurity ion whose trajectory is displayed in Figure 5.8.

5.5 Testing the Code Against Classical Transport Theory

The problem of collisional test particle transport in a uniform large aspect ratio tokamak plasma can be solved analytically as follows. In Chapter 2 we noted that a simple random walk argument leads to the following expression for the diffusion rate of charged particles across the magnetic field:

$$D_\perp \sim \frac{r_L^2}{\tau} \tag{5.5}$$

where $r_L = (T/m_Z)^{1/2} m_Z/ZeB$ is the typical ion Larmor radius. By definition, τ is the time taken for a particle to be deflected by a large angle due to collisions: when such a deflection occurs, it is evident that the particle's guiding centre can move across the magnetic field by a distance of order r_L. In toroidal plasmas of finite aspect ratio $A = R_0/a$, the diffusivity is enhanced by neoclassical effects, but the above equation is applicable to test particles undergoing purely collisional transport in the limit $A \to \infty$. Taking $D_\perp$ to be constant, and neglecting sources and sinks, the temporal evolution of the test particle density n_Z is then given by a simple

diffusion equation of the form

$$\frac{\partial n_Z}{\partial t} = \nabla \cdot (D_\perp \nabla n_Z) = \frac{D_\perp}{r}\frac{\partial}{\partial r}\left(r\frac{\partial n_Z}{\partial r}\right), \tag{5.6}$$

where $r = [(R - R_0)^2 + Z^2]^{1/2}$ is minor radial distance from the magnetic axis at $R = R_0$, $Z = 0$. This equation has separable solutions of the form

$$n_Z = n_0 \exp\left(-\gamma^2 D_\perp t/a^2\right) J_0(\gamma r/a) \tag{5.7}$$

where γ is an arbitrary constant, and J_0 is the Bessel function of order zero. However, this expression only gives the complete solution if we choose the initial profile to be of the form $n_Z(0, r) \propto J_0(\gamma r/a)$. For an arbitrary initial profile $n_Z(r)$, solutions of Eq. 5.7 satisfying the boundary condition $n_Z(a) = 0$ can be expressed as Fourier-Bessel series of the form [70]

$$n_Z(r, t) = \sum_{i=1}^{\infty} n_{0i} \exp\left(-\gamma_i^2 D_\perp t/a^2\right) J_0\left(\gamma_i \frac{r}{a}\right), \tag{5.8}$$

where γ_i is the i-th positive zero of J_0. If we set $t = 0$, and multiply by $xJ_0(\gamma_j x)$ where $x = r/a$, this gives

$$n_Z(r, 0) x J_0(\gamma_j x) = \sum_{i=1}^{\infty} x n_{0i} J_0(\gamma_i x) J_0(\gamma_j x). \tag{5.9}$$

Now integrating with respect to x, and making use of the orthogonality relation [71]

$$\int_0^1 x J_\alpha(x u_{\alpha,m}) J_\alpha(x u_{\alpha,n}) dx = \frac{\delta_{m,n}}{2} \left[J_{\alpha+1}(u_{\alpha,m})\right]^2, \tag{5.10}$$

which holds if $u_{\alpha,n}$ is the nth positive zero of J_α, results in

$$\int_0^1 n_Z(r, 0) x J_0(\gamma_j x) = \frac{1}{2} n_{0i} J_1^2(\gamma_j) \delta_{ij}, \tag{5.11}$$

where δ_{ij} is the Kronecker delta symbol and J_1 is the Bessel function of order 1. Hence the coefficients in Eq. 5.11 are given by

$$n_{0i} = \frac{2}{J_1^2(\gamma_i)} \int_0^1 x J_0(\gamma_i x) n_Z(ax, 0) dx. \tag{5.12}$$

We can evaluate these coefficients for the case in which all the minority ions initially lie at the magnetic axis $r = 0$, which we can represent by writing:

$$n_Z(r, 0) = n_0\delta(r)/r. \tag{5.13}$$

where δ is the Dirac delta function and n_0 is a constant that determines the total number of minority ions initially in the system, N_0. By definition

$$N_0 = \int_V n_Z(r, 0)dV \tag{5.14}$$

where, the volume element is, in the limit of very large aspect ratio R_0/a,

$$dV = 2\pi R_0 \times 2\pi r dr = 4\pi^2 R_0 r dr \tag{5.15}$$

and hence

$$N_0 = 4\pi^2 R_0 \int_0^a r n_Z(r, 0)dr \tag{5.16}$$

Substituting Eq. 5.13 into 5.16 gives

$$N_0 = 4\pi^2 R_0 n_0 \int_0^a \delta(r)dr = 2\pi^2 R_0 n_0 \tag{5.17}$$

using the fact that

$$\int_0^a \delta(x)dx = 1/2, \tag{5.18}$$

and hence

$$n_0 = \frac{N_0}{2\pi^2 R_0} \tag{5.19}$$

and thus

$$n_Z(r, 0) = \frac{N_0\delta(r)}{2\pi^2 R_0 r}. \tag{5.20}$$

Equation 5.8 then has the form

$$n_Z(r, t) = \sum_{i=1}^{\infty} \frac{J_0(\gamma_i r/a)}{\exp(\gamma_i^2 D_\perp t/a^2)} \frac{2}{J_1^2(\gamma_i)} \int_0^1 x J_0(\gamma_i x) \frac{N_0\delta(ax)}{2\pi^2 R_0 a x} dx. \tag{5.21}$$

Making the dummy variable subsitution $y = ax$ gives

$$n_Z(r,t) = \sum_{i=1}^{\infty} \frac{J_0(\gamma_i r/a)}{\exp(\gamma_i^2 D_\perp t/a^2)} \frac{1}{J_1^2(\gamma_i)} \int_0^a J_0(\gamma_i y/a) \frac{N_0 \delta(y)}{\pi^2 R_0 a^2} dy. \tag{5.22}$$

and, using Eq. 5.18 and $J_0(0) = 1$, this reduces to

$$n_Z(r,t) = \frac{N_0}{2\pi^2 R_0 a^2} \sum_{i=1}^{\infty} \frac{J_0(\gamma_i r/a)}{J_1^2(\gamma_i) \exp(\gamma_i^2 D_\perp t/a^2)} \tag{5.23}$$

After a few collisional diffusion times only the $J_0(\gamma_1 r/a)$ term in this expansion will contribute significantly, and n_Z then decays in a purely exponential fashion, the associated confinement time being $\tau_c = a^2/\gamma_1^2 D_\perp \simeq 0.17(a^2/r_L^2)\tau$ (since $\gamma_1 \simeq 2.41$). In setting $n_Z = 0$ at $r = a$ we have effectively assumed that the diffusion rate outside this radius is infinite. This can be simulated in `CUEBIT` by removing a particle permanently from the system as soon as it crosses the plasma boundary.

In order to compare the predictions of classical transport theory with results from `CUEBIT` in a way that minimises statistical noise in the latter, we compute the temporal evolution of the total number of particles remaining in the system, $N(t)$:

$$N(t) = 4\pi^2 R_0 \int_0^a r n_Z(r,t) dr. \tag{5.24}$$

Substituting Eq. 5.23 into 5.24 results in

$$N(t) = \frac{2N_0}{a^2} \sum_{i=1}^{\infty} \frac{1}{J_1^2(\gamma_i) \exp(\gamma_i^2 D_\perp t/a^2)} \int_0^a r J_0(\gamma_i r/a) dr \tag{5.25}$$

If we put $x = \gamma_i r/a$ then $rdr = (a^2/\gamma_i^2) x dx$ and then the integral in Eq. 5.25 becomes

$$\int_0^a r J_0(\gamma_i r/a) dr = \frac{a^2}{\gamma_i^2} \int_0^{\gamma_i} x J_0(x) dx \tag{5.26}$$

and making use of the identity

$$\frac{d}{dx}(x^p J_p(x)) = x^p J_{p-1}(x)$$

we see that

$$\frac{a^2}{\gamma_i^2}\left[xJ_1(x)\right]_0^{\gamma_i} = \frac{a^2}{\gamma_i}J_1(\gamma_i) \tag{5.27}$$

and hence

$$N(t) = 2N_0 \sum_{i=1}^{\infty} \frac{\exp[-\gamma_i^2 D_\perp t/a^2]}{\gamma_i J_1(\gamma_i)}. \tag{5.28}$$

The assumption of uniform $D_\perp$ used to derive this result requires in general that T, B and τ do not vary across the plasma.

We can prescribe constant T and τ in the collisional terms, but spatial variations in B are unavoidable in a tokamak of finite aspect ratio. To minimise these variations we set $a = 1$m and $R_0 = 10^2$m, giving an aspect ratio $A = 10^2$. The toroidal field B_0 was set equal to 3T, and the plasma current $I_p = 30$kA, giving a safety factor at the plasma edge $q_s \simeq 2\pi a^2 B_0/\mu_0 R_0 I_p \simeq 5$. As before, τ was set equal to 10^{-6}s. A total of 10^4 fully ionised carbon ions (C^{6+}) were launched from the magnetic axis at $t = 0$ with a Maxwellian velocity distribution at $T = 1$ keV. The dashed curve in Figure 5.11 shows the temporal evolution of the number of simulated C^{6+} ions remaining in the plasma. The solid curve in this figure shows $N(t)$ computed using Eq. 5.28. It can be seen that the theoretical prediction represented by this equation is in excellent agreement with the particle simulation results: the two curves deviate

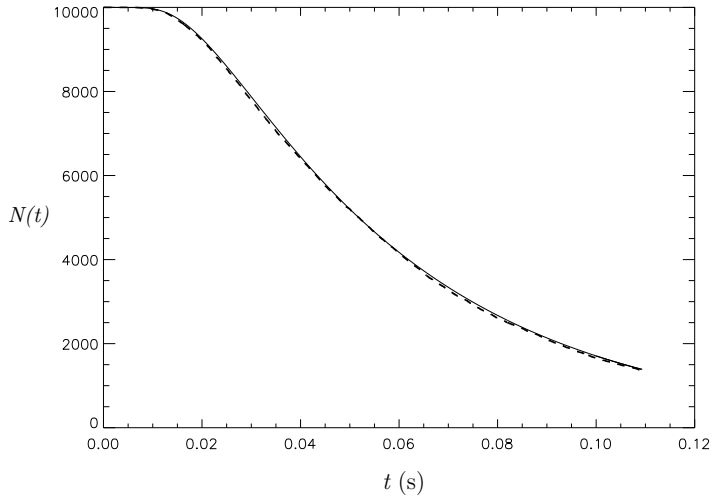

Figure 5.11: Computed $N(t)$ obtained using `CUEBIT` (dashed curve) and Eq. 5.28 (solid curve) for tokamak with aspect ratio $R_0/a = 10^2$. The collision time was set equal to $\tau = 10^{-6}$s and 10^4 particles were used in the simulation.

from each other by around 1% at most, which is again consistent with the expected level of statistical noise.

When the collision time is increased to 10^{-5}s we find that the particle confinement time inferred from `CUEBIT` is significantly shorter than the classical prediction (see Fig. 5.12). The model used to derive Eq. 5.28 is based on the premise that particles can only be transported across the magnetic field by collisions, whereas particles simulated using `CUEBIT` undergo grad-B and curvature drifts in any tokamak equilibrium with finite aspect ratio, however large. The orbit widths of trapped C^{6+} ions in the case of the results shown in Figure 5.11 are comparable to or greater than the plasma minor radius, and therefore such ions can be advected out of the plasma due to grad-B and curvature drifts (in the positive vertical direction). The drift timescale in this case is comparable to the confinement time, whereas in the case of the results shown in Figure 5.11 drift effects are negligible because the drift timescale is much longer than the confinement time. This is reflected by the fact that the poloidal distribution of C^{6+} ions at the end of the simulation with $\tau = 10^{-5}$s exhibits a strong up/down asymmetry that is not observed in the simulation with $\tau = 10^{-6}$s . Figure 5.12 indicates that drifts can cause the transport of test particles to be enhanced above the classical level even when, as in this case, the particles

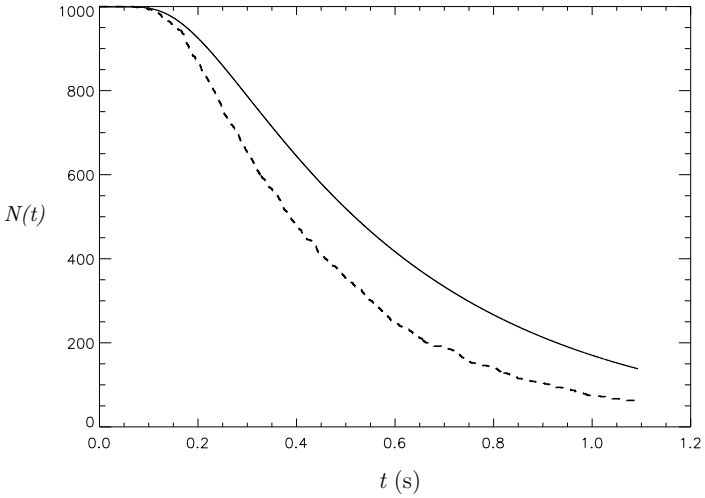

Figure 5.12: Computed $N(t)$ obtained using `CUEBIT` (dashed curve) and Eq. 5.28 (solid curve) for tokamak with aspect ratio $R_0/a = 10^2$. The collision time was set equal to $\tau = 10^{-5}$s and 10^3 particles were used in the simulation.

lie well within the Pfirsch-Schlüter regime throughout the plasma and the tokamak aspect ratio is much larger than unity.

We carried out a second set of simulations with aspect ratio $A = 10^4$ ($R_0 = 10^4$m, $a = 1$m) and very low current ($I_p = 1$A), thereby ensuring that the magnetic field was very nearly straight and uniform throughout the plasma: the ratio of poloidal to toroidal magnetic field was less than 10^{-7} and the fractional variation across the plasma of the flux surface-averged toroidal field was of the order of 10^{-8}. The other parameters were identical to those used previously, with collision times of 10^{-5}s and 10^{-4}s. Results obtained with the shorter value of τ are shown in Figure 5.13; it is clear that once again there is very good agreement between theory and simulation.

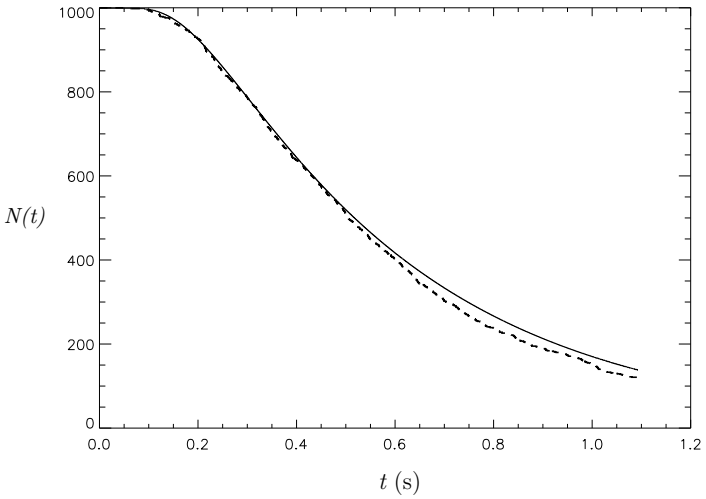

Figure 5.13: Computed $N(t)$ obtained using `CUEBIT` (dashed curve) and Eq. 5.28 (solid curve) for tokamak with aspect ratio $R_0/a = 10^4$. The collision time was set equal to $\tau = 10^{-5}$s and 10^3 particles were used in the simulation.

The difference between the two curves arising from statistical noise is somewhat greater than that in Figure 5.11 due to the fact that fewer particles were used in the simulation. A similar level of agreement was found in the simulation with $\tau = 10^{-4}$s. We have thus demonstrated that the scheme used to represent collisions in `CUEBIT` leads to classical test particle transport in the cylindrical limit, and can be applied with confidence to realistic tokamak scenarios.

"Sometimes it's hard to think
It's like your mind is on the blink
You sink deep and time just flew"

The Lightning Seeds
"Fishes On The Line"

Chapter 6

Test Particle Simulations of Collisional Impurity Transport in Rotating Spherical Tokamak Plasmas

6.1 Introduction: Our Work in Context

The use of high power tangential neutral beam injection (NBI) to deliver heat and angular momentum to plasmas in the MAST spherical tokamak has resulted in toroidal rotation velocities in excess of the sound speed in the plasma core [72]. The beamline geometry in MAST is fixed, but the direction of the plasma current I_p can be reversed so that the ions (deuterons) in a given beamline are born with toroidal velocity components in the counter-I_p direction rather than the more usual co-current direction. Despite the fact that a high proportion of beam ions are promptly lost in such cases, the use of counter-current NBI in MAST has produced high performance discharges, with energy confinement times greater than those achieved with co-current beam injection [72]. Bulk plasma toroidal rotation velocities in counter-NBI MAST plasmas are typically higher than those in plasmas

with co-current injection. Losses of counter-injected beam ions induce an inward-directed radial bulk ion return current, and hence a torque in the counter-current direction, which spins the plasma up to sonic Mach numbers M of order unity in the plasma core [73,74,75]. There is evidence that the improvement in energy confinement brought about by reversing the beam injection direction in MAST can be attributed to micro-turbulence suppression due to radial shear in the toroidal flow [72]. Toroidal rotation in tokamaks can also be beneficial in terms of suppressing MHD instabilities, including sawtooth oscillations [76], neoclassical tearing modes [77], and resistive wall modes [78].

Although rotating plasmas have attractive features with regard to the possibility of micro-turbulence suppression and MHD stability, the irreducible transport arising from particle collisions (i.e. neoclassical transport) can be enhanced rather than diminished by the presence of toroidal flow. For banana regime ions in a pure large aspect ratio plasma, Hinton and Wong [79] showed that rotation increases the neoclassical thermal conductivity by a factor $1 + \mathcal{O}(M^2)$. This analysis was subsequently extended to the case of an impure large aspect ratio plasma by Wong [80], who showed that the neoclassical transport coefficients of impurity ions are also enhanced in the banana regime. In general, as noted at the end of Chapter 2, it is desirable that impurity ions, specifically, are transported rapidly out of a burning plasma, since they dilute the fusion fuel.

Helander [81] pointed out a hitherto-overlooked mechanism whereby rotation could increase neoclassical banana regime transport, arising from the fact that the centrifugal force in a spinning plasma causes heavy impurity ions to accumulate on the low magnetic field side of each flux surface. At about the same time Romanelli and Ottaviani investigated the consequences of this effect for Pfirsch-Schlüter regime transport [82]. Low field side accumulation of impurity ions, observed experimentally using soft X-ray tomography in ASDEX [83] and JET [84], and reconsidered theoretically by Wesson [85], causes neoclassical particle diffusivities to be enhanced, since they scale inversely with the square of the field. In the case of ASDEX the measured impurity density also exhibited a substantial up/down asymmetry in the grad-B and centrifugal drift directions [83]. Hsu and Sigmar [86] considered the

Pfirsch-Schlüter regime in a strongly rotating plasma and showed that up/down impurity density asymmetry can be driven by parallel (to the magnetic field) friction between bulk and impurity ions. Fülöp and Helander [87] examined neoclassical transport in rotating impure plasmas with steep temperature and density profiles, and found that the impurities can accumulate on the *inboard* (high field) side of a flux surface if the gradients are sufficiently large. Recently, Newton and Helander [88] have demonstrated that the poloidal redistribution of impurity ions in a rotating plasma can increase significantly neoclassical momentum transport.

In view of the substantial body of literature on collisional transport in rotating impure tokamak plasmas, it is worthwhile adopting a direct numerical approach to this problem. To this end we use `CUEBIT` to study the transport of carbon impurity ions in collisional MAST-like plasmas with and without toroidal flows. The Monte Carlo test particle method provides an alternative to the usual approach based on the drift kinetic equation: it does not yield analytical results, but it has the considerable advantage of requiring no approximations to be made apart from the test particle assumption. Thus, the collisionality regime of the trace minority ions, the profiles of the bulk plasma particles with which they are colliding, and the equilibrium magnetic configuration, can all be prescribed arbitrarily. Like experiments, test particle simulations can yield unanticipated results that stimulate further, analytical, investigation. Particle simulation techniques, generally based on the guiding-centre approach, have previously been employed to study neoclassical transport in the core [89,90], edge [91] and internal transport barrier [92] regions of tokamak plasmas. Lin and co-workers [89] carried out gyrokinetic particle simulations of subsonically-rotating large aspect ratio plasmas, finding approximate agreement with the toroidal flow enhancement of neoclassical heat transport predicted by Hinton and Wong [79]. In this Chapter we use our full orbit code to investigate collisional transport in the transonic, low aspect ratio regime.

6.2 Model

6.2.1 Equilibrium

The presence of transonic toroidal flows means that the inertial and pressure gradient terms in the MHD momentum balance equation are necessarily of comparable magnitude, and the Grad-Shafranov equation determining the equilibrium poloidal flux ψ must be generalised to describe such flows [93]. Savenko *et al.* [94] solved this generalised equation numerically for a set of MAST-like equilibria with essentially identical boundaries and toroidal Mach numbers in the plasma core M_φ ranging from zero up to and exceeding unity. It was found that the rotation produced an outward shift of the magnetic flux surfaces inside the plasma, although the shift was small: less than 4cm (around 6% of the plasma minor radius) at the magnetic axis for $M_\varphi = 1$. For simplicity, we neglect the relatively small effect of transonic toroidal flows on flux surfaces and use the same equilibrium for the stationary and rotating cases. Specifically, we use the following solution of the Grad-Shafranov equation for stationary plasma equilibria [21,22] introduced in Section 2.3 (Eq. 2.35):

$$\psi(R,Z) = \psi_0 \left\{ \frac{\gamma}{8} \left[(R^2 - R_0^2)^2 - R_b^4 \right] + \frac{1-\gamma}{2} R^2 Z^2 \right\}, \tag{6.1}$$

where the notation is identical to that introduced previously. The magnetic axis lies at $R = R_0$, $Z = 0$ and the inner and outer edges of the plasma in the midplane are located at $R = (R_0^2 \pm R_b^2)^{1/2}$. The parameter γ determines the plasma elongation, with $\gamma = 0.5$ giving flux surfaces that are circular in the large aspect ratio limit and $\gamma \to 1$ giving flux surfaces that are highly elongated in the vertical direction [22]. The plasma boundary is defined by $\psi = 0$. If the plasma current is taken to be in the negative φ direction then ψ_0 is positive and $\psi \leq 0$ throughout the plasma. As we saw in Chapter 2, the poloidal flux ψ is defined such that

$$\mathbf{B} = -\frac{1}{R}\frac{\partial \psi}{\partial Z}\mathbf{e}_R + B_\varphi \mathbf{e}_\varphi + \frac{1}{R}\frac{\partial \psi}{\partial R}\mathbf{e}_Z, \tag{6.2}$$

where B_φ is the toroidal field and $\mathbf{e}_R$, $\mathbf{e}_\varphi$, $\mathbf{e}_Z$ are unit vectors in a right-handed (R,φ,Z) coordinate system, with φ denoting toroidal angle. Equation 6.1 is a solu-

tion of the Grad-Shafranov equation if RB_φ is constant, which we again assume, for simplicity.

Although, as noted above, the effects of even transonic toroidal flows on flux surfaces are fairly modest when the plasma boundary is held fixed, force balance in the bulk ion and electron fluids requires the presence of an electric field which must be taken into account when computing particle trajectories. Taking the limit of vanishing electron mass, and assuming that electron temperature T_e and ion temperature T_i are both flux functions, Thyagaraja and McClements [95] showed that the electrostatic potential associated with purely toroidal rotation in a two-fluid plasma (i.e. a plasma with only trace quantities of impurity ions) is given by

$$\Phi = \Phi_0(\psi) + \frac{m_i T_e \Omega^2 R^2}{2e(T_e + T_i)}, \tag{6.3}$$

where e is proton charge, Φ_0 is a flux function, m_i is bulk ion mass, and Ω is the toroidal rotation rate. For simplicity we assume that the entire bulk plasma is rotating as a single rigid body, so that Ω is a constant. For the case of purely toroidal flows in the ideal MHD limit we have $\mathbf{E} + \mathbf{v} \times \mathbf{B} = \mathbf{0}$ where

$$\mathbf{E} = -\nabla\Phi = -\left(\mathbf{e}_R \frac{\partial\Phi}{\partial R} + \mathbf{e}_\varphi \frac{1}{R}\frac{\partial\Phi}{\partial\varphi} + \mathbf{e}_Z \frac{\partial\Phi}{\partial Z}\right) \tag{6.4}$$

is the electric field (in cylindrical coordinates) and $\mathbf{v} = \Omega R \mathbf{e}_\varphi$. In the axisymmetric tokamak we are considering $\partial\Phi/\partial\varphi$ is zero, and combining these equations with Eq. 6.2 gives

$$\frac{\partial\Phi}{\partial R} = \frac{v_\varphi}{R}\frac{\partial\psi}{\partial R}, \tag{6.5}$$

$$\frac{\partial\Phi}{\partial Z} = \frac{v_\varphi}{R}\frac{\partial\psi}{\partial Z}, \tag{6.6}$$

which, if $v_\varphi/R = \Omega$ is assumed to be uniform across the plasma, results in

$$\Phi = \Omega\psi. \tag{6.7}$$

Comparing Eqs. 6.3 and 6.7, we identify Φ_0 with $\Omega\psi$. The second term on the right hand side of Eq. 6.3, which can be regarded as a non-ideal correction term,

is required in order to maintain quasi-neutrality when, as a consequence of the centrifugal force associated with toroidal rotation, the electron and ion densities are not constant on a given flux surface [85]. Despite the fact that this term is invariably much smaller than the first term under tokamak conditions, it is essential to take it into account since it is not a flux function; the electric field is therefore not purely radial. The correction to the electric field produces a force in the inward major radial direction, thereby reducing the effect of the centrifugal force. Indeed, since the major radial component of the electric field is

$$E_R = -\frac{\partial \Phi}{\partial R} = -\Omega R B_Z - \frac{T_e}{T_i + T_e}\frac{m_i \Omega^2 R}{e}, \tag{6.8}$$

it follows that for the case of fully ionised impurities ($Z/A \simeq 1/2$ where Z, A denote impurity ion charge state and mass number) in deuterium plasmas with $T_i \simeq T_e$, the electric force associated with the ideal MHD-violating part of Eq. 6.8 is approximately equal to one half of the centrifugal force $m_Z \Omega^2 R$ on co-rotating impurity ions of mass m_Z. Wesson [85] showed that for a trace impurity species in a plasma with singly-charged bulk ions, the density distribution on a given flux surface is of the form

$$n_Z = n_{Z0} \exp\left[\left(1 - \frac{T_e}{T_i + T_e} Z \frac{m_i}{m_Z}\right) \frac{m_Z \Omega^2 R^2}{2 T_Z}\right], \tag{6.9}$$

where T_Z is impurity ion temperature and n_{Z0} is a constant for the flux surface in question; the impurity ion distribution across the entire plasma cross-section can be modelled using this expression if n_{Z0} is taken to be a flux function.

For the purpose of computing impurity ion trajectories we also take into account the presence of a toroidal electric field associated with the plasma loop voltage. This field crosses on the poloidal magnetic field to give an inward-pointing $\mathbf{E} \times \mathbf{B}$ flow that causes impurity accumulation in the plasma core even without rotation (the Ware pinch effect, discussed in Chapter 2). It is sufficient for our purposes to include a constant toroidal electric field directed in the plasma current direction, i.e. the negative φ direction. Under steady-state conditions the loop voltage V in MAST is typically a few volts [96]: we set $E_\varphi = V/2\pi R = 0.3 \mathrm{Vm}^{-1}$.

6.2.2 Treatment of collisions

As we saw in Section 3.4, the `CUEBIT` code can be extended in a straightforward way to include Coulomb collisions. We can extend to the case of a rotating plasma by adding to the Lorentz force a drag term, resulting from collisions with bulk ions whose average toroidal velocity $v_\varphi = \Omega R$ is nonzero, and a noise term that ensures relaxation of the test particle population to a (co-rotating) Maxwellian distribution whose temperature T is equal to that of the bulk ions. In the laboratory frame the Lorentz force equation then takes the form

$$m_Z \frac{d\mathbf{v}}{dt} = Ze(\mathbf{E} + \mathbf{v} \times \mathbf{B}) - \frac{m_Z}{\tau}(\mathbf{v} - v_\varphi \mathbf{e}_\varphi) + m_Z \mathbf{r}(t). \tag{6.10}$$

Here τ is the collision time (assumed to be velocity-independent) and $\mathbf{r} = (r_x, r_y, r_z)$ is a set of random numbers, chosen independently for each particle and at each time step, with zero mean and variance

$$\sigma^2 = \frac{u_i^2}{\tau \Delta t}, \tag{6.11}$$

where $u_i = (2T/m_Z)^{1/2}$ is the desired test particle thermal speed and Δt is the time step used in the code [35]. The presence of noise terms in the three components of Eq. 6.10 ensures that collisional pitch angle scattering is taken into account. For the case of counter-current rotation, produced in MAST by counter-current neutral beam injection, $v_\varphi > 0$. The drag term on the right-hand side of Eq. 6.10 ensures that after a sufficiently long time the minority ions acquire the same mean flow velocity as the bulk ions with which they are colliding, i.e. $v_\varphi \mathbf{e}_\varphi$. We neglect collisions of the test particles with electrons and beam ions.

For the case of test particles interacting with a Maxwellian distribution of field particles the collision time τ, often referred to as the *slowing-down time*, is given by the expression [62]

$$\frac{1}{\tau} = \left(1 + \frac{m_Z}{m_i}\right) \Psi(x) \nu_0, \tag{6.12}$$

where $x = m_i v^2 / 2T$ (with temperature T in units of keV), v being the test particle speed in the mean rest frame of the field particles, the function Ψ is given by

$$\Psi(x) = \frac{2}{\sqrt{\pi}} \int_0^x t^{1/2} e^{-t} dt, \tag{6.13}$$

and for singly-ionised field particles of density n

$$\nu_0 = \frac{Z^2 e^4 n \ln \Lambda}{4\pi \epsilon_0^2 m_Z^2 v^3}, \tag{6.14}$$

where ϵ_0 is the permittivity of free space and $\ln \Lambda$ is the Coulomb logarithm. We assume that the test particle mass m_Z is large compared with the bulk ion mass m_i; if the test particles are Maxwellian-distributed with temperature T, we can then take the limit $x \ll 1$, in which case

$$\Psi \simeq \frac{4}{3\sqrt{\pi}} \left(\frac{m_i}{2T}\right)^{3/2} v^3, \tag{6.15}$$

and Eq. 6.12 reduces to

$$\frac{1}{\tau} = \frac{m_i^{1/2}}{m_Z} \frac{Z^2 e^4 n \ln \Lambda}{6\sqrt{2}\pi^{3/2} \epsilon_0^2 T^{3/2}}. \tag{6.16}$$

6.2.3 MAST simulation parameters

Unless otherwise specified, the parameters used in our MAST simulations are those listed in Table 6.1. We computed the orbits of test particle carbon impurity ions for three particular scenarios: $\Omega = 0$, $\Omega = 2 \times 10^5$ rad s^{-1} (counter-current rotation) and $\Omega = -2 \times 10^5$ rad s^{-1} (co-current rotation). The bulk ion temperature and density profiles used in the simulations are listed in Table 6.2, some of which are plotted versus R in the midplane of the plasma in Figures 6.1 and 6.2. In each case n_1 and T_1 are the edge bulk ion density and temperature respectively. The parameters n_0 and T_0 denote constants that, together with n_1 and T_1, determine the central bulk ion density and temperature. The quantity ψ_1 is the poloidal flux at the magnetic axis. The exponential factor in the density profiles of models 4-6 is prompted by the well-known result that the bulk ion density on a flux surface that is rotating rigidly in the toroidal direction varies as [85]

$$n_i \sim \exp\left[\frac{m_i \Omega^2 R^2}{2(T_i + T_e)}\right]. \tag{6.17}$$

Table 6.1: Basic parameters used in MAST simulations

Quantity	Description	Value	Units
R_0	major radius	0.964	m
ψ_0	flux normalisation constant	0.9	Tm^{-2}
γ	plasma elongation constant	0.8	-
R_b	positive constant	0.93	m
Z	test particle charge state	6	-
Δt	timestep normalised to Larmor period	0.1	-
$\log \Lambda$	Coulomb logarithm	15	-
n_0	bulk ion density constant	5×10^{19}	m^{-3}
n_1	edge bulk ion density	10^{19}	m^{-3}
T_0	bulk ion temperature constant	1	keV
T_1	edge bulk ion temperature	0.1	keV

Table 6.2: MAST bulk ion temperature/density profiles

Model No.	Temperature profile	Density profile
1	$T_0\left(\psi/\psi_1\right)+T_1$	$n_0\left(\psi/\psi_1\right)+n_1$
2	$T_0\left(\psi/\psi_1\right)+T_1$	$n_0\left(\psi/\psi_1\right)^{1/2}+n_1$
3	$T_0\left(\psi/\psi_1\right)^{1/2}+T_1$	$n_0\left(\psi/\psi_1\right)+n_1$
4	$T_0\left(\psi/\psi_1\right)+T_1$	$\left[n_0\left(\psi/\psi_1\right)+n_1\right]\exp\left\{m_i\Omega^2(R^2-R_0^2)/4T\right\}$
5	$T_0\left(\psi/\psi_1\right)+T_1$	$\left[n_0\left(\psi/\psi_1\right)^{1/2}+n_1\right]\exp\left\{m_i\Omega^2(R^2-R_0^2)/4T\right\}$
6	$T_0\left(\psi/\psi_1\right)^{1/2}+T_1$	$\left[n_0\left(\psi/\psi_1\right)^{1/2}+n_1\right]\exp\left\{(m_i\Omega^2(R^2-R_0^2)/4T\right\}$

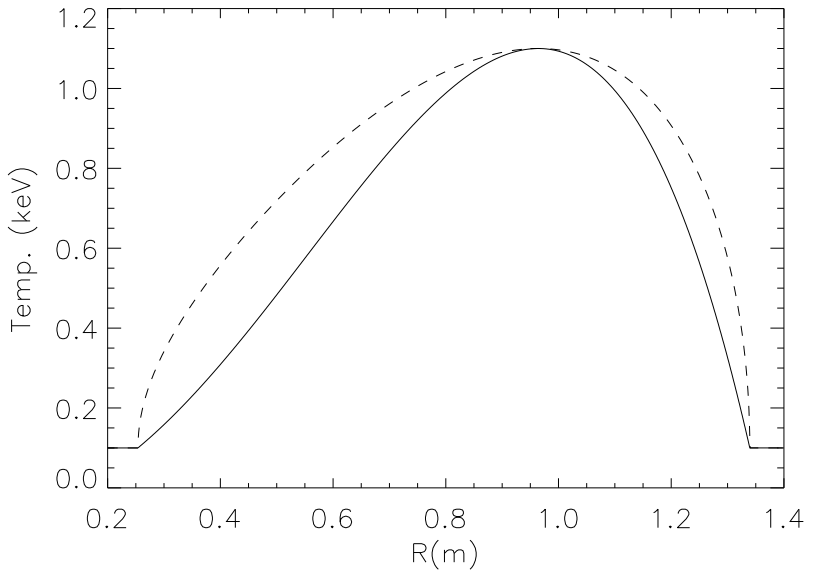

Figure 6.1: Temperature profile $T_0(\psi/\psi_1)+T_1$ (solid line) and $T_0(\psi/\psi_1)^{1/2}+T_1$ (dashed line) in the midplane of our MAST-like plasma.

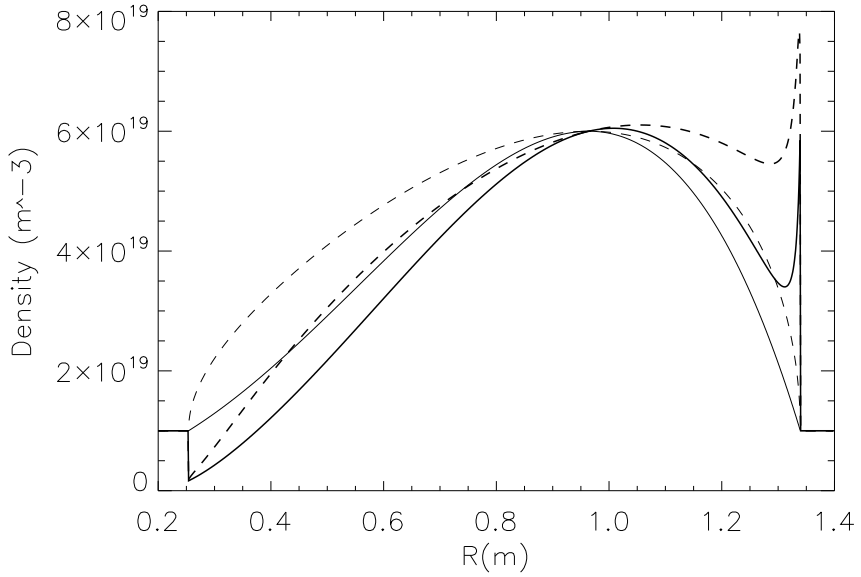

Figure 6.2: Density profiles corresponding to models 1 (faint solid line), 2 (faint dashed line), 4 (bold solid line) and 5 (bold dashed line) in the midplane of our MAST-like plasma.

We assume that $T_i = T_e \equiv T$: in the density profiles of models 4-6, T is given by the corresponding temperature profile in the second column of Table 6.2. The chosen dependence on ψ of the model profiles in Table 6.2 is motivated primarily by Thomson scattering measurements of electron temperature and density in MAST plasmas with co-current and counter-current NBI (Akers *et al.* [72]). In discharges

with co-current NBI, which have relatively low rotation rates, the density profile is typically rather broad while the temperature profile is strongly peaked at the magnetic axis. In contrast, discharges with counter-current NBI, and high (counter-current) rotation rates, tend to have peaked density profiles and broader temperature profiles. Although the various models listed in Table 6.2 are thus appropriate for different rotation scenarios, we have carried out simulations for every combination of profile model and rotation frequency, in order to separate effects arising purely due to rotation from those associated with the choice of profile. It should be noted that in models 4-6 the parameter n_1 is only equal to the bulk ion edge density at $R = R_0$.

6.3 MAST Simulation Results

6.3.1 Confinement of C^{6+} ions

In each simulation the orbits of 10^4 impurity ions, initially at rest at the magnetic axis ($R = R_0$) were computed for at least one confinement time (determined by the period taken for the number of confined ions to fall to $1/e$ of its initial value). Table 6.3 gives the confinement time obtained using `CUEBIT` for each model and rotation scenario.

Table 6.3: Computed confinement time of trace C^{6+} ions in MAST (ms)

Model No.	Stationary	Counter-rotating	Co-rotating
1	216.4	101.3	86.8
2	163.3	61.0	49.8
3	318.4	150.5	116.4
4	216.4	64.3	51.8
5	163.3	63.3	49.8
6	223.0	127.5	94.4

Before we discuss the results of Table 6.3, it is worth pointing out that, for the counter-rotating and co-rotating scenarios with model 2 profiles, a total of four in-

dependent simulations (each with 10^4 impurity ions) were carried out using different random number seeds in order to quantify the accuracy of the figures - the results of this are displayed in Table 6.4.

Table 6.4: Independent confinement times of C^{6+} ions for model 2 profile (ms)

Counter-rotating	Co-rotating
60.96	49.97
60.87	50.50
61.30	49.59
60.77	48.94

The standard deviations of these values were computed, and found to be 0.33% in the counter-rotation case and 1.15% in the co-rotation case. These figures are again broadly consistent with the expected noise level in simulations with 10^4 particles. Having established that the results are statistically significant, we can discuss their significance. Table 6.3 indicates that there is a strong dependence of confinement time on the temperature and density profiles of the bulk plasma: broadening the temperature profile for a given rotation scenario significantly increases the confinement time, while a broadening of the density profile generally degrades the confinement. Qualitatively, this trend is easily understood: since the central and edge temperatures are fixed, a broadening of the temperature profile makes the plasma on average less collisional, and hence increases the classical confinement time. A broadening of the density profile has the opposite effect.

For every profile model, the impurity ions are optimally confined when the plasma is non-rotating and least well-confined when it is co-rotating. The reduction in confinement in the rotating cases could be due either to the deconfining effect of centrifugal and $\mathbf{E} \times \mathbf{B}$ drifts, or an increase in neoclassical transport arising from the fact that the ions are displaced outward by the centrifugal force, encounter a lower magnetic field on average, and are thus subject to a higher neoclassical diffusion rate since this scales as r_L^2 [81]. To determine which of these mechanisms plays the dominant role, we plot in Figure 6.3 the positions of the ions inside the plasma in (R, Z) space at the end of the simulation for the cases (a) $\Omega = 0$, (b)

$\Omega = 2 \times 10^5$ rad s^{-1} and (c) $\Omega = -2 \times 10^5$ rad s^{-1}, using profile model number 1. The black curves tracing out sectors of the plasma boundary indicate the poloidal locations at which ions are lost from the system.

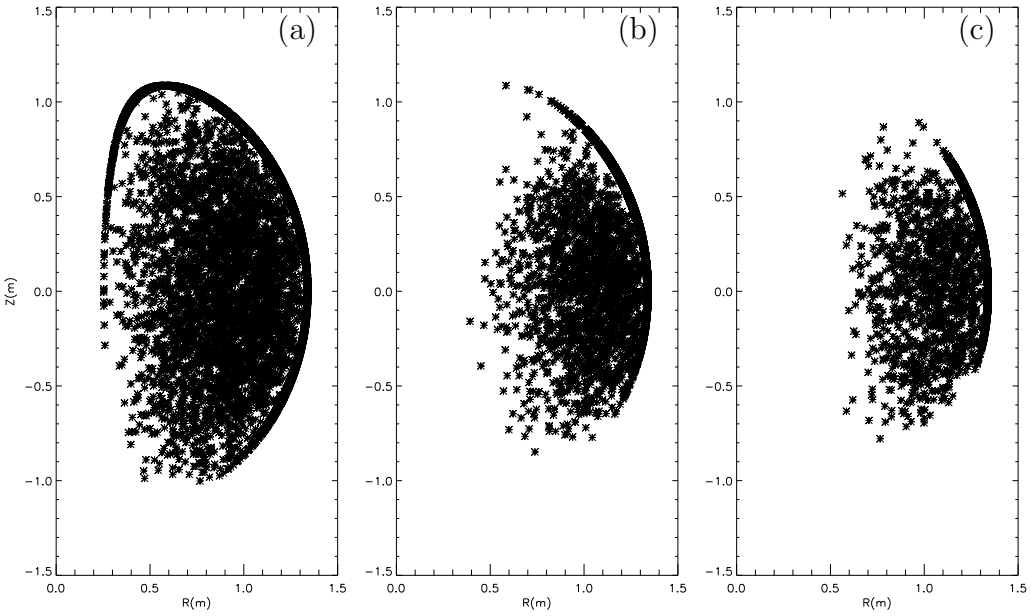

Figure 6.3: Distribution of final position of carbon impurity ions in (R, Z) plane for (a) $\Omega = 0$, (b) $\Omega = 2 \times 10^5$ and (c) $\Omega = -2 \times 10^5$ rad s^{-1}.

Comparing these plots, it is clear that the ions are indeed strongly displaced outboard by the net effect of the centrifugal force and the R-component of the electric field (as discussed earlier, the latter offsets the former to some extent). This suggests that our assumed profiles and parameters are such that the centrifugal effect discussed by Wesson [85] is dominant over the effect discussed by Fülöp and Helander [87] whereby steep density and temperature gradients can cause impurity ions to accumulate on the inboard side. In the counter-rotating case all of the impurity ion losses occur outboard of the magnetic axis; this is also true in the co-rotating case, with the losses concentrated in an even narrower range of poloidal angles. The fact that losses occur both above and below the midplane suggests that the confinement degradation in the rotating cases is due mainly to an enhancement in neoclassical transport, rather than being due to centrifugal and electric field modifications to the drift velocity, although in all cases there is a significant up-down asymmetry, suggesting that drifts are playing some role: most losses occur

above the midplane, and all the vertical drifts (grad-B, curvature, centrifugal and $\mathbf{E} \times \mathbf{B}$) are in the positive Z-direction. Reversing the sign of B_φ, we find in each scenario that the poloidal distribution of losses is an almost exact reflection in the midplane of that obtained in the $B_\varphi > 0$ case.

Plotting similar figures to 6.3 for the other profile models in Table 6.2 gives broadly similar results. The density profiles in the rotating cases look slightly odd because of the presence of a density "spike" near the outboard edge, caused by the fact that the temperature falls towards the outboard edge but the rotation rate does not, resulting in the exponential factor becoming large. This rather highlights a flaw with the rigid body rotation employed by our model and points to an area for improvement in future work (and will be briefly discussed in Chapter 7.2). Given that most of the particles are drifting in the vertical direction - either up or down, but mostly up, most particles are being lost from the vessel at values of R further inboard than where the density spike is located. However it is not the case for many particles, and the increased density of the pedestal may be acting as a barrier to particles escaping the plasma, resulting in the confinement times potentially being slightly overestimated in the cases of models 4 and 5, though as we aim to investigate the general trends and effects of varying the profiles, rather than trying to accurately model confinement times, this does not overly concern us. This possible overestimate of τ_c does not, however, change our belief that the centrifugal effect discussed by Wesson is dominant over the effect discussed by Fülöp and Helander for the cases of rotation given by profiles 4 and 5.

Another striking feature of the results listed in Table 6.3 is that confinement invariably deteriorates when, everything else being equal, the sign of rotation is changed from counter-current to co-current. This appears to be in qualitative agreement with visible bremsstrahlung data from rotating MAST plasmas [72], showing strong central peaking of effective charge (Z_{eff}) in the counter-rotating case, and also with much earlier experiments in the ORMAK [97] and PLT [98] tokamaks, indicating that a reversal in the direction of beam injection from co-current to counter-current, for a given level of beam power P_{NBI}, produced a higher flux of impurity radiation (because particles are not being lost so fast). Burrell *et al.* [99]

proposed that this result can be explained by effects arising purely from rotation, rather than the direct collisional interaction of impurity ions with the beam (we take the former but not the latter into account in our simulations). Specifically, Burrell *et al.* extended neoclassical theory to include the effects of inertial terms in the impurity ion momentum balance, which are important whenever the rotation velocity is comparable to or greater than the minority ion thermal speed, and found that co-rotation produces an outward radial particle flux while counter-rotation produces an influx.

It should be noted that the absolute rotation rates of counter-injected NBI plasmas generally differ from those of co-injected plasmas with the same P_{NBI}, and the plasma profiles are also dissimilar. Moreover the impurity sources tend to be different in the two injection scenarios, due to the fact that counter-injected ions are more likely to be lost promptly and cause sputtering from plasma-facing components [72]. Particular care is therefore required when comparing theory with experiment in this case. The results in Table 6.3 are consistent with the analysis in [99] insofar as they show that impurity ions undergoing purely collisional transport in co-rotating plasmas are significantly less well-confined than those in counter-rotating plasmas. However, in deriving their result Burrell *et al.* assumed large aspect ratio, circular cross-section geometry, subsonic rotation, and high (Pfirsch-Schlüter) impurity ion collisionality: none of these assumptions apply throughout the plasma in the simulations in Table 6.3.

6.3.2 Effect of ion charge state

It is also of interest to examine the dependence of the confinement time on the impurity ion charge state. The appearance of Z in the exponent on the right hand side of Eq. 6.9 indicates that the inboard-outboard asymmetry in the minority ion density is greatest for low charge states. In view of the transport enhancement mechanism identified by Helander [81], this suggests that singly-ionised carbon ions are likely to be less well-confined than C^{6+} ions in rotating plasmas. To test this hypothesis, we ran simulations similar to those carried out previously, utilising the same density and temperature profiles, but for singly-ionised rather than fully-ionised carbon

ions. We used two of the previously-introduced models for temperature and density, namely models 1 and 5: the results are shown in Table 6.5. It can be seen that the difference in confinement time between counter- and co-rotation is considerably more pronounced for C^+ ions than it is for fully-ionised carbon ions, with counter-rotation confining the ions for a time approaching almost double that of the co-rotation case. It is also interesting to note that changing the density/temperature profiles seems to have much less of an effect on singly-ionised ions than fully-ionised ones, particularly in the stationary and co-rotating cases.

Table 6.5: Confinement times of singly- and fully-ionised carbon ions (ms)

Model No.	Z	Stationary	Counter-rotating	Co-rotating
1	1	90.9	64.3	36.4
1	6	216.4	101.3	86.8
5	1	90.1	57.2	35.4
5	6	163.3	63.3	49.8

The reduction in confinement time brought about by changing Z from 6 to 1 is similar in the stationary and co-rotating cases, and greater than that found in the counter-rotating scenario. This suggests that the Z-dependence of the in-board/outboard impurity ion density asymmetry in a rotating plasma, given by Eq. 6.9, has little effect on confinement. Since both r_L^2 and τ scale as $1/Z^2$, the classical particle diffusivity given by Eq. 5.5 is independent of Z. However, whereas fully-ionised carbon ions are in the Pfirsch-Schlüter or plateau regimes across the greater part of the plasma in our simulations, C^+ ions are generally in the banana regime since they have a much lower collision frequency. For these ions the neoclassical enhancement of $D_\perp$ above the classical value is much greater than it is for C^{6+} (see Figure 2.13); this appears to account for the reduction in confinement times brought about by replacing $Z = 6$ with $Z = 1$. Examining individual particle trajectories helps make this point clearer. Figure 6.4 displays the full orbit of a C^+ ion in a co-rotating plasma with bulk ion profile model number 1. By plotting only every tenth timestep, we can more clearly resolve the large scale motions of this ion, which we show in Figure 6.5, along with the orbit of a fully-ionised carbon impurity ion in

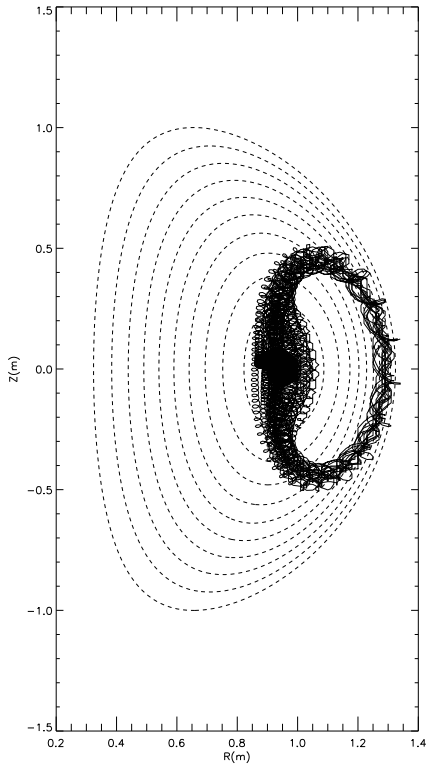

Figure 6.4: Fully resolved orbit of a C^+ impurity ion in co-rotating plasma with bulk ion profile number 1, launched from magnetic axis and simulated for approximately 1.8 milliseconds.

a co-rotating plasma in order to compare the two. We see that, once the C^+ ion has migrated out of the core of the plasma, it quickly begins to undergo wide banana orbits which take it very close to the plasma edge. The C^{6+} impurity ion does not execute wide banana orbits, but instead is slowly deflected by collisions across flux surfaces. The simulation time of each carbon ion in Figure 6.5 is rather arbitrary, and primarily designed to show how the C^+ ion diffuses across the flux surfaces to the outboard edge much quicker than the C^{6+} ion (although the actual confinement times of both are comparable to those given in Table 6.5). Similar behaviour is also observed in the counter-rotating case (Figure 6.6).

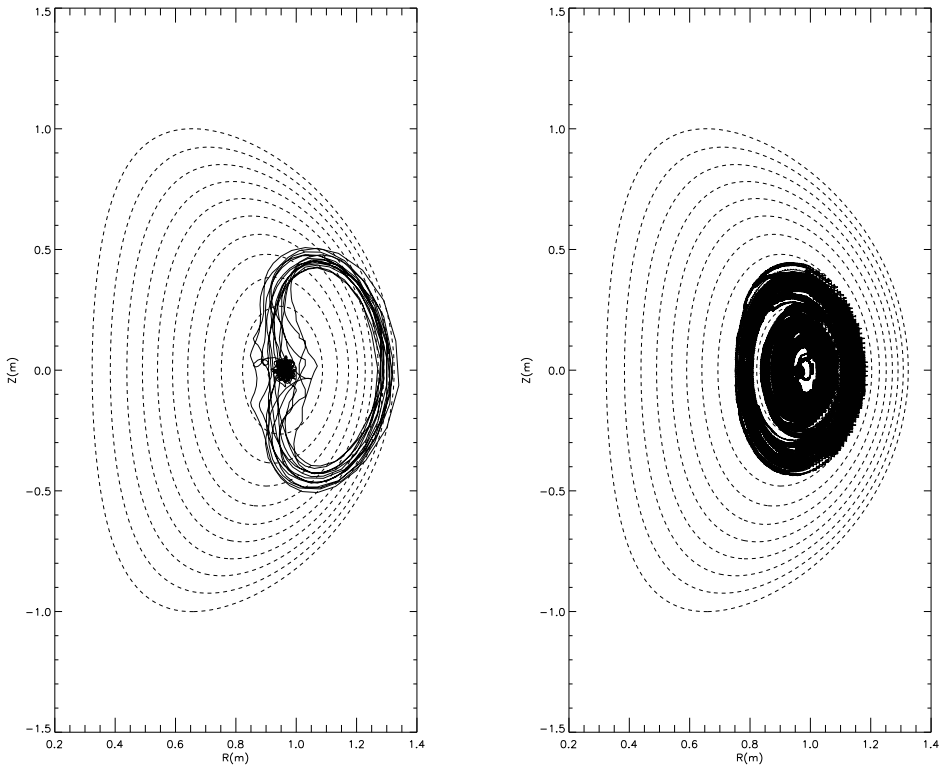

Figure 6.5: Comparison of orbits of C^+ (left) and C^{6+} (right) impurity ions in co-rotating plasma with bulk ion profile number 1, launched from magnetic axis and simulated for approximately 1.8 and 10 milliseconds respectively.

As we noted above the difference in confinement time τ_c between the 2 rotation scenarios was more pronounced for singly-ionised ions. This may be because the less-collisional C^+ ions are more affected by the radial electric field, which is directed inwards towards the plasma core in the counter-rotating case and outwards towards the plasma edge in the co-rotating case, and so smaller banana orbit "arcs" are produced in the co-rotating case. Comparing the orbits shown in the left-hand panels of Figures 6.5 and 6.6 we see that the C^+ ion in the co-rotating plasma is initially more deeply trapped, i.e. it spends very little time inboard of the magnetic axis, unlike the ion in Fig 6.6, the counter-rotating case, which clearly spends a sizeable proportion of its lifetime on the inboard side of the tokamak (noting, of course, that the timescales on both plots are not the same, but that the orbit of the C^+ ion in the co-rotating plasma does not exhibit any significantly different behaviour in the remaining course of its orbit). However it should be noted that this behaviour is not necessarily typical for C^+ ions in a counter-rotating plasma, as

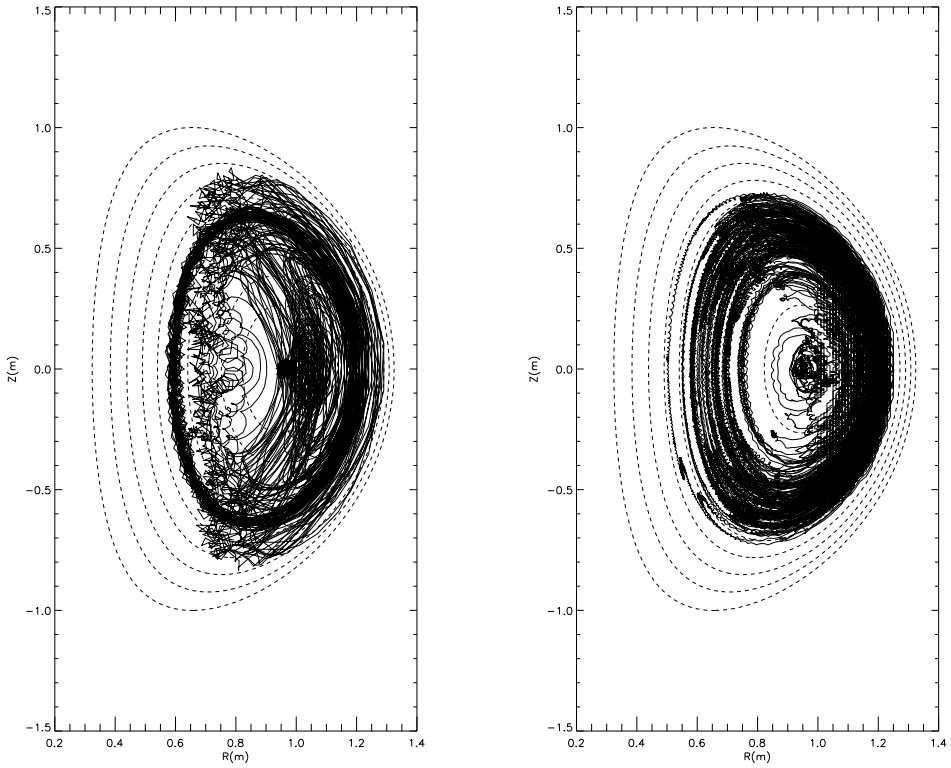

Figure 6.6: Comparison of orbits of C^{+} (left) and C^{6+} (right) impurity ions in a counter-rotating plasma with bulk ion profile number 1, launched from magnetic axis and simulated for approximately 15.7 and 32.2 milliseconds respectively.

illustrated by Figure 6.7. The C^{+} ions travel down a potential well towards the edge of the plasma in the co-rotating case and are lost much faster than ions of the same species in the counter-rotating plasma. The C^{6+} ions are more collisional and this additional effect is likely to be much less significant for them. In practice, given that the ionisation potential of C^{+} is around 24 eV, and the collision timescale is short, such ions are unlikely to exist in this ionisation state for long in MAST plasmas with core temperatures of around 1 keV.

6.3.3 Effect of toroidal rotation velocity

So far we have considered only the case in which the toroidal rotation speed is approximately equal to the local sound speed of the plasma, i.e. $M \sim \mathcal{O}(1)$. It is useful to consider also the case of subsonic rotation, so that the sensitivity of the results to M can be assessed. Table 6.6 lists computed confinement times for

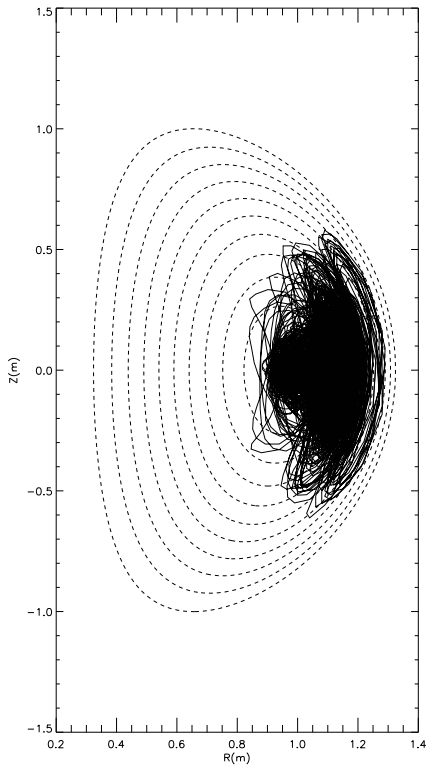

Figure 6.7: Orbit of a second C^+ ion in a counter-rotating plasma with bulk ion profile number 1, launched from the magnetic axis and simulated for approximately 24 milliseconds. This impurity spends considerably less time inboard of the magnetic axis than the ion in the left panel of Figure 6.6.

profile models 1 and 5 when the toroidal Mach number at the magnetic axis is 0.1; for comparison, the corresponding results obtained for stationary plasmas are also listed. As expected, reducing the toroidal rotation velocity of the plasma increases the confinement time of the carbon impurity ions, as centrifugal effects become less important. In this case the rotation causes only a very modest degradation in confinement and there is no significant difference between the results for counter- and co-rotation. This is to be expected if the dominant reason for the increase in transport in the rotating case is that identified by Helander [81], namely the peaking of impurity ion density on the low field side of the tokamak: for the case of fully ionised carbon in a deuterium plasma with $T_e = T_i = T_Z$ the argument of the exponential factor producing the density peaking is equal to $3M^2$ [cf. Eq. 6.9].

Table 6.6: Confinement times of C^{6+} ions in plasmas with $M = 0.1$ at $R = R_0$ (ms)

Model no.	Stationary	Counter-rotating	Co-rotating
1	216.4	211.1	212.1
5	163.3	161.6	158.4

6.3.4 Effect of ion mass

Having experimented with changing the charge state of the carbon impurity ions, we now consider a much heavier impurity: although for fully-ionised ions the ratio of m_i/m_Z is approximately constant with increasing Z, the extra factor of m_Z in the exponent on the right hand side of Eq. 6.9 indicates that the inboard-outboard asymmetry in the minority ion density will be greater for heavier impurities, and the mechanism proposed by Helander then suggests that heavier ions are likely to be significantly less well-confined than lighter ions in rotating plasmas. Thus it is of interest to perform similar simulations for an impurity such as fully-ionised tungsten (W), with $Z = 74$, $A = 184$ (the most common isotope of tungsten), which as we noted in Chapter 2 is intended for use in the divertor region of tokamak devices. We simulate fully-ionised tungsten even though strictly speaking the temperatures in our MAST-like simulations are far below those required to strip all the electrons away from the nucleus: however, we can still learn some useful things by considering this case. Table 6.7 shows the confinement times for tungsten ions launched from the magnetic axis at rest in the usual cases of transonic rotation, using density profile model number 1, and Figure 6.8 shows the spatial distribution of ions at the end of the simulation.

Table 6.7: Confinement times of W^{74+} ions (ms)

Model no.	Stationary	Counter-rotating	Co-rotating
1	321.6	5.8	5.2

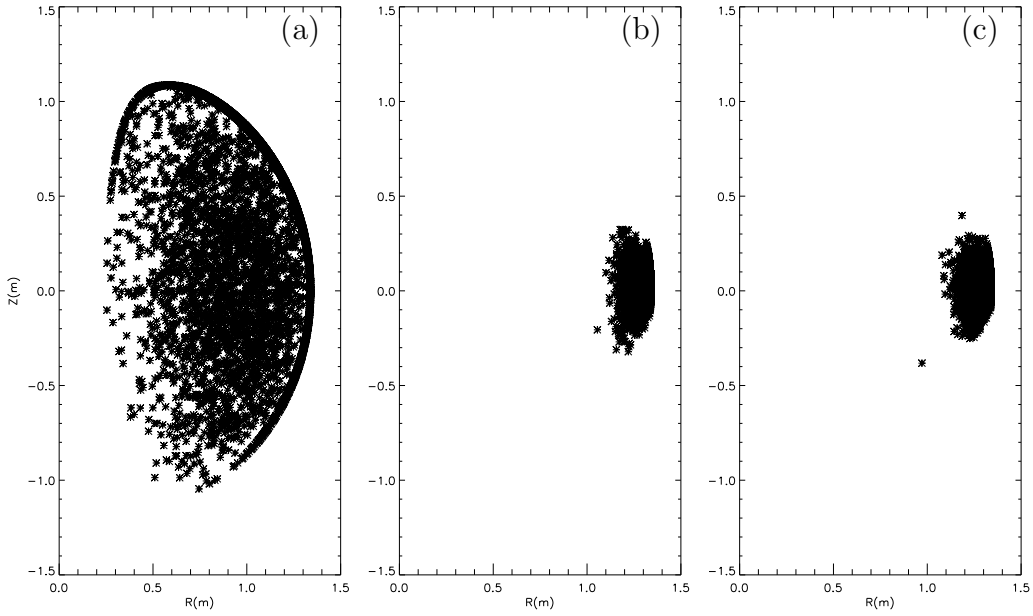

Figure 6.8: Distribution of tungsten impurity ions in (R, Z) plane for (a) $\Omega = 0$, (b) $\Omega = 2 \times 10^5$ and (c) $\Omega = -2 \times 10^5$ rad s^{-1}.

We see that the heavier W ions are confined in rotating plasmas for a significantly shorter period than the C ions. In the case of a stationary plasma, the confinement times suggest the opposite is true: tungsten ions are more well-confined. Additionally, the difference between the confinement times for rotating and non-rotating cases is much larger for tungsten than carbon. The difference in τ_c between the cases of co- and counter-rotation appears to be reduced to virtually nothing: if the ions are confined for such a short time, the centrifugal force dominates the radial electric field terms (compare the orbits of two individual ions, as seen in Figure 6.9) and hence there is little effect in changing the direction of the rotation. This is also illustrated in the plots of poloidal losses - the 2 panels (b) and (c) in Figure 6.9 are virtually identical. It is also interesting to note that the up-down asymmetry in the losses appears to be much reduced (if not negligible) in comparison with the case of carbon impurity ions.

These results can be understood as follows. Via collisions, the W^{74+} ions in the rotating plasmas are forced to co-rotate with the bulk plasma ions at a velocity v_φ that is considerably larger than the thermal speed of tungsten. The ions are confined to the outer midplane of MAST by an extreme version of the centrifugal effect

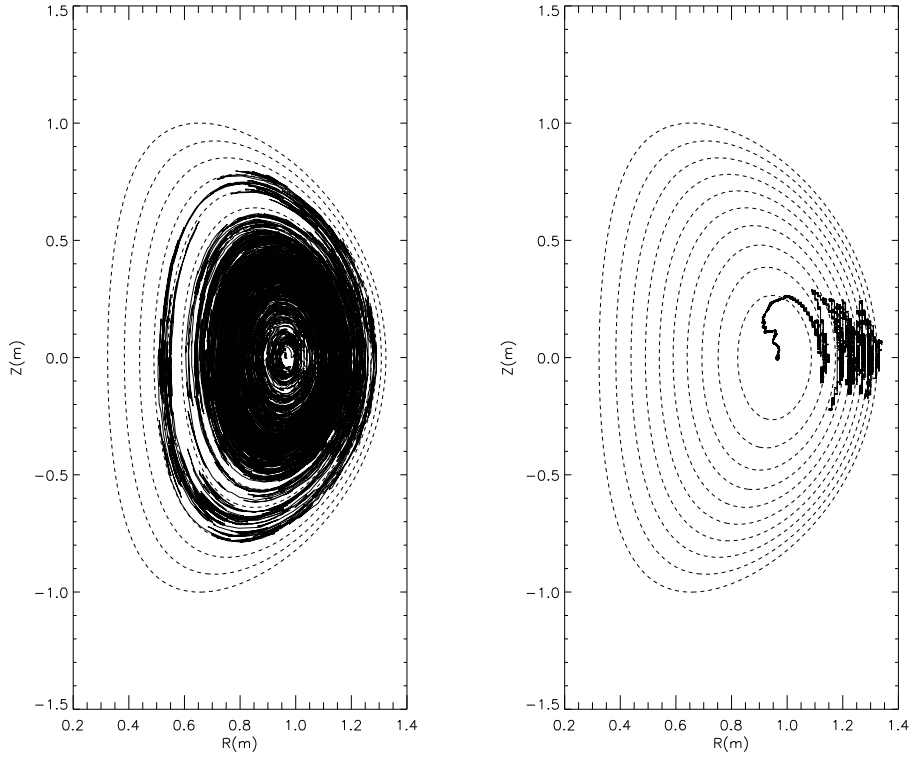

Figure 6.9: Comparison of orbits of W^{74+} impurity in stationary plasma (left) and co-rotating plasma (right), launched from magnetic axis and simulated for approximately 367 and 3.1 milliseconds respectively.

identifed by Wesson [85] (see Eq. 6.9). The particle diffusivity $D_\perp$ appears to scale approximately as the mass of the impurity m_Z, and the confinement time is correspondingly reduced. There are also indications that the diffusivity is independent of the charge Z: simulating 10^4 W^+ ions in a counter-rotating MAST-like plasma for the same model of temperature and density profile as that used in the case of fully-ionised tungsten (model number 1) gives a confinement time of 5.2ms, only slightly lower than the figure obtained for fully-ionised tungsten. It is not entirely clear why the diffusivity should scale with ion mass but, in view of the fact that the tungsten ions are rotating hypersonically in this regime, one might reasonably expect inertial forces (in particular the centrifugal force) to play an important role in determining the confinement time.

This result has significant implications for fusion reactors, since, as discussed in Chapter 2, tungsten has become the material of choice for the plasma divertor. Our simulations indicate that rotating, tight aspect ratio plasmas such as MAST are

highly efficient at expelling very high mass impurities, irrespective of whether the rotation is co-current or counter-current. This is particularly noteworthy in terms of maintaining the purity of a fusion plasma.

6.4 Discussion and Conclusions

We have employed a full orbit test particle code to investigate the collisional transport of both carbon and tungsten impurity ions in ST (MAST-like) plasmas with transonic and subsonic toroidal flows, both counter-current and co-current. We have demonstrated that counter-current transonic rotation causes a substantial reduction (by a factor of two or more) in the collisional confinement time of the carbon ions; subsonic rotation has been shown to cause only a slight drop in the confinement time. This behaviour can be attributed principally to the fact that the collisional diffusivity of impurity ions exceeds its flux surface-averaged value, the reason for this being that the ions are displaced outward from the tokamak symmetry axis by the net effect of centrifugal and electric field forces [81]. For a range of temperature and density profile models, we have shown that, for carbon ions, reversing the direction of rotation from counter-current to co-current causes a further significant reduction in the confinement time. Reducing the charge state of the carbon ions from 6 to 1 also causes a large drop in the confinement time, although this appears to be due mainly to the relatively low collisionality of C^+ ions rather than any effect associated specifically with rotation. In the cases of carbon impurity ions that we have studied, there is an up/down asymmetry in the losses that reflects the direction of the net vertical drift of the impurity ions, though this asymmetry is not seen for much heavier impurities. Increasing the mass of the impurity causes further significant drops in confinement time in rotating cases, though improves confinement in non-rotating plasmas.

Our results indicate that the removal of impurity ions is favoured by the use of co-current (rather than counter-current) NBI, as suggested by neoclassical theory in the large aspect ratio, Pfirsch-Schlüter, subsonic limit [99] and by measurements of impurity radiation from several past and present tokamaks [72,97,98]. However,

although the diffusivity increases, the effect of reversing rotation direction decreases with increasing impurity ion mass. We stress, though, that care should be taken to avoid simplistic comparisons with experimental data. Apart from the differences, noted previously, in the rotation rates, profiles and impurity sputtering rates of plasmas heated by co-NBI and counter-NBI, there is the important caveat that, except in the vicinity of transport barriers, impurity ions undergo turbulent as well as collisional transport. Indeed, the fact that relatively long energy confinement times have been achieved in MAST discharges with transonic counter-rotation [72] despite a predicted enhancement in neoclassical transport [81] illustrates the importance of non-collisional processes in determining tokamak plasma confinement. Notwithstanding the difficulties of making contact with experimental data, our results show that test particle simulations have a useful role to play in illuminating the physics of collisional transport in tokamak plasmas in regimes that are not easily accessible to analytical description.

"Early to rise and early to bed
Makes a man wise but socially
dead"

The Animaniacs

Chapter 7

Future Work

The CUEBIT code is extremely versatile, as we have already demonstrated by studying in detail a problem in solar astrophysics and another in fusion plasma physics. There are several other potential applications of the code, both extensions of what we have previously done and also new avenues of interest, that would be potentially fruitful to investigate. In this chapter we briefly examine a few of these, laying the possible groundwork for future research.

7.1 Fast Alfvén Wave Heating

7.1.1 Alternative wave profiles

In Chapter 4 we considered two perturbations: one with both inward- and outward-propagating components and one with only inward-propagating waves. If instead we had only outgoing waves (which might physically correspond to a situation in which reconnection occurring close to the null is generating fast waves which propagate out from that point) and if the initial perturbation consisted of a series of harmonics

$$\frac{\partial \psi}{\partial r} = \sum_{n=1}^{\infty} A_n \sin(n\pi r), \tag{7.1}$$

where, for example, the coefficients A_n could be chosen to have a power-law depen-

dence on the integer n, i.e.

$$A_n = A_0 n^{-\alpha} \tag{7.2}$$

where A_n and α are constants, with $\alpha > 0$ (this choice ensures that the series converges), as opposed to having a single Fourier harmonic $\partial\psi/\partial r = \sin(\pi r)$, then the solution becomes

$$\psi = -\frac{1}{\pi}\sum_{n=1}^{\infty}\frac{A_n}{n}\cos\left(n\pi r e^{-t}\right) = -\frac{1}{\pi}\cos\left(\pi r e^{-t}\right) \tag{7.3}$$

if we take $A_1 = 1$, and just keep the $n = 1$ term. Thus the corresponding electric field term would be

$$E_z = -\frac{\partial\psi}{\partial t} = r e^{-t}\sin\left(\pi r e^{-t}\right) \tag{7.4}$$

which means that the electric field is positive for all time t throughout the solution domain ($r \leq 1$), like the localised perturbation discussed in Chapter 4. Additionally, the advantage of this type of solution is that, with no inward-propagating waves the solution does not become steeper after $t = 0$ and thus the linearisation condition will remain valid for all time provided that it is satisfied at $t = 0$.

As discussed in Chapter 4, Miller and co-workers [55] argued that particles can be efficiently accelerated to high energies by a spectrum of fast waves with a range of values of $k_\parallel/k$ where $k_\parallel$ is the wave vector component parallel to the equilibrium magnetic field. The general wave-particle resonance condition is

$$\omega - k_\parallel v_\parallel - l\Omega/\gamma = 0, \tag{7.5}$$

where ω is the wave frequency, Ω is the particle gyrofrequency, γ is the particle Lorentz factor and l is an integer. Because we are considering Alfvénic waves at frequencies well below the ion cyclotron frequency, the only resonance we are likely to satisfy is $l = 0$, i.e.

$$v_\parallel = \frac{k}{k_\parallel}c_A \tag{7.6}$$

where c_A is the local Alfvén speed. A spectrum of waves could allow a particle to undergo a random walk in velocity space, resonating with different waves and, in some cases, being accelerated to high velocities.

An alternative solution that is well-behaved in the limit $r \to 0$ could be given by

$$\psi = r^2 e^{-2t}, \tag{7.7}$$

which is obtainable from the solution for outward radially-propagating wave (i.e. Eq. 4.25 with $f = 0$) by imposing the initial condition $\psi = r^2$. The electric field is then given by

$$E_z = -\frac{\partial \psi}{\partial t} = 2r^2 e^{-2t} \tag{7.8}$$

which is again positive definite for all t and thus could be expected to produce effective acceleration. It would be of interest to model perturbations of this type within `CUEBIT`.

Further, an oscillatory solution describing waves that propagate in different directions at any given point in space could also be constructed. The global and localised fast wave solutions we employed in Chapter 4 were based on the assumption that the perturbation to ψ is azimuthally symmetric. However, if we relax that assumption, while continuing to assume invariance in the longitudinal (z) direction, the wave equation becomes

$$\frac{\partial^2 \psi}{\partial t^2} = r \frac{\partial}{\partial r}\left(r \frac{\partial \psi}{\partial r}\right) + \frac{\partial^2 \psi}{\partial \varphi^2} = \frac{\partial^2 \psi}{\partial x^2} + \frac{\partial^2 \psi}{\partial y^2} \tag{7.9}$$

where $x = -\ln r$. We could seek solutions of this 2D wave equation satisfying both a periodic boundary condition in φ

$$\psi(t, r, \varphi + 2\pi) = \psi(t, r, \varphi) \tag{7.10}$$

as well as the condition

$$\frac{\partial \psi}{\partial r} \to 0 \tag{7.11}$$

in the limit $r \to 0$ (in order to guarantee that the linear approximation remains valid, and that ψ is regular in this limit) and use `CUEBIT` to see how bulk protons are energised by a non-azimuthally symmetric wave perturbation.

7.1.2 Inertial Alfvén wave acceleration of electrons

It has been proposed that electrons can be effectively accelerated in the Earth's auroral zones by *inertial Alfvén waves* (IAW's) [100], as these waves have a component of electric field that is parallel to the ambient magnetic field. IAW's are low-frequency ($\omega < \Omega$) dispersive Alfvén waves in a medium where the thermal velocity of electrons is less than the Alfvén speed v_A, and as such appear in low-beta plasmas when $\beta < m_e/m_i$ (for a review of dispersive Alfvén waves see e.g. Stasiewicz and co-workers [101]). In such a plasma the electron inertia becomes important in driving the parallel electric field, which in turn can accelerate particles by a number of different mechanisms such as bounce or Landau resonance.

Such waves have recently been considered in the context of solar flares, in order to explain the observed electron acceleration there. For example, Fletcher and Hudson [102] propose that the large-scale motion of plasma due to reconnecting fields relaxing to a state of lower magnetic stress will result in an amalgamation of many propagating MHD wave modes carrying energy along the field lines. In their model a reconfiguring coronal field launches a torsional Alfvén wave down towards the loop footpoints and into the chromosphere, offering two possible acceleration mechanisms. In the first instance the Alfvénic perturbation accelerates electrons by resonant interactions (the wave, travelling downwards through the loop, accelerates electrons as it propagates). The wave front, converging towards the chromosphere, may reflect and accelerate electrons multiple times, in a first-order Fermi acceleration process, up to energies estimated to be of the order of a few tens of keV. Additionally, when the torsional mode reaches the chromosphere it is expected that some of the energy will be transmitted and damped, leading to stochastic acceleration via a turbulent cascade of fast-waves that were mode-converted in the chromosphere. Some of the Alfvén wave energy would be expected to be reflected back up into the corona.

Bearing the above work in mind, it would be of interest to simulate electron

acceleration by IAW's in the solar corona by using the `CUEBIT` code, which is well-suited to this type of problem. To do this would require the appropriate electric and magnetic fields to be derived from Maxwell's equations and the relevant fluid equations, including the generalised Ohm's law in the limit of zero pressure and resistivity (i.e. Eq. 4.57 without the ∇p_e and η terms).

7.2 Impurity Transport in Tokamaks

7.2.1 Impurity density radial profiles

It would be useful, as well as determining the confinement times of impurity ions in tokamaks, to also determine the impurity density and the flux surface-averaged effective charge state (Z_{eff}) profiles across the radial extent of the plasma. In order to do this, we need to compute the volume enclosed by a specified range of flux surfaces in the Freidberg equilibrium that we employ in our model, given by Eq. 6.1.

Given a specified range of values of ψ, e.g. $\psi_1 \rightarrow \psi_1 + \Delta\psi$, we need to know the corresponding volume V in real space. If we transform (x, y) to (R, φ) and invoke toroidal symmetry by integrating over toroidal angle φ, formally we have

$$V = 2\pi \iint R dR dZ \tag{7.12}$$

To compute this double integral over the required region of (R, Z) space we transform the integration variables from (R, Z) to (ψ, θ), where θ can be arbitrarily defined so long as the Jacobian of the transformation $(R, Z) \rightarrow (\psi, \theta)$ is finite on the integration domain. An appropriate choice is $\theta = \tan^{-1}(Z/(R - R_0))$, allowing us to then write

$$V = 2\pi \int_{\psi_1}^{\psi_1+\Delta\psi} \int_0^{2\pi} R \frac{\partial(R, Z)}{\partial(\psi, \theta)} d\psi d\theta \tag{7.13}$$

Evaluating $\partial(\psi, \theta)/\partial(R, Z)$ we find that

$$R\frac{\partial(R, Z)}{\partial(\psi, \theta)} = \frac{2R[(R - R_0)^2 + Z^2]}{\psi_0 \left[\gamma R(R - R_0)^2(R + R_0) + 2(1 - \gamma)R(2R - R_0)Z^2\right]} \tag{7.14}$$

The quantity on the right hand side of Eq. 7.14 is not uniquely defined at the magnetic axis, $R = R_0, Z = 0$. We can avoid this problem by simply excluding from the ψ integration domain a small region close to the axis. Now we need to express the integrand as a function of ψ and θ. To solve this problem, we note that $Z = (R - R_0)\tan\theta$, so that on a given flux surface ψ

$$g(R) \equiv \psi - \psi_0 \left\{ \frac{\gamma}{8} \left[(R^2 - R_0^2)^2 - R_b^4 \right] + \frac{1-\gamma}{2} R^2 (R - R_0)^2 \tan^2\theta \right\} = 0 \qquad (7.15)$$

where θ is to be regarded as having a specified value. Eq. 7.15 can be solved numerically for R using Newton's method: if R_i is an estimate of the required root, an improved estimate R_{i+1} is given by a first order Taylor expansion of the function g about that point:

$$g(R_{i+1}) \simeq g(R_i) + (R_{i+1} - R_i) g'(R_i) \simeq 0 \qquad (7.16)$$

Thus

$$R_{i+1} = R_i - \frac{g(R_i)}{g'(R_i)}. \qquad (7.17)$$

The only remaining problem is to find a first estimate of the root R_1. It is sufficient for this purpose to take the large aspect ratio limit of Eq. 6.1, which means that we make the approximation $R \simeq R_0$ except in the factor $R - R_0$. Thus, we have

$$\psi \simeq \frac{\psi_0}{2} \left\{ \gamma \left[R_0^2 (R - R_0)^2 - \frac{R_b^4}{4} \right] + (1-\gamma) R_0^2 (R - R_0)^2 \tan^2\theta \right\} = 0 \qquad (7.18)$$

This equation can be solved for R to give

$$R = R_0 \pm \left(\frac{2\psi/\psi_0 + \gamma R_b^4/4}{\gamma R_0^2 + (1-\gamma) R_0^2 \tan^2\theta} \right)^{1/2} \qquad (7.19)$$

The choice of plus or minus in this equation depends on whether R lies outboard ($R > R_0$) or inboard ($R < R_0$) of the magnetic axis, which in turn is determined by whether θ lies in the range $[-\pi/2, \pi/2]$ or $[\pi/2, 3\pi/2]$. Eq. 7.19 provides a reasonably accurate first estimate of R; the iteration scheme represented by Eq.

7.17 then provides rapid convergence to the exact root. Having determined R in this way, we can then determine Z, and evaluate the integrand in the double integral using Eq. 7.14.

To determine profiles, one can then calculate the number of impurity ions within a set range of ψ to $\psi + \Delta\psi$ and convert this to give the impurity number density of a given region in ψ. We then evaluate Z_{eff} for a deuterium plasma containing only carbon impurities, through the equation [20]

$$Z_{\text{eff}} = \frac{\sum_j n_j Z_j^2}{\sum_j n_j Z_j}. \tag{7.20}$$

Since $\sum_j n_j Z_j = n_D Z_D + n_C Z_C$, where n_D is the density of deuterium and n_C the density of carbon, and $Z_D = 1$, $Z_C = 6$ for a deuterium plasma in which the carbon impurity ions are fully-ionised, then

$$Z_{\text{eff}} = \frac{1 + 36 n_C/n_D}{1 + 6 n_C/n_D} \tag{7.21}$$

Strictly speaking, the test particle assumption requires that $Z n_C \ll n_D$, so that the C^{6+} ions do not contribute significantly to the quasi-neutrality of the plasma. It is of course necessary to scale up the number of particles in the simulation to obtain a realistic impurity ion density. To do this, we infer the value of n_C/n_D by using measured values of Z_{eff} in MAST experiments, such as those described by Akers *et al.* [72] (see Figure 3 of this paper). That paper shows the Z_{eff} profile of MAST counter-NBI shot no. 8322, in which the core density was measured to be about 5×10^{19} m^{-3}. It is worth pointing out that values of $Z_{\text{eff}} \sim 2 - 3$ are typical for MAST counter-NBI heated discharges (though co-NBI discharges generally have much lower values of $Z_{\text{eff}} \sim 1$). We can determine Z_{eff} as a function of time and space by running our simulation and normalising the results by setting Z_{eff} equal to a particular value at one time and one point in space. If we set $Z_{\text{eff}} = 3$ at the magnetic axis, then $n_C/n_D \simeq 0.1$, and the test particle assumption is no longer strictly valid as $Z n_C \simeq n_D$, though it is informative to do so anyway as long as we bear in mind the idealised nature of the calculation. This provides results that can be compared directly with measured Z_{eff} profiles obtained from visible bremsstrahlung

data (see e.g. [103]). This process can be carried out at regular intervals throughout a given simulation, to illustrate the temporal evolution of Z_{eff}, or instantaneous snapshots of the Z_{eff} profiles can be plotted which may then be compared directly with experimental data.

Figure 7.1 displays some plots of Z_{eff} for C^{6+} ions in the counter-rotating scenario with bulk ion density profile model 2, splitting the total simulation time into 10 evenly-spaced time bins, although we only plot 6 of them here. The 6 panels show distributions corresponding to simulation times of $t = 0 - 30$ milliseconds at 6ms intervals. The radial extent of the plasma has been arbitrarily divided up into 250 "bins" - more or less bins can be used depending on the statistics of the particle distribution. The results are symmetric around the magnetic axis by design. These plots do not closely resemble the Akers experimental data: this is to be expected as they show the radial migration of a concentration of impurities from the magnetic axis out towards the plasma edge. The $t = 0$ plot differs from the prescribed initial delta-function only because of the finite size of the radial bins employed. It is worth pointing out as well that, to maximise particle statistics we count all the particles in a given shell of flux surfaces, whereas the Thomson scattering profiles typically show profiles in the midplane, and that to generate profiles that could be compared with experiment we would also need to include a continuous particle source and perhaps ionisation/recombination effects. However, now that the means of doing this have been established, incorporating more experimentally-relevant physics into the `CUEBIT` code (as will be discussed in the next subsection) and analysing the results this way would be a useful tool for studying test particle transport in tokamaks.

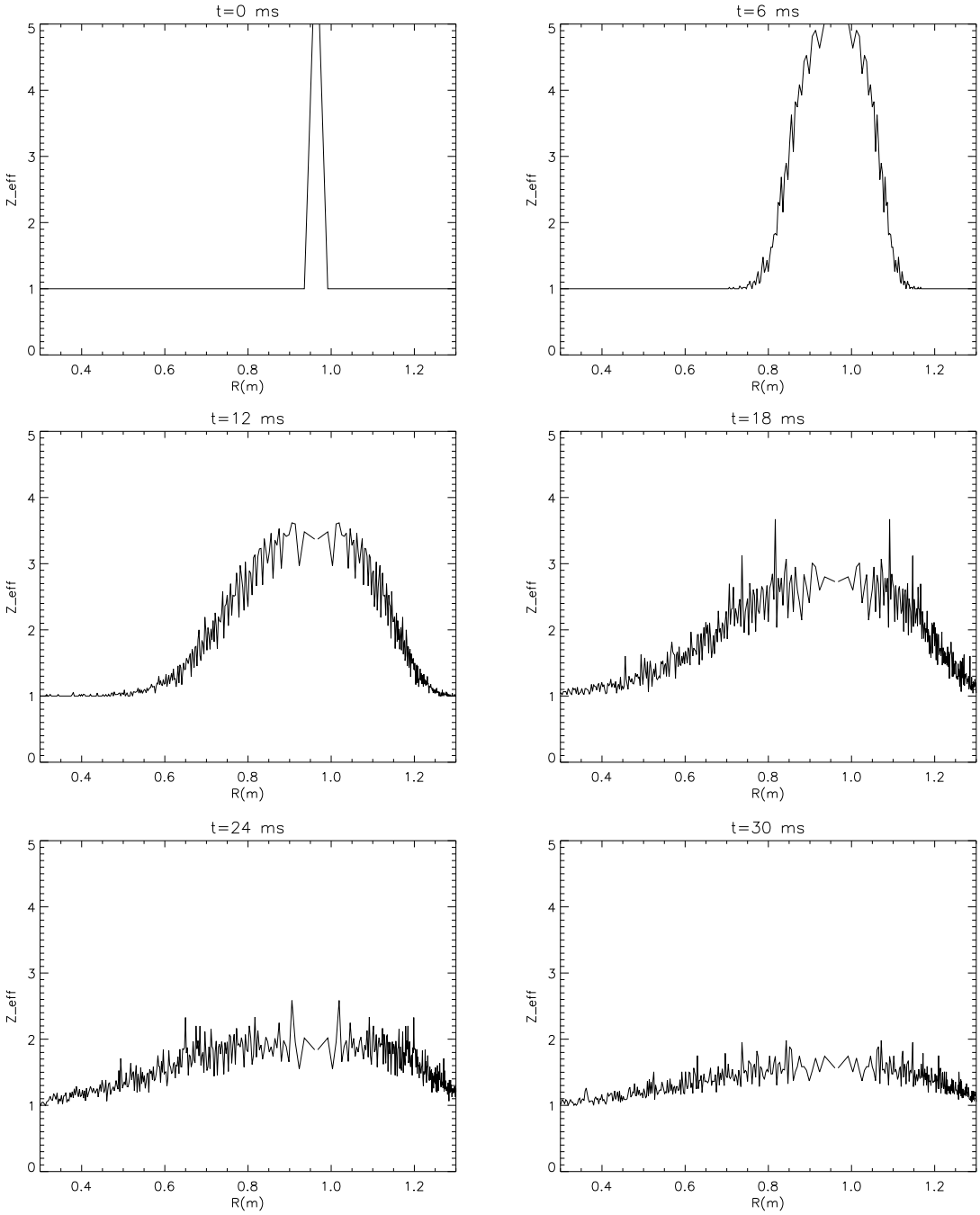

Figure 7.1: Plots of Z_{eff} for C^{6+} ions in counter-rotating case with bulk ion density profile model 2, taken at different times (t = 0, 6, 12, 18, 24 and 30 milliseconds respectively) throughout the simulation.

7.2.2 Improving the model

There are several extensions to our model that could be explored in conjunction with the radial profiles discussed in the previous subsection. In Chapter 6 we examined the simplest case of tokamak plasma rotation, namely rigid-body rotation of the

entire plasma. This is fine for a first approximation but in general tokamak plasmas do not rotate toroidally as a single rigid body: for example, Ghorannevis *et al.* have presented evidence from the CT-6B tokamak of non-rigid toroidal rotation of individual flux surfaces, a possibility that is implied by two-fluid analyses of tokamak equilibria, even in the absence of poloidal flows [95]. Allowing flux surfaces to rotate rigidly at different frequencies, with assumed rotation profiles modelled on experimental measurements such as those shown in Ref. [76] (see e.g. Figure 4 in this paper), would allow us to model more realistically the collisional transport of trace impurity ions in rotating MAST plasmas.

We comment, finally, that, as briefly discussed in the final paragraph of Chapter 6, turbulence plays a key role in determining so-called "anomalous" transport in tokamaks, with effects such as the formation of Internal Transport Barriers (ITB's), for example. ITB's are regions of relatively good confinement: the transport is thought to be locally reduced to roughly neoclassical levels in their immediate vicinity (although this could cause thermalised fusion alpha-particles to accumulate in the plasma core and dilute the fusion fuel). `CUEBIT` could potentially be used to study trace impurity transport at transport barriers since the usual orderings of neoclassical theory (in particular the assumption that particle orbit widths are small compared to the density scale length) do not necessarily apply in such cases [92]. The test particle simulation method could also be extended in a fairly straightforward manner to study trace impurity transport in a plasma with a prescribed spectrum of turbulence. This could be based either on experimental diagnostic information [105] or nonlinear numerical simulations of global tokamak turbulence [106,107]. For example, `CUEBIT` could be combined with the two-fluid global electromagnetic code `CUTIE` [106], the latter providing turbulent fields as input to the former.

Bibliography

[1] Prialnik D 2000 **An Introduction to the Theory of Stellar Structure and Evolution** (Cambridge)

[2] Hale G E 1908 **On the Probable Existence of a Magnetic Field in Sunspots** *ApJ* **28** 315

[3] Carroll B W, Ostlie D A 1996 **An Introduction to Modern Astrophysics** (Addison Wesley)

[4] Foukal P 1990 **Solar Astrophysics** (Wiley)

[5] Diver D 2001 **A Plasma Formulary for Physics, Technology, and Astrophysics** (Wiley-VCH)

[6] Priest E R, Forbes T G 2000 **Magnetic Reconnection** (Cambridge University Press)

[7] Hamilton B, McClements K G, Fletcher L, Thyagaraja A 2003 **Field-Guided Proton Acceleration at Reconnecting X-Points in Flares** *Solar Phys.* **214** 339.

[8] Aschwanden M J 2004 **Physics of the Solar Corona** (Praxis)

[9] Browning P K 1991 **Mechanisms of Solar Coronal Heating** *Plasma Phys. Control. Fusion* **33** 539

[10] Carrington R C 1859 **Description of Singular Appearance Seen on the Sun on September 1** *MNRAS* **20** p13-15

[11] Withbroe G L, Noyes R W 1977 **Mass and Energy Flow in the Solar Chromosphere and Corona** *Ann. Rev. Astron. Astrophys.* **15** 363

[12] Priest E R 1984 **Solar Magnetohydrodynamics** (Dordrecht)

[13] Parker E N 1988 **Nanoflares and the Solar X-Ray Corona** *ApJ.* **330** 474

[14] Tsuneta S 1997 **Moving Plasmoid and Formation of the Neutral Sheet in a Solar Flare** *ApJ.* **483** 507

[15] Lawson J D 1957 **Some Criteria for a Power Producing Thermonuclear Reactor** *Proc. Phys. Soc. B.* **70**

[16] Dendy R 1993 **Plasma Physics: An Introductory Course** (Cambridge)

[17] Gryaznevich M, Akers R, Carolan P G, Conway N J, Gates D, Field A R, Hender T C, Jenkins I, Martin R, Nightingale M P S, Ribeiro C, Robinson D C, Sykes A, Tournianski M, Valovic M, Walsh M J 1998 **Achievement of Record β in the START Spherical Tokamak** *Phys. Rev. Lett.* **80** p.3972

[18] Sykes A, Akers R J, Appel L C, Arends E R, Carolan P G, Conway N J, Counsell G F, Cunningham G, Dnestrovskij A, Dnestrovskij Yu N, Field A R, Fielding S J, Gryaznevich M P, Korsholm S, Laird E, Martin R, Nightingale M P S, Roach C M, Tournianski M R, Walsh M J, Warrick C D, Wilson H R, You S, MAST team, NBI team 2001 **First Results from MAST** *Nucl. Fusion* **41** 10

[19] See *http://www.fusion.org.uk/culham/annrep0607/index.html* for details

[20] Wesson J A 1997 **Tokamaks** 2nd edition (Oxford Clarendon Press)

[21] Solov'ev L S 1968 **Theory of Hydromagnetic Stability of Toroidal Plasma Configurations** *Sov. Phys. JETP* **26** 400

[22] Freidberg J P 1987 **Ideal Magnetohydrodynamics** (New York: Plenum)

[23] Kadomtsev B B 1992 **Tokamak Plasma: A Complex Physical System** (IoP Publishing)

[24] Chen F F 1984 **Introduction to Plasma Physics and Controlled Fusion** (Plenum)

[25] Miyamoto K 2006 **Controlled Fusion and Plasma Physics** (Taylor and Francis)

[26] Ware A A 1970 **Pinch Effect For Trapped Particles in a Tokamak** *Phys. Rev. Lett.* **25** 916

[27] Winter J 2000 **Dust: A New Challenge in Nuclear Fusion Research?** *Phys. Plasmas* **7** 10

[28] Winter J 1998 **Dust in Fusion Devices - Experimental Evidence, Possible Sources and Consequences** *Plasma Phys. Control. Fusion* **40** 1201-1210

[29] Neu R, Dux R, Kallenbach A, Pütterich T, Balden M, Fuchs J C, Herrmann A, Maggi C F, O'Mullane M, Pugno R, Radivojevic I, Rohde V, Slips A C C, Suttrop W, Whiteford A, and the ASDEX Upgrade team 2005 **Tungsten: an Option for Divertor and Main Chamber Plasma Facing Components in Future Fusion Devices** *Nucl. Fusion* **45** 209

[30] Dux R, Peeters A G 2000 **Neoclassical Impurity Transport in the Core of an Ignited Tokamak Plasma** *Nucl. Fusion* **40** 1210

[31] Swift D W 1996 **Use of a Hybrid Code for Global-Scale Plasma Simulation** *J. Comp. Phys.* **126** 109

[32] Hamilton B, Fletcher L, McClements K G, Thyagaraja A. 2005 **Electron Acceleration at Reconnecting X-Points in Solar Flares** *ApJ.* **625** 496

[33] Hamilton B 2005 **Particle Acceleration in Reconnecting X-Point Flare Models** *PhD. Thesis*

[34] See *www.nag.co.uk/nagware/mt/doc/g05ddf.html* for documentation

[35] Ermak D L, Buckholz H 1980 **Numerical Integration of the Langevin Equation: Monte Carlo Simulation** *J. Comput. Phys.* **35** 169

[36] Noci G 2003 **The Temperature of the Solar Corona** *Mem. S. A. It* **74** 704

[37] Doschek G A 1991 **High-Temperature Plasma in Solar Flares** *Phil. Trans. R. Soc. Lond. A* **336** 451

[38] Stasiewicz K 2006 **Heating of the Solar Corona by Dissipative Alfvén Solitons** *Phys. Rev. Lett.* **96** 175003

[39] Tsiklauri D, Sakai J-I, Saito S 2005 **Particle-in-Cell Simulations of Circularly Polarised Alfvén Wave Phase Mixing: A New Mechanism for Electron Acceleration in Collisionless Plasmas** *A&A* **435** 1105

[40] Porter L J, Klimchuk J A, Sturrock P A 1994 **The Possible Role of MHD Waves in Heating the Solar Corona** *ApJ* **435** 482

[41] Nakariakov V M, Verwichte E 2005 **Coronal Waves and Oscillations** *Living Rev. Solar Phys.* **2** 3

[42] Foullon C, Verwichte E, Nakariakov V M, Fletcher L 2005 **X-Ray Quasi-periodic Pulsations in Solar Flares as Magnetohydrodynamic Oscillations** *A&A* **440** L59-62

[43] Nakariakov V M, Foullon C, Verwichte E, Young N P 2006 **Quasi-periodic Modulation of Solar and Stellar Flaring Emission by Magnetohydrodynamic Oscillations in a Nearby Loop** *A&A* **452** 343-346

[44] Verwichte E, Nakariakov V M, Cooper F 2005 **Transverse Waves in a Post-flare Supra-arcade** *Astron. Astrophys. Lett.* **430** L65-68

[45] Cairns R A 1985 **Plasma Physics** (Glasgow: Blackie)

[46] Craig I J D, McClymont A N 1991 **Dynamic Magnetic Reconnection at an X-Type Neutral Point** *ApJ* **371** L41

[47] Hassam A R, Lambert R P 1996 **Shear Alfvénic Disturbances in the Vicinity of Magnetic Null X-Points** *ApJ* **472** 832

[48] Myra J R, D'Ippolito D A, Goedbloed J P 1997 **Generalized Ballooning and Sheath Instabilities in the Scrape-Off Layer of Divertor Tokamaks** *Phys. Plasmas* **4** 1330

[49] Bulanov S V, Syrovatskii S I 1981 **MHD Oscillations and Waves Near a Magnetic Null Line** *Sov. J. Plasma Phys.* **6** 661

[50] Bulanov, S V, Shasharina S G, Pegoraro F 1992 **Transformation of MHD Modes Near Magnetic Separatix Surfaces** *Plasma Phys. Control. Fusion* **34** 33

[51] McClements K G, Shah N, Thyagaraja A 2006 **The Coupling of Shear and Fast Alfvén Waves at a Magnetic X-Point** *J. Plasma Phys.* **72** 571

[52] Wentzel D G 1989 **Magnetohydrodynamic Wave Conversion and Solar-Wind Acceleration in Coronal Holes** *ApJ* **336** 1073

[53] Tsiklauri D 2006 **A Mechanism for Parallel Electric Field Generation in the MHD Limit: Possible Implications for the Coronal Heating Problem in the Two Stage Mechanism** *A&A* **455** 1073

[54] McClements K G, Thyagaraja A 2004 **Electron Inertial Effects on the Resistive Magnetohydrodynamic Spectrum of a Magnetic X-Point** *Plasma Phys. Control. Fusion* **46** 39

[55] Miller J A, LaRosa T N, Moore R L 1996 **Stochastic Electron Acceleration by Cascading Fast Mode Waves in Impulsive Solar Flares** *ApJ* **461** 445

[56] Stix T H 1992 **Waves in Plasmas** (New York: American Institute of Physics)

[57] Fisk L A 1976 **The Acceleration of Energetic Particles in the Interplanetary Medium by Transit Time Damping** *J. Geophys. Res.* **81** 4633

[58] Start D F H, Bartlett D V, Bhatnagar V P, Campbell D J, Challis C D, Cheetham A D, Corti S, Edwards A W, Eriksson L-G, Gill R D, Gottardi N A O, Hellsten T, Jacquinot J J, O'Rourke J, Mayberry M J, Moreau D,

Rimini F G, Salmon N A, Smeulders P, von Hellermann M 1990 **Electron Absorption of Fast Magnetosonic Waves by Transit Time Magnetic Pumping in JET** *Nucl. Fusion* **30** 2170

[59] Craig I J D, Watson P G 1992 **Fast Dynamic Reconnection at X-Type Neutral Points** *ApJ* **393** 385

[60] McLaughlin J A, Hood A W 2004 **MHD Wave Propagation in the Neighbourhood of a Two-Dimensional Null Point** *A&A* **420** 1129

[61] McClements K G, Thyagaraja A, Ben Ayed N, Fletcher L 2004 **Electron Inertial Effects on Rapid Energy Redistribution at Magnetic X-Points** *ApJ* **609** 423

[62] Huba J D 2000 **NRL Plasma Formulary** (Washington: Naval Research Laboratory)

[63] Priest E R 1982 **Solar Magnetohydrodynamics** (Dordrecht: Reidel)

[64] Mackay D H, Galsgaard K 2001 **Evolution of a Density Enhancement in a Stratified Atmosphere with Uniform Vertical Magnetic Field** *Solar Phys.* **198** 289

[65] Petrosian V, Huirong Y, Lazarian A 2006 **Damping of Mangetohydrodynamic Turbulence in Solar Flares** *ApJ* **644** 603

[66] von Steiger R, Geiss J, Gloeckler G, Galvin A B 1995 **Kinetic Properties of Heavy Ions in the Solar Wind from SWICS/Ulysses** *Space Science Reviews* **72** 71

[67] King D B, Nakariakov V M, Deluca E E, Golub L, McClements K G 2003 **Propagating EUV Disturbances in the Solar Corona: Two-Wavelength Observations** *A&A* **404** L1

[68] Williams D R, Phillips K J H, Rudawy P, Mathioudakis M, Gallagher P T, O'Shea E, Keenan F P, Read P, Rompolt B 2001 **High-Frequency Oscillations in a Solar Active Region Coronal Loop** *MNRAS* **326** 428

[69] Cooper F C, Nakariakov V M, Williams D R 2003 **Short Period Fast Waves in Solar Coronal Loops** *A&A* **409** 325

[70] Fourier J B J 1822 **La Théorie Analytique de la Chaleur** (Paris: Firmin Didot)

[71] Watson G N 1944 **A Treatise on the Theory of Bessel Functions, 2nd Edition** (Cambridge: Cambridge University Press)

[72] Akers R J, Helander P, Field A, Brickley C, Muir D, Conway N J, Wisse M, Kirk A, Patel A, Thyagaraja A, Roach C M and the MAST and NBI teams 2005 **Comparison of Plasma Performance and Transport Between Tangential Co- and Counter-NBI Heated MAST Discharges** *Proc. 20th IAEA Fusion Energy Conference* (Vilamoura, Portugal, 2004) paper EX/4-4 (Vienna: IAEA)

[73] Helander P, Akers R J and Eriksson L-G 2005 **On Neutral-Beam Injection Counter to the Plasma Current** *Phys. Plasmas* **12** 112503

[74] McClements K G, Thyagaraja A 2006 **Collective Electric Field Effects on the Confinement of Fast Ions in Tokamaks** *Phys. Plasmas* **13** 042503 (2006)

[75] Thyagaraja A, Schwander F, McClements K G 2007 **Rotation Driven by Fast Ions in Tokamaks** *Phys. Plasmas* **14** 112504

[76] Chapman I T, Hender T C, Saarelma S, Sharapov S E, Akers R J, Conway N J and the MAST Team 2006 **The Effect of Toroidal Plasma Rotation on Sawteeth in MAST** *Nucl. Fusion* **46** 1009

[77] Popov A M **Effect of Plasma Rotation on Neoclassical Tearing Modes in ITER** *Proceedings of the 33rd EPS Conference on Plasma Physics, Rome*, Vol. **30I**, P-1.106

[78] Liu Y Q, Chu M S, Garofalo A M, La Haye R J, Gribov Y, Gryazenich M, Hender T C, Howell D F, de Vries P, Okabayashi M, Pinches S D, Reimerdes

H and EFDA-JET contributors 2006 **Modelling of Resistive Wall Mode and its Control in Experiments and ITER** *Phys. Plasmas* **13** 056120

[79] Hinton F L, Wong S K 1985 **Neoclassical Ion Transport in Rotating Axisymmetric Plasmas** *Phys. Fluids* **28** 3082

[80] Wong S K 1987 **Transport of Impure Plasma with Arbitrary Toroidal Rotation** *Phys. Fluids* **30** 818

[81] Helander P 1998 **Neoclassical Transport in a Rotating Impure Plasma** *Phys. Plasmas* **5** 1209

[82] Romanelli M, Ottaviani M 1998 **Effects of Density Asymmetries on Heavy Impurity Transport in a Rotating Tokamak Plasma** *Plasma Phys. Control. Fusion* **40** 1767

[83] Smeulders P 1986 **Tomography of Quasi-Static Deformations of Constant-Emission Surfaces of High-Beta Plasmas in ASDEX** *Nucl. Fusion* **26** 267

[84] Alper B, Edwards A W, Giannella R, Gill R D, Ingesson C, Romanelli M, Wesson J, Zastrow K-D 1996 **Strong Asymmetries in Impurity Distributions of JET Plasmas** *23rd EPS Conf. on Controlled Fusion and Plasma Physics (Kiev, Ukraine)* ECA vol 20C part I p.163

[85] Wesson J A 1997 **Poloidal Distribution of Impurities in a Rotating Tokamak Plasma** *Nucl. Fusion* **37** 577

[86] Hsu C T, Sigmar D J 1990 **Transport Induced by Ion-Impurity Friction in Strongly Rotating, Collisional Tokamak Plasma** *Plasma Phys. Controlled Fusion* **32** 499

[87] Fülöp T, Helander P 1999 **Nonlinear Neoclassical Transport in a Rotating Impure Plasma with Large Gradients** *Phys. Plasmas* **6** 3066

[88] Newton S, Helander P 2006 **Neoclassical Momentum Transport in an Impure Rotating Tokamak Plasma** *Phys. Plasmas* **13** 012505

[89] Lin Z, Tang W M, Lee W W 1995 **Neoclassical Transport in Enhanced Confinement Toroidal Plasmas** *Phys. Plasmas* **2** 2975

[90] Wang W X, Hinton F L, Wong S K 2001 **Neoclassical Radial Electric Field and Transport with Finite Orbits** *Phys. Rev. Lett.* **87** 055002

[91] Chang C S, Ku S 2006 **Particle Simulation of Neoclassical Transport in the Plasma Edge** *Contrib. Plasma Phys.* **46** 496

[92] Kurki-Suonio T, Heikkinen J A, Lashkul S I 2007 **Guiding-Center Simulations of Nonlocal and Negative Inertia Effects on Rotation in a Tokamak** *Phys. Plasmas* **14** 072510

[93] Maschke E K, Perrin H 1980 **Exact Solutions of the Stationary MHD Equations for a Rotating Toroidal Plasma** *Plasma Phys.* **22** 579

[94] Savenko N, McClements K G, Thyagaraja A 2006 **Two-Fluid Equilibria of Rapidly-Rotating Spherical Tokamak Plasmas** *33rd EPS Conf. on Plasma Physics (Rome, Italy)* ECA Vol. 30I P-1.094

[95] Thyagaraja A, McClements K G 2006 **Toroidal and Poloidal Flows in Single-Fluid and Two-Fluid Tokamak Equilibria** *Phys. Plasmas* **13** 062502

[96] Helander P, Eriksson L-G, Akers R J, Byrom C, Gimblett C G, Tournianski M R 2002 **Ion Acceleration During Reconnection in MAST** *Phys. Rev. Lett.* **89** 235002

[97] Lyon J F, Isler R C, Murakami M, Bush C E, Dunlap J L, Howe H C, Jahns G L, Ketterer H E, Mihalczo J T, Neidigh R V, Paré V K, Wilgen J B 1977 **Relation of Neutral Beam Injection to Impurity Behaviour and Extension of Plasma Parameters in ORMAK** *8th European Conference on Controlled Fusion and Plasma Physics (Prague, Czechoslovakia)* (Prague: Czechoslovak Academy of Sciences) Vol 1, p 23

[98] Suckewer S, Eubank, H P, Goldston R J, McEnerney J, Sauthoff N R, Towner H H 1981 **Toroidal Plasma Rotation in the PLT Tokamak with Neutral-Beam Injection** *Nucl. Fusion* **21** 1301

[99] Burrell K H, Ohkawa T, Wong S K 1981 **Explanation of the Expulsion of Impurities from Tokamak Plasmas by Neutral-Beam Injection** *Phys. Rev. Lett.* **47** 511

[100] Thompson B J, Lysak R L 1996 **Electron Acceleration by Inertial Alfvén Waves** *J. Geophys. Res.* **101** 5359

[101] Stasiewicz K, Bellan P, Chaston C, Kletzing K, Lysak R, Maggs J, Pokhotelov O, Seyler C, Shukla P, Stenflo L, Streltsov A, Wahlund J-E 2000 **Small Scale Alfvénic Structure in the Aurora** *Space Sci. Rev.* **92** 423

[102] Fletcher L, Hudson H S 2008 **Impulsive Phase Flare Energy Transport by Large-Scale Alfvén Waves and the Electron Acceleration Problem** *ApJ.* **65** 1645

[103] Patel A, Carolan P G, Conway N J, Akers R J 2004 **Z_{eff} Profile Measurements from Bremsstrahlung Imaging in the MAST Spherical Tokamak** *Rev. Sci. Inst.* **75** 11

[104] Ghoranneviss M, Khorshid P, Wang L, Sari A H, Salem M K, Hojabri A 2005 **Investigation of Tokamak Plasmas as Non-Rigid Body Plasma** *32nd EPS Conf. on Plasma Physics (Tarragona, Spain)* ECA Vol. 29C P-4.065

[105] Donné A J H, van Gorkom J C, Udintsev V S,1, Domier C W, Krämer-Flecken A, Luhmann N C Jr, Schüller F C and TEXTOR team 2005 **Evidence for High-m Secondary Islands Induced by Large Low-m Islands in a Tokamak Plasma** *Phys. Rev. Lett.* **94** 085001

[106] Thyagaraja A 2000 **Numerical Simulations of Tokamak Plasma Turbulence and Internal Transport Barriers** *Plasma Phys. Control. Fusion* **42** B255

[107] Idomura Y, Tokuda S and Kishimoto Y 2003 **Slablike Ion Temperature Gradient Driven Mode in Reversed Shear Tokamaks** *Nucl. Fusion* **43** 234